

Heat Pipe Cooling of Metallurgical Furnace Equipment

by

Pietro Navarra

Department of Materials Engineering

McGill University, Montreal

A thesis submitted to McGill University
in partial fulfillment of the requirements of the degree of
Doctor of Philosophy

August 2006

© Pietro Navarra



Library and
Archives Canada

Bibliothèque et
Archives Canada

Published Heritage
Branch

Direction du
Patrimoine de l'édition

395 Wellington Street
Ottawa ON K1A 0N4
Canada

395, rue Wellington
Ottawa ON K1A 0N4
Canada

Your file Votre référence

ISBN: 978-0-494-32225-3

Our file Notre référence

ISBN: 978-0-494-32225-3

NOTICE:

The author has granted a non-exclusive license allowing Library and Archives Canada to reproduce, publish, archive, preserve, conserve, communicate to the public by telecommunication or on the Internet, loan, distribute and sell theses worldwide, for commercial or non-commercial purposes, in microform, paper, electronic and/or any other formats.

The author retains copyright ownership and moral rights in this thesis. Neither the thesis nor substantial extracts from it may be printed or otherwise reproduced without the author's permission.

AVIS:

L'auteur a accordé une licence non exclusive permettant à la Bibliothèque et Archives Canada de reproduire, publier, archiver, sauvegarder, conserver, transmettre au public par télécommunication ou par l'Internet, prêter, distribuer et vendre des thèses partout dans le monde, à des fins commerciales ou autres, sur support microforme, papier, électronique et/ou autres formats.

L'auteur conserve la propriété du droit d'auteur et des droits moraux qui protègent cette thèse. Ni la thèse ni des extraits substantiels de celle-ci ne doivent être imprimés ou autrement reproduits sans son autorisation.

In compliance with the Canadian Privacy Act some supporting forms may have been removed from this thesis.

Conformément à la loi canadienne sur la protection de la vie privée, quelques formulaires secondaires ont été enlevés de cette thèse.

While these forms may be included in the document page count, their removal does not represent any loss of content from the thesis.

Bien que ces formulaires aient inclus dans la pagination, il n'y aura aucun contenu manquant.


Canada

Abstract

Current water-cooling technology used in the metallurgical industry poses a major safety concern. In addition, these systems are expensive to operate and result in significant energy losses.

The purpose of the research presented in this thesis was to develop a viable cooling system based on novel heat pipe technology which addresses these problems. This technology employs boiling as the means to store and transfer heat energy. The large heat extraction capacity of the device is owed to two design features: firstly, a separate return line that generates a column of liquid working fluid which drains into the evaporator by gravity, and secondly, a helical flow modifier in the evaporator that stabilizes annular two-phase flow.

A full-scale copper tapblock and launder were designed with water-based heat pipe cooling systems. These systems were successfully tested under industrial heat loading conditions, using a gas burner to simulate the heat loads.

The tapblock cooling system was able to dissipate 142 kW per heat pipe, at heat fluxes as high as 2.4 MW/m^2 . These values are the largest to date using the novel water-based heat pipe technology. The launder system was the first to incorporate horizontal heat pipes, as well as have multiple evaporators feeding a single condenser.

The cooling systems used in both experiments were fundamentally safer than water-cooling systems, being operated at low pressures and with only several kilograms of water exposed to the heat source. The cooling water requirements of these systems represent a reduction of 80-95% compared to conventional water-cooling, with increased potential for energy recovery.

During the testing, dry-out and film boiling were identified as the main limitations. It was found that film boiling occurs when the flow in the evaporator is not great enough to generate a helical motion. The dry-out limitation was achieved when the velocity of the

flow within the evaporator was too great, causing a large pressure gradient that opposes the gravity head of the return line.

Both of these limitations are related to the configuration of the evaporator, i.e. the return line and the flow modifier. A methodology was developed to model the evaporator numerically using computational fluid dynamics. This methodology can be used to understand how the design parameters of the evaporator affect the flow patterns during operation.

Résumé

La technologie de refroidissement courante utilisée dans l'industrie métallurgique présente plusieurs problèmes de sécurité. De plus, ces systèmes sont coûteux à opérer et inefficaces énergétiquement.

L'objet des recherches présentées dans cette thèse est de développer un système de refroidissement viable basé sur une technologie de caloduc innovateur qui répond à ces besoins. Cette technologie utilise l'ébullition comme méthode de conservation et de transport de l'énergie thermique. La capacité d'extraction thermique considérable de cette technologie est attribuable à deux caractéristiques de conception: premièrement, une ligne de retour séparée produisant une colonne de fluide caloporteur qui est drainé dans l'évaporateur par gravité, et deuxièmement, un modificateur d'écoulement hélicoïdal dans l'évaporateur qui stabilise l'écoulement annulaire à deux phases.

Un bloc de coulée (*tapblock*) et une chute en cuivre de pleine grandeur ont été conçus avec des systèmes de refroidissement de caloduc basés sur l'eau. Ces systèmes ont été testés avec succès sous des bilans thermiques industriels, utilisant un brûleur pour simuler la chaleur.

Le système de refroidissement du bloc de coulée a réussi à dissiper 142 kW par caloduc, à des flux thermiques qui ont atteint $2,4 \text{ MW/m}^2$. Ces valeurs sont les plus hautes atteintes jusqu'à date avec la technologie de caloduc innovateur basée sur l'eau. Le système de chute a été le premier à incorporer des caloducs qui sont complètement horizontaux, et à posséder de multiples caloducs qui alimentent un seul condenseur.

Les systèmes de refroidissement utilisés dans les deux expériences sont fondamentalement plus sécuritaires que les systèmes de refroidissement d'eau conventionnels car ils sont opérés à basse pression et avec seulement quelques kilogrammes d'eau exposée à la source de chaleur. Les besoins d'eau de refroidissement de ces systèmes correspondent à une réduction de 80 à 95% par rapport aux besoins des

systèmes de refroidissement conventionnels, et ce, en plus d'un potentiel de recouvrement d'énergie plus élevé.

Durant les tests, l'assèchement (dry-out) et l'ébullition en film ont été identifiés comme les limitations majeures. Il a été déterminé que l'ébullition en film se produit quand l'écoulement dans l'évaporateur n'est pas assez grand pour générer une motion hélicoïdale. La limitation de séchage est survenue quand les vitesses de l'écoulement étaient trop élevées, causant un grand gradient de pression qui oppose la hauteur piézométrique de la ligne de retour.

Ces deux limitations sont reliées à la configuration de l'évaporateur, soit la ligne de retour et le modificateur de l'écoulement. Une méthodologie a été développée pour modéliser numériquement l'évaporateur en utilisant des logiciels de dynamique des fluides. Cette méthodologie peut être utilisée pour comprendre comment les paramètres de conception de l'évaporateur affectent le modèle d'écoulement durant l'opération.

Acknowledgements

I would like to thank my wife Adrienne Rispoli for her friendship and love. She was there with me through every painful and joyful step that I took. My successes are a reflection of the strength that she gives me.

I will always be grateful to have worked along side my thesis supervisor, Professor Frank Mucciardi. In a system which focuses increasingly on bureaucracy and administration, Professor Mucciardi has remained true to science, and to its implementation to better our society. Whenever I faced a problem which impeded my progress, his unwavering faith in the existence of a solution was both reassuring and inspiring. He had the wisdom to let me work independently and grow as a professional, and was a constant example of compassion through his dealings with others.

I would also like to express gratitude to my brother, Alessandro Navarra. I have learnt much from him despite being older. His raw determination and fearless pursuit of new challenges inspired me throughout my studies.

I would like to thank my friends Alexandre Blander and Hujun Zhao for their brilliance and insight. As well, this work would not have been successful without the experience and dedication of Walter Greenland and Robert Tariello at McGill, and Rudolf Verstappen at Umicore. I would also like to thank the researchers in Belgium for having believed in me: Maurits Van Kamp, Daniel Cheret, Mathias Chintinne, Tim Van Rompaey, Roderik Van Losenoord and Karel Verscheure.

I gratefully acknowledge and thank Canadian society for having given me the opportunity to better myself through the financial support of the Natural Sciences and Engineering Research Council of Canada. I would also like to acknowledge the financial support of Alcan Inc.

Dedicated to my father, Filippo Navarra, to whom I am indebted for his vision, intellect, and wide shoulders on which I am standing.

Table of Contents

ABSTRACT.....	I
RÉSUMÉ.....	III
ACKNOWLEDGEMENTS.....	V
TABLE OF CONTENTS.....	VII
LIST OF FIGURES.....	XI
LIST OF TABLES.....	XV
NOMENCLATURE.....	XVII
CHAPTER 1 INTRODUCTION.....	1
1.1 COOLING OF METALLURGICAL FURNACE EQUIPMENT – AN OVERVIEW.....	1
1.2 OBJECTIVES.....	2
1.3 THESIS ORGANIZATION.....	2
CHAPTER 2 LITERATURE SURVEY.....	4
2.1 WATER COOLING IN THE METALLURGICAL INDUSTRY.....	4
2.1.1 <i>Forced Convection Water Cooling</i>	4
2.1.2 <i>Concerns About Water Cooling</i>	5
2.1.3 <i>Trend Toward Process Intensification</i>	7
2.2 TAPHOLES.....	8
2.2.1 <i>Fundamentals</i>	8
2.2.2 <i>Importance to the Furnace</i>	8
2.2.3 <i>Copper or Refractory</i>	10
2.2.4 <i>Modern Copper Taphole Designs</i>	10
2.2.5 <i>Dynamic Nature of Tapping a Furnace</i>	13
2.2.6 <i>Effect of Process Intensification on the Taphole</i>	13
2.2.7 <i>Recent Improvements to Taphole Designs</i>	13
2.3 LAUNDERS.....	18
2.3.1 <i>Impact of Process Intensification on Launderers</i>	18
2.3.2 <i>Causes of Failure</i>	18
2.3.3 <i>Recent Improvements to Launderers</i>	18
2.4 THE NEED FOR ALTERNATE COOLING TECHNOLOGIES.....	20
2.5 BOILING HEAT TRANSFER	21

2.6	HEAT PIPE TECHNOLOGY.....	24
2.6.1	<i>Classical Heat Pipes.....</i>	24
2.6.2	<i>McGill Heat Pipes.....</i>	28
2.7	NUMERICAL MODELING TECHNIQUES.....	33
2.7.1	<i>Introduction to Numerical Modeling.....</i>	33
2.7.2	<i>Computational Fluid Dynamics.....</i>	33
2.7.3	<i>Solution Procedure.....</i>	34
2.7.4	<i>Sources of Error.....</i>	36
CHAPTER 3	HEAT PIPE COOLING OF A COPPER TAPBLOCK.....	37
3.1	INTRODUCTION.....	37
3.1.1	<i>Umicore and the Hoboken Blast Furnace.....</i>	37
3.1.2	<i>McGill Heat Pipe Cooling.....</i>	38
3.1.3	<i>Objective.....</i>	39
3.2	DESIGN CRITERIA.....	40
3.3	DESIGN, FABRICATION, AND EXPERIMENTAL SETUP.....	42
3.3.1	<i>Design Attributes.....</i>	42
3.3.2	<i>Experimental Setup.....</i>	47
3.3.3	<i>Sensors.....</i>	50
3.3.4	<i>Analysis of Design.....</i>	52
3.4	EXPERIMENTAL RESULTS.....	59
3.4.1	<i>Exploratory Test.....</i>	59
3.4.2	<i>Heat Extraction Capacity Test.....</i>	64
3.5	ANALYSIS OF RESULTS.....	67
3.5.1	<i>Modeling of the Experiment.....</i>	67
3.5.2	<i>Model Results.....</i>	70
3.5.3	<i>Simulation of Upset Conditions at the Hoboken Blast Furnace.....</i>	74
3.5.4	<i>Comparison with Conventional Water Cooling.....</i>	75
CHAPTER 4	HEAT PIPE COOLING OF A COPPER LAUNDER.....	78
4.1	INTRODUCTION.....	78
4.2	MODELING.....	79
4.2.1	<i>General Configuration of the Heat Pipe Cooled Launder.....</i>	79
4.2.2	<i>Operating Parameters and Assumptions.....</i>	80
4.2.3	<i>Material Properties.....</i>	81

4.2.4	<i>Geometry and Boundary Conditions</i>	83
4.2.5	<i>Flow Regime</i>	86
4.2.6	<i>Radiation Sub-Model</i>	86
4.2.7	<i>Monitors</i>	86
4.2.8	<i>Governing Equations and Solver Parameters</i>	88
4.2.9	<i>Initialization</i>	91
4.3	MODEL RESULTS	92
4.3.1	<i>Steady-State Model</i>	92
4.3.2	<i>Transient Model</i>	104
4.3.3	<i>Modeling Conclusions</i>	106
4.4	DESIGN, FABRICATION AND EXPERIMENTAL SETUP	107
4.4.1	<i>Design Attributes</i>	107
4.4.2	<i>Liquid Level Monitor</i>	112
4.4.3	<i>Analysis of Design</i>	117
4.4.4	<i>Experimental Setup</i>	119
4.5	RESULTS AND DISCUSSION	122
4.5.1	<i>Steady-State Testing</i>	122
4.5.2	<i>Impact Testing</i>	126
4.5.3	<i>Analysis of Results</i>	130
	CHAPTER 5 HEAT PIPE LIMITATIONS	140
5.1	INTRODUCTION	140
5.2	DRY-OUT LIMITATION	141
5.2.1	<i>Test Results</i>	141
5.2.2	<i>Operational Solution to Dry-out</i>	143
5.2.3	<i>Explanation of Dry-out</i>	144
5.2.4	<i>Elimination of Dry-out</i>	147
5.3	FILM BOILING LIMITATION	149
5.3.1	<i>Test Results</i>	149
5.3.2	<i>Explanation of Film Boiling</i>	152
5.3.3	<i>Elimination of Film Boiling</i>	153
5.3.4	<i>Copper Temperature Curves</i>	154
5.3.5	<i>Improved Startup Methodology</i>	155
5.3.6	<i>Improved Heat Pipe Design</i>	156
5.4	Maximizing the Heat Extraction Capacity	156

CHAPTER 6 EVAPORATOR MODELING METHODOLOGY.....	158
6.1 MODELING OF THE HEAT PIPE.....	158
6.2 OBJECTIVE.....	159
6.3 EVAPORATOR MODEL.....	159
6.3.1 Geometry.....	159
6.3.2 Meshing.....	162
6.3.3 Boundary Conditions.....	165
6.3.4 Material Properties.....	166
6.3.5 Governing Equations.....	166
6.3.6 Multiphase Models.....	167
6.3.7 Solution Procedure.....	167
6.3.8 Convergence.....	168
6.4 RESULTS.....	168
6.4.1 Single Phase Flow.....	168
6.4.2 Two-phase flow.....	171
CHAPTER 7 CONCLUSIONS.....	173
STATEMENT OF ORIGINALITY.....	176
REFERENCES.....	179
APPENDIX A SLAG LAUNDER RADIATION ANALYSIS.....	190

List of Figures

Figure 2.1	Decommissioned copper tapping block.....	9
Figure 2.2	Typical modern metal/matte taphole assembly.....	11
Figure 2.3	Typical modern slag taphole assembly.....	12
Figure 2.4	Profile of a metal taphole incorporating a waffled hotface.....	17
Figure 2.5	Modern copper launder design.....	19
Figure 2.6	Bottom of a launder with failure points.....	19
Figure 2.7	Natural and forced convection boiling curves.....	22
Figure 2.8	Internal forced convection boiling flow regimes.....	24
Figure 2.9	Classical heat pipe.....	25
Figure 2.10	Heat flux transformer.....	26
Figure 2.11	Saturated vapour pressure of water.....	30
Figure 2.12	Diagram of heat pipe design and operation.....	31
Figure 2.13	Typical CFD solution procedure.....	35
Figure 2.14	Meshed geometry and solution of a taphole.....	35
Figure 3.1	Simplified flowsheet of the Hoboken smelter	38
Figure 3.2	Drawing and diagram of the insert block at Hoboken.....	41
Figure 3.3	Diagram of the evaporator coupling section.....	43
Figure 3.4	Flow modifier used in the evaporator of a McGill heat pipe.....	43
Figure 3.5	Condenser design and fabrication.....	45
Figure 3.6	Dimensions of the tapblock and heat pipe cooling system.....	46
Figure 3.7	Installation of the condensers.....	47
Figure 3.8	Installation of the cooling water hoses and sensors.....	48

Figure 3.9	Experimental setup.....	49
Figure 3.10	Thermocouple positioning.....	51
Figure 3.11	Diagram of the evaporator.....	54
Figure 3.12	Exploratory test results.....	60
Figure 3.13	Burner applying a heat load to the tapblock.....	61
Figure 3.14	Left heat pipe temperature.....	63
Figure 3.15	Maximum cooling capacity test.....	65
Figure 3.16	Tapblock model meshing and boundary conditions.....	70
Figure 3.17	Left evaporator heat flux and \bar{v}_{\min} distribution.....	71
Figure 3.18	Temperature contours of the heat pipe-cooled copper tapblock.....	72
Figure 3.19	Modeling of upset condition at Hoboken.....	74
Figure 4.1	Refractory-based slag launder.....	78
Figure 4.2	Slag launder geometry.....	80
Figure 4.3	Slag heat capacity vs. temperature.....	82
Figure 4.4	Geometric parameters.....	84
Figure 4.5	Boundary conditions.....	85
Figure 4.6	Monitors.....	87
Figure 4.7	Temperature contours of the launder simulations.....	94
Figure 4.8	Convergence of the steady-state heat load.....	96
Figure 4.9	Steady-state evaporator heat flux.....	97
Figure 4.10	Convergence of the steady-state skull formation.....	99
Figure 4.11	Steady-state liquid fraction contours, HSF = 3 cm.....	100
Figure 4.12	Steady-state liquid fraction contours, HSF = 6 cm.....	100
Figure 4.13	Contours of surface heat flux.....	101

Figure 4.14	Velocity field of the slag channel.....	103
Figure 4.15	Transient results for HSF=3cm.....	105
Figure 4.16	Final slag launder drawings.....	109
Figure 4.17	Cast copper slag launder.....	109
Figure 4.18	Complete drawing and assembly of the slag launder/cooling system.....	110
Figure 4.19	Flow modifiers.....	111
Figure 4.20	Volume of liquid vs. voltage reading.....	113
Figure 4.21	Experimental liquid level sensor readings.....	114
Figure 4.22	Diagram of the liquid level monitor retrofitted onto the condenser.....	114
Figure 4.23	Liquid level monitor retrofitted onto the condenser.....	116
Figure 4.24	Experimental setup.....	119
Figure 4.25	Applying a heat load using the burner.....	120
Figure 4.26	Diagram of the sensor positioning.....	121
Figure 4.27	Steady-state test results.....	123
Figure 4.28	Impact test results.....	127
Figure 4.29	Breakdown of the assumed heat flux distribution.....	132
Figure 4.30	Temperature contours of the modeled 65 kW test.....	133
Figure 4.31	Evaporator heat flux contours during the 65 kW steady-state test.....	134
Figure 4.32	Comparison of copper launder temperature contours.....	136
Figure 4.33	Transient results for a copper-only launder, HSF=3cm.....	137
Figure 4.34	Average evaporator void fraction vs. heat load (steady-state).....	139
Figure 5.1	Dry-out test results (left side of the copper tapblock).....	142
Figure 5.2	Dry-out limitation in McGill heat pipes.....	144
Figure 5.3	Conceptual diagram of the tapblock heat pipe cooling system.....	146

Figure 5.4	Film boiling test results (copper launder).....	150
Figure 5.5	Hot spot in a McGill heat pipe after removing the flow modifier.....	153
Figure 5.6	Comparison of different flow modifiers.....	157
Figure 6.1	Geometric parameters of the evaporator.....	160
Figure 6.2	Examples of evaporator geometries.....	161
Figure 6.3	Typical equiangle skew distribution of the evaporator.....	164
Figure 6.4	Equiangle skew of a typical evaporator mesh.....	164
Figure 6.5	Gauge pressure, turbulent kinetic energy, and velocity magnitude contours of the evaporator (single phase flow).....	169
Figure 6.6	Cross-sectional slice of the evaporator velocity field.....	170
Figure 6.7	Axial slice of the return line discharge velocity field.....	170
Figure 6.8	Contours of liquid volume fraction in the evaporator.....	171

List of Tables

Table 2.1	NICICO taphole operating data.....	9
Table 2.2	Comparison of heat transfer mechanisms of liquids.....	21
Table 2.3	Properties of selected working fluids.....	28
Table 3.1	Cooling circuit data from the slag tapblock at Hoboken	40
Table 3.2	Typical heat fluxes encountered at different areas of a blast furnace.....	41
Table 3.3	Comparison of the evaporator and condenser thermal requirements.....	52
Table 3.4	Comparison of heat pipe laboratory dry-out conditions to the expected tapblock operating range.....	58
Table 3.5	Steady state operating parameters.....	64
Table 3.6	Summary of the solver parameters.....	68
Table 3.7	Comparison of the experimental and model temperatures.....	69
Table 3.8	Comparison of conventional forced convection and heat pipe cooling requirements.....	76
Table 4.1	Summary of the operating parameters and assumptions.....	80
Table 4.2	Material properties.....	81
Table 4.3	Slag composition.....	81
Table 4.4	Boundary conditions.....	85
Table 4.5	Reynolds number.....	86
Table 4.6	Summary of the solver parameters.....	90
Table 4.7	Summary of the steady-state model results.....	92
Table 4.8	Selected cross-sectional areas of the condenser and level monitor.....	115
Table 4.9	Predicted values of \bar{v}_{\min} for the HSF=3cm simulation configuration.....	118
Table 4.10	Comparison between the experimental and simulation results.....	131

Table 4.11	Equivalent cooling water requirement calculation summary.....	138
Table 5.1	Operating parameters of the right side of the tapblock.....	141
Table 5.2	Comparison of the tapblock test operating parameters and results.....	148
Table 5.3	Explanation and comparison of aggressive and passive flow modifiers...	157
Table 6.1	Evaporator geometric parameters.....	160

Nomenclature

Symbol	Description	Units
A	area	m^2
A_{mush}	the mushy zone constant	$kg/m^3 \cdot s$
c_p	specific heat	$J/kg \cdot ^\circ C$
D	hydraulic diameter	m
E	energy	J
g	gravitational acceleration	m/s^2
H	enthalpy	J
H_{fs}	latent heat of fusion	J/kg
H_{fg}	latent heat of vaporization	J/kg
h	heat transfer coefficient	$W/m^2 \cdot ^\circ C$
Δh	condenser height with respect to return line discharge	m
J	diffusion flux	$kg/m^2 \cdot s$
k	thermal conductivity	$W/m \cdot ^\circ C$
M	molecular weight	$kg/kmol$
m	mass flow rate	kg/s
P	pressure	Pa
Q	mass flow rate	m^3/s
q	heat load	W
q''	heat flux	W/m^2
r	radius	m
Re	Reynolds number	
S_{energy}	energy source term	$W/m^3 \cdot s$
S_{mass}	mass source term	$kg/m^3 \cdot s$
$S_{momentum}$	momentum source term	N/m^3
T	temperature	$^\circ C$
t	time	s

V	volume	m^3
v	velocity	m/s
x	position	m

Greek Characters Description

α	void fraction	
β	liquid fraction	
μ	dynamic viscosity	$Pa \cdot s$
θ	angle	radians
ρ	density	kg/m^3
σ	surface tension	N/m
υ	voltage	V

Subscripts Description

av	average
$c-s$	cross-sectional
cr	condenser reservoir
CHF	critical heat flux
cum	cumulative
eff	effective
$evap$	evaporator
H	hydraulic
l	liquid
llr	liquid level reservoir
max	maximum
min	minimum
p	pull (for the pull velocity)
ref	reference
rl	return line
sat	saturated
v	vapour

Superscripts	Description	
—	average	
•	rate	1/s

Operators	Description	
∇	gradient operator	1/m
$\nabla \cdot$	divergence operator	1/m

Chapter 1 Introduction

1.1 Cooling of Metallurgical Furnace Equipment – An Overview

Areas of a metallurgical furnace subjected to extreme conditions, such as tapholes or launders, are typically water-cooled. There are three main disadvantages to such systems: firstly, when operated beyond design parameters, catastrophic failure of the cooling channels may occur. Secondly, to compensate for the safety issue, excessively large quantities of water are passed through the cooling channels, leading to extensive and costly water-pumping infrastructure. Thirdly, because of the large quantities of water used, the heat energy extracted from the furnace equipment is of such low grade that it cannot be recovered or recycled economically for use elsewhere in the plant.

However, many engineers working in the field of process metallurgy accept forced convection water cooling as the status quo, and focus on improving and optimizing designs based on this technology. Indeed, there is a perception across the industry that when the cooling of metallurgical equipment is required, forced convection water cooling is the only option possible. This may be due to the fact that this technology and its application to industry has changed very little over the last century, and is now perceived as an absolute.

It is acknowledged that evaporation has tremendous potential as a heat transfer mechanism. However, the technology available which utilizes a phase change to transfer heat, referred to as the heat pipe, has several inherent limitations which prevent its use in high-intensity applications.

Recent advances in heat pipe technology have resulted in a new type of heat pipe with the following properties:

- the capacity, versatility and responsiveness to accommodate the heat loading conditions of a metallurgical furnace
- a cooling water circuit which is located remotely from the heat source
- requires little maintenance

- in the event of a failure, a catastrophic event can be avoided

1.2 Objectives

The purpose of the research presented in this thesis is the following:

- to design a heat pipe cooling system capable of cooling metallurgical furnace equipment
- to evaluate the effectiveness of the cooling system in addressing the safety, cost, and environmental concerns of the industry
- to further develop the theory explaining the operation of the novel heat pipe design, including the present limitations of the device

1.3 Thesis Organization

Chapter 2 reviews the literature pertaining to this thesis. A summary of the current state of cooling technology in the field of metallurgy is given. Forced convection water cooling is described together with some of the more demanding applications, particularly tapholes and launders.

A case is made to support the need for alternate cooling technology in the field of pyrometallurgy. Evaporation is identified as a suitable alternative heat transfer mechanism. Classical heat pipe technology is reviewed, and reasons are given explaining why this evaporation-based technology has not been implemented. A novel heat pipe recently developed at McGill University is described, and evidence of its applicability to metallurgical applications as a viable cooling technology is given.

Finally, numerical modeling is reviewed, as it was employed extensively in the design of the prototype equipment and in the analysis of the results presented in this thesis.

Chapters 3 and 4 describe the design and testing of a full-scale heat pipe-cooled copper tapblock and copper launder, respectively. In both cases, the cooling systems represent the first full-scale water-based cooling applications of their kind. The performance is

evaluated under industrial heat loads, and a comparison is made between the novel heat pipe technology and conventional forced convection cooling technology.

The theory explaining the operating limitations of the novel heat pipe cooling technology is developed in Chapter 5.

Chapter 6 presents progress made in the numerical modeling of the novel heat pipe. The purpose of the modeling is to understand the relationship between the configuration and operating limits of the device. It is the hope that future work in this field will lead to even safer heat pipe designs with greater cooling capacity and wider applicability.

Chapter 7 summarizes the conclusions of this work, and a statement of originality is appended.

Chapter 2 Literature Survey

2.1 Water Cooling in the Metallurgical Industry

Cooling of equipment is a fundamental need for the pyrometallurgical industry. The corrosive environments coupled with the elevated temperatures of numerous processes in this industry can cause the disintegration of even the most resistant materials available. Therefore furnace equipment which is subjected to these intense conditions must be cooled in order to retain its integrity.

There has traditionally been only one cooling option available to metal producers which delivers a large cooling capacity: a process known as “forced convection water cooling”, or simply “water cooling”. This technology essentially consists of pumping water through internal passages. The internal passages are typically cast into the furnace equipment during fabrication, and are positioned in a configuration that delivers sufficient cooling for the application [1, 2, 3].

2.1.1 Forced Convection Water Cooling

Heat transfer in forced convection water cooling systems is accomplished through the transfer of sensible energy (changes in temperature). The furnace equipment has a heat load applied to it from within the furnace. Energy is dissipated from the surface of the cooling channel ($T_{surface}$) to the cooling water which is at a lower temperature (T_{bulk}). The rate of heat transfer is given by Newton’s law of cooling:

$$q'' = \bar{h} \cdot (T_{surface} - T_{bulk}) \quad (2-1)$$

where q'' is the convective heat flux (W/m^2) and \bar{h} is the average convective heat transfer coefficient ($\text{W}/\text{m}^2 \cdot ^\circ\text{C}$). Therefore for a given application, a certain value of \bar{h} must be maintained to retain steady-state conditions.

In forced convection water cooling systems, the heat transfer coefficient is mainly controlled by the water velocity. Larger velocities increase the value of \bar{h} , enhancing heat transfer. In practice, water velocities are typically in the order of 1-3 m/s [4, 5, 6].

Cooling water is often demineralized to prevent deposits inside cooling channels, which act as a thermal resistance at the solid/fluid interface. Extensive water-pumping and recycling infrastructure is therefore required and is a significant contributor to overall capital and operational expenses of metallurgical furnaces [7].

2.1.2 Concerns About Water Cooling

2.1.2.1 Safety

Well-designed water cooling systems that are correctly operated are generally safe and effective. However operational difficulty can be encountered with the formation of a film of water vapour within one of the cooling channels. This can occur during a temporary increase in the applied heat flux during upset process conditions. The vapour film can be limited to a location in the cooling channel where a pressure drop exists, which reduces the local boiling temperature (in a badly designed cooling channel).

Once the vapour is present, it insulates the cooling channel and heat transfer from this hot spot to the water is reduced, contributing to a further increase in temperature (a situation known as “vapour-lock”, “steam blanketing” or “film boiling”) [8]. This results in a vicious cycle of decreased cooling capacity, increased surface temperature, and increasingly stable vapour lock. This vicious cycle eventually causes the cooling channel to get so hot that it starts to lose its integrity and a crack may form. The water then leaks into the furnace wall [9].

Many refractory materials react with water, and disintegrate rapidly, further compounding the heat load on the cooling channel. If the problem is not detected before this point, a complete cooling channel failure occurs, causing large quantities of water to contact the molten furnace products. Although cooling channel failures are relatively unlikely, the consequences are catastrophic. The result is a violent water or hydrogen explosion that can damage and blowout equipment and injure workers [10]. This encompasses the first disadvantage of water-cooling: safety [11, 12, 13].

2.1.2.2 Cost

The problem of safety leads into the next disadvantage of water-cooling: cost. In order to minimize the safety risks, water cooling systems are operated with comfortable safety margins. This implies that excessively large flow rates of water are used in order to increase the convective heat transfer coefficient (\bar{h}). This ensures that the cooling system can dissipate the required heat loads as sensible heat. However, expenses related to water demineralization, pumping and cooling are increased.

2.1.2.3 Waste Energy

The final disadvantage of water-cooling is that it produces waste energy. These cooling systems use excessive amounts of cooling water to avoid cooling channel failures. The heat energy extracted into the water is therefore very dilute. This being the case, it becomes very difficult to recover the energy stored in water that has only increased in temperature by 4-10°C, which is typically the case.

For example, the copper cooling elements around the tapping holes of the Stahlwerke Bremen blast furnace in Germany use 120 tonnes of cooling water per hour, 13% of the overall water requirements of the entire furnace hearth. The taphole cooling system has a designed capacity of 1.15 MW, which corresponds to a maximum water temperature increase of 8°C [14]. From an energy recovery standpoint, temperature increases of this order are not useful. Therefore, the heat extracted from the cooling systems is typically dissipated into the environment in cooling towers or large cooling basins.

2.1.3 Trend Toward Process Intensification

An increasingly competitive market has forced metal producers throughout the world to increase production rates without increasing the size of their furnaces. This trend has been termed *process intensification* in the literature, and is defined as maximizing returns by minimizing furnace size while maximizing throughput [4, 15].

2.1.3.1 Impact on Water Cooling Systems

Larger throughputs inevitably lead to larger heat loads and erosion rates. Therefore achieving process intensification without sacrificing furnace integrity has implied the incorporation of more extensive forced-convection water cooling systems.

A great deal of effort has been expended on how to optimize the configuration of the water cooling circuits in furnace cooling elements, and the results have been largely satisfactory. The development of numerical modeling techniques (described in section 2.7) and their application to furnace design has played a key role in these improvements [3].

However, the disadvantages of water cooling systems, namely safety, remain a concern even with the most sophisticated water cooling systems.

2.2 Tapholes

2.2.1 Fundamentals

One of the ways a molten product can be removed from a metallurgical furnace is via a taphole. The product is typically either slag, matte, or metal. A taphole is literally a hole within the side of a furnace wall. The side of the taphole facing the inside of the furnace is termed the *hotface*, whereas the side facing the environment is referred to as the *cold face*.

When necessary, the taphole is sealed using a clay plug, which upon insertion into the taphole, is baked and hardens, preventing the further tapping of any molten product from the furnace. To open the taphole, the clay insert is either drilled out, or is consumed by use of an oxygen lance, or both [7, 16].

2.2.2 Importance to the Furnace

The taphole is a particularly critical area of a furnace as local heat loads and furnace wall erosion rates are amplified as a result of the increased velocities in this vicinity [17]. Frequent drilling, plugging, and inaccurate oxygen lancing are additional contributors to the disintegration of the tapping channel [18, 19, 20].

In order to maintain the integrity and safety of this region, rigorous taphole maintenance and repair programs are exercised while the furnace is in operation. Nevertheless, the hotface of the taphole is eventually worn out and must be rebuilt during a total shutdown, and is often the limiting factor in a furnace campaign [4].

The decommissioned tapping block seen in Figure 2.1 is relatively small (Tapblock dimensions: 61cm x 46 cm x 23 cm, designed taphole diameter: 5cm), and was designed to tap copper matte from a copper smelter (NICICO, Iran). Note the external cooling pipes protruding from the bottom left side of the tapblock, and the baked plug sealing the taphole. The taphole, now resembling an oval rather than a circle, has an enlarged diameter of over 9 cm. The expansion of the taphole over its operating life is most likely due to drilling/lancing, and to the solubility of copper in copper matte.

The design heat load of the tapblock is 14 kW. The temperature increase of the cooling water used is only 4°C, illustrating the inefficient usage of the cooling water in order to prevent vapour formation in the cooling channels [21]. This translates into a water consumption rate of 40 l/min, which is relatively high considering the small heat load dissipated. Refer to Table 2.1.

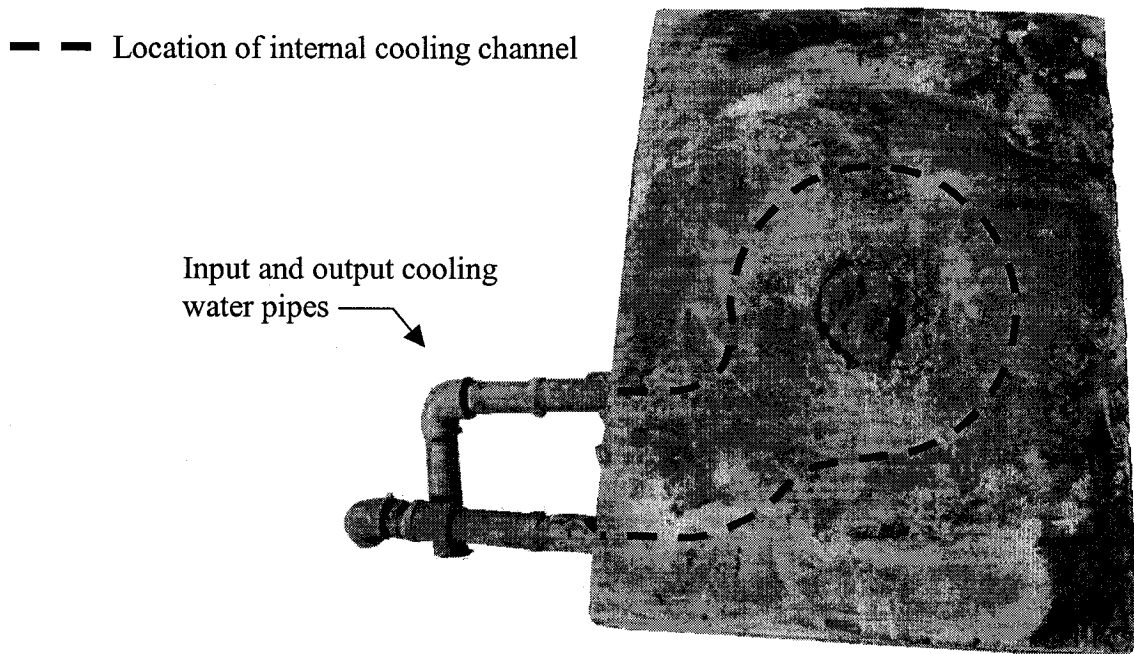


Figure 2.1 Decommissioned copper tapping block (NICICO)

Table 2.1 NICICO taphole operating data

Taphole diameter	5 cm
Cooling channel diameter	2.5 cm
Input water temperature	45°C
Output water temperature	49°C
Cooling water flow rate	40 l/min
Water velocity	1.32 m/s
Tapblock material	Cathodic copper
Heat load	13.7 kW

2.2.3 Copper or Refractory

There are generally two types of tapholes: refractory-based and copper-based. Refractory-based tapholes are simple to design and operate, but are vulnerable to erosion and thus offer limited campaign life. Copper-based tapholes have superior mechanical properties which lead to substantially longer campaign lives [17] and require less maintenance [4], but require cooling [8].

Process intensification together with the critical nature of the taphole to the furnace's productivity has caused a trend in industry to use copper tapblocks [22, 23, 24]. Because of their relevance to the present thesis, the focus of the remainder of this section will be on copper-based tapholes.

2.2.4 Modern Copper Taphole Designs

Conventional copper-based tapholes are composed of a block of copper, known as a *tapblock*, with a hole in the center through which the furnace product flows, referred to as the *taphole*. The taphole can be circular or square. Cooling channels are incorporated either by casting pipes into the copper block during its fabrication [17] or by the use of sand cores [25]. Copper block tapholes are particularly common in the non-ferrous industry [26].

A taphole is designed either to tap continuously, in which case it is rarely plugged during its life, or intermittently, where it is tapped and plugged frequently. Slag tapholes tend to be continuous or semi-continuous, whereas metals and matte tapholes tend to be intermittently tapped [17]. Metal and matte tapholes typically have diameters between 50 and 100 mm, whereas slag tapholes are larger, with diameters reaching up to 150 mm [26].

Modern metallurgical furnaces typically design tapholes consisting of more than a single module. The totality of the parts used to construct the area through which a furnace is tapped is known as the taphole assembly. Taphole assemblies vary significantly from one furnace to another, but also have many similarities.

Modern taphole designs can be roughly characterized into two categories: metal/matte tapholes, and slag tapholes, described in the following sections.

2.2.4.1 Matte/Metal Tapholes Assemblies

Figure 2.2 is a schematic of a standard taphole assembly typically used to tap metal, based on the design used at WMC Resources Olympic Dam in South Australia. This particular taphole extracts blister copper, and requires maintenance every 2-3 weeks (faceplate and refractory insert) [26].

This type of assembly is composed of four surround copper cooling blocks, one on each side of the main tapping block, along with a water-cooled copper faceplate. The four surround blocks enclose refractory brick in the center which forms the tapping channel [27]. The faceplate (or tapping block) secures a replaceable refractory insert [17]. The surround blocks reduce the operating temperature of the inner refractory bricks and thus increase their operating life, as well as solidify small amounts of metal/matte which may impregnate the refractory as it cracks from thermo-mechanical stresses [8]. The outer insert is most often replaced, as it is regularly damaged during the plugging and drilling/lancing operations [4]. The replacement procedure is a relatively minor one and can be done within a single shift [16, 28].

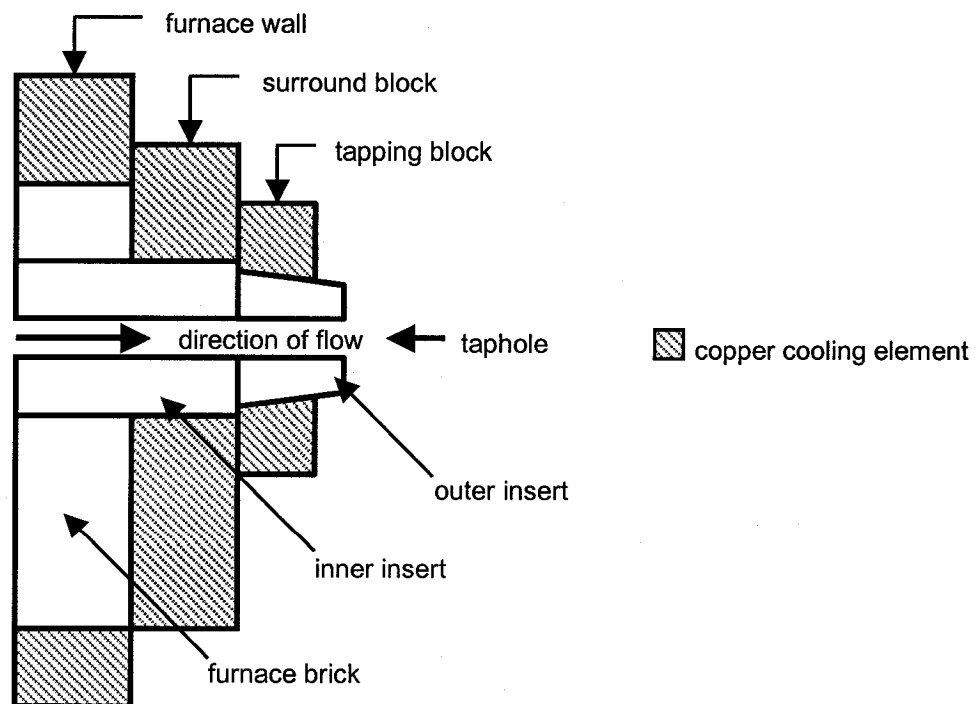


Figure 2.2 Typical modern metal/matte taphole assembly
(Olympic Dam, Australia)

2.2.4.2 Slag Taphole Assemblies

A typical modern slag tapblock consists of two water cooled modules: an inner host-block and an outer replaceable insert block secured to the host block with bolts [29]. Additional water-cooled copper elements are sometimes located below the taphole assembly to increase the life of the furnace wall in that area [17]. The host block is set deep into the furnace wall (approximately 0.5 m) and usually has a designed operational life of the entire furnace campaign (several years) [28]. Refer to Figure 2.3.

Slags have thermal conductivities which are a fraction of those encountered with matte or metal [4]. The heat fluxes that result are approximately one order of magnitude smaller than for matte/metal applications [8]. Therefore, the reduced heat fluxes allow for the omission of refractory inserts from the taphole assembly, as the slag freezes directly onto the copper elements and forms an insulating layer itself [29].

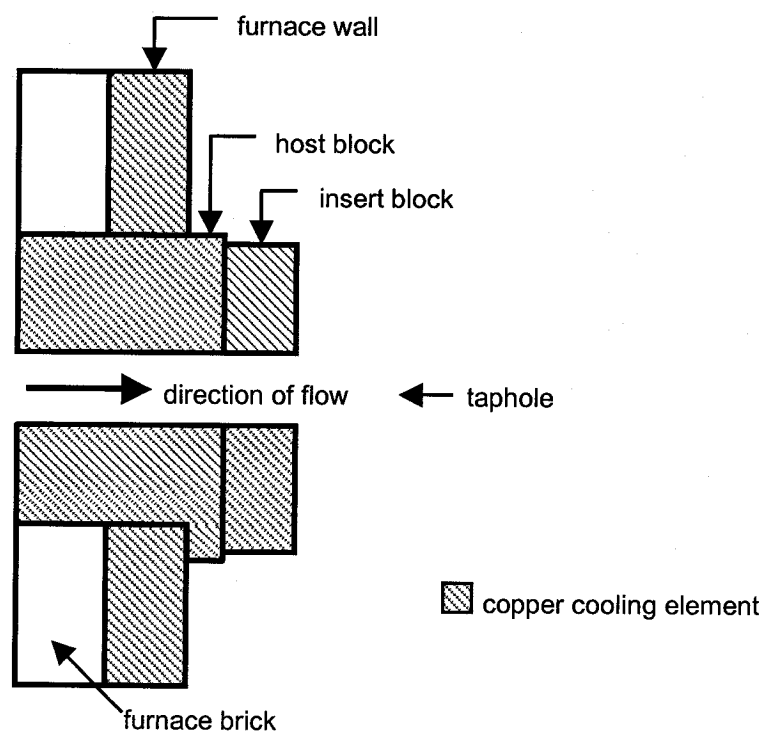


Figure 2.3 Typical modern slag taphole assembly
(Olympic Dam, Australia)

2.2.5 Dynamic Nature of Tapping a Furnace

Tapping molten product from a furnace is a complex procedure. Changing furnace parameters such as melt temperature, level, charge composition, and refractory integrity, often exhibit themselves during the tapping process through changes in product viscosity and corrosiveness, and on the thermal load applied to the taphole assembly. In addition, downstream plant requirements must be taken into account.

The complexity of tapping a furnace is the main reason why this procedure is particularly labour intensive. Despite the efforts made to automate as much of a metallurgical process as possible, even modern tapholes require the close attention of an experienced furnace operator during tapping and plugging operations [6, 22].

The frequent presence of furnace operators, together with the presence of large quantities of water passing in close proximity of the molten stream, makes the taphole one of the most hazardous areas of the furnace.

2.2.6 Effect of Process Intensification on the Taphole

The taphole is particularly affected by the larger throughputs as the increased flow of superheated molten material accelerates the already considerable erosion rate in this area of the furnace [28]. Existing tapholes are often inadequate to deal with these more aggressive conditions, and must therefore be upgraded [8]. These upgrades often consist of the replacement of refractory tapholes with copper ones, or with the introduction of more extensive cooling systems [13, 20, 30].

2.2.7 Recent Improvements to Taphole Designs

In the past, efforts to standardize furnace design methodology throughout the world had largely ignored the taphole. Many tapholes were awkwardly designed and consequently difficult to manage, leading to an unnecessarily higher risk to furnace operators [31, 32].

The widespread identification of the furnace taphole as a hazardous area in the 1990's lead to a strong response from industry and academia to re-evaluate current taphole design, maintenance, and operational practices [31]. The goal of such research was

primarily to minimize the risks to furnace operators, but also to reduce furnace maintenance and avoid production disruptions [4]. These innovations are summarized below.

2.2.7.1 Modular Design

Many modern tapholes are designed with a modular approach. The assembly is designed in such a way that modules which experience a higher degree of wear can be replaced while leaving the more structurally critical modules in their place. This approach enables for the maintenance of the taphole without the need for a complete furnace shutdown. The disadvantage of this system is that in the event of a cooling channel failure, the smaller components are more likely to be blown out from the furnace wall [26].

2.2.7.2 Interlocking Modules

By incorporating interlocking grooves, the modules of the taphole assembly retain each other in place, and reduce the risk of individual modules being ejected violently from the furnace wall in the event of a cooling channel failure [29, 32].

2.2.7.3 Refractory Inserts

The non-ferrous industry is tending to incorporate easily replaceable refractory inserts in the taphole assembly. The inserts protect the tapping channel, extending its life. However, thermal stressing of the refractory can lead to its eventual disintegration, and metal/matte seepage between the components of a modular design. Research is currently being done on wear monitoring systems within the refractory inserts based on embedded thermocouples [4].

2.2.7.4 Tapping Channel Geometry

Some metal producers have experimented with the geometry of the tapping channel by either widening or narrowing it towards the hot face of the furnace. The advantage of widening the taphole towards the hotface is that it minimizes the risk of drilling and lancing errors that damage the taphole and reduce its operational life. The disadvantage of this technique is that it becomes difficult to plug the taphole. Conversely, narrowing

the tapping channel towards the hot face facilitates the sealing of the tapping channel with a clay plug, but requires more accurate drilling and lancing techniques [22, 33].

2.2.7.5 Protective Faceplates

Some taphole assemblies include an easily replaceable faceplate whose function is to protect the more important components from drilling and lancing inaccuracy. The faceplates also keep the internal modules in compression in the axis parallel to the tapping channel, preventing the seepage of metal through cracks in the refractory insert. The faceplates are composed of either steel (not cooled) [4] or copper (cooled), and are fastened to the coldface of the taphole assembly [32].

2.2.7.6 Anhydrous Tapping Clays

Anhydrous tapping clays are the primary means of sealing the tapping channel at the conclusion of a tap. The clay is typically applied by use of an automatically fed mudgun, also known as a claygun [4, 16]. Anhydrous clays bake faster than classically used tapping clays, and have a higher success rate for producing a reliable seal of the tapping channel, making the area less hazardous to operators.

In conjunction with the use of anhydrous clays, some furnace operators use a soaking bar drill. This technique begins by hammering a steel bar through the center of the plug while it is baking. The conductivity of the steel bar from the melt within the furnace aids in the improved baking of the plug. Once tapping is desired, the bar is reverse-hammered out of the plug, yielding a consistently sized hole.

The disadvantage of this technique is that hammer drilling can dislodge/damage part of the taphole refractory. In addition, the insertion of the steel bar can dislodge the plug and involuntarily force it deep within the tapping channel [15].

2.2.7.7 Ceramic Plugs

While most tapholes are sealed using anhydrous clays which are baked once deposited, some furnace operators opt to use prefabricated solid ceramic plugs. This type of plug has a long steel bar cast into its center, which is used to ram the plug into the taphole.

This steel bar is then further used as a guide for lancing during reopening of the taphole. The advantages of this technique is that the plug can be rammed deep within the tapping channel to allow for the replacement of the outer taphole assembly modules, such as the outer insert and the tapping block. As well, the reopening of the taphole is much more predictable as the pre-baked ceramic plug has properties which are consistent from one plug to another, in contrast with anhydrous clays which are baked in-situ.

The disadvantage of this type of plug is that it is not conducive to conventional rotary drills, and must be pulverized using a hammer drill in order to initiate a tap. Over a long period of time, the impacting action of a hammer drill towards the interior of the furnace can be much more damaging to the integrity of the furnace wall and internal refractory brick, compared to a conventional rotary drill [26].

2.2.7.8 Waffle Cooling Elements

The development of a waffled copper cooling surface has led to the successful incorporation of such cooling elements in furnaces around the world. The technology consists of conventional copper cooling elements that have dove-tailed grooved surfaces rammed with castable refractory on the hotface. The grooves retain the refractory against the thermo-mechanical wear of the furnace environment. The refractory and copper are configured in a waffle pattern, such that in the event of excessive wear, the exposed surface will consist of a grid of copper and refractory. Therefore the copper surface is only ever partially exposed to the bath and can accommodate a certain degree of metal/matte seepage, which solidifies and therefore protects the internal cooling passages. Refer to Figure 2.4. This technology has been applied to copper block tapholes with some success. The taphole hotface is normally waffled, and in some cases, the tapping channel is waffled as well [25]. However, this technology is copper-intensive and therefore requires a large capital investment [8].

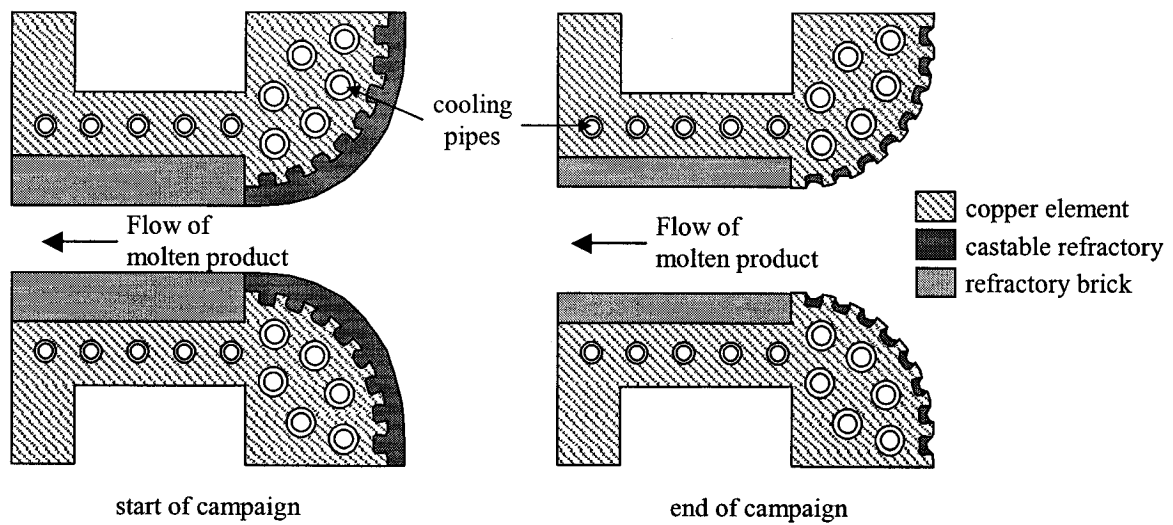


Figure 2.4. Profile of a metal taphole incorporating a waffled hotface [2-3]

2.2.7.9 Sensors to Detect the Onset of Failure

Research programs have been initiated which investigate the benefits of inserting multiple thermocouples within the taphole assembly. Data from these experiments are aimed at the identification of critical areas where the temperatures being measured can be indicative of the wear on the refractory inserts. The data can also help detect the occurrence of an unexpected event, such as vapour lock [29, 31]. The goal of the research is to predict the onset of failure in order to be able to take appropriate preventative measures [34, 35].

2.3 Launders

Launders are open conduits through which molten furnace products flow. Their main purpose is to transfer material from one process vessel to another. For example, launders are often joined to a furnace taphole, and channel molten products to downstream processing vessels, such as a ladle.

Similar to tapholes, launders are subjected to heat loads and erosion rates which are enhanced due to the flow, and can be either refractory or copper-based. Refractory launders do not need to be cooled, and can be easily repaired. However, they require frequent maintenance as refractory can break apart as a result of thermal cycling [7]. Copper launders require water cooling, and thus can lead to water explosions in the case of a failure. Cooling channels are often damaged after a failure and thus copper launders are rarely repaired. However, copper launders require little maintenance.

2.3.1 Impact of Process Intensification on Launders

Because a launder is not as critical to a furnace's operation as a taphole, many metal producers have opted for refractory-based designs in the past. Not surprisingly, with the obligation to increase throughputs in order to stay competitive, the use of copper launders is becoming popular due to their increased reliability and reduced downtime [16]. To reflect the content of this thesis, only copper launders are discussed.

2.3.2 Causes of Failure

The most common source of copper launder failures begins with the inaccurate monitoring of the phase levels within a furnace. This can result in accidentally tapping molten metal from a slag taphole, for example. The metal is then sent down a launder with a cooling system that is significantly underdesigned.

2.3.3 Recent Improvements to Launders

Launders have received significantly less attention in the literature compared to tapblocks. Therefore designs are often based on the metal producer's past practices and experiences. However, there exists a handful of engineering companies which specialize in launder design and fabrication. Selected modern design features are described in the following two subsections.

2.3.3.1 Safer Cooling Channel Configuration

The application of numerical modeling techniques in recent years has lead to new copper launder designs with minimal risks associated with water cooling. For example, the thermal profile of many modern designs no longer require the inclusion of cooling pipes directly below the launder channel. Refer to Figure 2.5.

Therefore in the case of a failure, which typically occurs through the bottom of the launder, the molten product does not contact the water channels [5].

2.3.3.2 Controlled Failure

Failure points can be designed into the bottom of the launder. These points consist of sections where the copper wall is thin (Figure 2.6). In the case where the launder is thermally overloaded, these copper sections burn-through, and the molten product flows out of the launder and into an emergency pit [5].

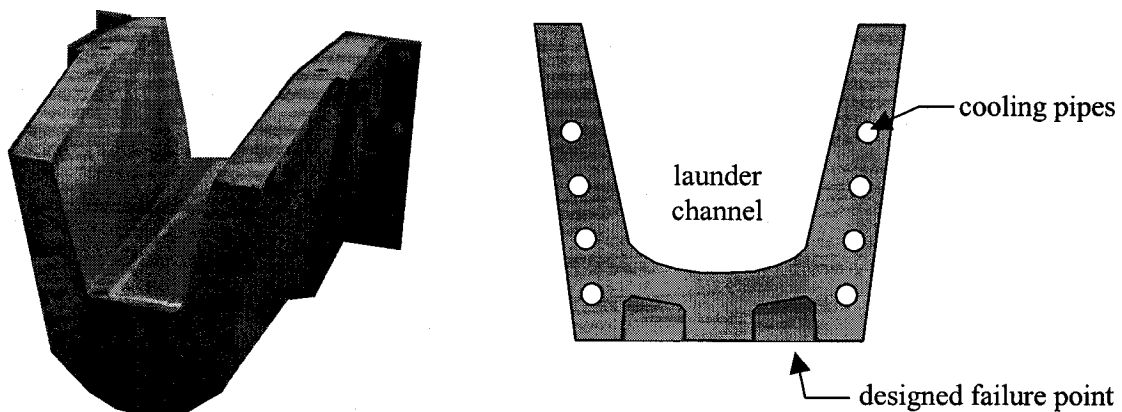


Figure 2.5 Modern copper launder design

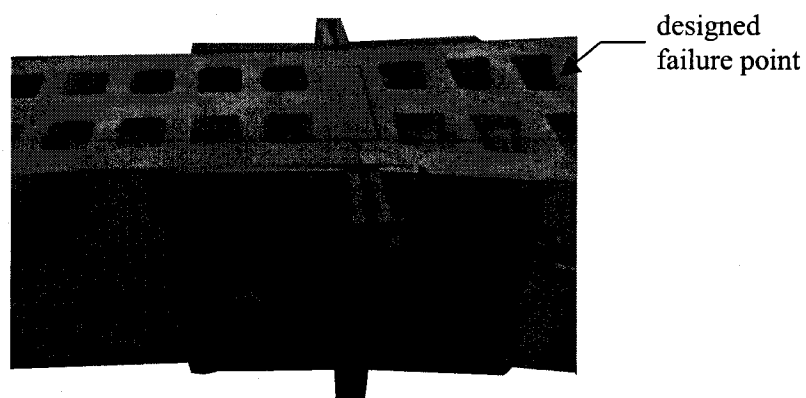


Figure 2.6 Bottom of a launder with failure points

2.4 The Need for Alternate Cooling Technologies

As summarized in the previous sections, the approach to address the safety problem associated with water cooled furnace equipment has been the following:

- to optimize cooling system designs, often with bolstered cooling water flow rates [7, 36]

For example, Gulf Chemical and Metallurgical Corporation redesigned their tapblocks with additional cooling elements near the hot face and with increased water flow rates to suppress film boiling [29]. The flow rates in the more modern tapblocks can reach velocities as high as 8 m/s [4].

- to develop a reliable means to predict an impending failure in order to avoid a catastrophic event [7]

For example, following a series of water explosions caused by refractory wear of the inner insert of their matte tapblock assembly which actually dislodged their tapblock, Olympic Dam Smelting replaced their original graphite insert with a silicon carbide one, as the latter wears more evenly and predictably [26].

When analyzing these modifications, Trapani writes that: “this does not change the fact that the underlying design flaw that permitted the explosion was the proximity of cooling water to the (molten product) stream” [26].

Despite the current paradox, very little research aimed at the reevaluation of forced convection water cooling has been initiated in recent years. Therefore no alternatives have been developed. As a result, metal producers have little choice but to use conventional water cooling systems to meet their furnace cooling requirements, as this is presently the only commercially available technology.

2.5 Boiling Heat Transfer

Boiling, or *convection with a phase change*, is defined as evaporation occurring at a solid-liquid interface. Utilizing the latent heat of vaporization as a means to store and transfer heat can greatly enhance heat transfer. For example, one can store only 405 Joules into a single gram of water as sensible heat by increasing its temperature from 0°C to 100°C. However, by boiling this same gram of water (without a temperature change) at 100°C, one can store 2260 Joules. This concept is further illustrated in Table 2.2, which compares typical ranges of heat transfer coefficients for forced convection and convection with a phase change. Refer to Newton's law of cooling (2-1).

Table 2.2 Comparison of heat transfer mechanisms of liquids [27]

Cooling process	Heat transfer coefficient, \bar{h} (W/m ² ·K)	Technology
forced convection	100 – 20,000	water cooling
convection / phase change	2,500 – 100,000	heat pipe

Nukiyama identified the existence of several boiling regimes [37], namely natural convection boiling, nucleate boiling and film boiling. His experiment consisted of passing an electrical current through a wire (platinum or nichrome) immersed in water at atmospheric conditions. By measuring the power through the wire, the temperature of the wire ($T_{surface}$) and the temperature of the water which was maintained at the saturation temperature (T_{sat}), the classical boiling curve shown in Figure 2.7 was constructed.

This curve delineated by points A to E describes pool boiling. The x-axis represents the temperature difference across the thermal boundary layer at the solid/liquid interface ($T_{surface} - T_{sat}$). The y-axis represents the heat flux (q'') being removed from the wire.

The curve between points A and B represents natural convection boiling, where bubbles are being formed on isolated spots and fluid mixing occurs principally by natural convection. The curve between points B and C represents nucleate boiling, where the surface becomes densely populated with bubbles, and bubble separation induces considerable mixing. Point C is the critical heat flux (CHF), beyond which film boiling is initiated. From point C to point D, partial film boiling occurs, whereas the section between point D and point E represents fully developed film boiling.

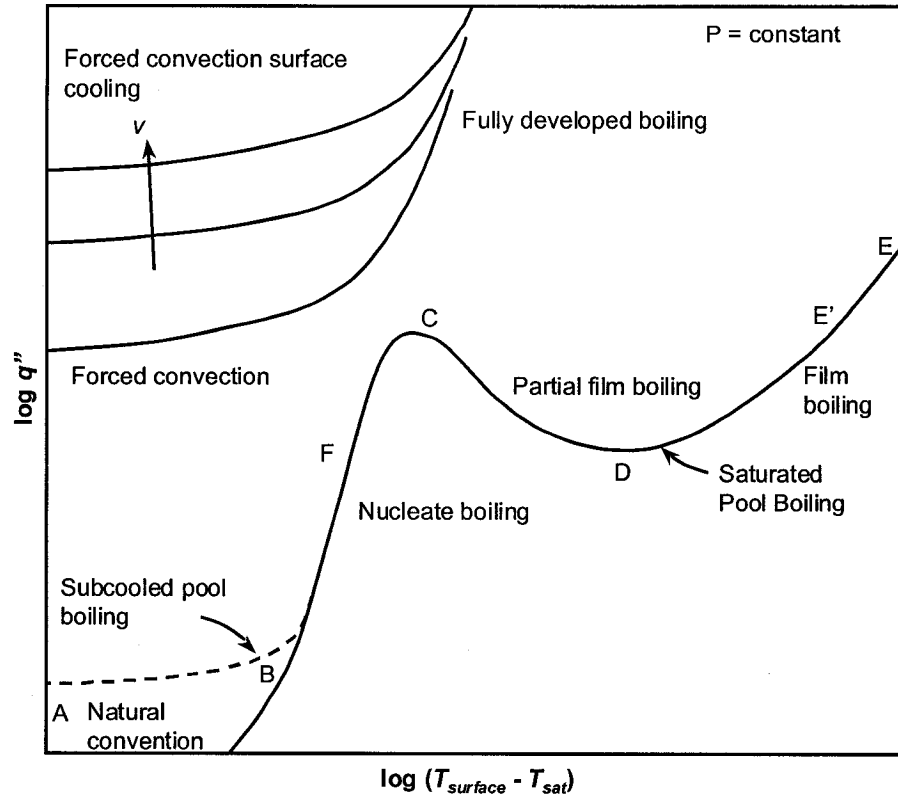


Figure 2.7 Natural and forced convection boiling curves [36]

Film boiling occurs when the vapour bubble density at the solid/fluid interface is large enough to cause coalescence. This forms a stable vapour film, which encompasses a large thermal resistance and temporarily reduces heat transfer. During this time, the applied heat load is not being completely removed from the solid. Therefore, the surface temperature increases until steady-state is again achieved (point E'). Equation (2-2) can be used to predict the critical heat flux for nucleate pool boiling [39, 40, 41].

$$q_{CHF}'' = 0.149 H_{fg} \rho_v \left[\frac{\sigma g (\rho_l - \rho_v)}{\rho_v^2} \right]^{1/4} \quad (2-2)$$

where

q_{CHF}'' is the critical heat flux (W/m²)

H_{fg} is the latent heat of vaporization of the fluid (J/kg)

ρ_v and ρ_l are the densities of the vapour and liquid, respectively (kg/m³)

σ is the surface tension (N/m)

g is the gravitational acceleration normal to the surface (m/s²)

Assuming that ρ_v is much smaller than ρ_l , equation (2-2) implies that the critical heat flux increases with:

- fluids with larger values of H_{fg}
- larger vapour densities (at larger pressures)
- larger body forces normal to the solid surface

In practice, heat exchangers which utilize boiling to transfer heat are operated in the nucleate boiling regime. In the case where the heat flux is beyond the CHF of the heat exchanger, film boiling results in surface temperatures, $T_{surface}$, which lead to failure. Therefore using boiling as a heat transfer mechanism is a double-edged sword: although very large heat transfer coefficients are attainable, care must be taken never to attain the critical heat flux and induce film boiling.

The curves in the upper-left corner of Figure 2.7 represent forced convection boiling, or *two phase flow* for internal systems. These curves describe situations where the fluid motion is induced by external means as well as by natural convection and bubble-induced mixing. Note that with a given liquid saturation temperature, T_{sat} , and a given interfacial wall temperature, $T_{surface}$, a larger heat extraction from the wall is achieved with forced convection boiling. Also note that the curves shift upwards with an increased velocity. This is due to the turbulence which tends to break apart and transport away vapour bubbles from the surface, preventing the formation of a stable vapour film and suppressing film boiling [42, 43].

Figure 2.8 illustrates the forced convection boiling flow regimes inside a tube. They are (in order of increasing vapour fraction): the bubbly flow regime, the slug flow regime, the annular flow regime, the transition regime, and the mist flow regime. Therefore heat exchangers which utilize forced convection boiling should be operated in the annular flow regime to attain maximum heat extraction capacity, as seen on the graph in Figure 2.8.

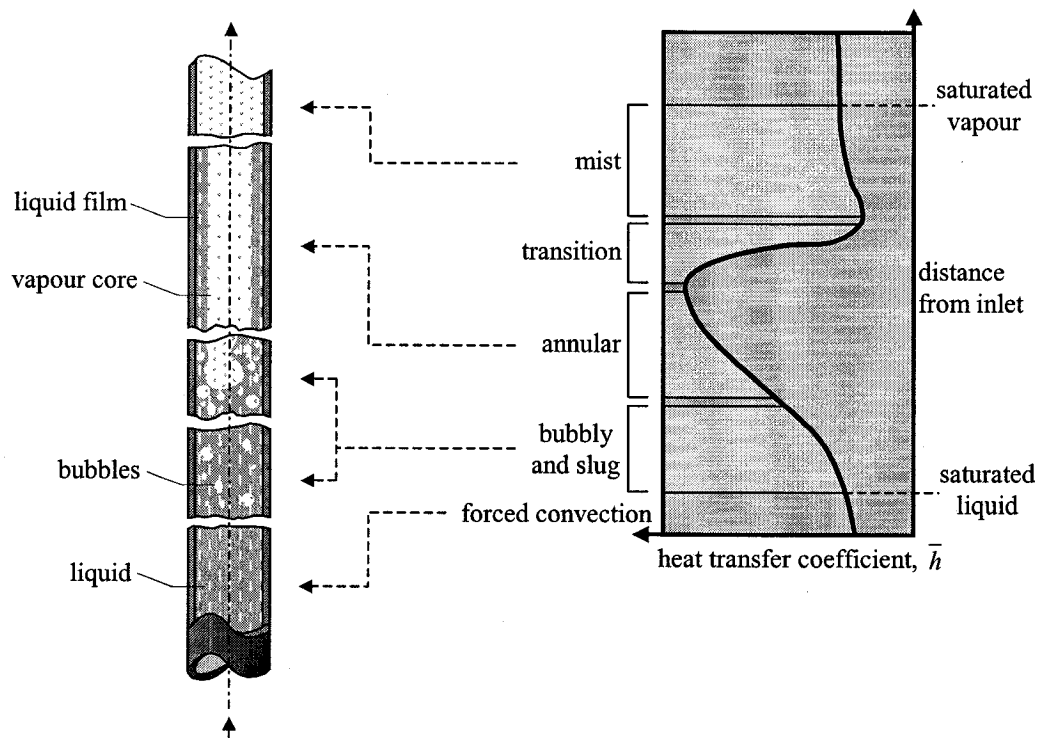


Figure 2.8 Internal forced convection boiling flow regimes [42]

2.6 Heat Pipe Technology

2.6.1 Classical Heat Pipes

2.6.1.1 Historical Development

The notion that boiling can be used to efficiently cool equipment is what initially inspired scientists to develop the device known as the heat pipe. The classical heat pipe was invented in the 1960s as part of the US space program [45, 46], and has matured into a standard heat transfer device [47].

Present applications of classical heat pipes include electronics, plastic mould injection, cryogenic medicine, and cutting tools. Possibly the most renowned application of heat pipes is in the Trans-Alaskan pipeline where heat pipes function as thermal diodes and are used to stabilize the permafrost foundation of the pipeline. In space applications, heat pipes are used as temperature equalization devices in orbital platforms such as satellites, where one side is exposed to the intense radiation of the sun and the other side is exposed to deep space [48, 49, 50].

2.6.1.2 Design and Operation

A heat pipe is a sealed container of any shape that is evacuated of any substance other than an appropriate working fluid (Figure 2.9). Therefore the working fluid exists both as a liquid and a gas within the container, and is constantly at the saturation pressure and temperature, i.e. the working fluid is constantly at its boiling point. The basic construction of a classical heat pipe consists of the following:

- an evaporator section, where an external heat source is applied
- a condenser section, where external cooling is applied
- a capillary structure (wick)

Working fluid inside the device is boiled in the evaporator, is then transported to the condenser as a vapour via pressure-driven flow, and is then subsequently condensed. The condensed working fluid is returned to the evaporator primarily by capillary forces supplied by the wick [51, 52].

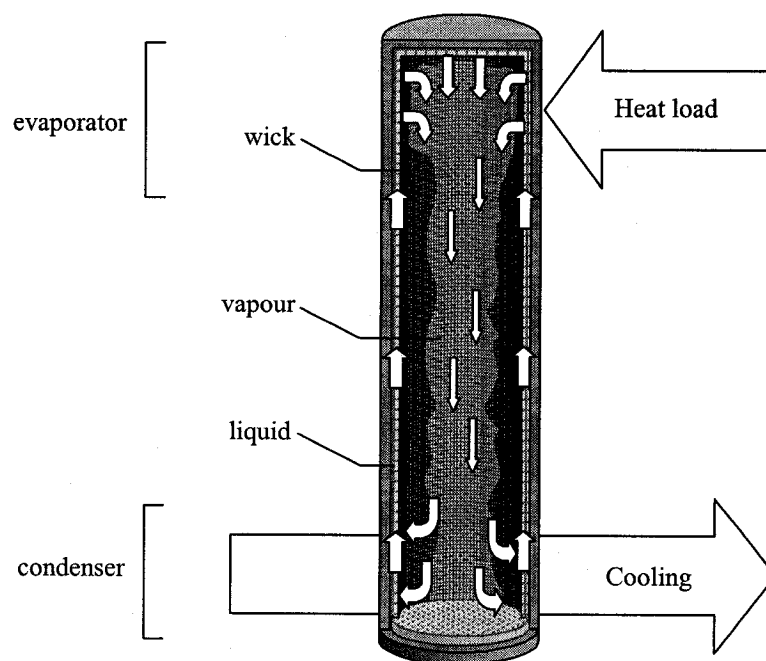


Figure 2.9 Classical heat pipe

Heat energy is stored in the working fluid as a phase change. In the evaporator, the following process occurs:

liquid + heat from heat source \rightarrow vapour

And in the condenser, the following occurs:

vapour \rightarrow liquid + heat to external cooling circuit

Therefore by adding the above equations, the overall process at steady-state is:

heat from heat source \rightarrow heat to external cooling circuit

2.6.1.3 Properties of the Classical Heat Pipe

The numerous advantages of heat pipes were quickly observed and include the following:

- Ability to dissipate considerable heat loads over appreciable distances with a minimal temperature drop
- The ability to act as a thermal flux transformer (see Figure 2.10)
- No external work is required on the system

Other advantages include exceptional flexibility, simple construction, and ease of control [53].

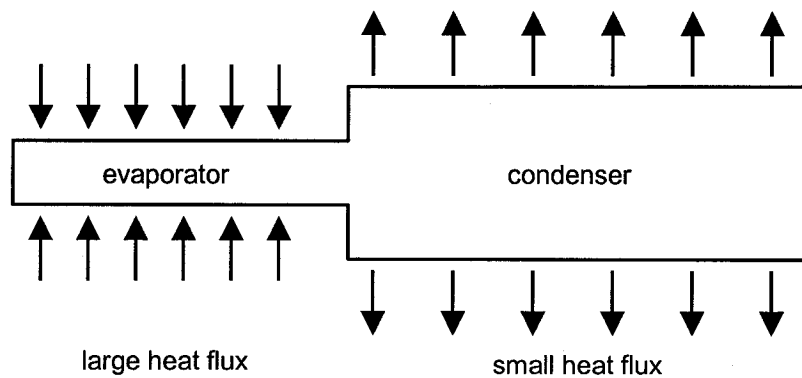


Figure 2.10 Heat flux transformer

2.6.1.4 Limitations of the Classical Heat Pipe

There exist several limitations which can diminish or arrest heat transfer in the classical heat pipe. Some of the less significant limitations include the vapour pressure limit, the sonic limit, the flooding limit, and the dry-out limit. The three most significant limitations of classical heat pipes are the capillary, entrainment and film boiling limitations [53]:

- The Capillary Limitation: For a given heat load, the capillary limitation occurs when the capillary forces provide inadequate pumping of the working fluid to keep the wick saturated with liquid in the evaporator. This results in the progressive dry-out of the wick starting from the end furthest from the condenser.
- The Entrainment Limitation: The flow of fluid within conventional heat pipes is counter-current: i.e. the vapour travels from the evaporator to the condenser, and liquid travels from the condenser to the evaporator. Therefore, a shear force exists at the free liquid/vapour interface. The entrainment limitation occurs at large vapour velocities where a significant portion of the returning liquid can be entrained into the vapour stream, causing evaporator dry-out.
- The Film Boiling Limitation: In a classical heat pipe, the wick is the primary means by which liquid working fluid refluxes the evaporator. However, at elevated heat fluxes, vapour formed at the liquid/gas interface can expel liquid working fluid from the wick. The porous nature of the wick can effectively trap the vapour, stabilizing a vapour film, and enhancing film boiling.

The inherent limitations of classical heat pipes have impeded the realization of boiling's full potential as a heat transfer mechanism, and thus heat pipes have only been successful in applications with relatively small heat fluxes and heat loads. These limitations have effectively prevented the metallurgical industry from using heat pipes as heat exchangers.

2.6.2 McGill Heat Pipes

2.6.2.1 Development

Recent research at McGill University has led to the development of a specialized heat pipe, referred to in the literature as a “McGill heat pipe” [54, 55, 56, 57]. This type of heat pipe is capable of overcoming the traditional limitations encountered at large heat loads and heat fluxes [58]. In this thesis, the term “heat pipe” refers to the novel design recently developed at McGill University.

Laboratory experiments conducted by Yuan in 2002 indicated that the new design had sufficient heat extraction capacity to operate in high intensity applications [59]. Several applications were developed in parallel with the work presented in this thesis, and include oxygen injection for metallurgical furnaces [60], light metals permanent mould cooling [61, 62, 63, 64, 65], and cooling for light metals thermal analysis probes [66, 67, 68].

2.6.2.2 Design and Operating Principles

Similar to conventional heat pipes, McGill heat pipes consists of three main components: a sealed vessel composed of a condenser and an evaporator section, as well as a working fluid contained within. The working fluid used in McGill heat pipes is usually either water or sodium, based on (1) their favourable properties suited for high heat fluxes, and (2) operating temperatures which fall within those desired for metallurgical applications.

Table 2.3 Properties of selected working fluids

Working fluid	Typical operating temperatures	Critical heat flux
water	80 - 180°C	1.5 MW/m ²
sodium	550 - 850°C	~ 10 MW/m ²

Because of the many similarities to classical heat pipes, further details of McGill heat pipes will concentrate on the unique features and their function.

2.6.2.2.1 Reservoir and Return Line

The most radical deviation from classical heat pipe design is that McGill heat pipes do not contain a capillary wick and rely solely on gravity to return the condensed working fluid to the evaporator. Therefore the condenser section of a McGill heat pipe must be located above the evaporator section. The return of liquid working fluid is done via a pipe referred to as *the return line*.

The role of the return line is to provide a separate path through which the liquid can travel down to the bottom of the evaporator. Thus liquid can be returned to the evaporator without any entrainment from the rising vapour. This is possible because of the pressure head between the reservoir and the return line discharge.

The reservoir is a section at the bottom of the condenser in which condensed working fluid collects. The return line drains liquid from the reservoir into the evaporator.

It should also be mentioned that an excess of liquid typically flows through the return line to the evaporator, the excess being entrained by the vapour back to the condenser. This has the effect of transforming the evaporator section of McGill heat pipes into co-current devices, rather than counter-current, as is the case with classical heat pipes. To make this more clear, consider the return line as part of the condenser. Therefore liquid is being fed from the bottom of the evaporator, and is entrained with the rising vapour, feeding liquid to the remainder of the evaporator from the bottom to the top.

Therefore the liquid entrainment caused by the co-current vapour flow in McGill heat pipes is used to distribute the liquid along the entire length of the evaporator. This is in contrast to classical heat pipes where liquid entrainment caused by the counter-current vapour flow prevents the transport of the liquid along the entire length of the evaporator causing dry-out [69, 70].

2.6.2.2.2 Flow Modifier

Aside from liquid return, capillary wicks also serve as a way to distribute liquid homogeneously over the entire evaporator in classical heat pipes. In McGill heat pipes, a helical flow modifier performs this function [71, 72].

The flow modifier imposes a resistance on the rising fluid in the evaporator, causing it to rotate. Although there is still some uncertainty, it is believed that the resulting helical flow propels the denser liquid against the inner evaporator wall due to the centrifugal forces generated, which ensures homogeneous wetting and stabilizes the annular two-phase flow regime. The centrifugal forces together with the helical flow:

- break apart any vapour film which may form
- cause heat transfer which is naturally induced, but is similar to forced convection boiling

2.6.2.3 Working Fluid Circuit

When a heat source is applied to the evaporator, the working fluid evaporates creating a greater pressure there. The condenser is cooled via an external cooling circuit, and is thus at a lower temperature, T , and pressure, P , as defined by the Clausius-Clapeyron equation where C is a constant and R is the ideal gas constant (8.314 J/mol·K). See Figure 2.11.

$$\ln P = -\frac{H_{fg}}{RT} + C \quad (2-3)$$

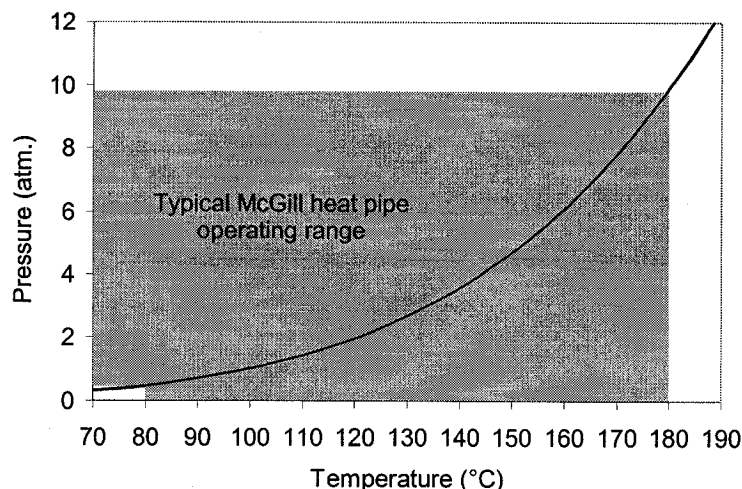


Figure 2.11 Saturated vapour pressure of water

The vapour formed at the evaporator flows down the pressure gradient towards the condenser. It enters the condenser via an overflow pipe and condenses onto the cooled condenser walls. The condensed working fluid percolates downwards by gravity and collects in a reservoir at the bottom of the condenser. The liquid working fluid drains from the reservoir into a return line that is packaged within the evaporator. The working fluid is then discharged from the return line at the bottom of the evaporator completing the cycle. See Figure 2.12.

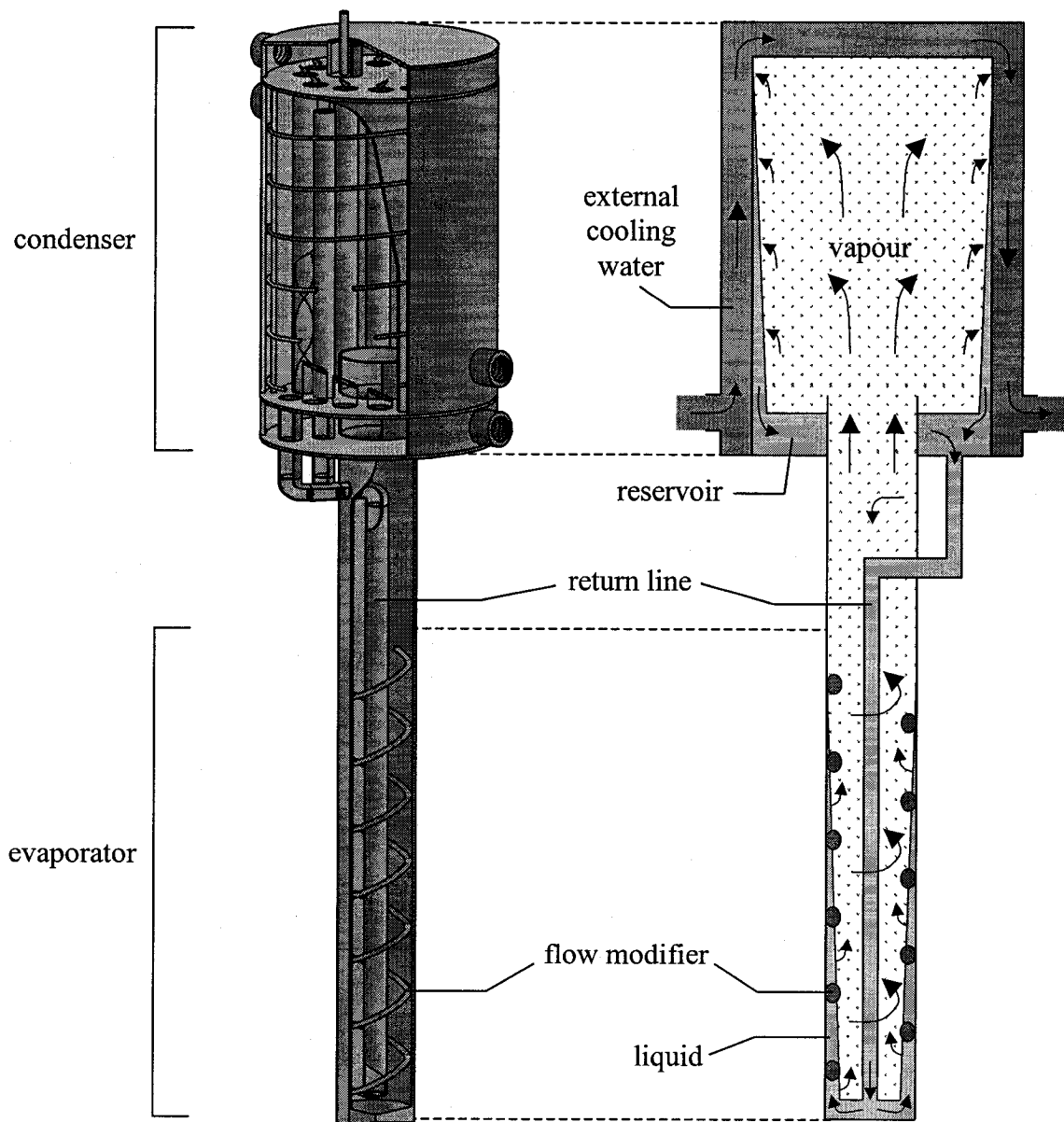


Figure 2.12 Diagram of heat pipe design and operation
 Note : The condenser in the diagram on the right has been simplified for clarity.

2.6.2.4 Greater Thermal Heat Flux and Heat Load Capability

McGill heat pipes are capable of dissipating greater heat loads at heat fluxes which are several times larger than equivalent classical heat pipes. This is due to three major factors:

- Because they have no wick, McGill heat pipes do not have a capillary limit.
- The centrifugal force caused by the flow modifier acting on the liquid within the evaporator suppresses film boiling and raises the critical heat flux.
- The presence of the reservoir and return line acts to improve the return of liquid to the evaporator, minimizing entrainment.

These improvements have enabled the device to operate at the large heat fluxes encountered in the metallurgical industry.

2.7 Numerical Modeling Techniques

2.7.1 Introduction to Numerical Modeling

The theory to solve equations numerically has existed for over 300 years. However, the computational power required to apply this theory in a practical manner has only become widely available recently. From a mathematical, computational and engineering point of view, this has spawned a revolution in the development of solution procedures to complex systems of equations.

In engineering, numerical modeling is primarily applied to equations which cannot normally be solved analytically. Therefore the fields of fluid dynamics and heat transfer, which are defined largely by complex partial differential equations (PDEs), has greatly benefited from the recent advances in numerical modeling.

2.7.2 Computational Fluid Dynamics

For many engineering systems, the dominant equations (referred to as “governing” equations) are the mass, momentum, and energy transport equations, given by (2-4), (2-5) and (2-6), respectively. The numerical modeling of systems which are governed by these equations is referred to as computational fluid dynamics, or CFD [73, 74].

Mass transport equation:

$$\frac{\partial \rho}{\partial t} + \nabla \cdot (\rho \vec{v}) = S_{mass} \quad (2-4)$$

Momentum transport equation:

$$\frac{\partial}{\partial t} (\rho \vec{v}) + \nabla \cdot (\rho \vec{v} \vec{v}) = \nabla P + \nabla \cdot (\vec{\tau}) + \rho \vec{g} + S_{momentum} \quad (2-5)$$

Energy transport equation:

$$\frac{\partial}{\partial t} (\rho E) + \nabla \cdot (\vec{v} (\rho E + P)) = \nabla \cdot \left(k_{eff} \Delta T - \sum_j H_{sensible,j} J_j + (\vec{\tau}_{eff} \cdot \vec{v}) \right) + S_{energy} \quad (2-6)$$

where ρ is the density (kg/m^3)

t is time (s)

\vec{v} is the velocity vector (m/s)

S is the source term for either mass ($\text{kg/m}^3 \cdot \text{s}$), momentum (N/m^3), or energy (W/m^3)

P is the pressure (Pa)

$\vec{\tau}$ is the stress tensor (Pa)

g is gravitational acceleration (m/s^2)

E is the sum of the potential, kinetic and pressure energy (J)

k_{eff} is the effective thermal conductivity ($\text{W/m} \cdot \text{K}$)

$H_{sensible,j}$ is the sensible enthalpy of species j (J/kg)

J_j is the diffusion flux of species j ($\text{kg/m}^2 \cdot \text{s}$)

The theory behind computational fluid dynamics is complex, and is beyond the scope of this thesis. Briefly stated, the solving of the governing equations involves approximating each of them by a system of ordinary differential equations (ODEs). There are several methods of doing this, e.g. finite differences, finite elements, spectral methods, and finite volumes. In this thesis, CFD modeling using the finite volume method is employed, which stores cell values of the domain (e.g. pressure, temperature, velocity, etc.) in the respective cell centers.

The system of ODEs can then be approximated by a system of linear equations by discretizing them throughout space (meshing), thus creating the domain. For transient problems, time is also discretized. Discretization affects the solution procedure, and carelessness can result in increased errors or divergence [74].

2.7.3 Solution Procedure

Once the domain has been defined, material properties must be supplied. Conditions that reflect the physical problem are applied to the boundaries. These conditions are referred to as *boundary conditions*, and can include the defining of fluxes or variables at the domain boundaries (eg. a constant mass flux, or constant temperature).

Additional equations and variables can be included in the problem, such as turbulence or solidification models.

Initialization serves as a “first guess” for the solution, and most likely violates the governing equations. The solver algorithm then refines the model iteratively, attempting to converge to a solution which satisfies the governing equations across each cell. A reasonable initial condition facilitates rapid convergence, and for more complex models, may be required to attain convergence at all [75]. See Figures 2.13 and 2.14.

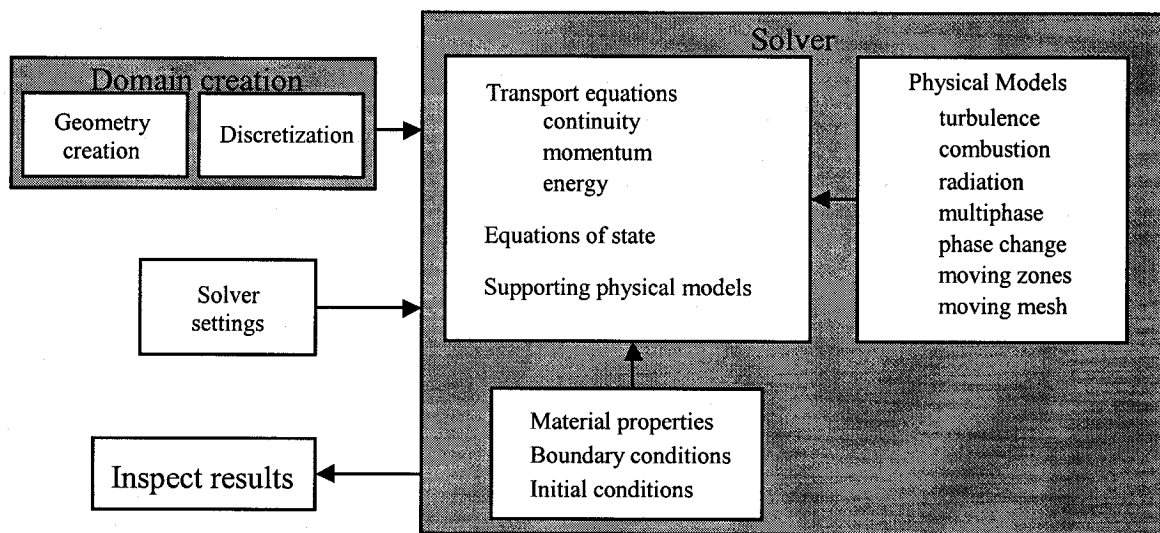


Figure 2.13 Typical CFD solution procedure [73]

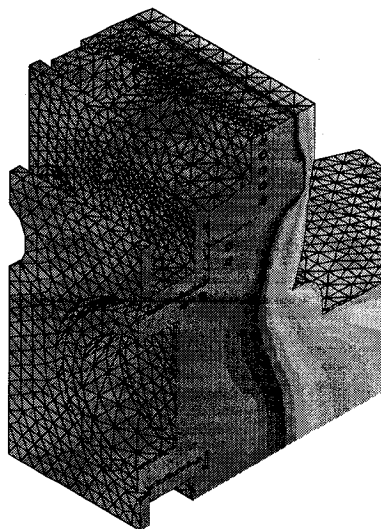


Figure 2.14 Meshed geometry and solution of a taphole [5]

2.7.4 Sources of Error

The numerical solving of mathematical models creates several types of errors, some of which are described below [76]:

- Rounding error occurs when a value is stored numerically as a binary representation.
- Truncation error occurs when the differential equations are approximated as linear equations.
- Propagation error is the result of truncation errors that cause additional errors in the downstream cells or in the next time step.

The errors created during numerical modeling can be significant and can lead to divergence of the solution, or to solutions which are unphysical. Although the mathematical theory and computer science behind CFD has been well developed, there are still many areas of the field which require improvement, such as turbulence modeling. Therefore, the modeler must have a good understanding of the limitations of numerical modeling and of CFD. As well, the modeler is relied upon to identify erroneous results by having a good understanding of the physical processes being modeled.

Chapter 3 Heat Pipe Cooling of a Copper Tapblock

3.1 Introduction

3.1.1 Umicore and the Hoboken Blast Furnace

Umicore is a large global metals producer with major industrial operations in North America, Europe, Asia, and Australia. One of Umicore's operations is the Hoboken smelter located in Antwerp, Belgium.

Economic reasons necessitated the transformation of the Hoboken smelter from a traditional lead blast furnace in 1997. Today, the Hoboken smelter is quite exceptional as it specializes in the treatment of secondary products composed of lead and copper.

The ability to treat complex materials and a high recovery of precious metals reporting to the blister copper has made the Hoboken blast furnace a technological and economic success story for Umicore. A brief description of the process flowsheet is given below.

The Hoboken smelter is actually composed of two separate plants, an "Isasmelt"-type copper smelter and a lead blast furnace. Lead-bearing secondary copper products and copper matte from the blast furnace are fed to the copper smelter and produce blister copper and lead slag. The blister copper is sent to a copper refinery in Olen, Belgium, whereas the lead slag is fed to the blast furnace.

The blast furnace produces three products: a lead bullion, a matte phase (fed to the copper smelter), and a slag phase. The slag phase is sold to the concrete industry and the lead phase is sent for refining [77].

Figure 3.1 presents a simplified flowsheet of the Hoboken process. The location of the slag tapblock (discussed in the present chapter) and launder (discussed in Chapter 4) are indicated.

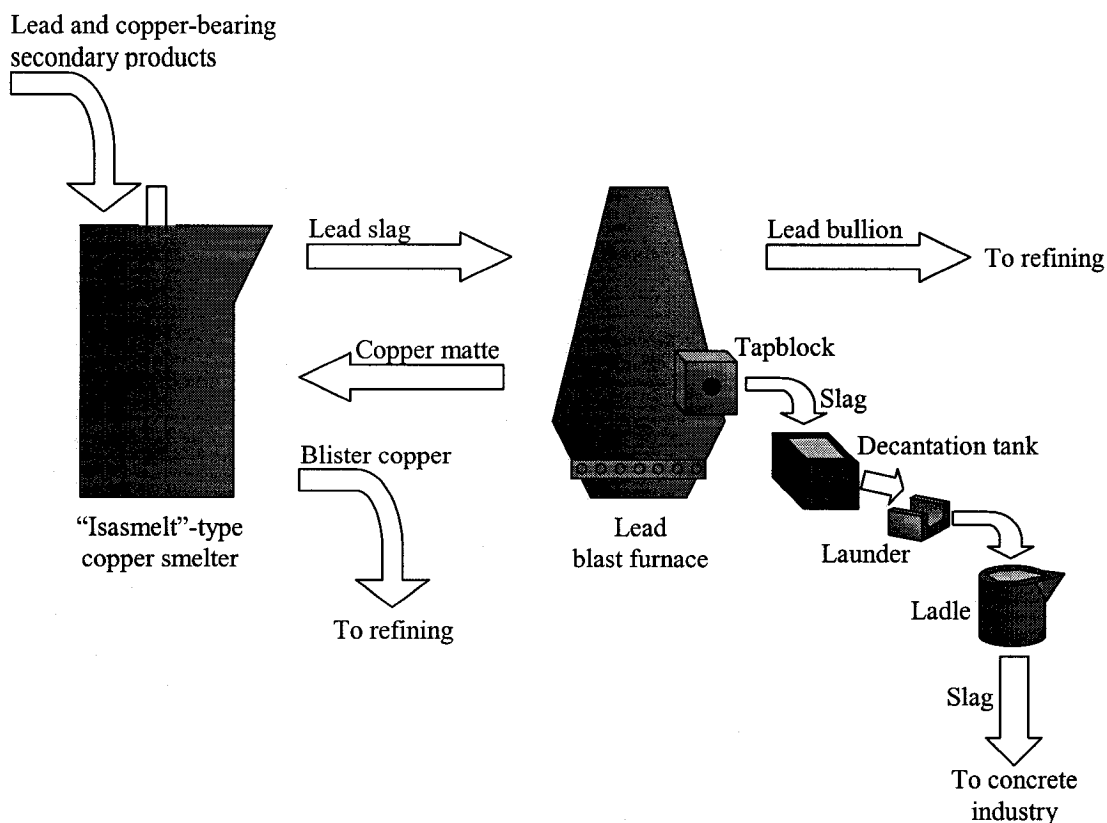


Figure 3.1 Simplified flowsheet of the Hoboken smelter

In 2000, the Hoboken operation suffered a tapblock cooling system failure which caused a steam explosion that resulted in injuries to personnel and a long-term interruption of production. This incident, together with a tradition in taking technological leaps, served as the driving force for Umicore to develop an alternate tapblock cooling technology.

3.1.2 McGill Heat Pipe Cooling

A research project was initiated in October of 2002 between Umicore and McGill to develop and test a heat-pipe-based cooling system and evaluate its suitability for eventual use at the Hoboken lead blast furnace.

The tapblock and heat pipe cooling systems were tested at Umicore Research's pilot plant, located in Olen, Belgium. The tests simulated the heat loading conditions applied to the slag tapblock at the Hoboken plant, and the performance of the heat pipe cooling system was evaluated.

3.1.3 Objective

The objective of the tapblock project was to develop a novel copper tapblock cooling system inherently safer than the conventional forced-convection water cooling system currently used in the Hoboken plant and in the vast majority of similar metallurgical operations. Based on previous laboratory work, it was theorized that a heat pipe-based system would have the following advantages over conventional cooling systems:

1. Increased safety
2. Reduction in cooling water flow requirements
3. Increased potential for energy recovery

3.1.3.1 Increased safety

This property of the proposed heat pipe cooling system stems from many of the heat pipe's characteristics. For example, because the heat pipe is a super-conductor of heat, the thermal energy from the tapblock can first be moved away from the molten metal, and can then be dissipated into the cooling water remotely.

This eliminates the necessity to pass high-pressure (7-10 atm), high-velocity (1-3 m/s) water close to the tapping hole of the copper block. Instead, only a small quantity of working fluid contained within the heat pipe at a relatively low pressure (0.5 to 3 atm) is located close to the heat source.

Another characteristic which improves safety is the ability of the heat pipe to act as a thermal flux transformer. Otherwise said, the heat pipe system can absorb thermal energy in the evaporator section (tapblock) at a high heat flux, and dissipate this energy at the condenser section into the external cooling water at a much lower heat flux over a larger surface area. Dissipating heat into a water circuit at lower heat fluxes significantly reduces the risk of local film boiling in the cooling circuit, which is normally a major safety concern.

3.1.3.2 Reduction in Cooling Water Flow Requirements

Metal producers operate conventional water cooling systems with large safety factors to avoid film boiling. Thus, the quantities of water which are used are much greater than the minimum theoretical requirement.

Because a heat pipe almost completely eliminates the possibility of film boiling within the cooling circuit, water in the cooling circuit can be allowed to reach greater temperatures. Reduced cooling water flow rates can therefore be used, which are closer to the minimum theoretical requirement to dissipate the applied heat load as sensible heat.

3.1.3.3 Increased Energy Recovery Potential

Because a heat pipe cooling system can operate safely with a reduced cooling water flow rate, a water effluent can be generated at an elevated temperature compared with the water produced in conventional water cooling systems. The resulting heat energy stored is therefore easier to recover, or can be used elsewhere in the plant.

3.2 Design Criteria

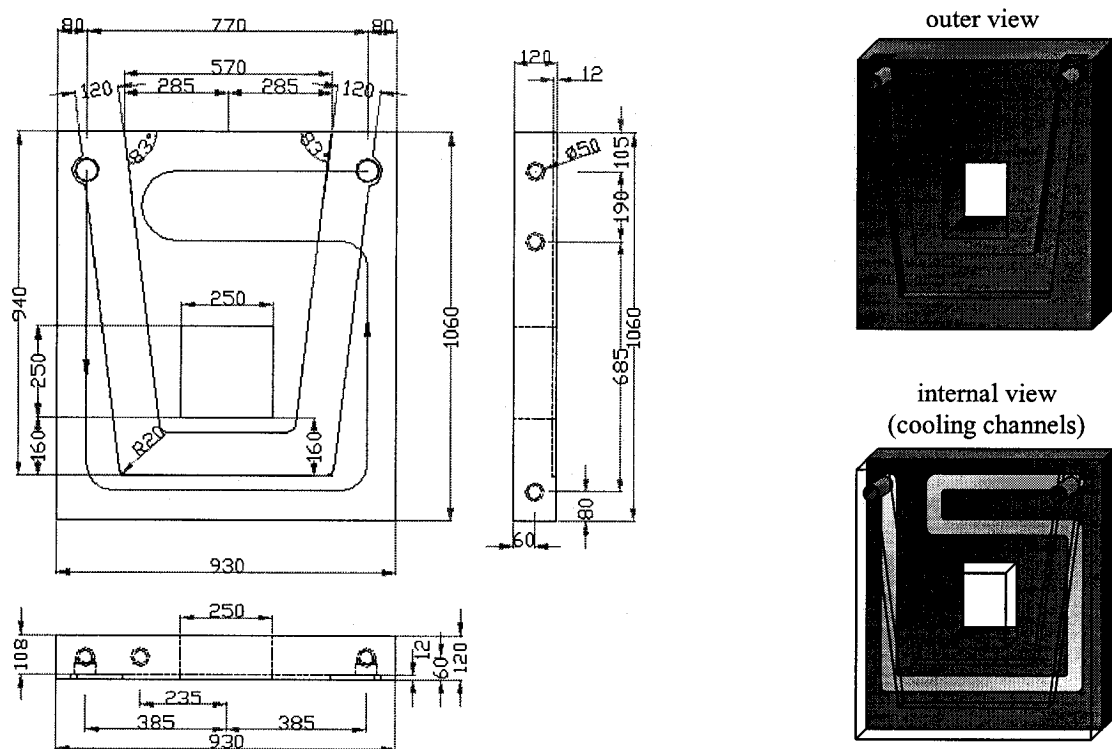
The slag tapblock at Hoboken is a typical two-piece design composed of a large host block and a smaller insert block. The tapblock is continuously tapped and is therefore subjected to a constant heat load. Table 3.1 summarizes the operating data supplied by Umicore for their slag tapblock cooling system. Table 3.2 lists typical heat fluxes of a blast furnace under normal conditions. Recall that the hotface of the tapblock at Hoboken measures one square meter. Figure 3.2 presents the insert block design of the Hoboken slag tapblock.

Table 3.1 Cooling circuit data from the slag tapblock at Hoboken

Internal cooling channel diameter	2" (50.8 mm)
Input water temperature	35°C
Output water temperature	43°C
Cooling water flow rate	30,000 l/hr
Heat load	300 kW

Table 3.2 Typical heat fluxes encountered at different areas of a blast furnace [6]

	Heat flux (kW/m ²)
Stove	2
Refractory-based tapblock	2 – 4
Water-cooled tapblock	10 – 25
Hearth wall	5 – 50
Graphite/copper stack	150 – 300
Copper cooling blocks (staves) on stack	150 - 300

Figure 3.2 Drawing and diagram of the insert block at Hoboken
(dimensions are given in millimeters)

For simplicity and to reduce the cost, it was decided to design and test only the insert block with heat pipe cooling. Although this component of the tapblock is subjected to a fraction of the total heat load, it was agreed that the heat pipe cooling system would be designed to dissipate the entire tapblock design heat load of 300kW.

3.3 Design, Fabrication, and Experimental Setup

The equipment needed for the experiments essentially consisted of two parts: the tapblock and the cooling system. Umicore fabricated the tapblock, whereas McGill fabricated all components related to the cooling system. The components fabricated by McGill were produced in the Chemical and Metallurgical Engineering machine shop located in the Wong pavilion. These components were then shipped to Umicore Research, in Olen (Belgium).

3.3.1 Design Attributes

The following is a summary of the main characteristics of the heat pipe-tapblock design. All components other than the copper tapblock were fabricated out of 304 stainless steel due to its good strength and corrosion resistance.

3.3.1.1 Tapblock, Evaporators and Flow Modifiers

- The tapblock was sized similarly to the slag tapblock at Hoboken, which measures 1.06 m x 0.93 m x 0.12 m. The final dimensions of the prototype tapblock were set at 1.1 m x 1.0 m x 0.16 m, with a 150 mm diameter circular taphole.
- The prototype tapblock was fabricated out of anode copper (> 99.9% copper) because of its availability to Umicore (from their copper refinery) and because of its good thermal conductivity. Industrial tapblocks are typically fabricated from a copper alloy that has very high copper content (> 99%), such as C81100. Therefore any differences between the physical properties of the experimental and actual tapblock were considered negligible.
- Two 0.94m-long evaporators were incorporated into the tapblock, on either side of the taphole. The inside diameter of the evaporator was equal to that of the cooling channel in the conventional tapblock at Hoboken (ϕ 2 inches, or 50.8 mm).
- In order to eliminate any contact resistance between the copper and the evaporator wall, the evaporators simply consisted of two vertical holes drilled directly into the copper tapblock. Boiling would therefore occur directly on the tapblock surface.

- The evaporator hole coupling sections were composed of a pipe welded to a flange. The pipe was threaded and a rim was machined into it. The top of both evaporator holes were bored out so that the outer diameter of the pipe could fit into them, and also to form a ledge. The holes were then threaded, and the coupling sections were screwed into the evaporator holes. A teflon o-ring (maximum operating temperature: 260°C) was used to seal the joint, being compressed between the ledge in the evaporator hole and the rim of the coupling section pipe. See Figure 3.3.

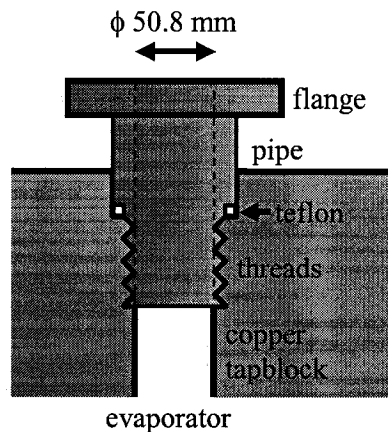


Figure 3.3 Diagram of the evaporator coupling section

- The flow modifiers used in the evaporator were sized based on past experience, where the pitch is approximately equal to the evaporator diameter, and the thickness is approximately equal to one tenth of the evaporator diameter. Refer to Figure 3.4.

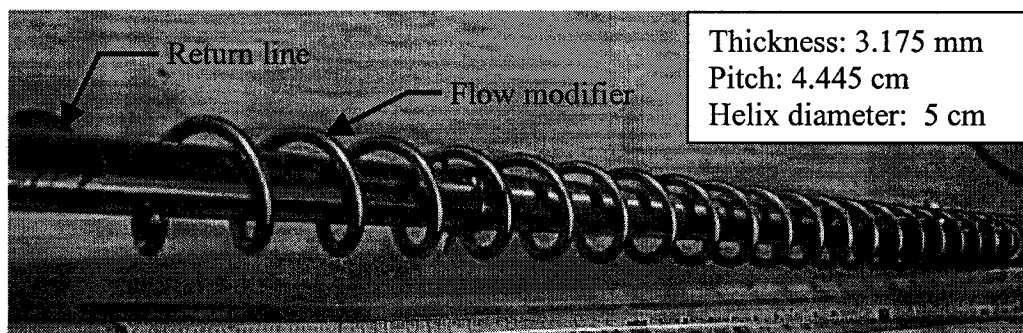


Figure 3.4 Flow modifier used in the evaporator of a McGill heat pipe

3.3.1.2 Working Fluid

- Water was chosen as the working fluid, as it is chemically compatible with copper and typically operates at temperatures suitable for copper. Previous work [59] has shown that water can dissipate a heat flux in excess of 1.5 MW/m^2 (design heat flux) without experiencing film boiling. Sodium could not be used as a working fluid for two reasons: (1) it is chemically incompatible with copper and (2) it would need to operate at temperatures ($\sim 600^\circ\text{C}$) which would cause copper to oxidize in the atmosphere ($> 350^\circ\text{C}$). In addition, sodium is flammable and requires special startup procedures as it is solid at room temperature.
- Each heat pipe was charged with 4 liters of working fluid. This quantity of water is sufficient to completely fill the evaporator, return line, and piping linking the evaporator to the condenser. This ensures that the evaporator walls are completely wetted when starting a test (i.e. the evaporator is flooded).

3.3.1.3 Reservoir and Return Line

- The return line had an inner diameter of 2 cm and an outer diameter of 2.5 cm.
- A valve was installed into the return line in order to be able to effectively turn off the heat pipe. By shutting off the valve, the flow of liquid to the evaporator would be stopped and the evaporator eventually dried out. In the absence of liquid working fluid in the evaporator, no cooling would take place.
- The reservoir was designed with a 6-liter capacity. This volume is large enough to contain all of the working fluid (4 liters) in the case where the evaporator must be dried-out by shutting off the return line valve.

3.3.1.4 Condenser and External Cooling Fluid

- The condenser was located 1.9 m above the return line discharge. The resulting head of liquid between the condenser and the return line discharge was judged as large enough to ensure the adequate flow of working fluid to the evaporator.

- Two condensers were fabricated in a shell-and-tube configuration, each being fed from a single evaporator. Therefore the cooling system was composed of two completely independent heat pipes. The condenser:evaporator area ratio was designed as 12:1. Refer to Figures 3.5 and 3.6.
- Water was chosen as the external cooling fluid. The external cooling fluid used to cool the condenser section of the heat pipe system is typically either air or water. The relatively low operating temperature of water-based heat pipe systems ($\sim 100^{\circ}\text{C}$) coupled with the large heat load requirement of the tapblock (300kW) precluded the use of air, because it is not sufficiently efficient as a coolant due to its low density.

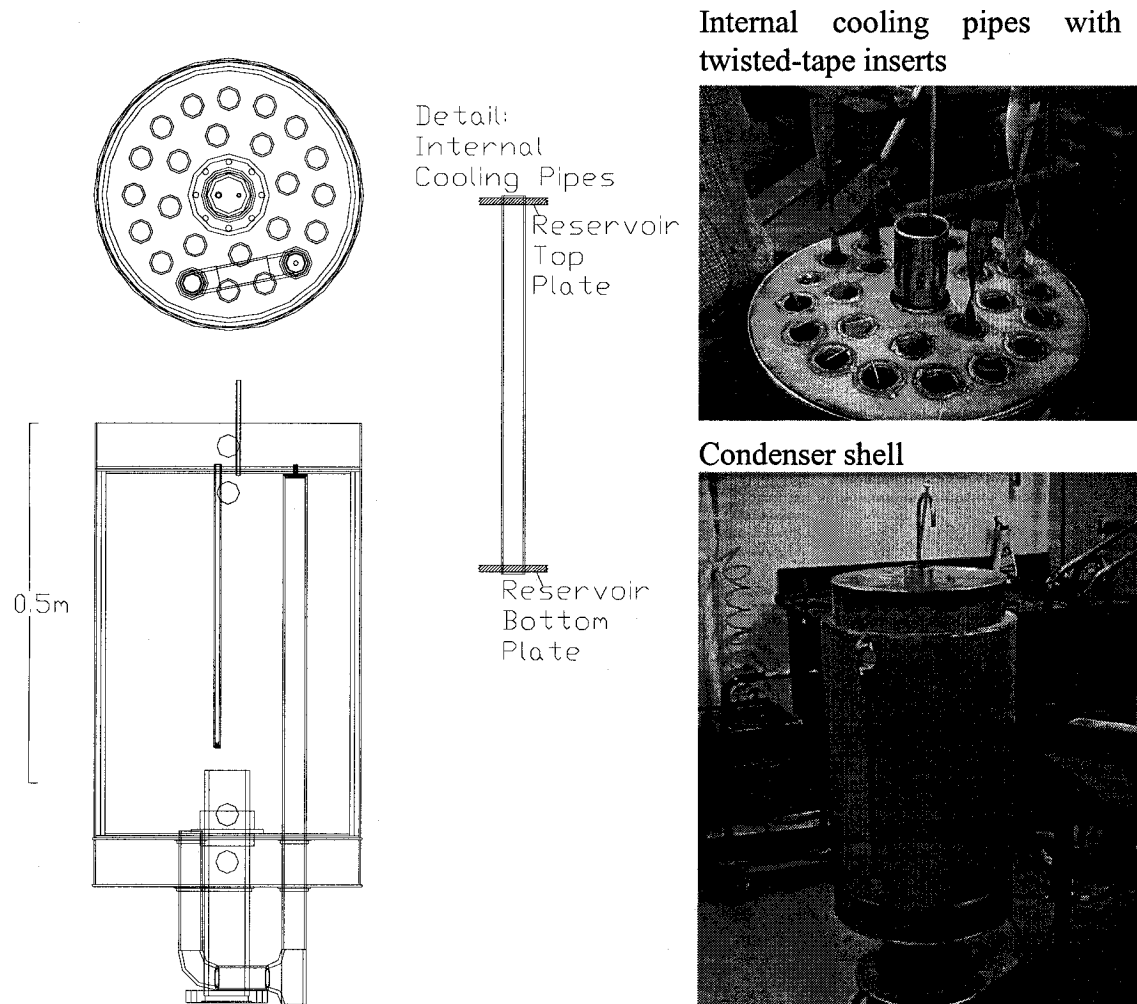


Figure 3.5 Condenser design and fabrication

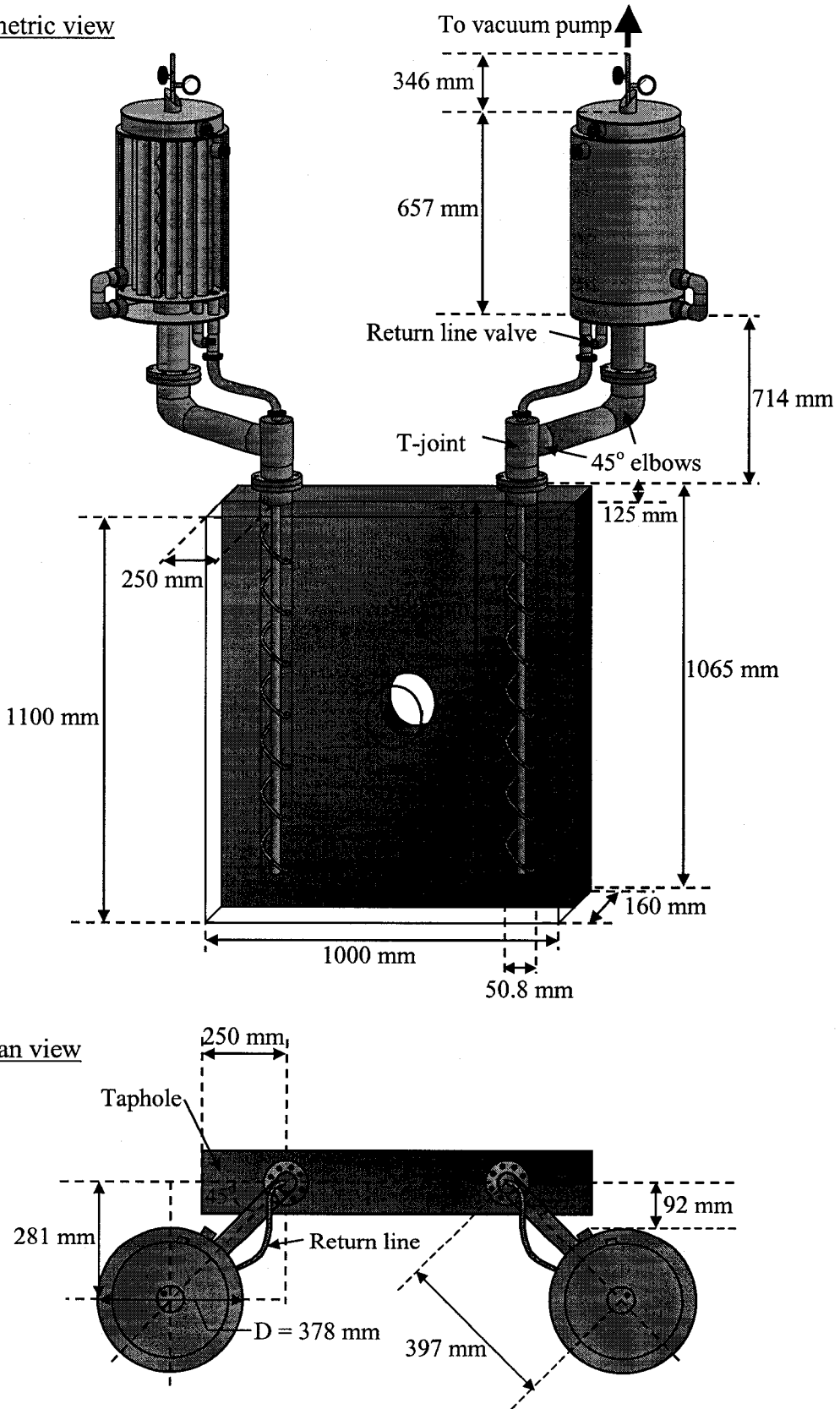


Figure 3.6 Dimensions of the tapblock and heat pipe cooling system

3.3.2 Experimental Setup

As previously mentioned, the tests were performed at Umicore's Research facility located in Olen, Belgium. The use of an oxygen-natural gas burner present in the pilot plant was used to simulate the heat loading conditions outlined (300 kW). In order to satisfy the positioning constraints of the burner, a steel frame was constructed to raise the copper tapblock. The steel frame was also meant as a support for the various other components of the cooling system. Refer to Figures 3.7, 3.8 and 3.9.

A cooling skid and two air coolers located outside the pilot plant were used to supply the cooling water needed for the external cooling circuit of both condensers. The cooling water was in closed circuit. When changes were done to the cooling water system, additional water was added to replenish any water lost, and the system purged of air.

After charging the heat pipes with working fluid (water), a vacuum pump was used to evacuate the heat pipes of any air that was trapped within.

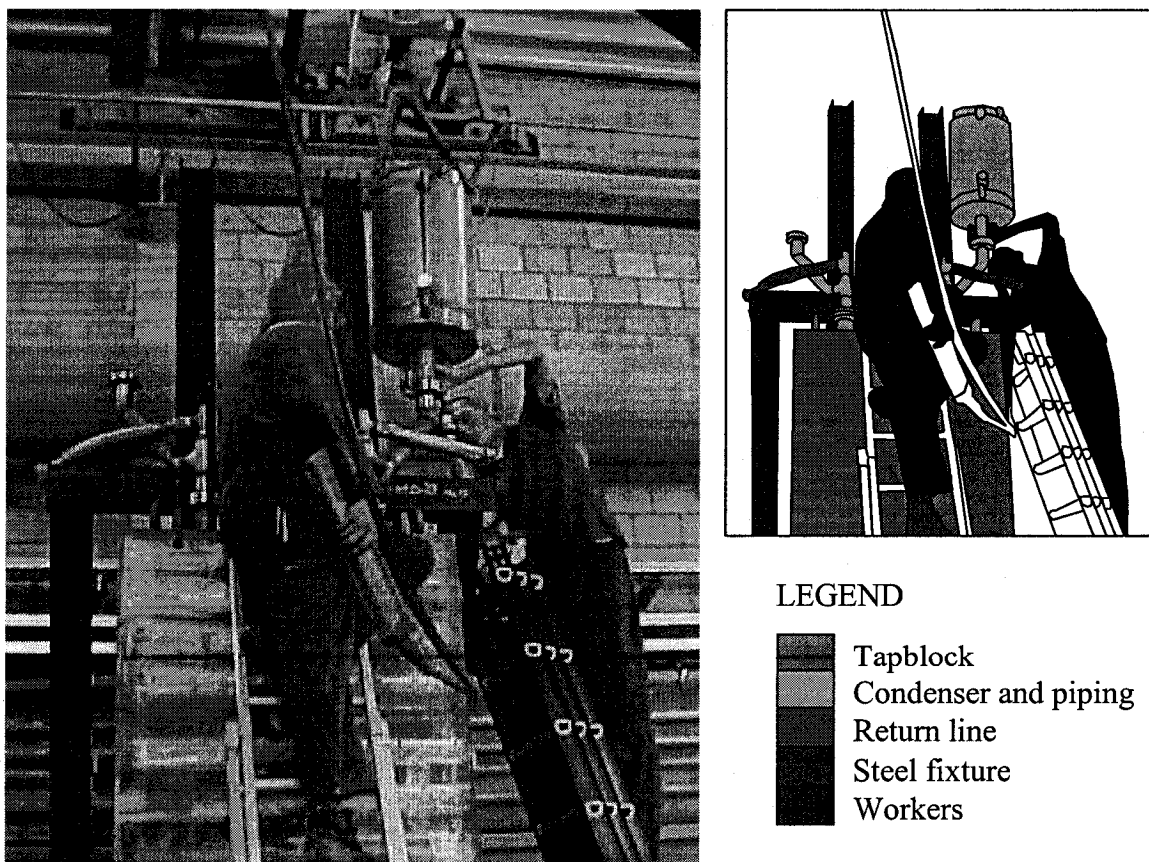
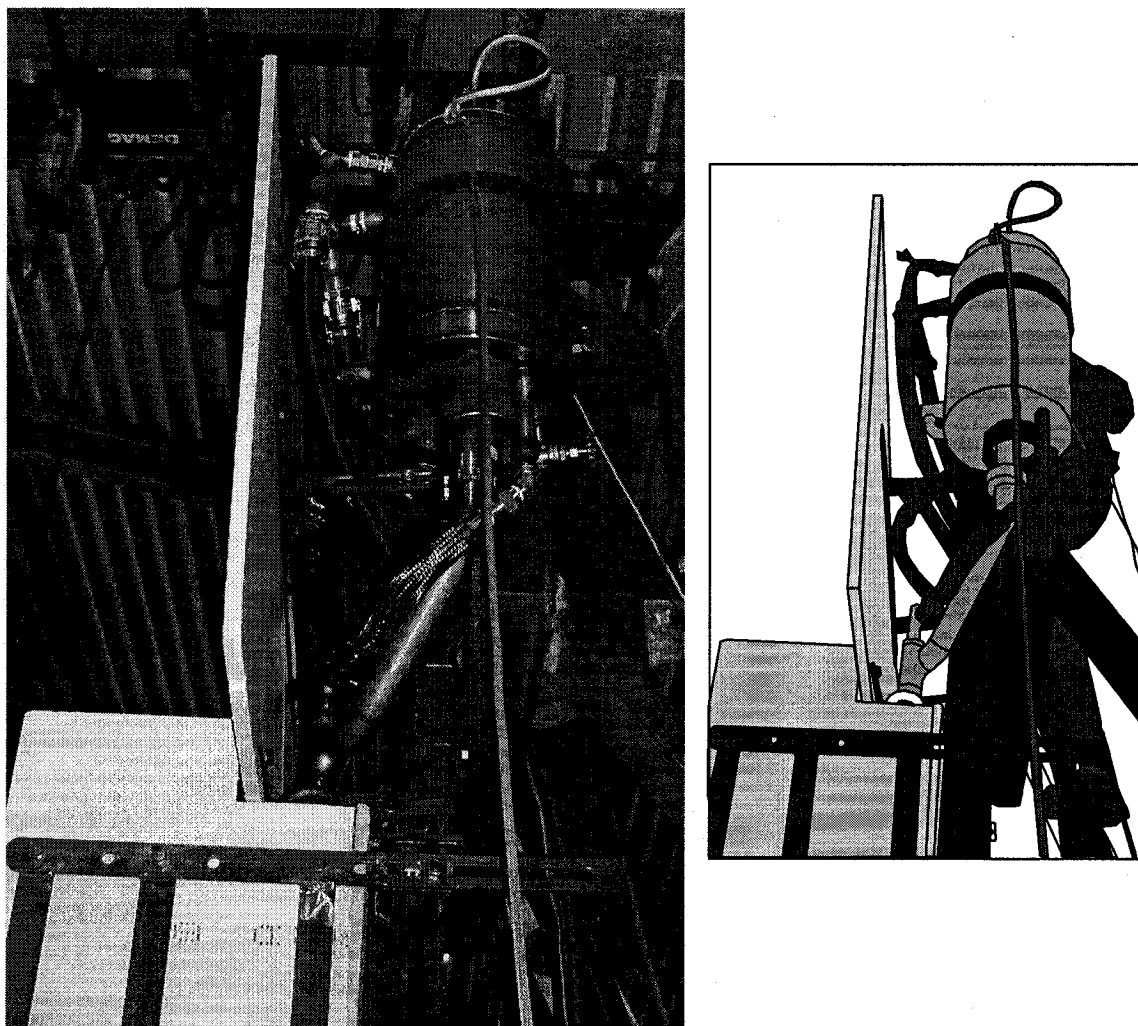


Figure 3.7 Installation of the condensers



LEGEND








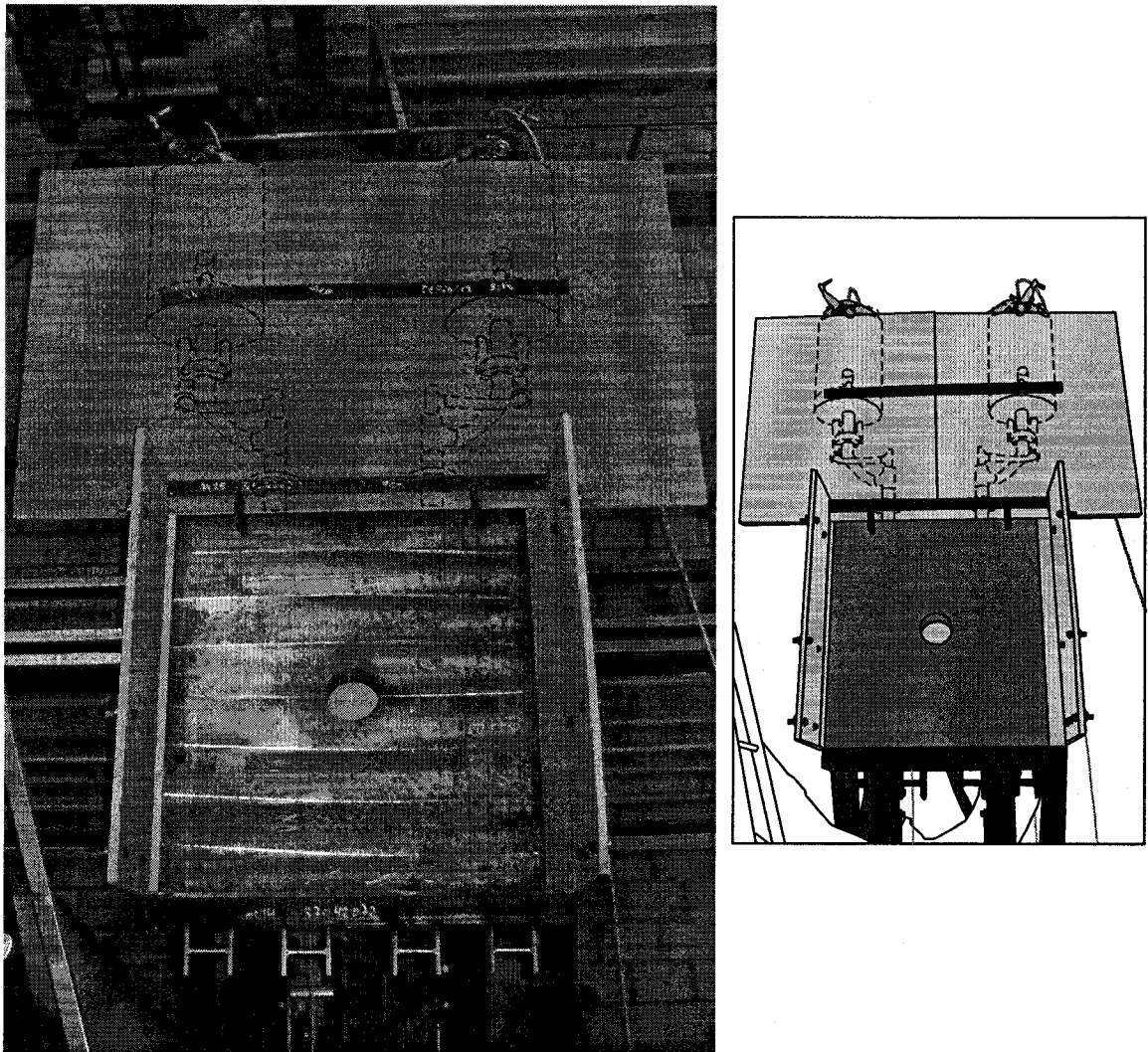
	Return line
	Condenser and piping
	Steel fixture
	Freeboard insulation
	External cooling water
	Vacuum line
	Technician

Figure 3.8 Installation of the cooling water hoses and sensors



LEGEND

	Tapblock
	Condenser and piping
	Steel fixture
	Freeboard insulation
	External cooling water
	Vacuum line
	Outline of heat pipes located behind freeboard

Figure 3.9 Experimental setup

3.3.3 Sensors

Two thermocouple wells were incorporated into each heat pipe. One of the thermocouple wells ran along the length of the return line, protruding slightly out of the return line at the bottom end of the evaporator. A thermocouple placed here gave the temperature at the bottom of the evaporator.

The other thermocouple well protruded into the condenser of each heat pipe, next to the vacuum line. Two thermocouples were inserted at different depths, yielding the temperatures of the top and center of the condenser.

The temperature readings from the evaporator and condenser indicated the operating temperature of the heat pipe. In a correctly operating heat pipe, all of these thermocouples should register almost identical temperatures, indicating good heat transfer.

Four thermocouple wells were drilled 8 cm into the backside of the tapblock, opposite the burner. These temperature readings were used to monitor the tapblock temperature.

The input and output temperatures of the cooling water to the condensers were also measured at the cooling skid along with the cooling water flow rate. These values allowed for the calculation of the heat extraction rate of each heat pipe, using the following equation:

$$q = \dot{m} c_p \Delta T \quad (3-1)$$

where q is the heat extraction rate (kW), \dot{m} is the cooling water flow rate to the condenser (kg/s), c_p is the specific heat capacity of water, taken as 4.19 kJ/kg·°C, and ΔT is the difference between the input and output cooling water temperature.

The flow of natural gas to the burner was also monitored, and the oxygen:fuel ratio was automatically adjusted to maintain the maximum flame temperature.

A data acquisition system was used to monitor and record the sensor measurements during testing. Figure 3.10 presents the location of the sensors, viewed from the burner.

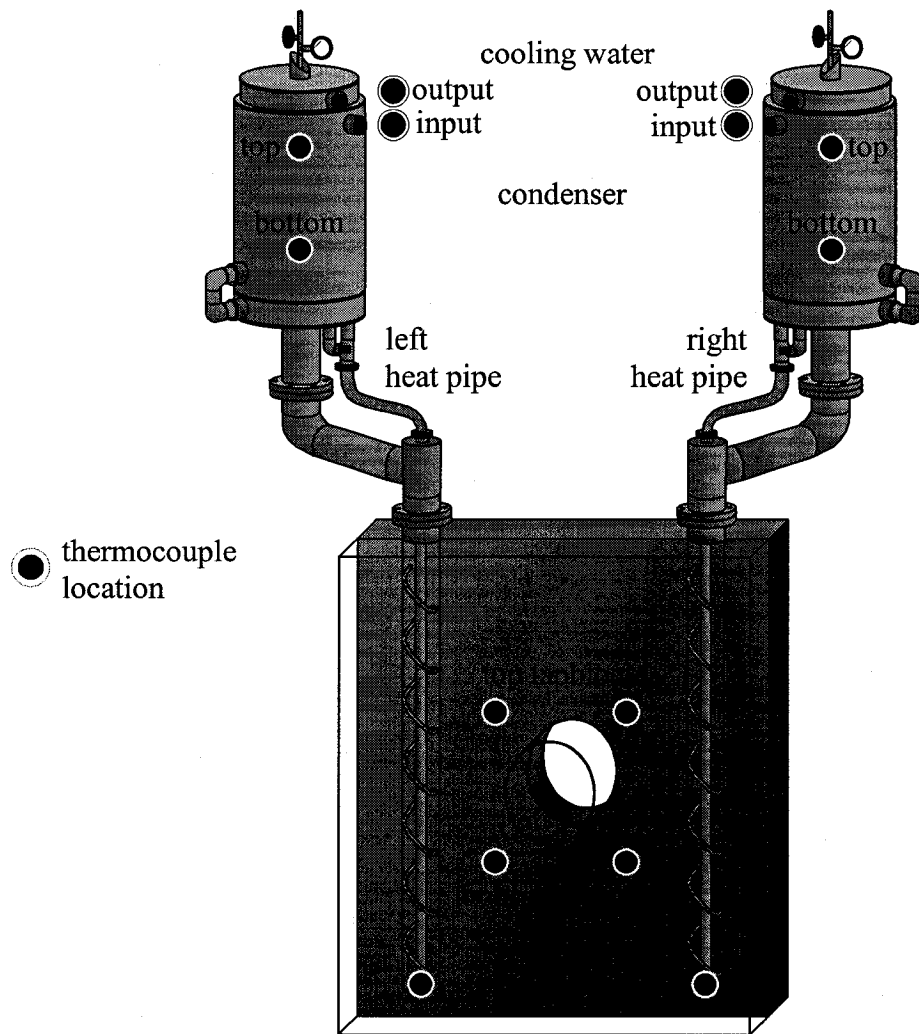


Figure 3.10 Thermocouple positioning

3.3.4 Analysis of Design

3.3.4.1 Condenser Heat Flux

The purpose of the condenser is essentially to dissipate the latent heat of vaporization of the working fluid into the external cooling fluid circuit as sensible heat. The shell-and-tube configuration of the condenser allows a relatively large heat exchange area to be contained within a comparatively small volume.

By conservatively assuming that all of the heat from the evaporators must be dissipated in the condensers (all components of the heat pipe are adiabatic except for the condenser heat exchange area), the heat flux required in the condenser was calculated to be 90 kW/m^2 . This value is generally a very safe heat flux to dissipate thermal energy into water at, as it is well below the critical heat flux for water [78]. Refer to Table 3.3.

Table 3.3 Comparison of the evaporator and condenser thermal requirements

	Evaporator	Condenser
Design heat load	150 kW	150 kW
Heat exchange area	0.14 m^2	1.66 m^2
Average heat flux	1.1 MW/m^2	90 kW/m^2

3.3.4.2 Evaporator Heat Flux

Laboratory-scaled experiments by Yuan with a water-based heat pipe similar in design to the present heat pipe successfully dissipated heat fluxes in excess of 1.5 MW/m^2 [59]. Analysis of these experiments concluded that the heat fluxes obtained were limited by the heat source, and not by the heat pipe capacity.

Therefore it was concluded that the heat pipe designed for the tapblock would be capable of dissipating the required heat fluxes.

3.3.4.3 Methodology for the Comparison of Dry-out between Heat Pipes

Dry-out is a limitation of McGill heat pipe technology, and is discussed in detail in Chapter 5. Yuan's experiments indicated that the dry-out limitation is strongly related to the vapour velocity generated in the evaporator. At large heat loads and under low operating temperatures, the increased vapour velocities cause large pressure gradients to develop across the evaporator and main piping. This pressure gradient opposes the pressure head between the reservoir and return line ($\rho g \Delta h$), which causes the return of liquid working fluid to the evaporator. Therefore understanding the pressure drop across the evaporator is essential to understanding the dry-out limitation.

The pressure drop within a pipe is generally found to be a function of the velocity of the fluid flowing inside of it. Because of the complexity (both geometric and mechanical) of the evaporator, very little theory is available to predict the velocity field within it.

However, knowing the heat load, q , and evaporator configuration, the minimum axial component of the velocity averaged over the annular cross-section of the evaporator outlet, \bar{v}_{\min} , can be determined. For engineering purposes, it is possible to qualitatively predict if a system will be in danger of experiencing dry-out by comparing values of \bar{v}_{\min} between experiments. The following is a derivation of an expression for \bar{v}_{\min} .

3.3.4.3.1 Derivation of \bar{v}_{\min}

Consider the configuration shown in Figure 3.11 below, which represents a heat pipe evaporator. This diagram consists of a cylindrical surface of radius r_{evap} through which a variable heat flux, q'' , is being added. This surface represents the inner surface of a McGill heat pipe evaporator. Inside this larger cylinder exists a smaller cylinder of radius r_{rl} . This solid cylinder represents the return line of a McGill heat pipe which is concentric with the evaporator inner surface, as is the case in the configuration considered. In a correctly operating McGill heat pipe, the return line is filled with liquid working fluid, which is discharged at the bottom of the evaporator. Therefore, in the configuration shown below, the return line may be considered as being a rigid rod.

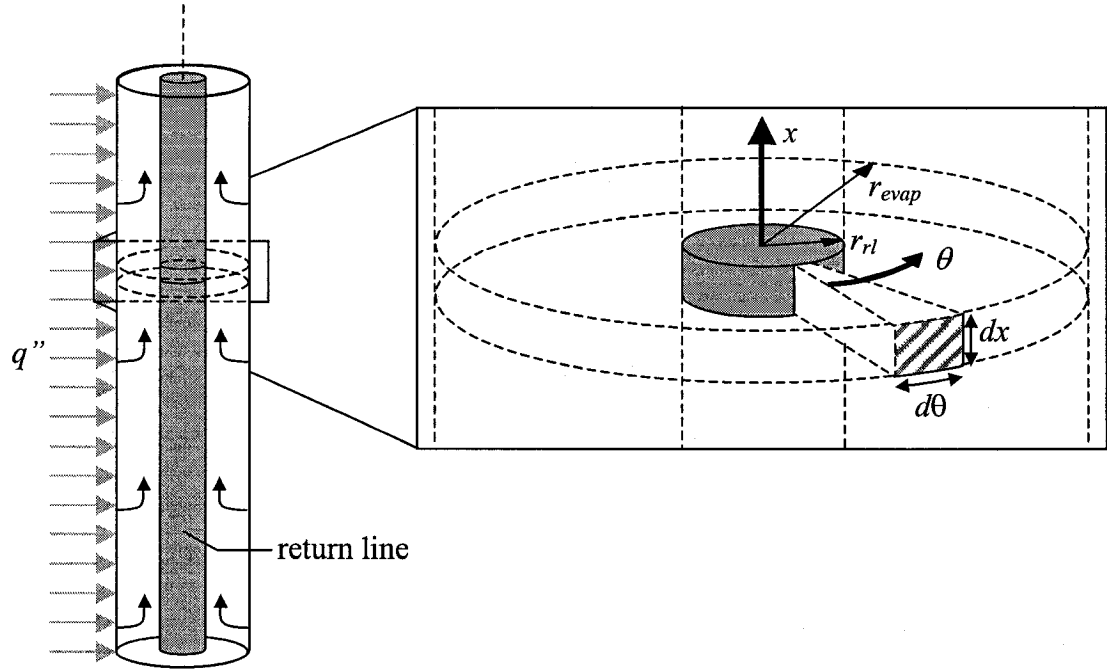


Figure 3.11 Diagram of the evaporator

Now consider that the evaporator inner surface delineated by r_{evap} is continuously wetted by a liquid working fluid. The latent heat of vaporization of the fluid, H_{fg} is assumed to be constant, and the fluid is assumed to be incompressible in liquid form (ρ_l is constant). The liquid/vapour working fluid interface is assumed to be at equilibrium, and thus the vapour exists at its saturated vapour pressure. Therefore all thermal energy being transmitted into the system through the evaporator inner surface is transmitted to the working fluid and is stored as a phase change from liquid to vapour.

The bottom surface of the configuration is sealed, whereas the top is open. Therefore the vapour formed fills the annular space between the evaporator inner surface and the return line. As vapour is formed, it flows upwards towards the open end of the evaporator and is discharged into the condenser.

At any point x along the evaporator, the equation (3-2) can be applied:

$$q_{cum} = \int_{x=0}^x \int_{\theta=0}^{\theta=2\pi} q'' r_{evap} d\theta dx + q^{x=0} \quad (3-2)$$

where q_{cum} is the cumulative rate of heat being inputted into the system from $x=0$ to x , q'' is the radial heat flux being inputted into the system over the area element represented by the arc length $r_{evap} d\theta$ multiplied by the height dx , and $q^{x=0}$ is the heat load being applied to the bottom surface of the evaporator.

Assuming steady state at the evaporator wall interface, the cumulative thermal energy being transmitted into the system across this interface from $x=0$ to x can also be expressed by equation (3-3).

$$q_{cum} = \dot{m}_{cum,l \rightarrow v} H_{fg} \quad (3-3)$$

where $\dot{m}_{cum,l \rightarrow v}$ is the cumulative mass transfer rate of liquid working fluid being converted to vapour from $x=0$ to x , and H_{fg} is the latent heat of vaporization of the working fluid which is considered constant.

Equation (3-3) also assumes that no other reactions are occurring and that the system is isothermal. In actuality, the isothermal assumption is not possible because the vapour must flow down a pressure gradient in the evaporator to overcome the flow resistance along it. This pressure gradient is generated by cooling the condenser and causing a lower vapour pressure there. Typically, the pressure gradient along an evaporator is such that the temperature difference from bottom to top is a few degrees Celsius or less. This small temperature gradient has a minimal effect on the physical properties of the working fluid and thus the isothermal assumption for the purpose of this derivation is judged acceptable.

Substituting equation (3-3) into (3-2) and differentiating with respect to x , the following can be obtained :

$$\frac{d\dot{m}_{cum,l \rightarrow v}}{dx} = \frac{1}{H_{fg}} \int_{\theta=0}^{\theta=2\pi} q'' r_{evap} d\theta \quad (3-4)$$

Assuming the vapour within the evaporator behaves as an ideal gas and exists in the evaporator as a saturated vapour, then the Clausius-Clapeyron equation applies and can be written as the following:

$$\ln P = -\frac{H_{fg}}{R} \frac{1}{T_{sat}} \quad (3-5)$$

The isothermal assumption therefore implies that the pressure, P , is a constant. It therefore follows from the ideal gas law that the vapor density, ρ_v , is constant. Therefore the cumulative mass flow rate can be equated as follows:

$$\dot{m}_{cum,l \rightarrow v} = Q_{cum,v} \rho_v \quad (3-6)$$

where $Q_{cum,v}$ is the cumulative volumetric flow rate of vapour being produced in the evaporator between $x=0$ and x .

Because the vapour is assumed as incompressible, continuity implies that no vapour is accumulating at any point in the evaporator. Therefore the axial volumetric flow rate at any point x along the evaporator, $Q_{axial,v}^x$, must be equal to the cumulative volumetric flow rate of vapour being produced in the evaporator from $x=0$ to x , $Q_{cum,v}$.

$$Q_{cum,v} = Q_{axial,v}^x = \bar{v} A_{c-s}^{effective} \quad (3-7)$$

where \bar{v} is the average axial velocity component of the vapour at a point x along the evaporator, and $A_{c-s}^{effective}$ is the effective cross-sectional area through which vapour can flow at a point x along the evaporator, given by equation (3-8).

$$A_{c-s}^{effective} = \frac{\pi(r_{evap}^2 - r_{rl}^2)}{\alpha} \quad (3-8)$$

where α is the vapour fraction (commonly referred to as the *void fraction* in literature related to multiphase flows). Below the return line discharge, there is no return line, and the cross-sectional area is πr_{evap}^2 . But because this represents a very small part of the

evaporator, equation (3-8) can be assumed to be true throughout the length of the evaporator. Therefore equation (3-4) can be rewritten as the following:

$$\bar{v} = \frac{1}{A_{c-s}^{effective} \rho_v H_{fg}} \left[\int_{x=0}^x \int_{\theta=0}^{\theta=2\pi} q'' r_2 d\theta dx + q^{x=0} \right] \quad (3-9)$$

This is the general equation that defines the average axial vapour velocity distribution along a McGill heat pipe evaporator.

In practice, the vapor fraction is an unknown and is difficult to measure. Therefore for engineering purposes, assuming the void fraction as 100% implies that the effective cross-sectional area is equal to the actual cross-sectional area. Doing so also implies that the velocity given by equation 3.9 is the minimum vapour velocity.

Another assumption that can be made is that the applied heat flux q'' is a constant throughout the evaporator. As well, the heat flux applied to the bottom of the evaporator can be assumed as relatively small and can be neglected. Therefore equation (3-9) can be expressed as the following:

$$\bar{v}_{min} = \frac{2q''}{\rho_v H_{fg}} \frac{r_{evap}}{(r_{evap}^2 - r_{rl}^2)} x \quad (3-10)$$

3.3.4.3.2 Comparison of \bar{v}_{min}

Table 3.4 compares the results from Yuan's laboratory experiments with a water-based heat pipe to the predicted operation of the tapblock heat pipe cooling system. As no information on the heat flux distribution was available, values for \bar{v}_{min} at the top of the evaporator were compared.

Table 3.4 Comparison of heat pipe laboratory dry-out conditions to the expected tapblock operating range

	Laboratory heat pipe [59]	Tapblock heat pipe		
Evaporator inner diameter	2.8 cm	5.08 cm		
Return line outer diameter	1.1 cm	2.5 cm		
Evaporator length, $L_{\text{evaporator}}$	30 cm	94 cm		
Reservoir height	0.5 m	1.9 m		
Heat load	8.85 kW	150 kW		
Operating temperature	42°C	100°C	120°C	140°C
Operating pressure	0.08 atm	1 atm	1.96 atm	3.56 atm
Vapour density	55 g/m ³	597 g/m ³	1122 g/m ³	1962 g/m ³
\bar{v}_{\min} at $x = L_{\text{evaporator}}$	496 km/hr	263 km/hr	140 km/hr	80 km/hr
Status	Onset of dry-out	Increasingly stable operation →		

From a metal producer's viewpoint, operating a heat pipe at a lower temperature is desirable, as this tends to prolong the life of the tapblock and surrounding refractory. Ideally, the tapblock cooling system should operate at a temperature slightly greater than 100°C. Therefore in the case of a small leak, steam would slowly escape from the system at a pressure only slightly greater than 1 atmosphere. Therefore the system can continue to operate for a prolonged period of time (several days) until problems due to lack of working fluid can be detected and appropriate measures can be taken.

However under maximum heat loading conditions (150kW), Table 3.4 indicates that operating at 100°C would lead to large vapour velocities ($\bar{v}_{\min}=263$ km/hr). These velocities are approximately half the vapour velocities attained in Yuan's dry-out experiment ($\bar{v}_{\min}=496$ km/hr). However, it was conceded that factors associated with the scale-up of the technology (such as the length of the evaporator), which are presently still not completely understood, may necessitate the operation of the cooling system at greater temperatures (up to 140°C). These operating temperatures and associated operating pressures were considered as satisfactory given the fact that in application, the maximum heat load would only be attained in very exceptional circumstances.

Therefore it was judged that it would be possible to operate the heat pipe cooling system at the design heat load of 300kW without experiencing the dry-out limitation.

3.4 Experimental Results

The heat pipe system was tested over several days from July 15th to July 24th, 2003. Two tests are presented in this thesis. The first of these was a preliminary test, which explored the operability of the heat pipes (section 3.4.1). The second test aimed to determine the maximum heat extraction capacity of the cooling system (section 3.4.2).

3.4.1 Exploratory Test

It was considered prudent to first investigate the general operation of the heat pipes at lower heat loads. Therefore, the purpose of this test was to become comfortable with the operation of the heat pipe system. Figure 3.12 presents the test results. Figure 3.13 shows the burner applying a heat load to the tapblock.

The test is divided into three parts, as defined by the dashed lines on Figure 3.12, and explained in the following three sections.

3.4.1.1 Part 1 - Startup and Steady-State Operation (0:00 to 1:05)

The burner was initially positioned over the left heat pipe, centered vertically, and was ignited at a gas flow rate of 45 Nm³/hr. The cooling water feeding the condensers was set to flow rates of 2.6 l/s and 1.2 l/s for the left and right condensers, respectively.

The temperature readings of the tapblock initially began to increase at rates of approximately 3.6°C/s for the left side and 2.3°C/s for the right side. The larger temperature gains were observed on the left side of the tapblock, explained by the position of the burner over the left side of the tapblock.

The heat pipe temperatures began to increase as well, following the same trend as the tapblock temperatures. This initiated heat transfer in the condensers. The output cooling water temperatures began to increase relative to the input temperature, indicating increased heat extraction rates and the proper functioning of the heat pipes.

The cooling provided by the heat pipes had the effect of dampening the tapblock temperature increase, which slowed asymptotically to values of between 110°C and 150°C. Steady-state conditions were achieved at this setting, during which the heat extraction rates were observed to be 55kW and 15kW for the left and right heat pipes, respectively.

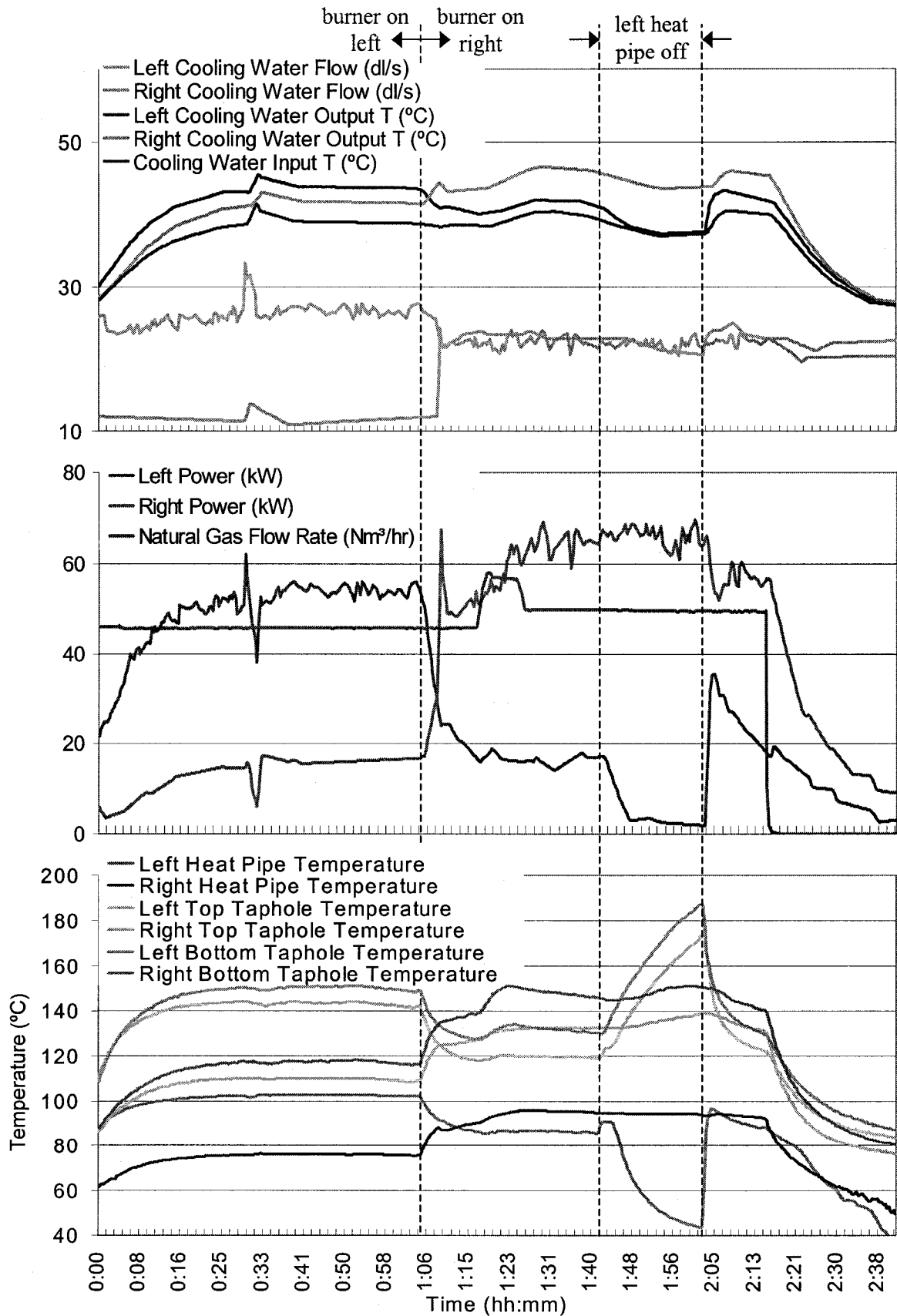


Figure 3.12 Exploratory test results

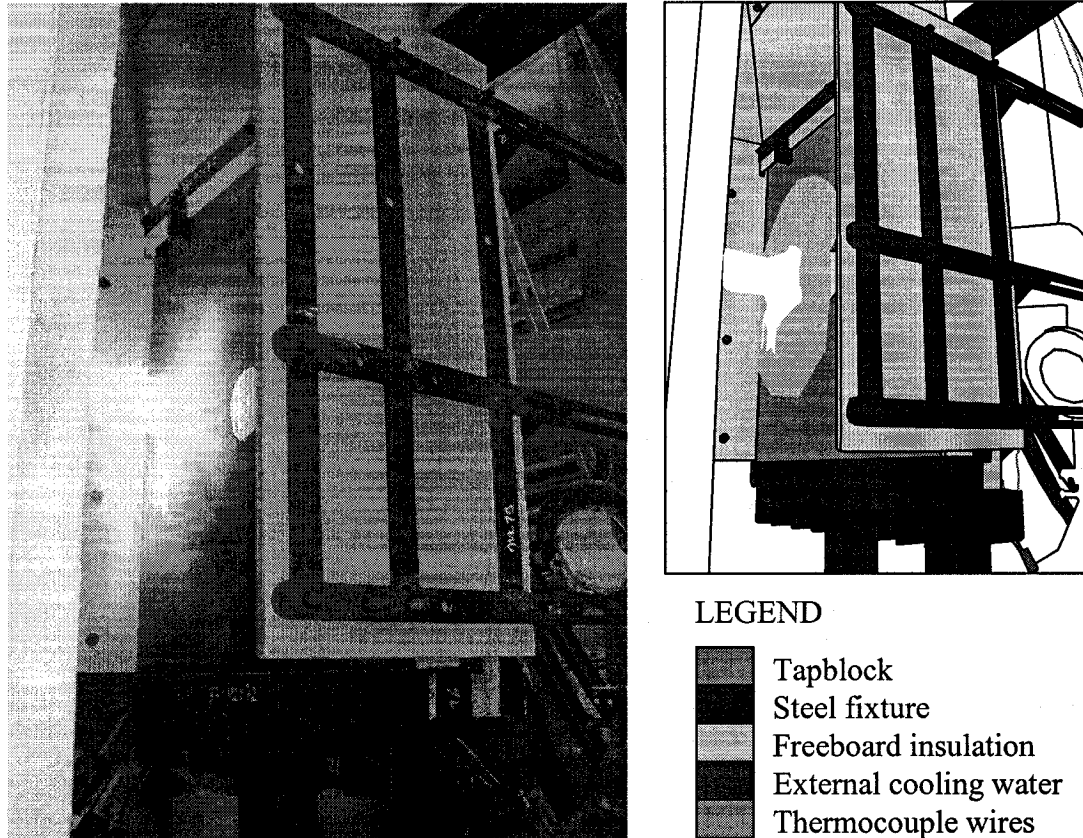


Figure 3.13 Burner applying a heat load to the tapblock
 NOTE: The burner is positioned over the left side of the tapblock in this case.

3.4.1.2 Part 2 - Responsiveness to Transient Conditions (1:05 to 1:41)

It was then decided that the heat extraction capacity of the right heat pipe would be evaluated. Therefore, the burner was moved to the right side of the copper block, centered vertically. The natural gas flow rate was also increased from $45\text{Nm}^3/\text{hr}$ to $57\text{Nm}^3/\text{hr}$ for several minutes and then down to $50\text{Nm}^3/\text{hr}$. The condenser cooling water flowrates were adjusted to approximately 2.2 l/s for both condensers.

These changes caused the temperature readings from the tapblock to invert, increasing the temperatures on the right side and decreasing them on the left side.

The cooling system responded rapidly to these changes, establishing new steady-state conditions. The heat extraction rate of the right heat pipe increased from 15kW to 65kW , with a corresponding increase in the heat pipe operating temperature from 75°C to 95°C . Meanwhile, the left heat pipe's heat extraction rate decreased from 55kW to approximately 16kW , while the operating temperature decreased by almost 20°C to 85°C .

3.4.1.3 Part 3 – On/Off Capability of the Heat Pipe (1:41 to 2:00)

It was decided to turn off the left heat pipe in order to demonstrate its cooling influence on the tapblock. Therefore, the return line valve of the left heat pipe was closed at 1:41, completely constricting the return line.

With no condensed working fluid refluxing the evaporator, the working fluid within it quickly evaporated. Once this occurred, virtually no more heat transfer took place. Therefore the temperature of the left side of the tapblock began to increase rapidly (3°C/s), while the heat extraction rate from the left heat pipe decreased to almost zero.

At 2:00, the return line valve of the left heat pipe was opened again. The effect is remarkable, as the tapblock temperature decreased at rates of up to 25°C/min . The temperature of the left heat pipe increased rapidly as vapour was generated in the evaporator, condensing in the condenser, and heated the cooling water at a power of up to 35 kW.

The burner was turned off at 2:15, ending the test.

3.4.1.4 Discussion of Heat Pipe Temperature Measurements

Temperature gradients within heat pipes are generally very low. The evaporator is the hottest portion of the heat pipe whereas the top of the condenser is the coldest. Therefore in practice, the heat pipe operating temperature is approximated as the bottom condenser temperature because it is between the hottest and coldest sections (as is the case in Figure 3.14 for example).

Figure 3.14 presents the left heat pipe temperature readings from 1:40 to 2:05. Note how the heat pipe temperatures while the heat pipe is turned on (return line valve open) are in the following ascending order: evaporator, top condenser, bottom condenser. Therefore the evaporator temperature was the lowest whereas it is normally expected to be greatest. A similar trend in the temperature readings were observed in the operating heat pipes throughout all the tapblock tests.

The low evaporator temperature can be explained by the fact that the corresponding thermocouple was located directly beneath the return line discharge. Therefore, this thermocouple measured the liquid working fluid temperature. After being condensed in

the condenser, the liquid working fluid has a finite residence time in the reservoir, during which it is further cooled by the external cooling water. Thus, the working fluid is sub-cooled before being drained to the evaporator. This explains why the “evaporator” thermocouple yielded the lowest temperature readings.

After the return line valve was closed, the evaporator temperature increased to 91°C, which is just slightly higher than the bottom condenser temperature of 90°C. The heat pipe continued to operate like this for 2-3 minutes. After this time (1:45), the evaporator began to dry-out. Therefore less vapour was being generated, causing a decrease in the temperature of the condenser.

At 1:52, the evaporator was completely devoid of any liquid working fluid. Therefore the evaporator temperature began to increase rapidly (6°C/min) to match the temperature of the surrounding copper.

At 2:00, the return line valve was partially opened, feeding some liquid working fluid to the evaporator. However, the heat pipe began to function at maximum capacity at 2:02, at which time the return line valve was completely re-opened.

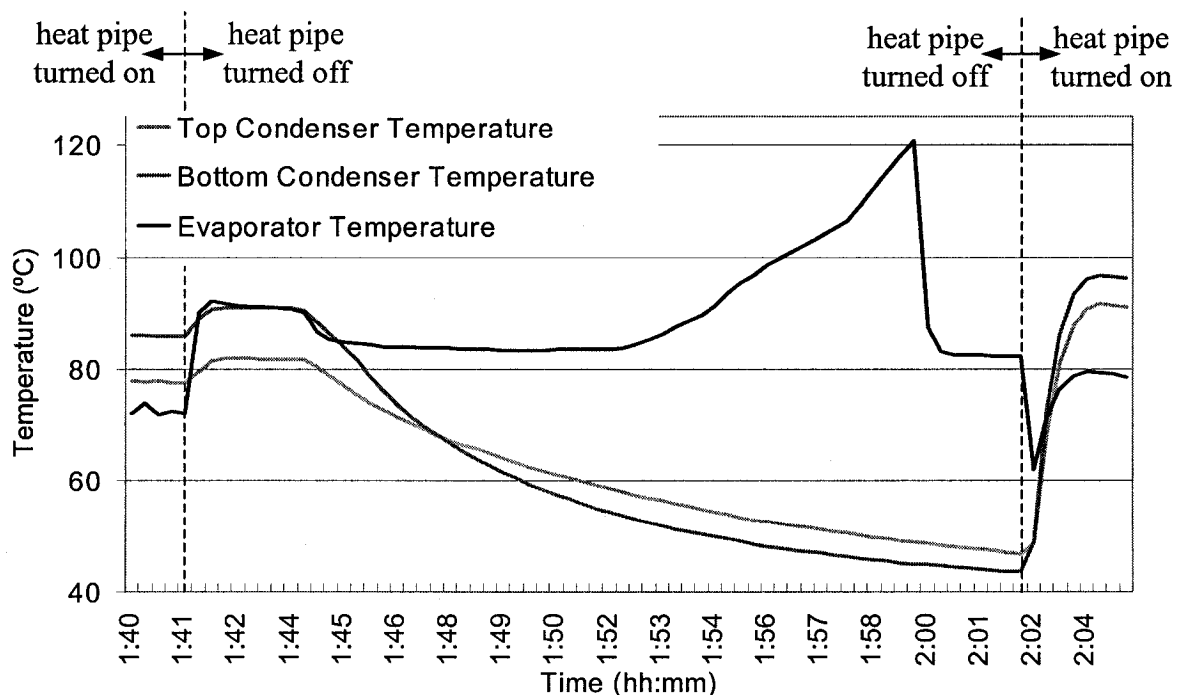


Figure 3.14 Left heat pipe temperature

3.4.2 Heat Extraction Capacity Test

After a few days of experimentation, it became evident that the heating efficiency of the burner had been overestimated. It was concluded that the burner was not powerful enough to simulate the design heat load of 300kW. As a compromise, it was decided that an attempt to apply 150kW to a single heat pipe (the left one, in this case) would be made. Evaluating a single heat pipe's performance under these circumstances was judged as reasonably equivalent to the original objective of 300kW for both heat pipes.

Therefore the purpose of this test was to determine the maximum heat extraction rate that can be achieved in a single heat pipe. Refer to Figure 3.15.

The burner was positioned directly over the left heat pipe, centered vertically, and was ignited. The gas flow rate was initially set at 40 Nm³/hr. Steady-state conditions were achieved approximately 15 minutes later, with the left heat pipe extracting 135kW of heat. Table 3.5 summarizes the test conditions.

Table 3.5 Steady state operating parameters (time 0:15 to 1:00 of Figure 3.15)

	Left	Right
Heat pipe cooling power	135kW	35kW
Heat pipe operating temperature	120°C	100°C
Heat pipe operating pressure	2.0 atm	1.0 atm
\bar{v}_{min} at the top of evaporator	125 km/hr	61 km/hr
Input cooling water temperature	38°C	
Cooling water flowrate	0.81 l/s	0.24 l/s
Output cooling water temperature	78°C	72°C
Tapblock temperature	160-175°C	130-135°C

Several attempts to further increase the heat extraction rate of the left heat pipe were made between 1:00 and 3:40. This was done by increasing the burner fuel consumption to 55 Nm³/hr and by adjusting the burner position. The desired effect did not develop, as the changes caused a larger portion of the load to be diverted to the right heat pipe. This was hindering the evaluation of the maximum heat extraction capacity of the left heat pipe. Therefore, the return line valve of the right heat pipe was turned off at a test time of 3:40.

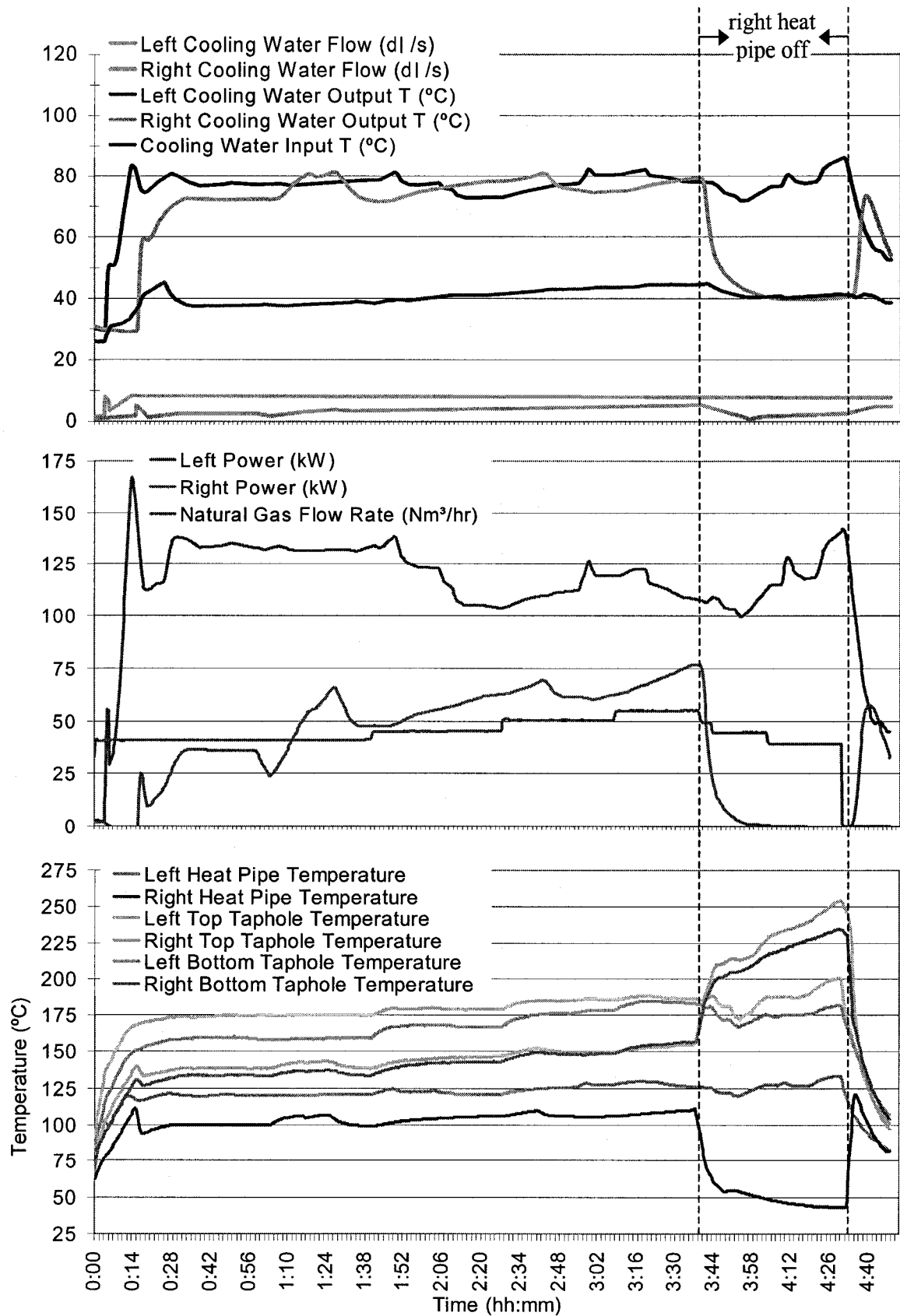


Figure 3.15 Maximum cooling capacity test

By turning off the right heat pipe, it was thought that a larger heat load would be forced to flow into the left heat pipe. By performing a few more adjustments to the burner positioning, a transient heat extraction rate of 142kW was achieved in the left heat pipe. Unfortunately, time constraints forced the test to be ended at this point.

3.4.2.1 Tapblock Temperature Readings

While the right heat pipe was turned off, the thermocouples of the right side of the tapblock measured temperatures higher than those measured on the left side. These measurements may initially seem counterintuitive, as the burner was positioned directly over the left evaporator.

However, as modeling results show in the next section of this chapter (section 3.5.2), the temperature gradients generated by the burner are so great that a portion of heat applied to the tapblock was diverted to the right side of the tapblock. This caused greater temperatures in the right side of the tapblock. The heat then doubled-back and flowed to the back side of the left evaporator, opposite the burner.

3.5 Analysis of Results

3.5.1 Modeling of the Experiment

A commercial mesh generation (GAMBIT 2.1.6) and a CFD solver (FLUENT 6.2.16) software package was used to model the prototype tapblock under steady-state conditions. The test conditions at time 4:30 of Figure 3.15 were simulated (section 3.4.2), as this corresponds to the time where the greatest heat load was applied to a single evaporator (142 kW).

3.5.1.1 Governing Equation and Material Properties

The model representing the tapblock test is a very simple system. Essentially, the problem consists of the 3D energy equation. As there are no fluids being modeled, the convective terms are removed. Because steady-state is assumed, the transient term also cancels out. The remaining terms are given by equation (3-11).

$$\nabla \cdot (k \nabla T) = 0 \quad (3-11)$$

Therefore only the thermal conductivity of the material, k , was required as a material property, taken as 387.6 W/m·°C [79].

3.5.1.2 Solver Parameters

As described in section 2.7.2, the finite volume method is a control-volume-based technique which ultimately yields a system of linear equations that approximates each governing equation across the domain. However, the respective system of linear equations approximating each governing equation can be solved simultaneously (coupled) or separately in series (segregated). In general, the segregated solver is more stable, but requires more iterations to reach a solution, whereas the coupled solver is more rapid, but may lead to divergence. Because the time required to converge the present model to a solution was trivial, the segregated solver was chosen.

It should be mentioned that only implicit linearization is available with the segregated solver in the Fluent software package. This signifies that each equation of the linear equation system approximating a given governing equation includes an unknown for the

respective cell together with unknowns of neighbouring cells (implicit), which requires that the system of equations be solved simultaneously.

Recall that the finite volume method stores cell values of the domain in the respective cell centers. Therefore, the fluxes of energy etc., which are required at the cell interfaces, must be extrapolated from the cell centroids. The second-order upwind scheme uses more information from the upwind cell compared with lower-order schemes to compute the flux across each interface, and is considered more sophisticated and precise. Therefore second-order upwind discretization was used to extrapolate the heat fluxes between cells. Table 3.6 summarizes the main solver parameters used for the tapblock model.

The default criteria of the Fluent CFD software was retained to verify convergence of the solution.

Table 3.6 Summary of the solver parameters

Parameter	Setting chosen	Rationale
Numerical solver	segregated	more stable iterative procedure
Linearization	implicit	only option available with segregated solver
Spatial discretization scheme – energy	second-order upwind	yields more precise results, good convergence for simple models

3.5.1.3 Initialization

The entire tapblock domain was initialized at 120°C. However, the simplicity of the present model caused convergence of the solution irrespective of the initialization procedure.

3.5.1.4 Boundary Conditions

The area of the tapblock which heat was applied to was modeled based on visual observations of the burner and flame during testing. By comparing the experimental temperature readings of the tapblock to the simulated temperatures at the same locations, the simulated applied heat load was refined. This was done several times using a guess-and-test methodology. Table 3.7 compares the experimental and modeled temperature readings. Given the temperature gradients which are observed in the model results (up to $1400^{\circ}\text{C}/\text{m}$), the error between the model and experimental results are within the tolerances of the thermocouple locations.

Table 3.7 Comparison of the experimental and model temperatures

	Tapblock temperatures ($^{\circ}\text{C}$)			
	Top left	Bottom left	Top right	Bottom right
Experimental	201	183	255	234
Modeled	207	188	242	225

The following is a list of the final boundary conditions used. Refer to Figure 3.16.

- The total heat load was 142kW.
- The left evaporator surface temperature was isothermal at 120°C .
- The right heat pipe was adiabatic (turned off).
- All other surfaces of the tapblock were assumed as adiabatic.
- The area through which heat was added to the system consisted of an ellipse centered 50 cm from the top surface of the tapblock and 25 cm from the left side of the tapblock. The ellipse had a vertical height of 55 cm, and a horizontal width of 40 cm.
- The heat flux being applied to the tapblock across the elliptical area was constant ($870\text{kW}/\text{m}^2$, for a total of 142kW).

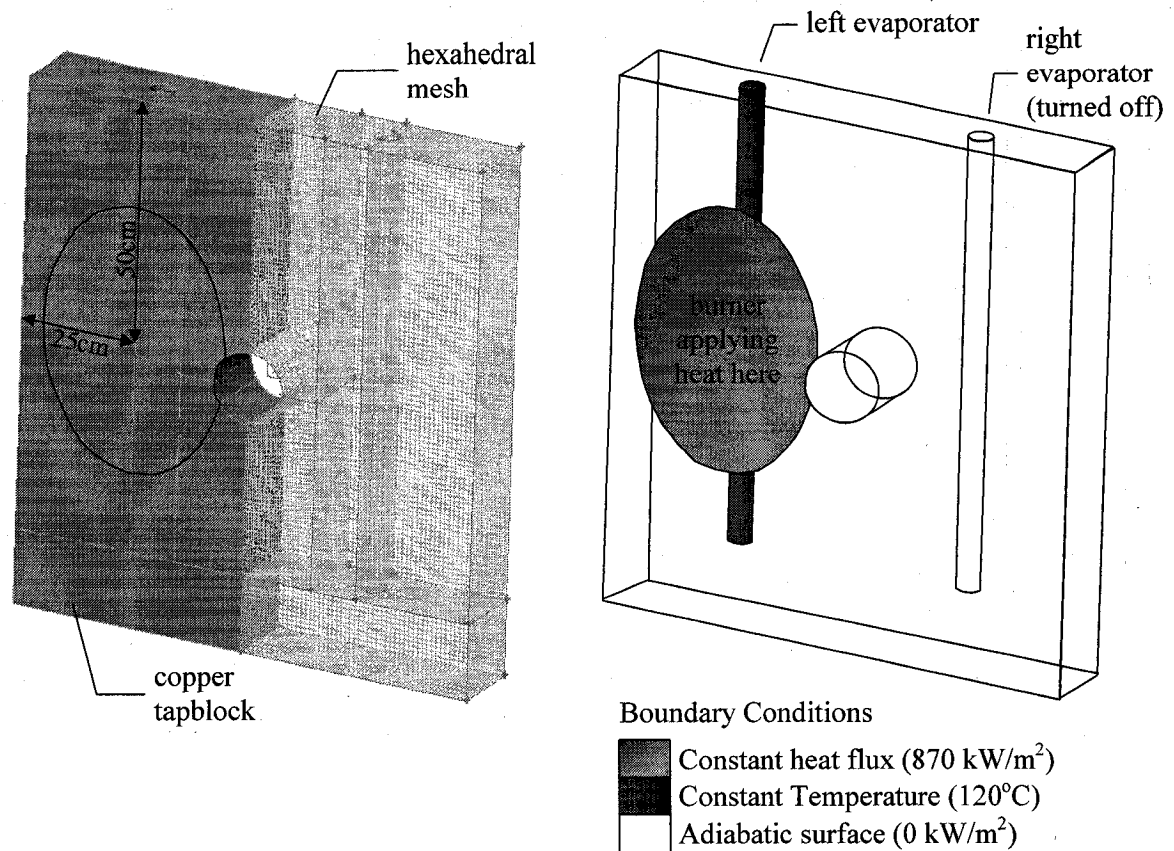


Figure 3.16 Tapblock model meshing and boundary conditions

3.5.2 Model Results

Figure 3.17 presents the heat flux across the evaporator/tapblock interface, viewed from three angles of rotation relative to the front face of the tapblock.

According to the modeling, the maximum heat flux attained experimentally was of the order of 2.4MW/m². This heat flux is significantly greater than the heat flux of 1.5MW/m² previously achieved in Yuan's laboratory experiment using a similar water-based heat pipe design [59].

To put these values into perspective, the most advanced water-based classical heat pipes must be operated at temperatures in excess of 300°C in order to dissipate heat fluxes of only 525 kW/m² at a total heat load of 2 kW [80]. Operating at these temperatures and corresponding pressures (85 atm) is clearly unacceptable for metallurgical applications.

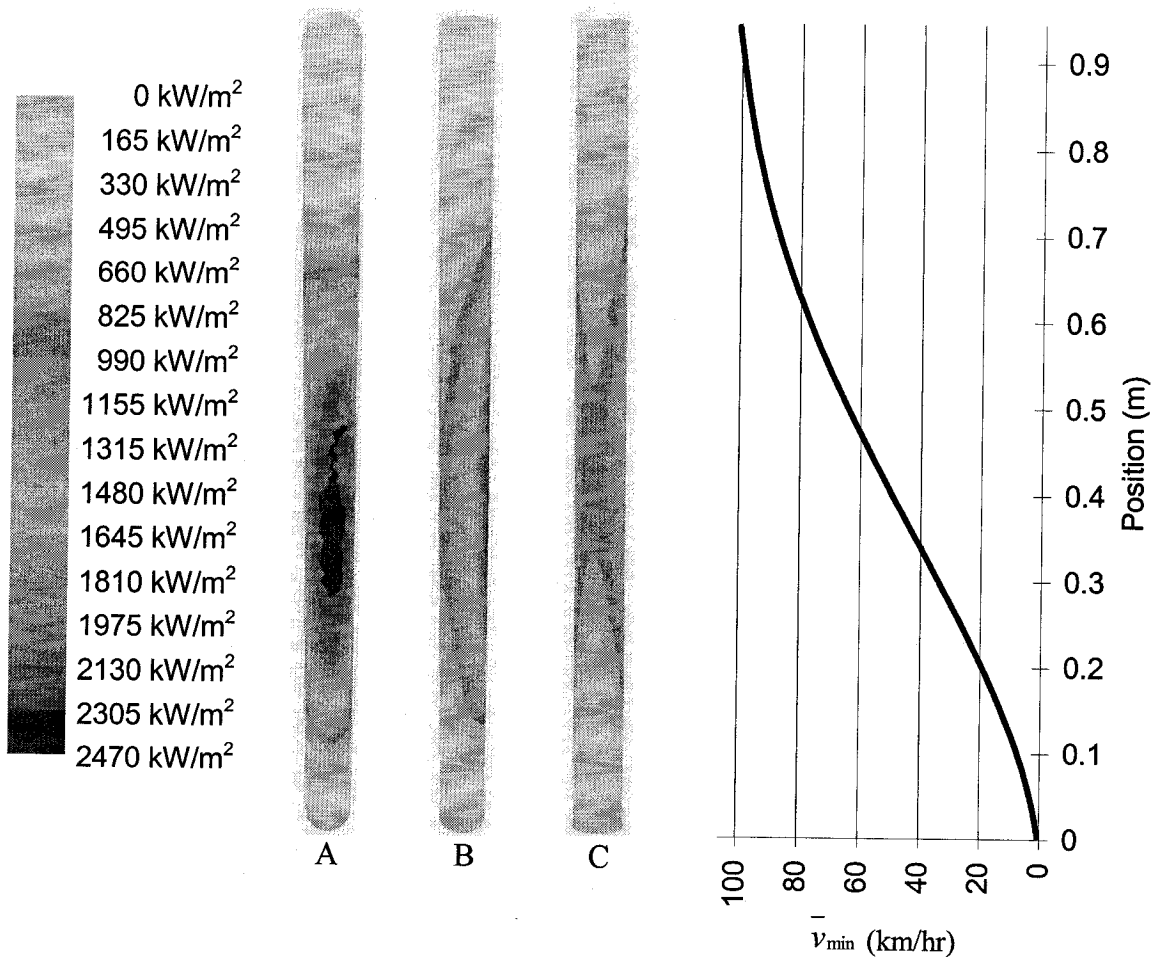


Figure 3.17 Left evaporator heat flux and \bar{v}_{\min} distribution

- A) 0° relative to the front of the tapblock
- B) 90° relative to the front of the tapblock
- C) 180° relative to the front of the tapblock

The velocity distribution (\bar{v}_{\min}) in Figure 3.17 is calculated by integrating the heat flux over the evaporator area using equation (3-9) assuming $\alpha=1$. Note how the velocity increases towards the upper end of the evaporator as more vapour is generated below. The greatest increases in velocity per unit of evaporator length occurs at the center part of the evaporator, because of the larger heat loads being applied there.

The graph in Figure 3.17 suggests that if the velocity field inside the evaporator can be understood more fully, future heat pipe flow modifiers may be tailored to the expected velocity distribution. For example, the helical parameters of the spring (pitch and

thickness) can be designed for lower velocities at the bottom of the evaporator, and gradually be changed to suit larger velocities at the top of the evaporator. The goal of the design would of course be to maximize heat pipe stability and heat extraction capacity. The concept of an engineered flow modifier is discussed in more detail in Chapters 5 (section 5.4) and 6.

Figure 3.18 presents the temperature distribution of the copper tapblock, viewed in horizontal slices, 10cm apart from one another. Note that the tapblock is being viewed from the “back” side, i.e. the side opposite the burner.

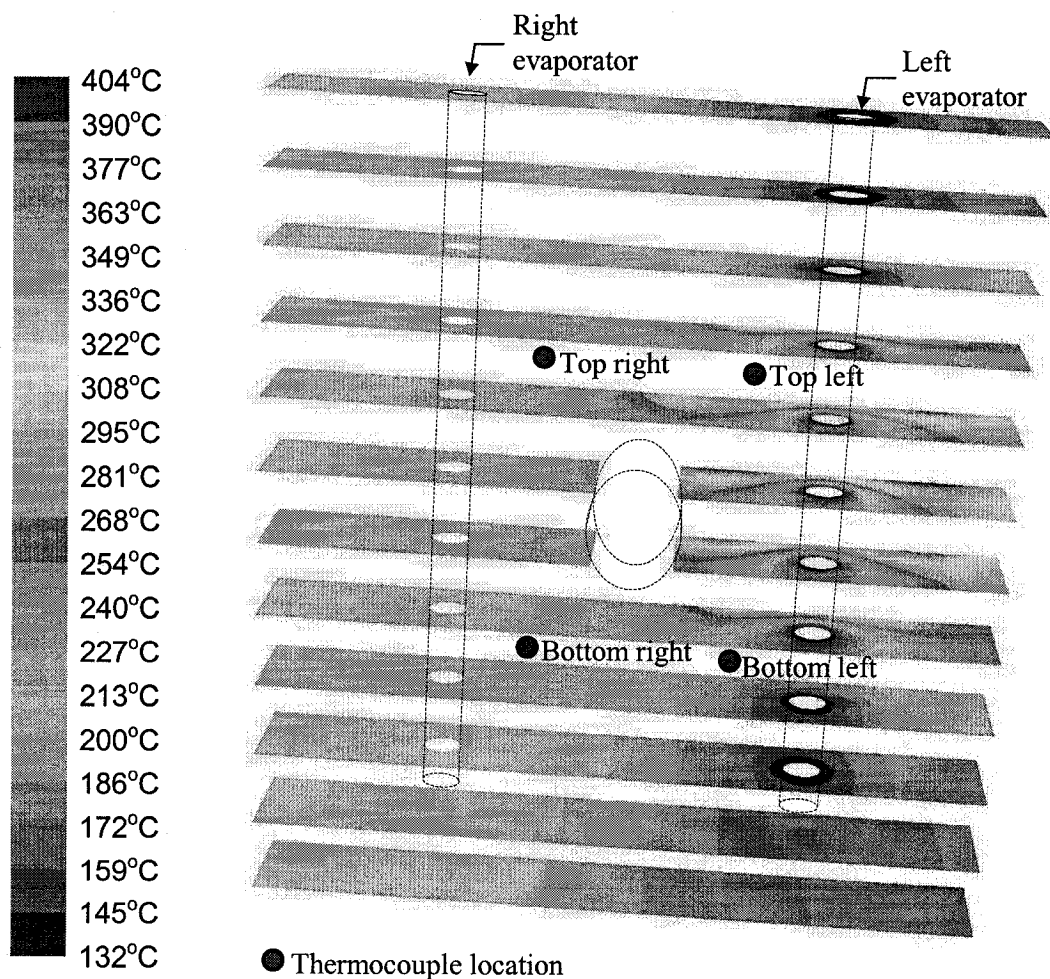


Figure 3.18 Temperature contours of the heat pipe-cooled copper tapblock

It is interesting to note from the temperature distribution in Figure 3.18 that while most of the heat is being fed into the front side of the left evaporator (from the high temperature gradients observed there), some of the heat is also diverted around the evaporator through the copper, and eventually fed into the back side of the evaporator. This is analogous to a drain that is being overloaded with liquid from one side, causing some of the liquid to flow around the drain, and then eventually flow back into the opposite side of the drain. Figure 3.17(C) confirms this observation as heat fluxes of between 300kW/m^2 and 1MW/m^2 are applied to the back of the evaporator (180° from the burner side).

This explains why the temperature readings on the right side of the tapblock ($235^\circ\text{C} - 255^\circ\text{C}$) were greater than the temperature readings on the left side ($180^\circ\text{C} - 205^\circ\text{C}$) while the right heat pipe was turned off (Figure 3.15 at a time of 4:30).

The heat flux applied by the burner during the tests was concentrated over a limited area of the tapblock, causing high temperatures in the tapblock locally (up to 400°C according to the model). However, no significant scaling was detected on the copper block upon further inspection. This is of interest because CuO tends to start forming at temperatures between 200°C and 300°C , and is prone to scaling. The absence of scaling across the high-temperature region of the tapblock may be due to a protective atmosphere generated by the burner combustion products.

In an actual tapblock installed at the Hoboken plant operating under normal conditions, the temperature distribution would probably be different than what is presented here because (1) the heat load would be significantly lower, and (2) the heat flux distribution applied to the tapblock would most likely be more uniform. The heat fluxes entering the evaporator would be therefore distributed more evenly across the evaporator. Similarly, the maximum temperatures occurring at the surface of the tapblock would be significantly lowered. This suggests that a similar system installed in the Hoboken plant would perform at least as well as the system tested in the pilot plant.

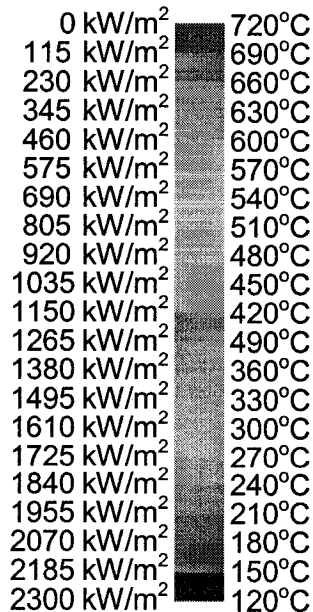
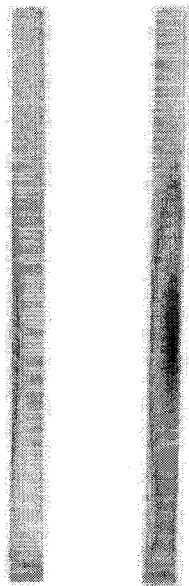
3.5.3 Simulation of Upset Conditions at the Hoboken Blast Furnace

The model described in section 3.5.1 was modified to simulate heat loading conditions that may be encountered at Hoboken. A heat load of 300 kW served as the basis for the present tapblock project, representing upset operating conditions. In order to be as conservative as possible, this entire heat load was applied to the inside circumferential area of the taphole. In reality, some of the heat would be applied from the lateral surfaces and from the hotface of the tapblock. Concentrating the entire heat load has the effect of increasing the heat fluxes to the area of the evaporators around the taphole.

The modeling results show that the copper around the taphole would reach temperatures of over 650°C. Therefore operating the tapblock under these conditions even for a short time would damage it.

A maximum heat flux of approximately 2.35 MW/m² would be applied to the evaporators. As previous modeling indicated that heat fluxes of this magnitude were successfully dissipated experimentally, all indications suggest that the McGill heat pipe cooling system would be adequate to handle even the most extreme scenarios at Hoboken.

Evaporator heat flux contours



Tapblock temperature contours

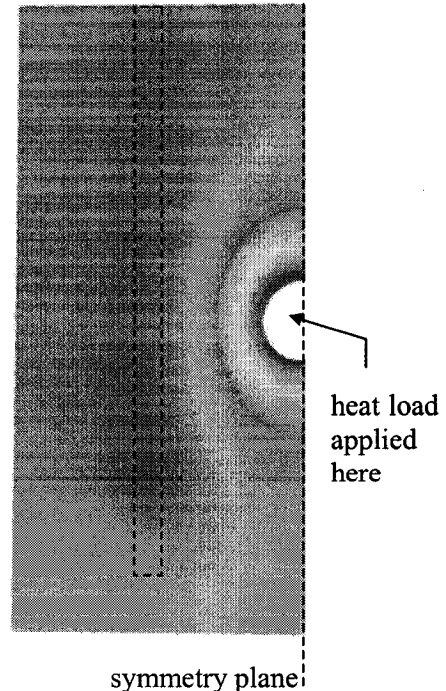


Figure 3.19 Modeling of upset condition at Hoboken

3.5.4 Comparison with Conventional Water Cooling

3.5.4.1 Flow Requirements

One of the most widely used empirical relationships for conjugate heat transfer in a straight pipe under turbulent conditions is the Dittus-Boelter equation, given by equation (3-12).

$$\overline{Nu}_D = 0.023 Re_D^{0.8} Pr^n \quad (3-12)$$

where \overline{Nu}_D is the average Nusselt number based on the pipe diameter

Re_D is the Reynolds number of the fluid

Pr is the Prandtl number of the fluid (4.33 for water at 39°C)

n is equal to 0.4 for heating (i.e. $T_{surface} > T_{bulk}$)

The dimensionless numbers are defined as:

$$\overline{Nu}_D = \frac{\overline{h}D}{k} \quad (3-13)$$

$$Re_D = \frac{\rho v D}{\mu}, \quad Re_D \geq 10,000 \quad (3-14)$$

$$Pr = \frac{\mu c_p}{k}, \quad 0.7 \leq Pr \leq 160 \quad (3-15)$$

where

\overline{h} is the average heat transfer coefficient across the wall/fluid interface ($W/m^2 \cdot ^\circ C$)

D is the pipe inside diameter, in this case 0.0508 m (same as heat pipe evaporator)

k is the thermal conductivity of the fluid, in this case 0.647 $W/m \cdot ^\circ C$ for water at 39°C

ρ is the density of the fluid, in this case 994 kg/m^3 for water

v is the velocity of the fluid (m/s)

μ is the kinematic viscosity of the fluid, in this case $7.19 \cdot 10^{-4}$ Pa·s for water at 39°C

c_p is the specific heat capacity of the fluid, in this case 4.18 $kJ/kg \cdot ^\circ C$ for water at 39°C

The Dittus-Boelter equation can be used to calculate the average coolant velocity (v) required to attain a desired average heat transfer coefficient (\overline{h}), knowing the coolant properties and pipe diameter [38]. Newton's law of cooling defines the heat transfer

coefficient given a heat flux and temperature differential between the pipe surface and coolant bulk. Refer to equation (3-1).

Assuming the boiling mechanism at the working fluid-evaporator wall interface comprises a negligible thermal resistance, the cooling element surface temperature, $T_{surface}$, can be assumed as equal to the experimental heat pipe operating temperature. The data obtained from Umicore indicates that their present taphole cooling system operates with an average bulk water temperature of 39°C (Table 3.1). It is therefore possible to calculate the flowrate required by a conventional water cooling system to dissipate the heat fluxes achieved experimentally via heat pipe cooling. A comparison can then be made to the condenser cooling water flowrate required for the heat pipe system.

Table 3.8 summarizes the calculations done for both the average and maximum heat fluxes applied to the evaporators according to the modeling of the experiment (section 3.5.2), taken as 947 kW/m² and 2.4 MW/m², respectively.

Table 3.8 Comparison of conventional forced convection and heat pipe cooling requirements

	Average heat flux	Maximum heat flux
Applied heat flux, q''	947 kW/m ²	2.4 MW/m ²
Pipe interface temperature, $T_{surface}$	120°C	120°C
Cooling water bulk temperature, T_{bulk}	39°C	39°C
Average heat transfer coefficient, \bar{h}	11,700 W/m ² ·°C	29,600 W/m ² ·°C
Nu_D	940	2,400
Re_D	280,000	895,000
Required cooling water velocity, v	3.6 m/s	11.6 m/s
Required cooling water flowrate (conventional water cooling, calculated)	7.3 l/s	23.5 l/s
Cooling water flowrate (heat pipe cooling, from experiments)	0.78 l/s	
Increase in cooling water requirement for conventional cooling	840 %	2900 %

The results indicate that to safely operate an equivalent conventional water cooling system subjected to the same heat fluxes as the heat pipe system tested experimentally, 8 to 30 times more cooling water would be required.

Because of the critical nature of the tapblock to furnace operation and worker safety, furnace operators would most likely operate the cooling system conservatively, and perhaps use even more cooling water than the calculated requirement. The water velocities, calculated at between 3.6 m/s and 11.6 m/s, are significantly greater than typical water velocities in conventional systems (approximately 2 m/s) [4]. A furnace operator may therefore opt for an alternate tapblock design, such as a refractory or composite assembly.

3.5.4.2 Energy Recovery Potential

The output cooling water temperatures attained values of 85°C during the experiments. These temperatures are much larger than what is typically permitted in conventional cooling water circuits (maximum ~45°C).

Therefore the cooling water generated from this test is much more likely to be used elsewhere in a metallurgical plant as hot water. Otherwise, the water can be cooled and recycled again as cooling water. The greater water temperature implies a larger temperature gradient with the atmosphere, for example, and therefore can be cooled more efficiently, reducing the need for extensive heat exchange systems.

Chapter 4 Heat Pipe Cooling of a Copper Launder

4.1 Introduction

The results from the tapblock tests described in Chapter 3 were encouraging. However, due to the critical nature of this tapblock to furnace operations, it was agreed that more development and testing of the novel heat pipe technology were required to evaluate its long-term performance in an industrial environment. The main objective of this second phase of testing was to further develop the design/operating criteria to ensure proper heat pipe cooling capacity.

A refractory-based slag launder installed as part of a decantation assembly at the Hoboken blast furnace, shown in Figure 4.1, was chosen as an ideal application to attain this objective because it was not considered a particularly critical component of the blast furnace. This launder was fabricated from copper many years ago, but this design was abandoned due to leaks and occasional explosions associated with the water cooling system. Replacing the present-refractory-based launder with a copper heat pipe-cooled launder (water-based) offered the same advantages as a water-cooled launder without many of the safety concerns associated with forced convection water cooling [81].

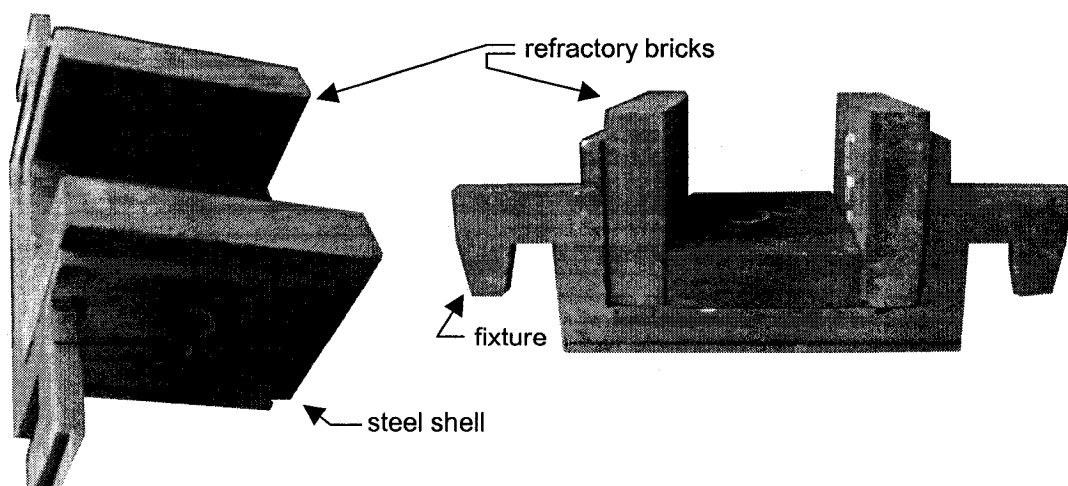


Figure 4.1 Refractory-based slag launder

4.2 Modeling

The most important step in designing a cooling system is obtaining an accurate estimate of the heat load that will be applied during operation. Unlike the tapblock tests, no heat load information was available for the slag launder application. Computational Fluid Dynamics (CFD) modeling was done to predict the heat load, as well as analyze and compare possible designs while accounting for geometric constraints on the cooling system. Commercial mesh generation (GAMBIT 2.1.6) and CFD solver (FLUENT 6.2.16) software packages were used [82].

4.2.1 General Configuration of the Heat Pipe Cooled Launder

The geometry used for the model was based on the design of the refractory-based launder currently used at Hoboken, with several minor differences. For example, the cross-section of the slag channel was enlarged in order to allow for the formation of a slag skull and avoid the constriction of the slag flow.

It was decided to position the evaporators at the bottom of the slag launder, perpendicular to the flow of slag. This configuration made it easy to insert the return line and flow modifier into each evaporator. In addition, the main pipes, through which the steam/water mixture flows towards the condenser, can be extended out of the decantation area enclosure without difficulty in a future industrial test.

The symmetry of this design allowed for only half of the volume to be modeled, which effectively halved the computational effort required. This demi-volume was taken as the domain for the present model, seen in Figure 4.2.

Briefly stated, the model includes the solid copper launder which is cooled by three cast-in monel heat pipes. Molten slag flows through the launder channel and is cooled in the vicinity of the launder wall. Therefore, heat is transferred from the molten slag to the copper launder via conjugate heat transfer. The heat is then funneled through the copper launder across the monel evaporator wall and into the heat pipe evaporators by conduction. In the process, a slag skull is formed in the slag channel, which acts as a thermal insulator.

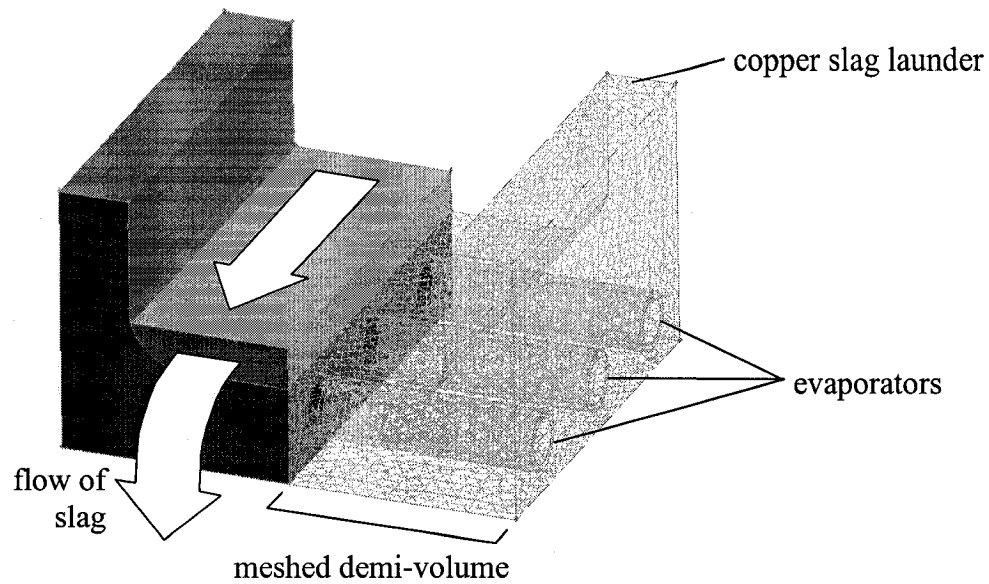


Figure 4.2 Slag launder geometry

4.2.2 Operating Parameters and Assumptions

Operational data related to the slag production rate and process temperature was supplied by Umicore's Hoboken facility. The slag production rate was used to calculate the bulk flow rate of slag across the launder. By estimating the height of the slag in the slag channel, the corresponding slag velocity at the inlet boundary of the model was calculated.

Based on the favourable results obtained for copper, described in a report submitted to Umicore [83], the present model assumed the slag launder to be fabricated out of copper and also assumed no contact resistance at the slag skull/copper launder interface, and no contact resistance at the copper launder/monel pipe interface. The heat pipe operating temperature was assumed to be 100°C, which is a typical value for water-based systems. Refer to Table 4.1.

Table 4.1 Summary of the operating parameters and assumptions

Parameter	Value	Value used in model
Slag production	400-450 tonnes/day	450 tonnes/day
Slag process temperature	1200-1220°C	1220°C
Copper/monel contact resistance	unknown	0 m ² ·K/W
Slag/copper contact resistance	unknown	0 m ² ·K/W
Heat pipe operating temperature	80-150°C	100°C

4.2.3 Material Properties

Table 4.2 summarizes the material properties used in the model. These values were obtained either from available literature [84, 85] or from Umicore staff [86].

Table 4.2 Material properties

Material	Property	Value	Value used in model
Slag	Density (ρ)	3500–3700 kg/m ³	3700 kg/m ³
	Heat capacity (c_p)	Figure 4.3	Figure 4.3
	Thermal conductivity (k)	1.2 – 1.8 W/m·°C	1.5 W/m·°C
	Molecular weight (M)	58 - 67 kg/kmol	66 kg/kmol
	Viscosity (μ)	equation (4-1)	equation (4-1)
	Melting heat (H_{fs})*	-	1 J/kg
	Solidus temperature ($T_{solidus}$)	-	910°C
	Liquidus temperature ($T_{liquidus}$)	-	911°C
Copper alloy C81100L	Density (ρ)	8940 kg/m ³	8940 kg/m ³
	Heat capacity (c_p)	377.1 J/kg·°C	377.1 J/kg·°C
	Thermal conductivity (k)	346.1 W/m·°C	346.1 W/m·°C
Monel 400 series alloy	Density (ρ)	8840 kg/m ³	8840 kg/m ³
	Heat capacity (c_p)	430 J/kg·°C	430 J/kg·°C
	Thermal conductivity (k)	21.7 W/m·°C	21.7 W/m·°C

* Note that the latent heat of fusion is essentially taken into account in the heat capacity.

In order to obtain values for the slag molecular weight (M) and heat capacity (c_p), the slag composition was obtained from Umicore's Hoboken facility. The composition was then normalized using commercial chemical thermodynamics software (FactSage), with the results given in Table 4.3 below. Figure 4.3 displays the calculated heat capacity of the slag versus process temperature, also derived using FactSage.

Table 4.3 Slag composition

Component	Weight %
FeO	35.7
SiO ₂	33.6
CaO	21.6
Fe ₂ O ₃	1.6
ZnO	7.5

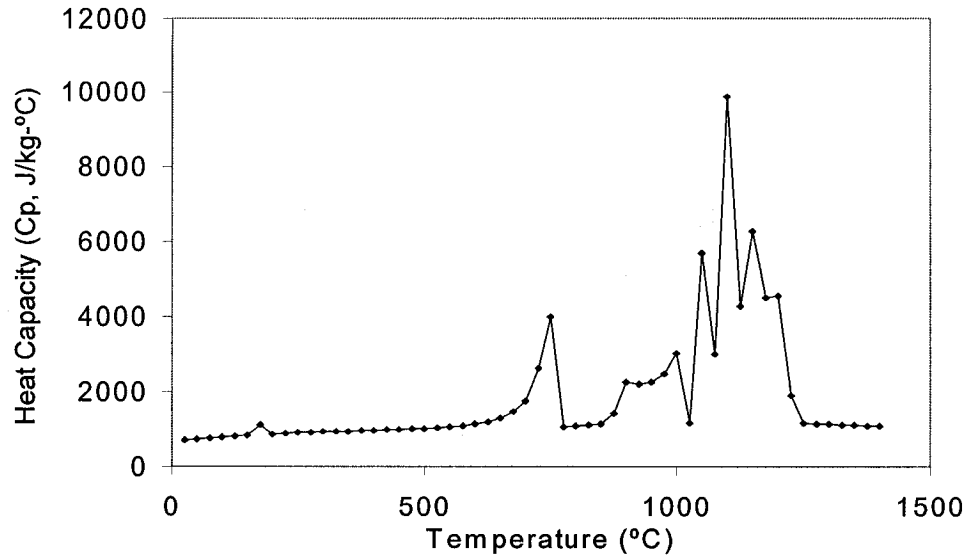


Figure 4.3 Slag heat capacity vs. temperature

The slag viscosity was given by Yen using the following empirical correlation for a similar lead blast furnace slag [87]:

$$\mu = (6.881 \cdot 10^{-6})T^2 - (0.0182)T + 12.156 \quad (4-1)$$

where

μ is the dynamic viscosity of the slag (Pa·s)

T is the temperature of the slag (°C)

It was assumed that the slag would be quenched against the cooled slag launder. Therefore the solidified slag would be an amorphous glass, such that the equation for the viscosity may be extrapolated below the liquidus temperature of the slag. The glass transition temperature was found to be about 910°C, corresponding to a viscosity of 1.3 Pa·s. Modeling results indicated that the slag velocity was negligible if the viscosity exceeded 1.3 Pa·s. The precipitation of solids from the slag and its effects on the slag viscosity were not taken into account.

4.2.4 Geometry and Boundary Conditions

4.2.4.1 Parametrization

An important characteristic of the model was the parametrization of the geometry, meshing, and boundary conditions. This essentially involved encoding the commands required to model the slag launder into a simple software program, with all geometric and boundary condition parameters set as variables. These variables could be easily changed, and a new model domain could be constructed almost instantly in the mesh generation software. The domain was then imported into the CFD solver, the new boundary conditions were imposed, and new results were generated. The additional effort required to produce the software was offset by the ability to model dozens of slag launder configurations under a variety of heat loading conditions.

4.2.4.2 Geometry

Figure 4.4 presents an index of the geometric parameters used for the final model. In order to obtain an accurate estimate of the height of the slag flow (HSF), a detailed model of the entire slag decantation assembly would have been required. Therefore, HSF values of 3 cm and 6 cm were used for the model, based on visual observations of the present refractory-based slag launder currently used at Hoboken. These two sets of results are presented in this thesis (HSF = 3cm, 6cm). It was expected that the actual system will behave within the range given by these two models.

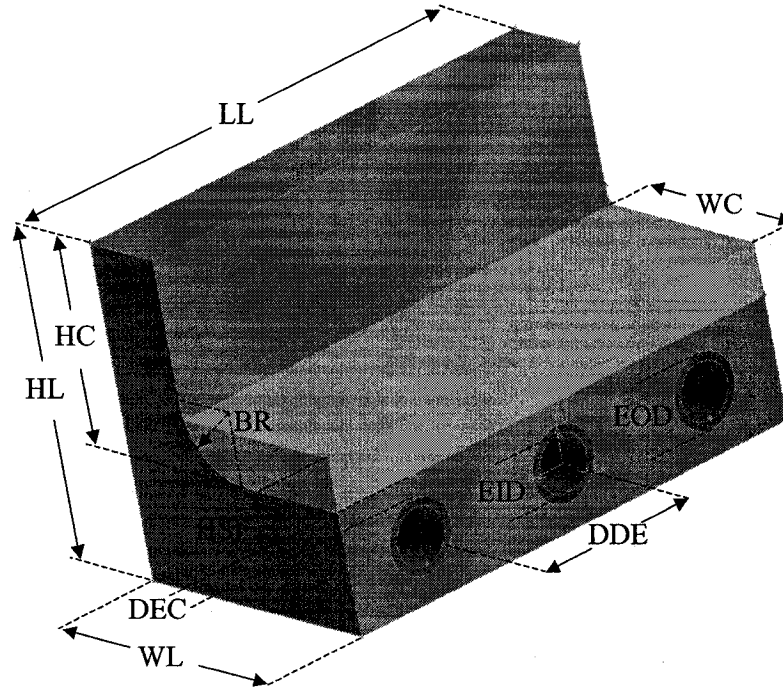
4.2.4.3 Boundary Conditions

Figure 4.5 and Table 4.4 present the boundary conditions used in the model. These boundary conditions were sufficient to ensure that the problem was well-posed, and that a unique solution existed.

The top boundaries for the three slag channel volumes were set as symmetry boundaries. With the assumption that there is a zero-friction condition and no heat or momentum flow at this interface, the symmetry boundary condition could be applied.

The pre-flow volume was created to allow the FLUENT solver to attain fully-developed flow conditions prior to the volume of interest (slag channel). The post-flow volume was

created in order to allow the development of any flow features such as flow separation or eddies, and ultimately aided in the convergence of the model. This avoided a computational phenomenon known as *reversed flow* at the outlet boundary.



Label	Description	Value in Present Model
Laundry		
LL	Laundry Length	30 cm
HL	Laundry Height	19 cm
WL	Laundry Width	16.5 cm (33 cm full length)
BR	Bevel Radius	4 cm
WC	Channel Width	11.5 cm (23 cm full length)
HC	Channel Height	12 cm
Evaporators		
EID	Evaporator Inner Diameter	3.51 cm
EOD	Evaporator Outer Diameter	4.22 cm
DEC	Evaporator Distance from Slag	1.56 cm
DDE	Evaporator Spacing	10 cm
Slag Flow		
HSF	Slag Flow Height	Varied: 3 cm and 6 cm
Not shown	Pre-flow Volume Length	7 cm
Not shown	Post-flow Volume Length	30 cm

Figure 4.4 Geometric parameters

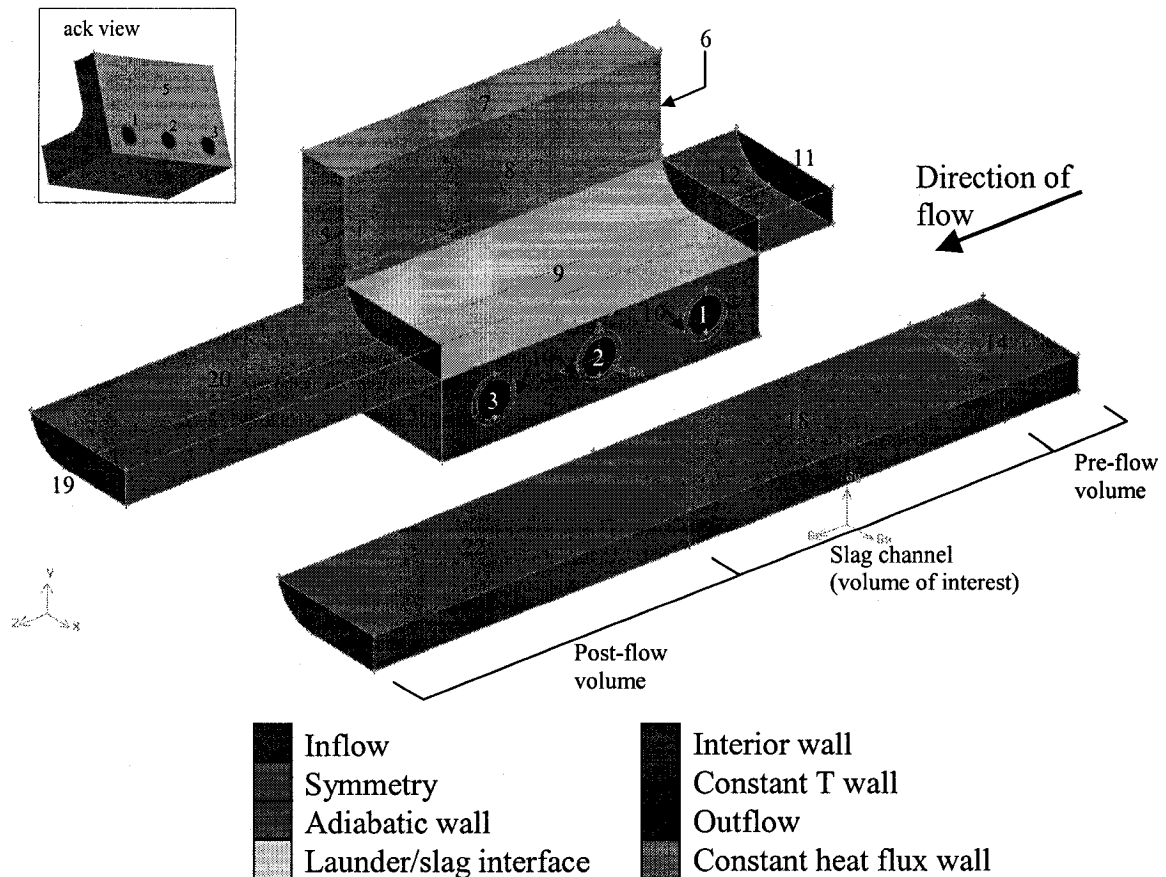


Figure 4.5 Boundary conditions

Table 4.4 Boundary conditions

#	Boundary name	Description
Launder		
1-3	Evaporator walls	Constant temperature wall (each set at 100°C)
4	Launder symmetry	Symmetry boundary
5	Launder misc. walls	Constant heat flux walls, facing away from slag/burner (adiabatic)
6	Launder front wall	Constant heat flux walls, in contact with decantation vessel
7	Launder top wall	Constant heat flux wall (HSF=3cm: 38 kW/m ² ; HSF=6cm, 29 kW/m ²)
8	Launder inner wall	Constant heat flux wall (HSF=3cm: 76 kW/m ² ; HSF=6cm, 58 kW/m ²)
9	Launder / slag contact	Interior wall with no-slip condition, contact resistance = 0 m ² ·K/W
10	Monel / copper contact	Interior wall, contact resistance = 0 m ² ·°C/W
Pre-flow volume		
11	Inflow	Constant velocity (HSF=3cm: 0.23 m/s; HSF = 6cm: 0.11 m/s), 1220°C
12	Pre-flow wall	Adiabatic copper wall with no-slip condition
13	Pre-flow symmetry	Symmetry boundary
14	Pre-flow top	Symmetry boundary
Slag channel		
15	Pre-flow interior	Interior boundary (free flow across this interface)
16	Post-flow interior	Interior boundary (free flow across this interface)
17	Slag channel symmetry	Symmetry boundary
18	Slag channel top	Symmetry boundary
Post-flow volume		
19	Outflow	Velocity distribution computed from the model
20	Post-flow wall	Adiabatic copper wall with no-slip condition
21	Post-flow symmetry	Symmetry boundary
22	Post-flow top	Symmetry boundary

4.2.5 Flow Regime

From the boundary conditions, the Reynolds number was calculated, with the details given in Table 4.5. The results clearly indicated that the flow regime of the slag launder at Hoboken would be laminar ($Re < 2300$).

Table 4.5 Reynolds number

	Slag Flow Height (HSF)	
	3 cm	6 cm
Hydraulic diameter (D_H)	0.10 m	0.17 m
Cross-sectional area	0.0062 m ²	0.013 m ²
Wetted perimeter	0.26 m	0.32 m
Density (ρ)	3700 kg/m ³	3700 kg/m ³
Average velocity (v_{av})	0.23 m/s	0.11 m/s
Viscosity (μ)	0.19 Pa·s	0.19 Pa·s
Reynolds number (Re)	420	340

4.2.6 Radiation Sub-Model

A simple radiation model was included in the simulation to calculate the radiative heat flux from the slag to the inner and top walls of the launder. The model assumes radiation from the slag surface and decantation tank opening (slag channel inlet less the slag), taken as having a temperature of 1220°C and an emissivity of 1. Refer to Appendix A for more details on the assumptions and methodology used.

The radiative heat flux applied to the *launder inner wall* was set to 76 kW/m² and 58 kW/m² in the model for a slag flow height (HSF) of 3 cm and 6 cm, respectively. Overall, the radiative heat load in both models was relatively small, calculated as 2.5 kW and 1.4 kW for the HSF=3cm and HSF=6cm scenarios, respectively.

4.2.7 Monitors

In order to analyze the simulations quantitatively after solving, five monitors were programmed (see Figure 4.6). The first 3 monitors were used to record the total heat load applied to each heat pipe evaporator by integrating the heat flux across the evaporator walls.

The remaining two monitors were used to record the average slag skull thickness along the slag channel. The first of these monitors obtained the area-weighted average solid fraction across the symmetry surface of the slag channel. Because the solid/liquid interface was continuous and well defined, multiplying this value by the surface height (either 3cm or 6cm) yielded the average skull thickness. The final monitor was used to calculate the total volume of slag solidified onto the copper launder, from which the mass of solidified slag could easily be obtained.

Note that the *heat load* and *slag mass* monitors recorded values of half the slag channel. Therefore, these values should be doubled to correspond to an actual slag launder operating at Hoboken.

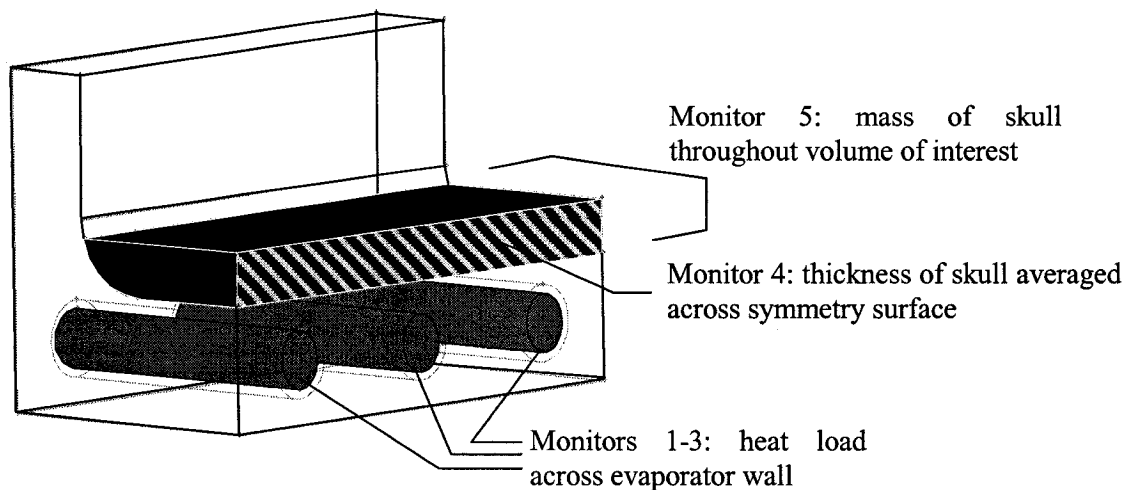


Figure 4.6 Monitors

4.2.8 Governing Equations and Solver Parameters

4.2.8.1 Governing Equations

The energy, mass, and momentum conservation equations were used (see section 2.7.2) along with a solidification model. The flow was assumed to be laminar, as indicated in section 4.2.5 and so no turbulence modeling was necessary.

In order to have a full understanding of the modeling results, a description of the solidification model is required. In this case, the energy equation is defined as

$$\frac{\partial}{\partial t}(\rho H) + \nabla \cdot (\rho \vec{v} H) = \nabla \cdot (k \nabla T) + S_{energy} \quad (4-2)$$

where the enthalpy of the material, H , is defined as the sum of the sensible enthalpy, $H_{sensible}$, and the latent heat, ΔH_{fs} :

$$H = H_{sensible} + \Delta H_{fs} \quad (4-3)$$

The right-hand terms are defined by equations (4-4) and (4-5) :

$$H_{sensible} = H_{ref} + \int_{T_{ref}}^T c_p dT \quad (4-4)$$

$$\Delta H_{fs} = \beta H_{fs} \quad (4-5)$$

where H_{ref} is a reference enthalpy, T_{ref} is the corresponding reference temperature, c_p is the specific heat at constant pressure, H_{fs} is the latent heat of fusion of the material, and β is the liquid fraction, given by the lever rule:

$$\begin{aligned} \beta &= 0 \text{ if } T < T_{solidus} \\ \beta &= 1 \text{ if } T > T_{liquidus} \\ \beta &= \frac{T - T_{solidus}}{T_{liquidus} - T_{solidus}} \text{ if } T_{solidus} < T < T_{liquidus} \end{aligned} \quad (4-6)$$

In equations (4-2) and (4-3), both the temperature T and the liquid fraction β are unknown. Therefore, these variables are solved for iteratively, using a numerical method proposed by Voller and Swaminathan [88].

In order to account for the momentum loss of the fluid within the mushy zone, the enthalpy-porosity technique is used [75], which treats the semi-solid region as a porous medium. The momentum sink is expressed as :

$$S_{momentum} = \frac{(1-\beta)^2}{(\beta^3 + \varepsilon)} A_{mush} (\vec{v} - \vec{v}_p) \quad (4-7)$$

where ε is a small number to avoid division by zero (0.001), A_{mush} is the mushy zone constant, and \vec{v}_p , the pull velocity, is equal to zero for the present application (there is no external force applied to the solidifying slag).

The mushy zone constant is specific to the problem being modeled, and represents the degree of momentum dampening which takes place. The literature suggests that this value is typically between 10^4 and 10^7 [75]. For the purposes of this model, a conservative value of 10^4 is taken to minimize the loss of momentum of the fluid flowing within the mushy zone (enhancing the calculated heat transfer).

4.2.8.2 Solver Parameters

The segregated solver was used for the present model, as convergence was found to be relatively rapid. Recall that only implicit linearization is available with the segregated solved. Refer to section 3.5.1.2 of Chapter 3.

To extrapolate mass and energy fluxes across cell interfaces for more complex flows, second-order schemes are more accurate but are more likely to lead to divergence. However, as the slag launder model is a relatively simple conjugate heat transfer system, the second-order scheme was chosen. When performing transient modeling, the transient term of the governing equations were also discretized using a second-order scheme for a higher degree of accuracy.

Other solver settings which were used include the “Simple” algorithm for pressure-velocity coupling and linear interpolation for interfacial pressures. Table 4.6 summarizes the solver parameters used for the slag launder system.

Table 4.6 Summary of solver parameters

Parameter	Setting chosen	Rationale
Numerical solver	segregated	more stable iterative procedure
Linearization	implicit	only option available with segregated solver
Spatial discretization scheme – energy, momentum	second-order upwind	yields more precise results, good convergence for simple models
Temporal discretization (transient modeling)	second-order	yields a higher degree of accuracy compared with using a first-order scheme

For the steady-state modeling, the default convergence criteria of the Fluent software was retained. Convergence was further verified by examining the data obtained from the monitors described in section 4.2.7.

For the transient modeling, an adaptive time stepping method was used, with the maximum number of iterations per time step set to 100. Again, the default convergence criteria were retained. Briefly explained, adaptive time stepping methods modify each successive time step to maintain convergence to within the specified tolerances. If convergence occurs with fewer iterations than what is desired, the time step is increased, whereas if convergence requires more iterations than desired, the time step is decreased. The purpose of this is to generate solutions as rapidly as possible while maintaining a given level of accuracy.

4.2.9 Initialization

4.2.9.1 Steady-State Modeling

For the present model, the slag parameters were initialized from the inlet boundary condition. Therefore, the entire slag domain was initialized at a temperature of 1220°C and a velocity of 0.23 m/s or 0.11 m/s in the z-direction for slag flow heights of 3cm or 6cm, respectively. There was no slag skull initially, and the copper launder was initialized at a uniform temperature of 100°C.

4.2.9.2 Transient Modeling

Unlike for steady-state modeling, the solution to transient problems are dependant on the initial condition, which is assumed as the solution at time 0. For the transient model, the initial conditions were chosen similarly to the initial condition described for the steady-state modeling (section 4.2.9.1).

Physically, this can be considered as roughly corresponding to a newly-installed slag launder. The launder is preheated to a temperature of 100°C, at which time a slag tap is initiated, instantly filling the slag channel.

4.3 Model Results

4.3.1 Steady-State Model

The key values of the steady-state model are summarized in Table 4.7 below. As previously mentioned, the slag flow height was assumed as either 3cm or 6cm, including the predicted thickness of the skull. The results from these two models gave a conservative range within which an actual slag launder is expected to operate in industry.

Table 4.7 Summary of the steady-state model results

	Slag Flow Height (HSF)	
	3 cm	6 cm
Slag launder		
Total heat load*	15.0 kW	11.3 kW
Average heat flux to launder channel	325 kW/m ²	210 kW/m ²
Peak heat flux to launder channel	1.35 MW/m ²	910 kW/m ²
Launder temperature range	100-220 °C	100-220 °C
Average launder temperature by mass	160 °C	150 °C
Slag/launder contact area**	0.0383 m ²	0.0473 m ²
Slag bulk velocity	0.23 m/s	0.11 m/s
Average skull thickness	3.9 mm	6.3 mm
Skull mass***	600 g	1220 g
Heat pipes		
Leading evaporator		
Heat load*	6.8 kW	5.2 kW
Average heat flux	380 kW/m ²	290 kW/m ²
Peak heat flux	660 kW/m ²	450 kW/m ²
Middle evaporator		
Heat load*	4.5 kW	3.3 kW
Average heat flux	250 kW/m ²	190 kW/m ²
Peak heat flux	375 kW/m ²	280 kW/m ²
Trailing evaporator		
Heat load*	3.7 kW	2.8 kW
Average heat flux	210 kW/m ²	150 kW/m ²
Peak heat flux	310 kW/m ²	240 kW/m ²

* Recall that the heat loads presented here correspond to one half of the actual launder.

** Recall that the contact area presented here corresponds to one half of the actual launder.

*** Recall that the mass of solidified slag presented here is calculated over half the slag channel volume.

The key factor to consider when comparing the results between the two simulations is that the velocity in the HSF=3cm simulation is significantly greater than the velocity in the HSF=6cm simulation. The different velocities are necessary to maintain the overall slag production rate of the Hoboken blast furnace, taken as 450 tonnes/day (from actual plant data).

Intuitively, it may be assumed that the HSF=6cm simulation is more thermally intense than the HSF=3cm simulation, as the former has a larger contact area with the copper launder. This is not the case. The increase in the slag height from 3 cm to 6 cm increases the contact area with the launder by only 24 %. However increasing the slag height has the effect of decreasing the slag bulk velocity by a factor of ~2. The smaller velocity in the HSF=6cm simulation corresponds to decreased convective heat transfer, and allows a thicker skull to form. The enlarged slag skull, which is essentially a thermal resistance ($k = 1.5 \text{ W/m} \cdot ^\circ\text{C}$), further contributes to a decreased heat load applied to the slag launder as observed in the results for a slag flow height (HSF) of 6cm.

An overall view of both models is presented in Figure 4.7, which displays the temperature contours. Note the difference in the slag height between both models. Also, note the fact that the majority of the temperature gradient occurs in the slag skull, indicating that this region of the model indeed constitutes the most important thermal resistance.

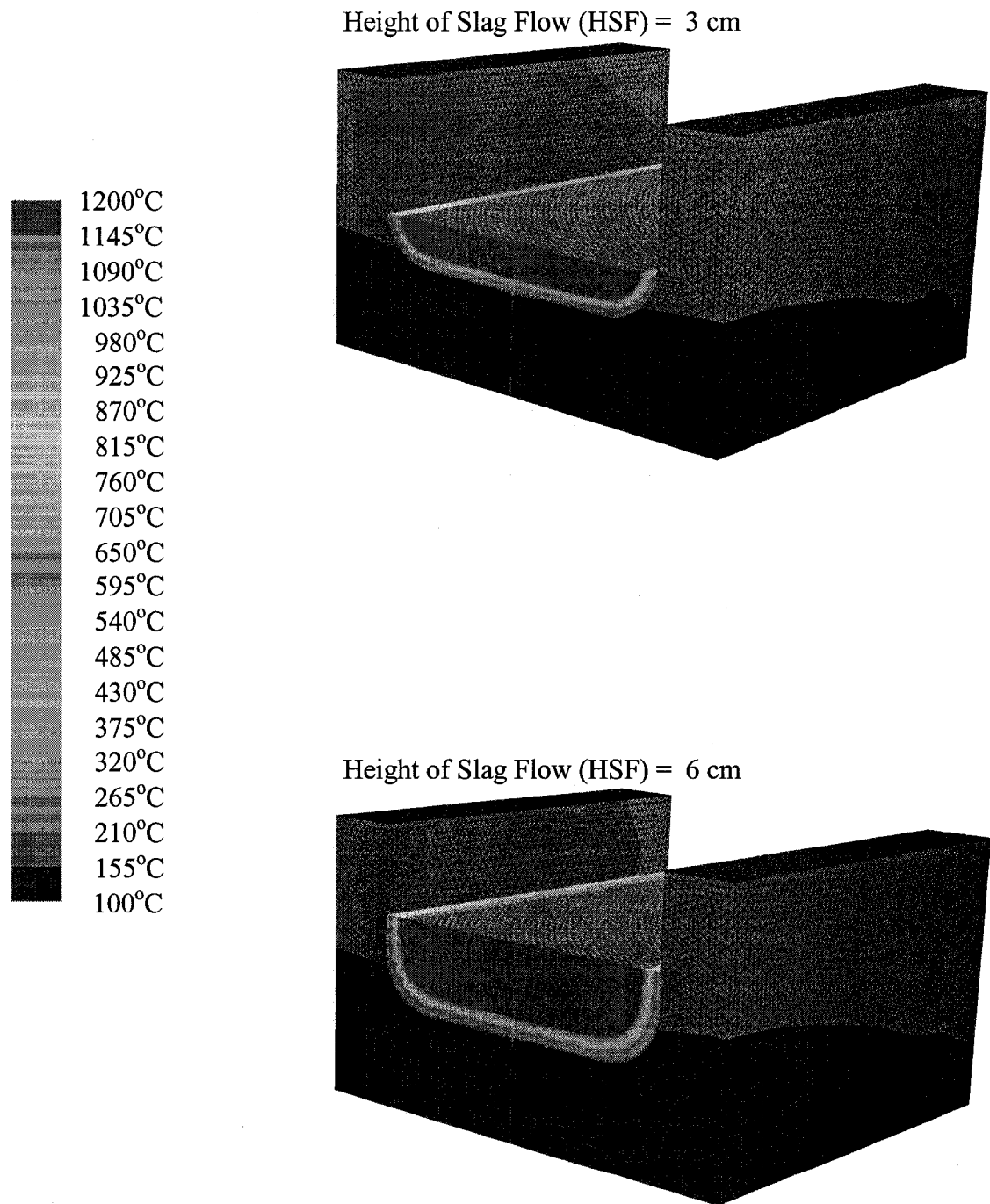


Figure 4.7 Temperature contours of the models

4.3.1.1 Evaporator Heat Load / Heat Flux

Figure 4.8 presents the steady-state model results for the heat load applied to the evaporators. For reasons discussed in section 4.3.1, the heat load in the HSF=3cm simulation is greater than in the HSF=6cm simulation, settling at values of 15.0 kW and 11.3 kW, respectively. Of course, this corresponds to values of 30.0 kW and 22.6 kW for the full launder (two halves).

An interesting observation is that the leading evaporator (closest to the slag inlet) in both simulations is subjected to a heat load significantly greater than for the other two evaporators. This is due to the fact that the slag requires a certain distance along the launder to cool and develop a skull. Therefore, the trailing end of the launder is better insulated than the leading end. Refer to section 4.3.1.2 for details pertaining to the slag skull profile.

It should also be noted that an increased heat load should cause an increased operating temperature (and pressure differential to drive more vapour from the evaporators). This is not taken into account in the model. However, the temperature increase should be relatively minor, and should not comprise a large source of error. Better evaporator models are forthcoming and will take these effects into account (see Chapter 6).

The evaporator heat load results are mirrored in Figure 4.9, which shows the heat flux contours across the evaporators. The more intense thermal conditions in the HSF=3cm simulation produces a peak heat flux of 660 kW/m^2 across the leading evaporator, as compared to 450 kW/m^2 in the HSF=6cm model. Another interesting observation is that the top evaporator surfaces, which are closer to the molten slag, are exposed to heat fluxes 2-3 times greater than their respective bottom surfaces.

A further observation is the fact that the heat flow originating from the sidewalls is of lesser importance in the HSF=3cm simulation compared with the HSF=6cm simulation. For example note that for the middle and trailing evaporators of the HSF=6cm simulation, the peak heat flux occurs below the sidewall, away from the centerline (symmetry plane). No such phenomenon is observed in the HSF=3cm simulation. Once again, these results are as expected as more heat is anticipated to flow into the launder via the sidewall when the slag flow height is greater.

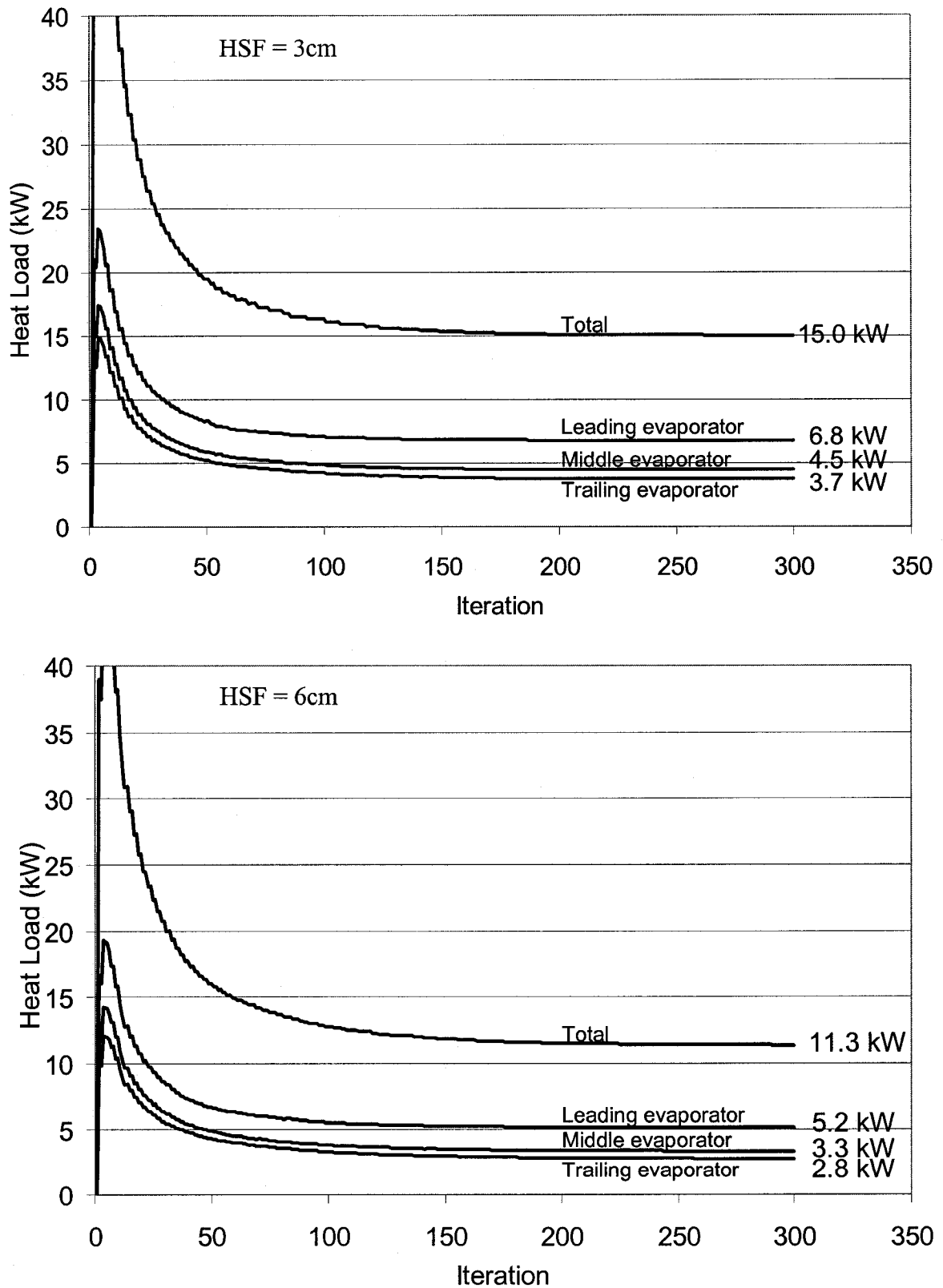


Figure 4.8 Convergence of the steady-state heat load *

* Recall that the heat loads presented here correspond to one half of the actual launder.

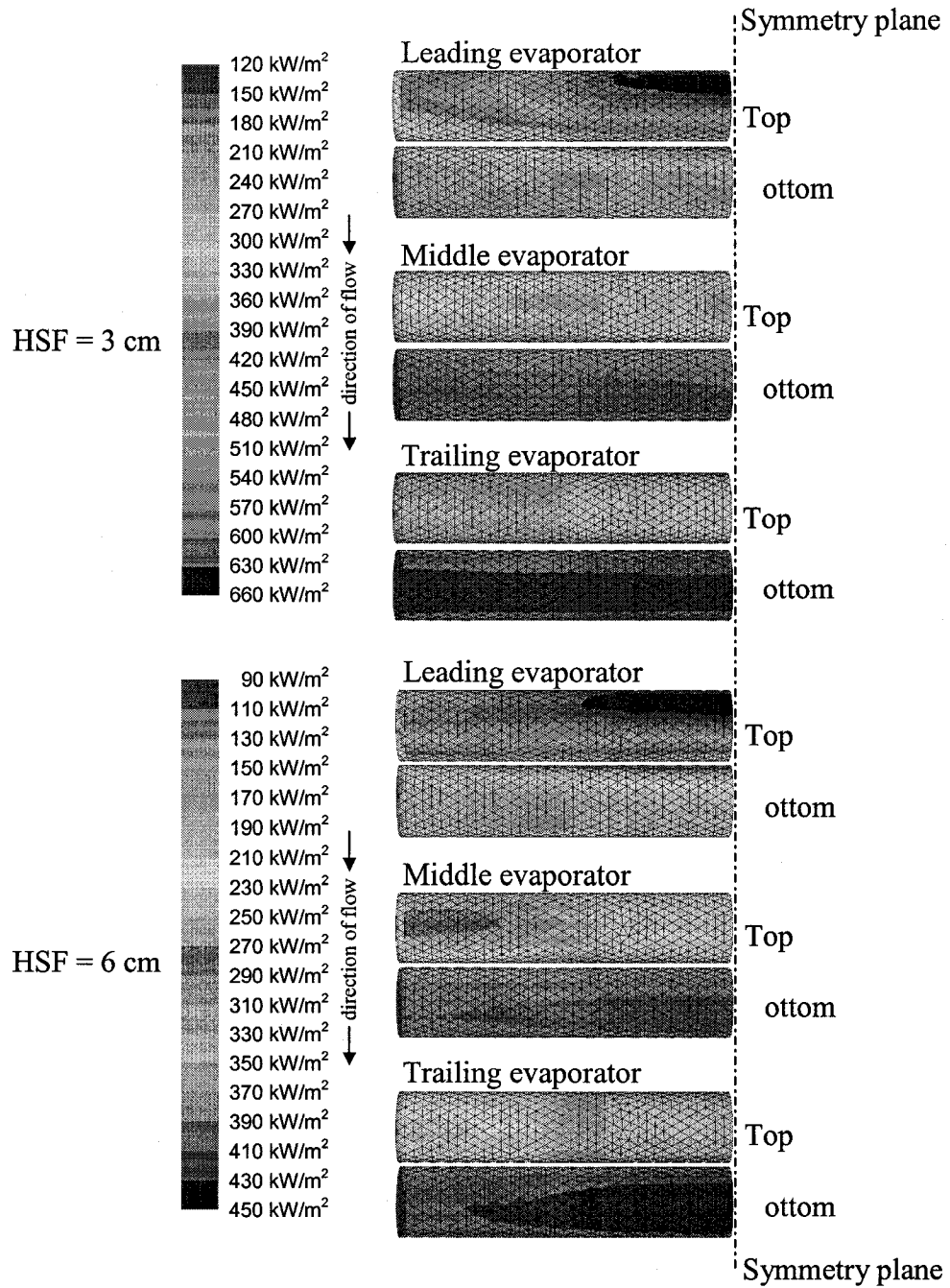


Figure 4.9 Steady-state evaporator heat flux

4.3.1.2 Skull Profile

Figure 4.10 presents the results from the model related to the formation of the slag skull. As previously mentioned, the enhanced convective heat transfer in the HSF=3cm model generates a thinner slag skull, which constitutes a smaller thermal resistance. This is evident in Figure 4.10 where a total heat load of 15.0 kW is predicted with an average skull thickness of 3.9 mm. Conversely, the HSF=6cm model predicts a lower total heat load of 11.3 kW, due to smaller slag velocities. Therefore, a thicker skull of 6.3 mm is predicted.

Figures 4.11 and 4.12 present the liquid fraction contours of both models, in which the solidified skull profile is clearly visible. Note how the slag thickness increases as a function of the distance from the inlet. As the slag passes over the launder, an increasing amount of slag is cooled such that it is essentially solid. The solid slag is deposited in the launder channel, and insulates the copper launder. Therefore, the skull is very thin at the leading end of the launder, which explains why the leading evaporator is subjected to a greater heat load (previously discussed in section 4.3.1.1).

Figure 4.13 presents the heat flux profile applied to the slag launder channel. The peak heat fluxes exist at the leading edge of the channel (HSF=3cm: 1.35 MW/m²; HSF=6cm: 910 kW/m²), where very little slag has solidified. Therefore this figure conforms with the observations regarding the skull profile and the larger evaporator heat load at the leading end of the slag launder.

The average heat flux applied to the launder is predicted as 325 kW/m² and 210 kW/m² for the HSF=3cm and HSF=6cm simulations, respectively. This compares well with conservative heat flux estimates used in practice for slags, typically assumed as 300 kW/m² when engineering furnace equipment [86].

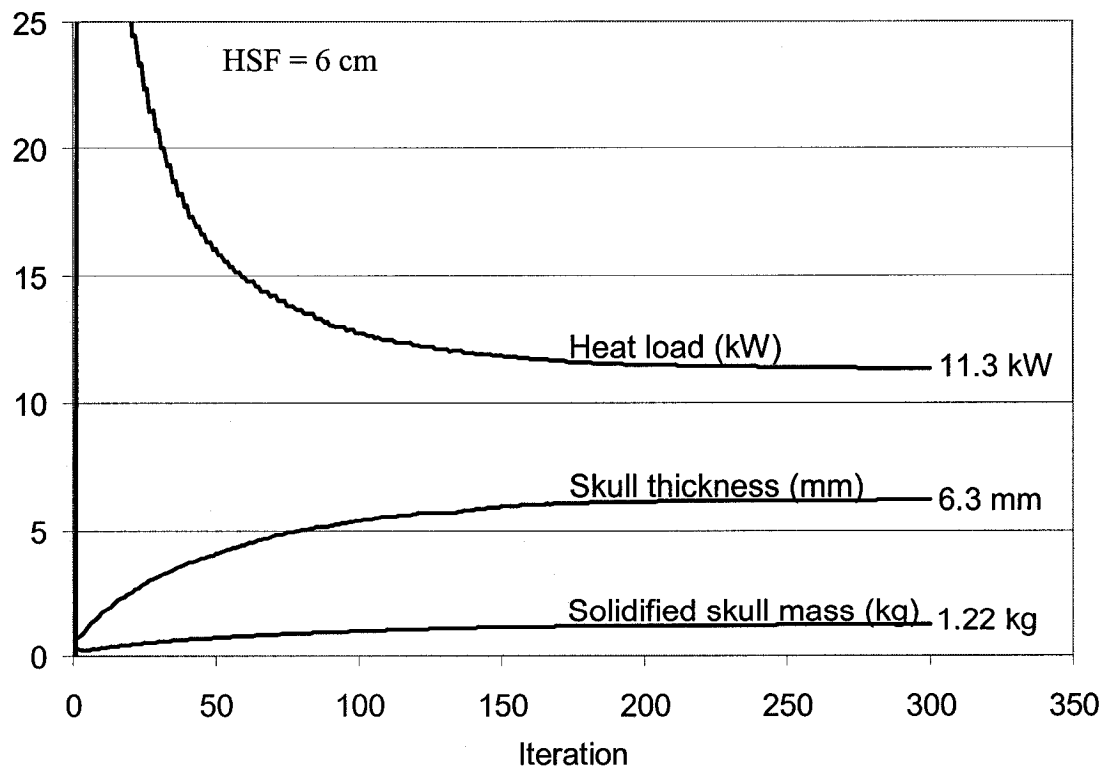
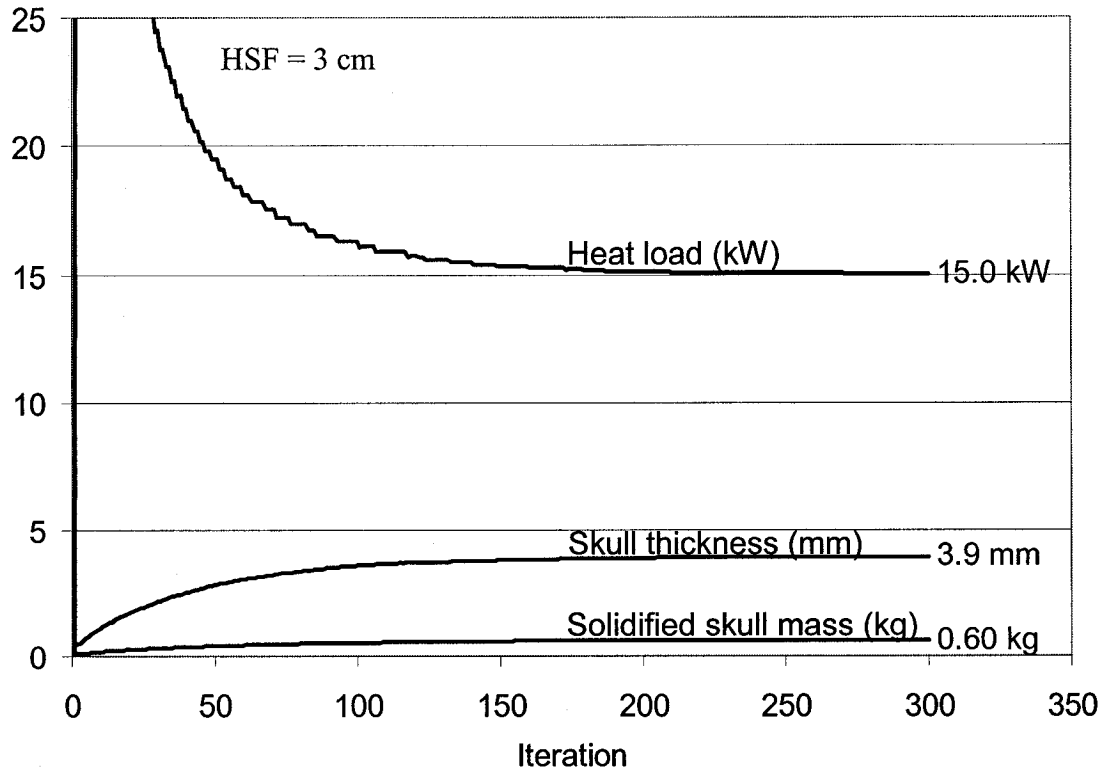


Figure 4.10 Convergence of the steady-state skull formation*

* Recall that the heat load and skull mass presented here correspond to one half of the actual launder.

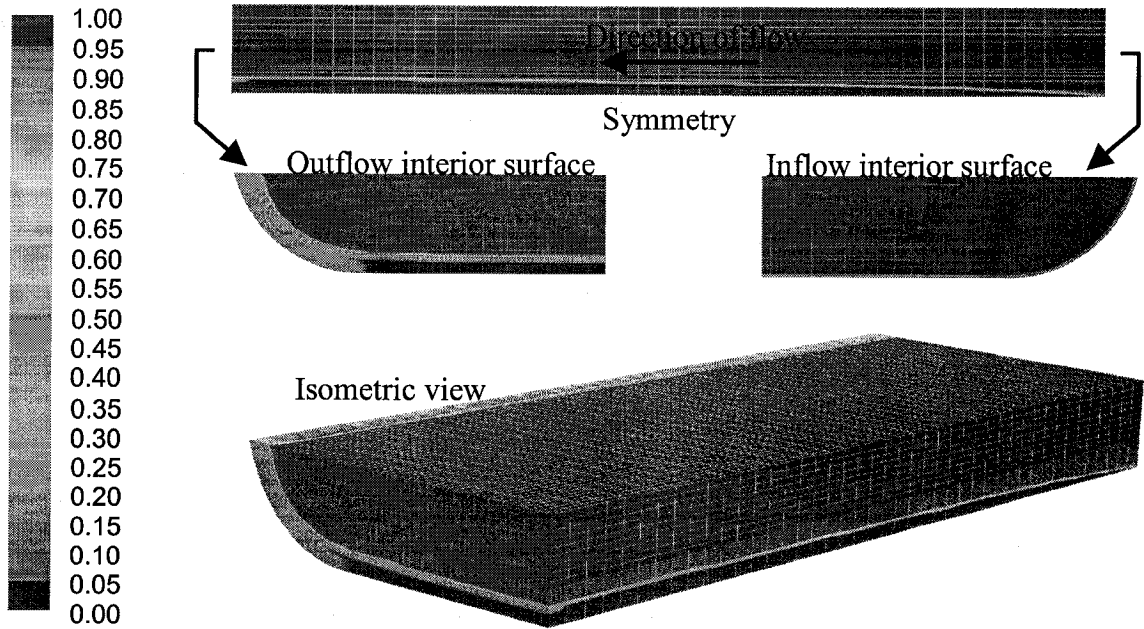


Figure 4.11 Steady-state liquid fraction contours, Slag Flow Height (HSF) = 3 cm

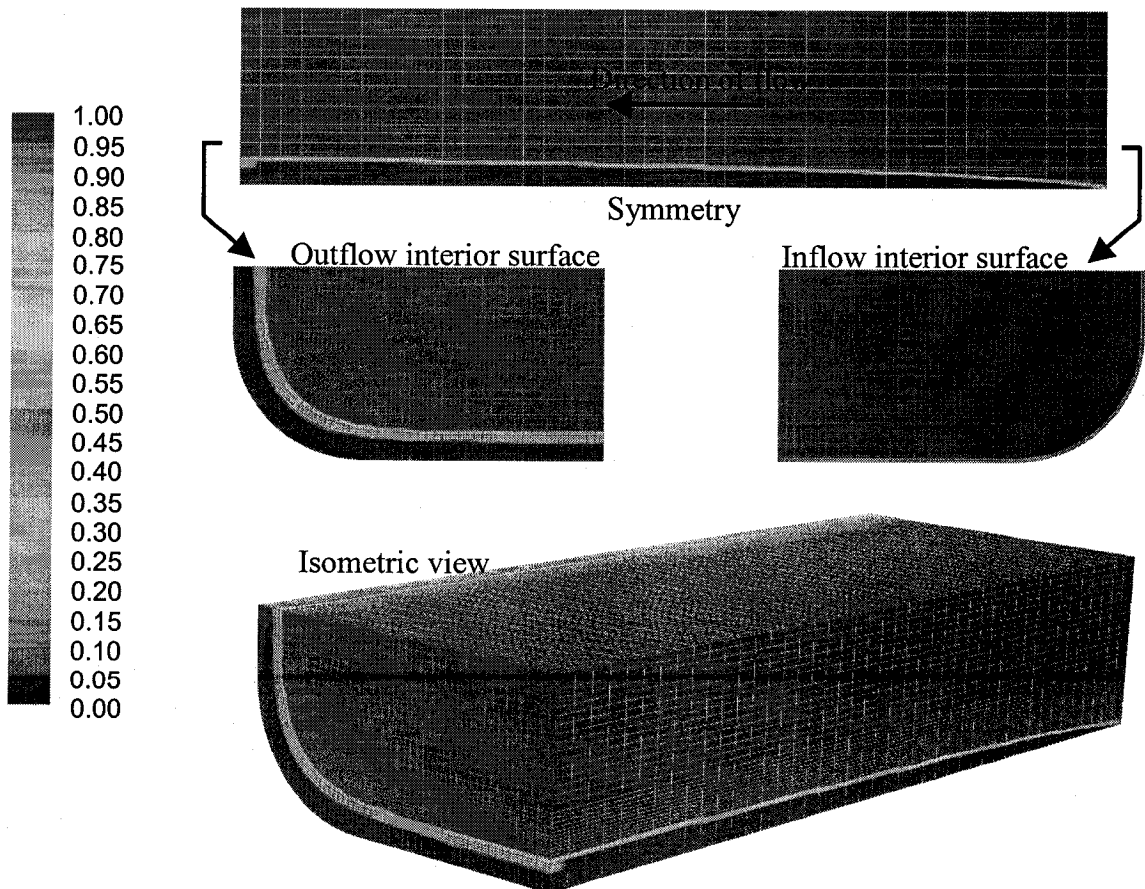


Figure 4.12 Steady-state liquid fraction contours, Slag Flow Height (HSF) = 6 cm

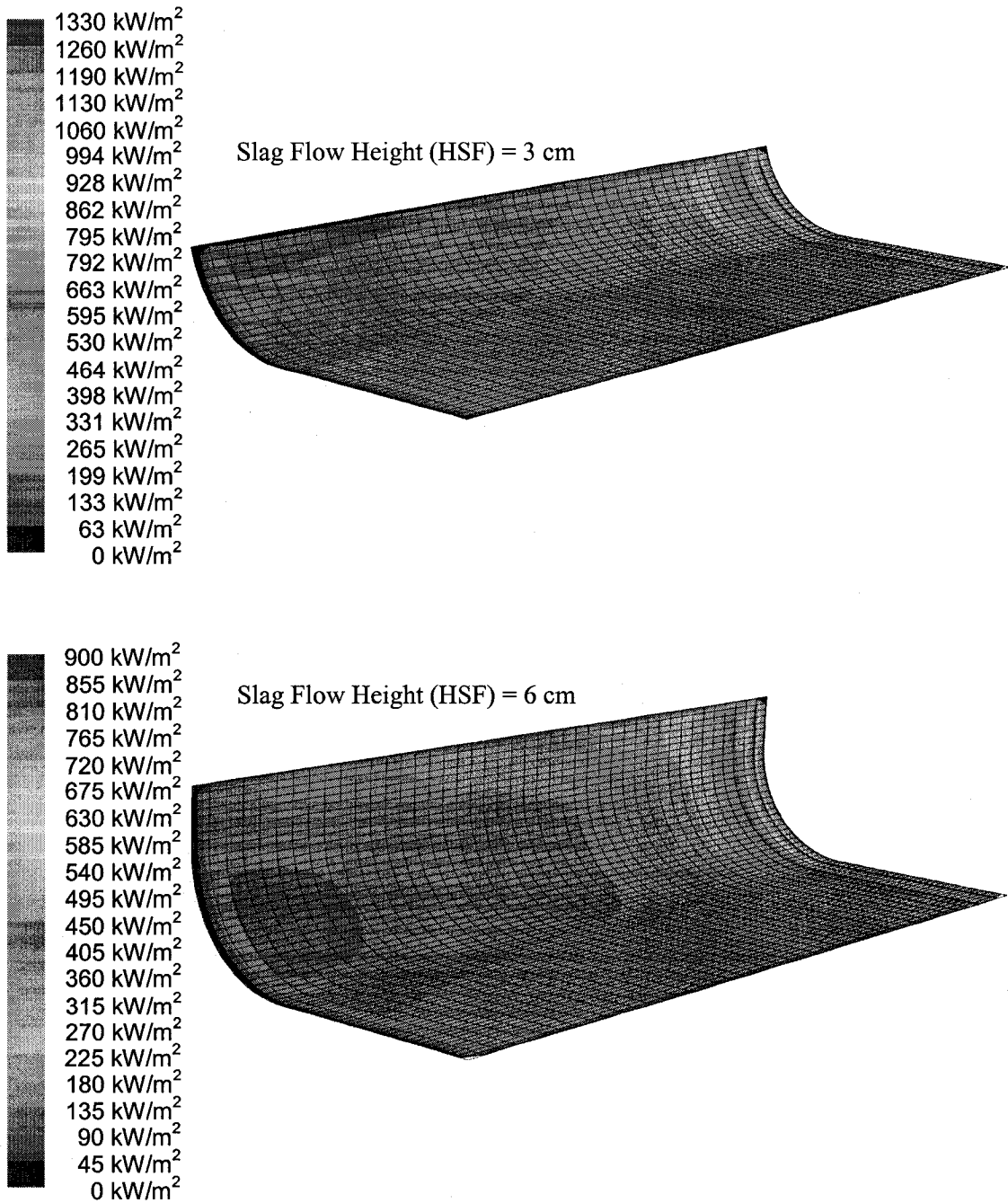


Figure 4.13 Contours of surface heat flux*
 *Only the wetted portion of the launder channel is shown

During normal slag launder operation, the slag channel may periodically be constricted by a solid obstruction (piece of refractory etc). In this case, the obstruction must be broken apart using a long metal rod, which may also dislodge part of the slag skull. Mechanically breaking apart the slag skull may lead to transient heat loads, discussed in section 4.3.2. As copper has good mechanical properties at the operating temperatures predicted ($100^{\circ}\text{C} - 220^{\circ}\text{C}$), breaking apart the slag skull should not significantly damage the launder. This is in contrast to refractory-based launders, which are often damaged in this type of situation.

4.3.1.3 Velocity Field

Figure 4.14 presents the velocity fields of both models. Once again, note the difference in the slag flow height between the two models. Because of this difference, the velocities predicted in the HSF=3cm simulation are more than two times greater than for the HSF=6cm simulation. The velocity fields in both simulations are calculated to satisfy the governing equations while maintaining a slag production rate of 450 tonnes/day.

The region of very low velocity (blue) corresponds to the slag skull. Just above this region, the boundary layer is resolved. The remainder of the slag channel can be referred to as the bulk. However, note that as the slag skull develops from the leading end of the launder to the trailing end, the slag channel becomes increasingly constricted causing the slag to flow at a greater velocity.

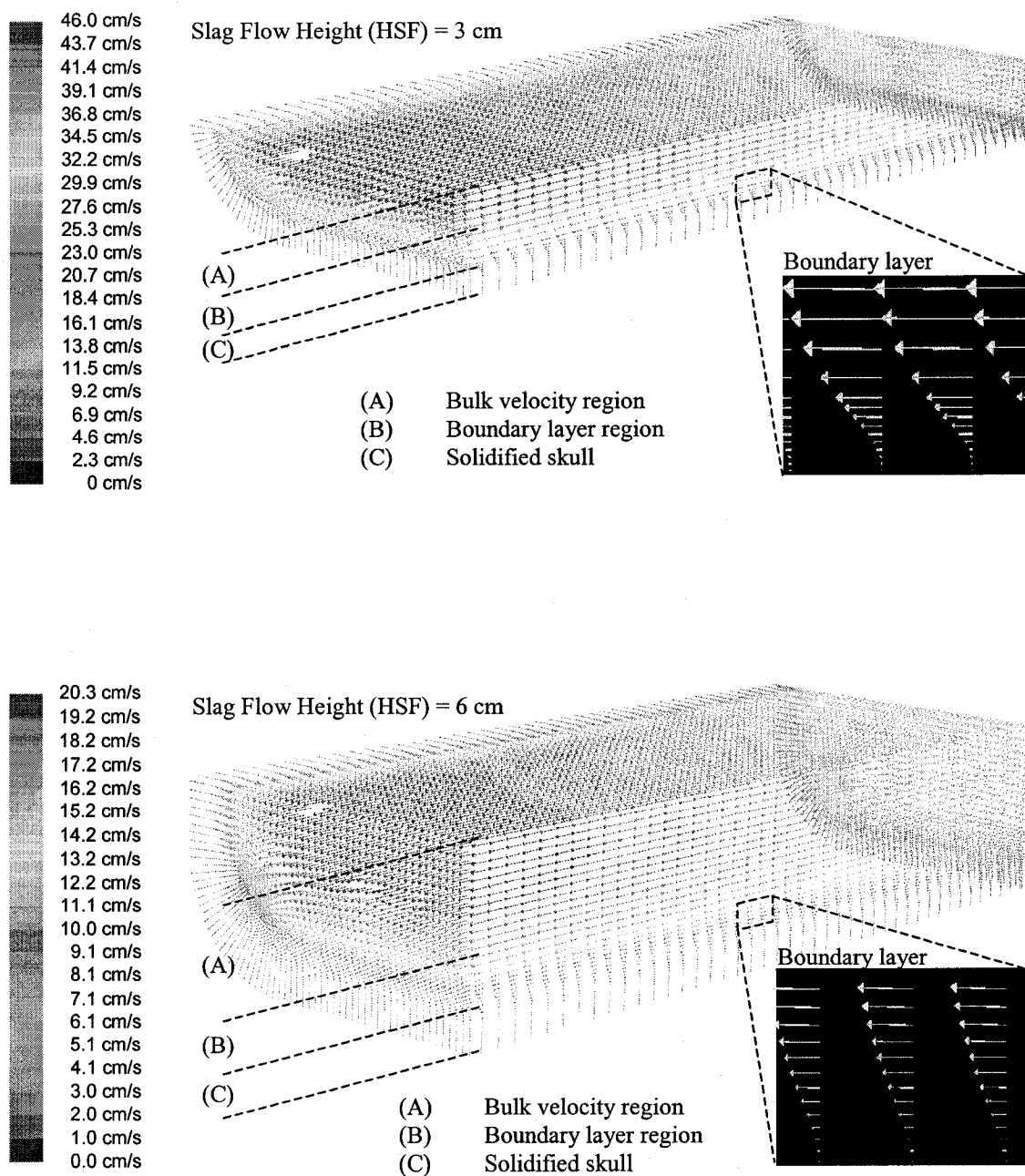


Figure 4.14 Velocity field of the slag channel

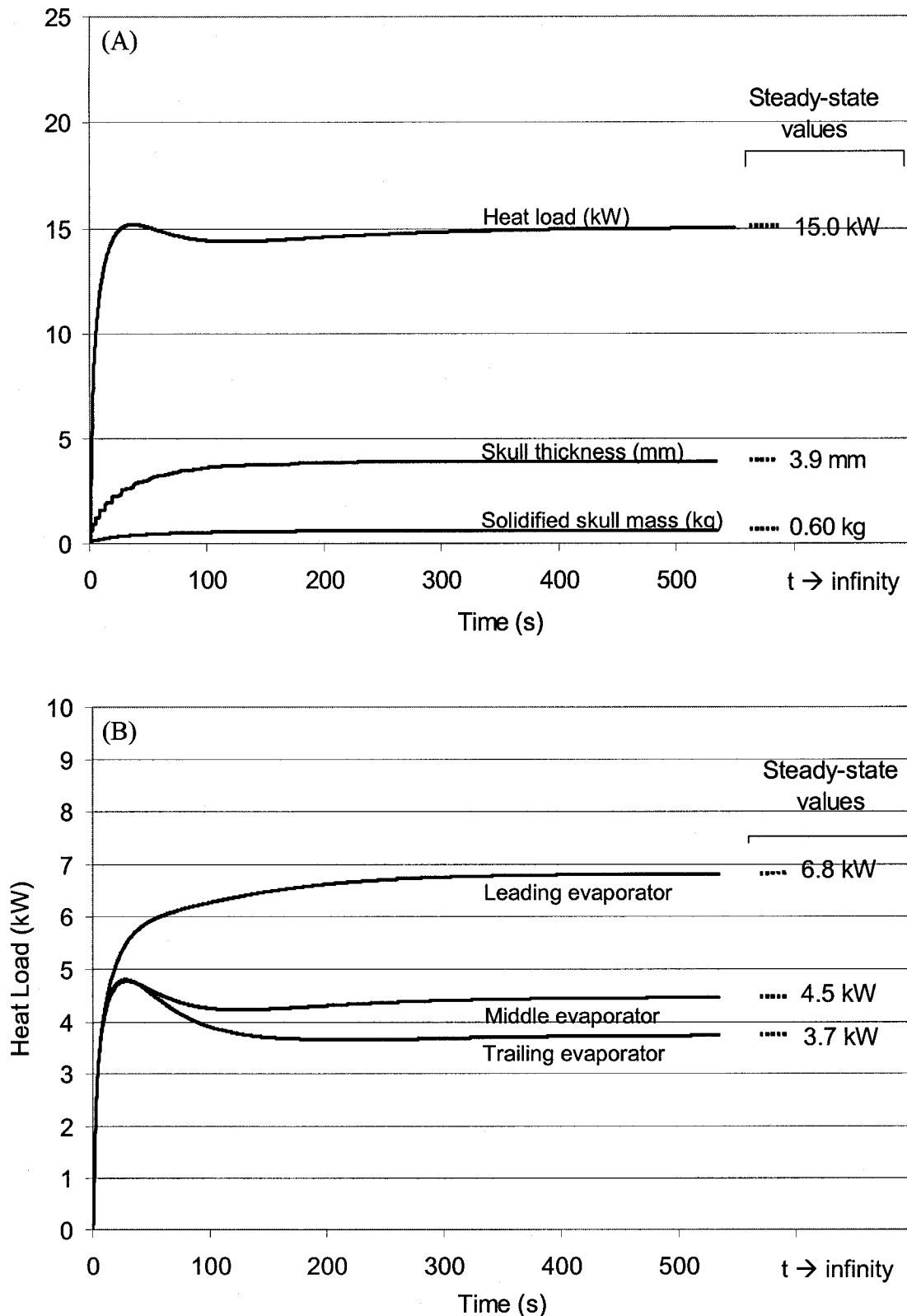
4.3.2 Transient Model

For the purpose of this thesis, transient modeling was performed only with a slag flow height of 3cm (HSF=3cm). The results are presented in Figure 4.15. The transient model indicates that as time progresses, an increasingly thick slag skull will solidify, consequently insulating the slag channel and decreasing the flow of heat into the cooled launder.

Note the rapid increase in the heat load for the first 40 seconds of the simulation. This increase is a result of the initial condition (time = 0s), when the slag launder is filled with molten slag at 1220°C to a height of 3 cm with an initial velocity along the slag channel (z-axis) of 0.23 m/s. At this time, there does not exist a slag skull insulating the launder. Therefore, during the time it takes for the slag to solidify onto the launder (quasi steady-state is reached at approximately 300s), the slag launder is subjected to a large heat load. As a consequence of the mass of the copper launder (~90 kg) and the thermal resistance of the monel pipe ($k = 21.7 \text{ W/m}\cdot^\circ\text{C}$), the large heat load is mostly absorbed by the launder as sensible heat during this time. Therefore, the copper launder acts as a thermal mass (buffer) that dampens the heat flow to the evaporators, which is why no large peak in the heat load to the evaporators is predicted.

Because of the dampening effect of the copper launder, startup heat loads predicted in the model are not great enough to induce instability in the cooling system. It may nonetheless be prudent to take precautionary steps during a startup.

For example, a temporary castable refractory coating can be applied to the slag channel. The refractory would insulate against any excessive transient heat loads during the startup procedure. After the startup, this refractory would gradually disintegrate and be replaced with a layer of solidified slag.

Figure 4.15 Transient results for $HSF=3\text{cm}^*$

(A) Summary of the total heat load and skull solidification

(B) Breakdown of the evaporator heat load

* Recall that the heat loads and slag skull mass presented here correspond to one half of the actual launder.

4.3.3 Modeling Conclusions

The results from the present model are based on some fairly conservative operating parameters. Possibly the most conservative of these parameters is the assumption that there is no contact resistance between the copper launder and the slag skull. This tends to exaggerate the predicted heat loads (22.6 to 30.0 kW). To be even more conservative, it was decided that the heat pipe cooling system should be designed to dissipate a minimum of 50 kW on a continual basis. Details of the design are given in the following section.

4.4 Design, Fabrication and Experimental Setup

4.4.1 Design Attributes

The favorable model results from the configuration discussed in section 4.3 lead to the design of the slag launder system of a similar configuration.

The following is a summary of the main characteristics of the heat pipe-cooled slag launder design:

- The dimensions of the slag launder were chosen similarly to those of the refractory-based launder presently used at the Hoboken blast furnace. The external dimensions were 30cm x 33cm x 19cm, with a slag channel measuring 30cm x 23cm x 12 cm. The launder was fabricated from copper alloy C81100L for its high thermal conductivity and good castability. Refer to Figures 4.16, 4.17 and 4.18.
- A three evaporator-single condenser approach was used. Therefore one of the condensers constructed for the taphole cooling test was reused for the present project. Refer to Chapter 3 for a detailed description of the condenser.
- The three evaporators, consisting of standard 1¼” monel pipes (400-series) cast into the bottom of the launder, were positioned perpendicular to the direction of slag flow. This allowed for the simple coupling of the accessory piping connecting the evaporators to the condenser. The flow modifiers are shown in Figure 4.19. Water was chosen as the working fluid for reasons similar to those given for the tapblock experiments (section 3.3.1.2)
- The height of the column of condensed working fluid (return line) was set at 1.5 m. This height was judged as adequate to promote the refluxing of the evaporators and avoid dry-out at the required heat loads.
- The manifold joining the three evaporators into a single pipe prior to entering the condenser was positioned close to the condenser. This was done in order to prevent the “overflow” of one evaporator into another in the case where there may be a significant difference in heat load between evaporators.

- A liquid level monitor system was retrofitted onto the condenser to detect the presence of leaks over long periods of operation.
- Flexible hoses were used to adjust for pipe misalignment.
- The cooling system was designed in a modular format such that future adjustments to the design could be made by replacing the modules rather than by modifying existing components, which can often be difficult.
- All connections were made via flanges that use copper gaskets. From experience, these types of connections are less likely to leak compared with threaded connections.

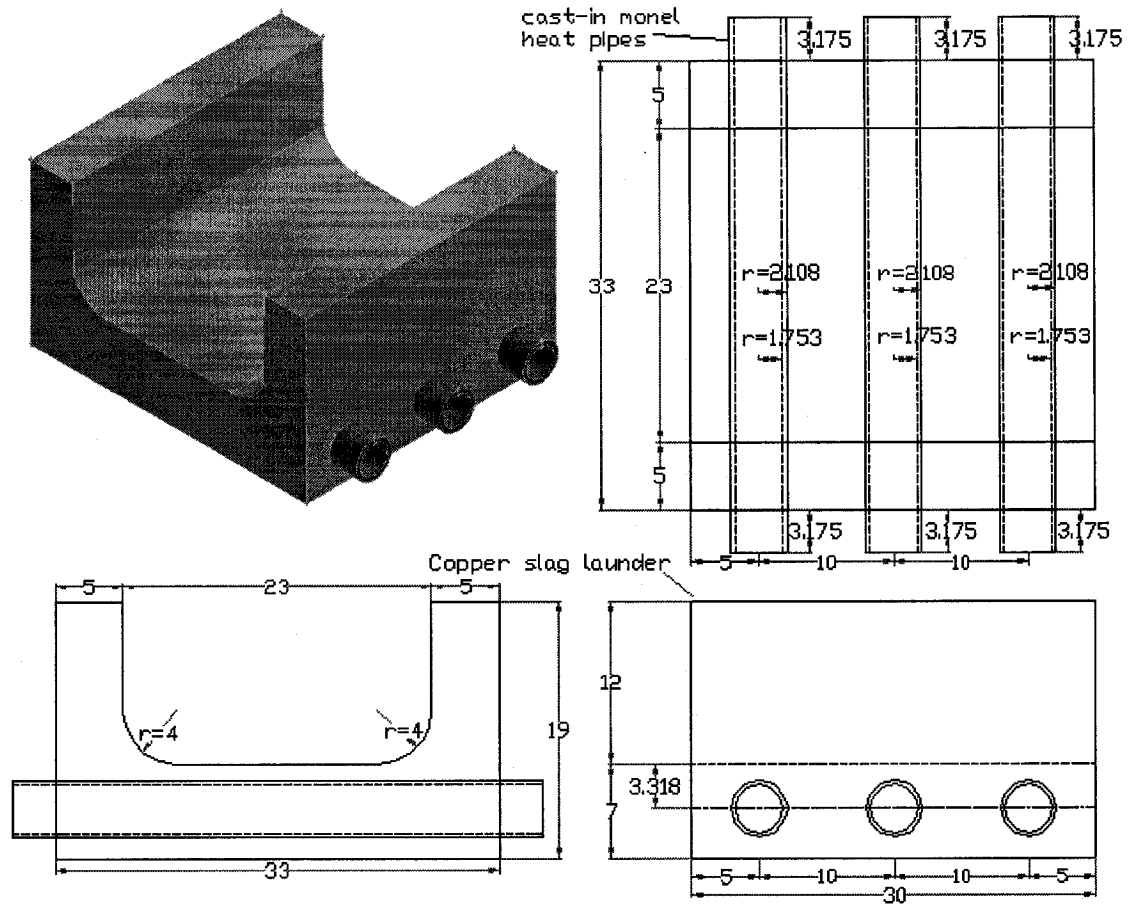


Figure 4.16 Final slag launder drawings
(measurements in cm)

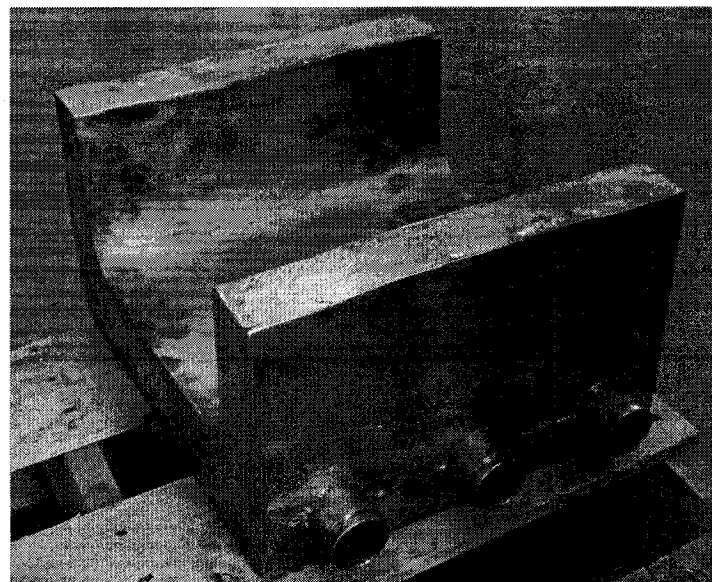


Figure 4.17 Cast copper slag launder

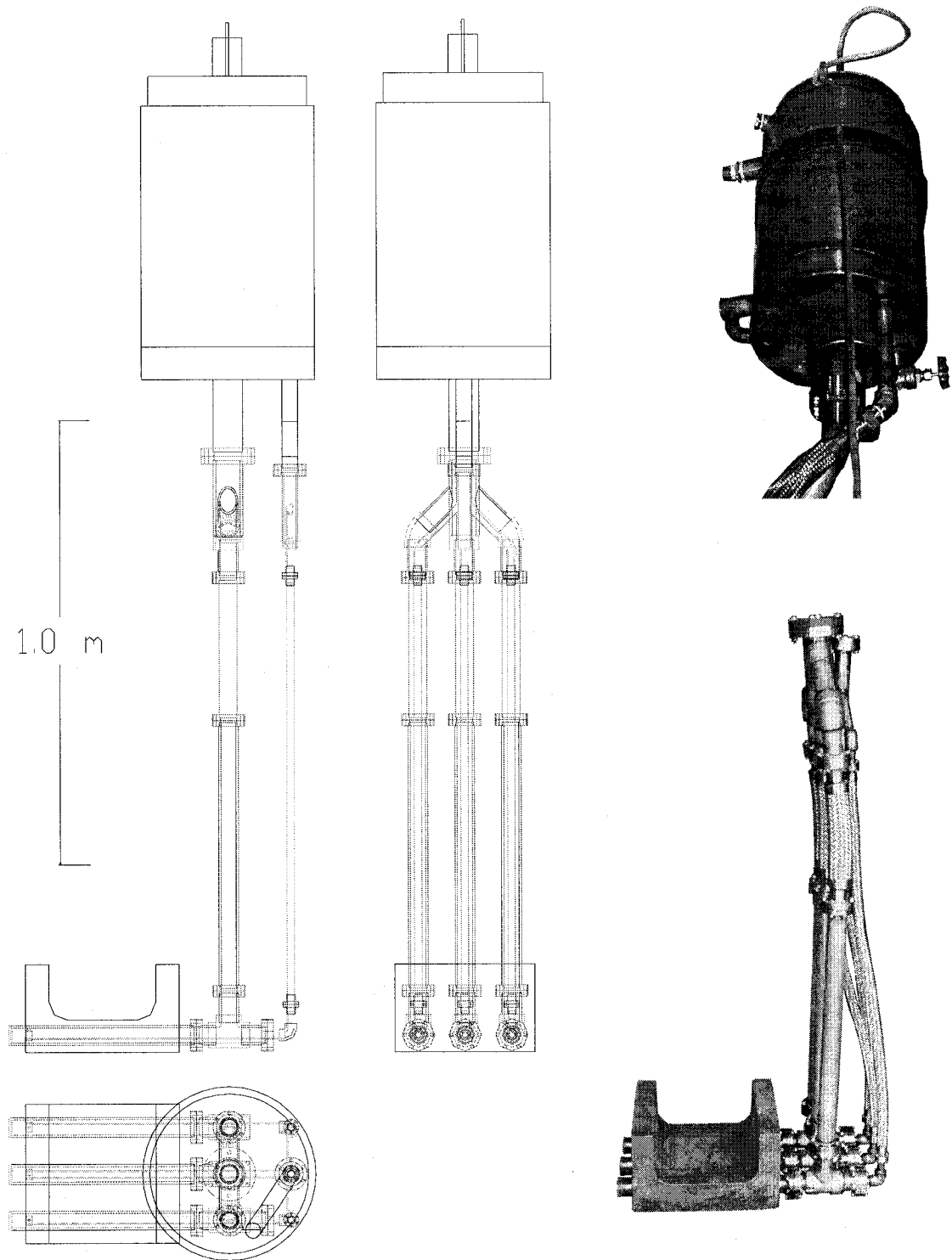
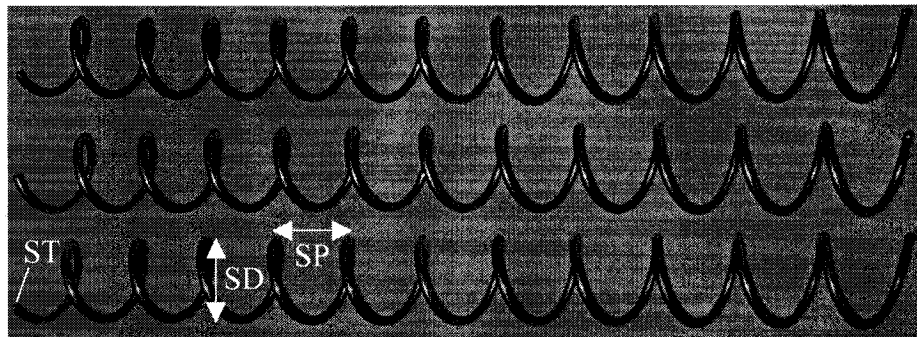


Figure 4.18 Complete drawing and assembly of the slag launder/cooling system
(fabricated at the McGill chemical/metallurgical engineering machine shop)



SP (spring pitch): 31 mm
SD (spring diameter): 31 mm
ST (spring thickness): 3.2 mm

Figure 4.19 Flow modifiers

4.4.2 Liquid Level Monitor

A liquid level sensor was retrofitted onto the condenser in order to monitor the working fluid level in the reservoir. In addition to the detection of leaks and of operating phenomena such as dry-out, the values from this sensor were translated to the average void fraction (vapour fraction) in the evaporator section of the heat pipe cooling system during operation. This information is particularly useful in determining whether or not a heat pipe is operating correctly.

Because of the novelty of the liquid level sensor as part of a heat pipe cooling system, the setup and calibration of this sensor is described in detail in this section, and can be subdivided into 4 parts:

- step 1 – general calibration of the liquid level monitor
- step 2 – joining the sensor to the condenser
- step 3 – determining the height within the liquid level monitor which corresponds to the bottom of the condenser reservoir
- step 4 – obtaining a relationship to calculate the evaporator void fraction

Figure 4.20 is the calibration curve for the liquid level sensor reservoir obtained experimentally with water at room temperature and with air as the gas phase, prior to the sensor being joined to the condenser. A linear trend line was fit to the data using the method of least squares with excellent correlation:

$$\text{Liquid Volume (ml)} = 556.3 * \text{Voltage (V)} + 118.3 \quad (R^2 = 0.999) \quad (4-8)$$

Therefore, an increase in the voltage reading by 1V corresponds to 556.3 ml more liquid present in the liquid level monitor reservoir, or a height increase of 0.0386 meters per Volt (cross-sectional area of the liquid level monitor reservoir is 0.014395 m²). This value is defined as a constant, a (0.0386 m/V).

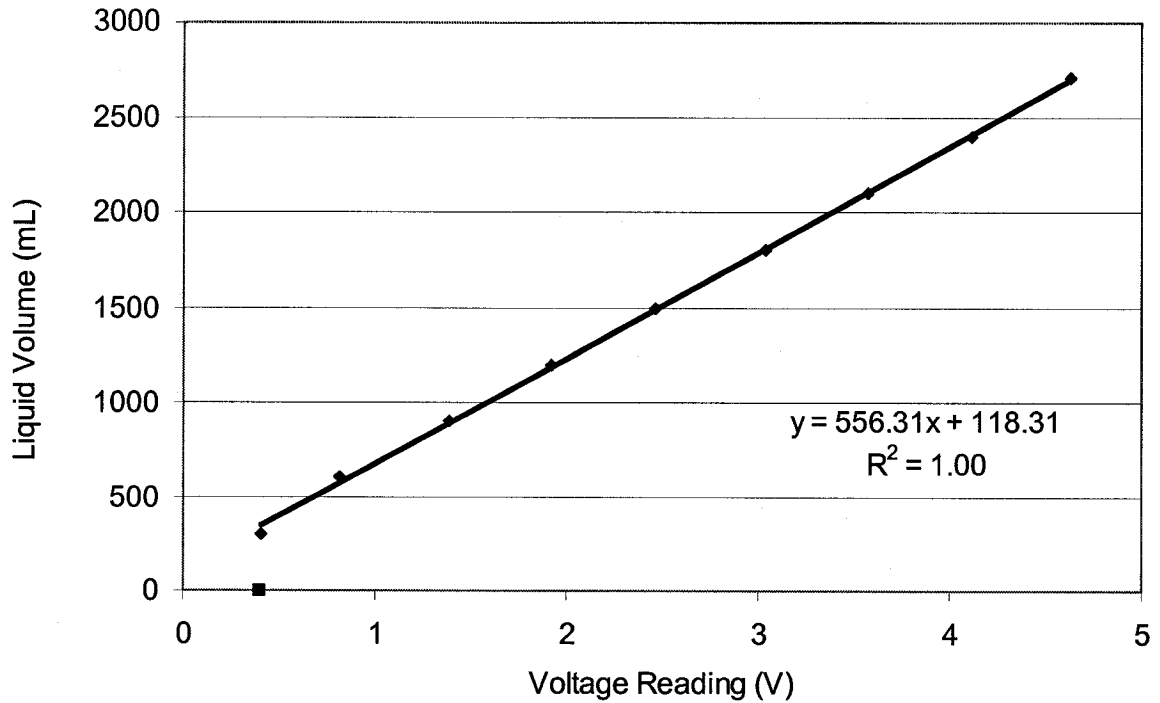


Figure 4.20 Volume of liquid vs. voltage reading

Figure 4.21 is a graph composed of data points taken at steady-state during the pilot scaled- tests described in section 4.5. The change in the slope of the points corresponds to the liquid level reservoir being at the same level as the bottom of the condenser reservoir. Therefore the points to the left correspond to the return line and liquid level monitor reservoir being filled with working fluid (scenario A of Figure 4.22). The points to the right correspond to the condenser reservoir and liquid level monitor reservoir being filled (scenario B of Figure 4.22).

Linear trendlines were fit to both sets of points in Figure 4.21, using the method of least squares, again with excellent correlation:

Scenario A:

$$\text{Voltage Reading (V)} = 0.007672 * \text{Heat Load (kW)} + 1.896 \quad R^2 = 0.9998 \quad (4-9)$$

Scenario B:

$$\text{Voltage Reading (V)} = 0.04054 * \text{Heat Load (kW)} + 0.5240 \quad R^2 = 0.9908 \quad (4-10)$$

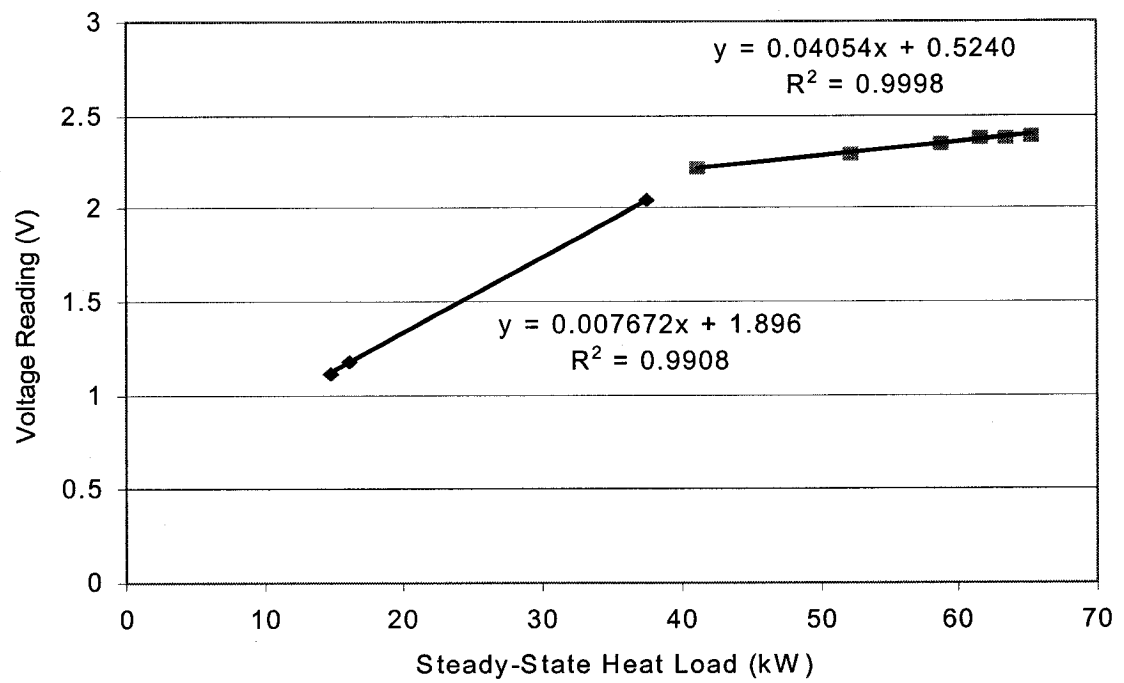


Figure 4.21 Experimental liquid level sensor readings

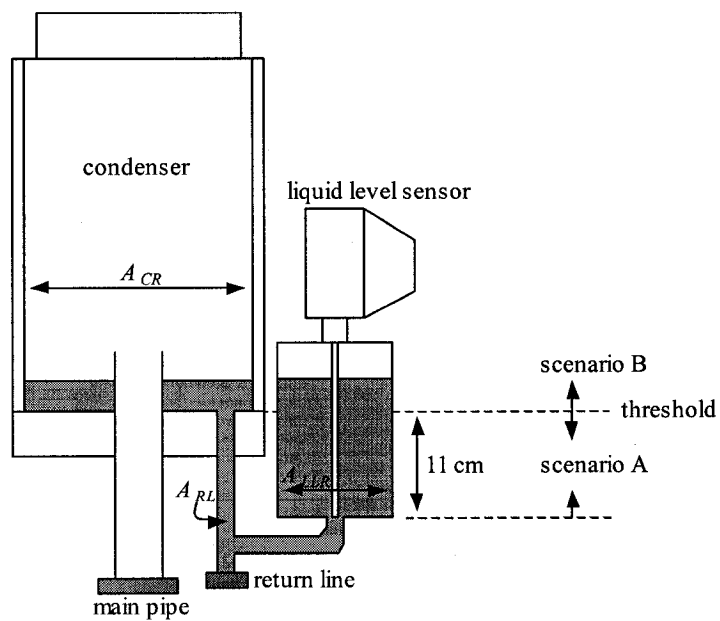


Figure 4.22 Diagram of the liquid level monitor retrofitted onto the condenser

By setting the right side of equations (4-9) and (4-10) equal to one another, the heat load and corresponding voltage reading where the apparent change in slope takes place can be determined. This was found to take place at a threshold voltage reading ($v_{threshold}$) of 2.22 V. Therefore, this corresponds to a volume of 1350 ml. Knowing the inner cross-sectional area of the liquid level monitor reservoir (0.014395 m^2), the corresponding height of ~11cm can be calculated. This signifies that at a liquid height of 11cm within the liquid level monitor reservoir, the bottom of the condenser reservoir is at the onset of being filled.

The height of 11cm is comparable to the height found from the drawings, which is 9.6cm (see Figure 4.23). However, the former value is taken as the correct value.

Table 4.8 summarizes the relevant cross-sectional areas of the heat pipe condenser and liquid level monitor.

Table 4.8 Selected cross-sectional areas of the condenser and level monitor

Description	Variable	Value
Inner cross-sectional area of the return line	A_{rl}	0.000624 m^2
Inner cross-sectional area of the liquid level monitor reservoir	A_{llr}	0.0144 m^2
Equivalent cross-sectional area of the condenser reservoir (cooling pipes & main pipe not included)	A_{cr}	0.0691 m^2

Therefore,

$$v < v_{threshold} \quad A_{c-s} = A_{rl} + A_{llr} \quad (4-11)$$

$$v > v_{threshold} \quad A_{c-s} = A_{llr} + A_{cr} \quad (4-12)$$

After having assembled the slag launder heat pipe system and charged the working fluid into it, it was found experimentally that when the heat pipe system was at rest, i.e. zero heat load with the return line valve completely open, the nominal voltage reading, $v_{nominal}$, was 0.584 V.

Under these conditions, the evaporators are completely flooded with liquid.

Therefore, the volume of working fluid displaced from the evaporators ($V_{displaced}$) during heat pipe operation can be found as follows:

$$v < v_{threshold} \quad V_{displaced} = a \cdot (v - v_{nominal}) \cdot (A_{rl} + A_{llr}) \quad (4-13)$$

$$v > v_{threshold} \quad V_{displaced} = a \cdot [(v_{threshold} - v_{nominal}) \cdot (A_{rl} + A_{llr}) + (v - v_{threshold}) \cdot (A_{llr} + A_{cr})] \quad (4-14)$$

Finally, knowing the volume of the evaporators and main pipes (not including the return lines), $V_{evap} = 0.00476 \text{ m}^3$, the average void fraction can easily be found as:

$$\text{Void Fraction (\%)} = \frac{V_{displaced}}{V_{evap}} \cdot 100\% \quad (4-15)$$

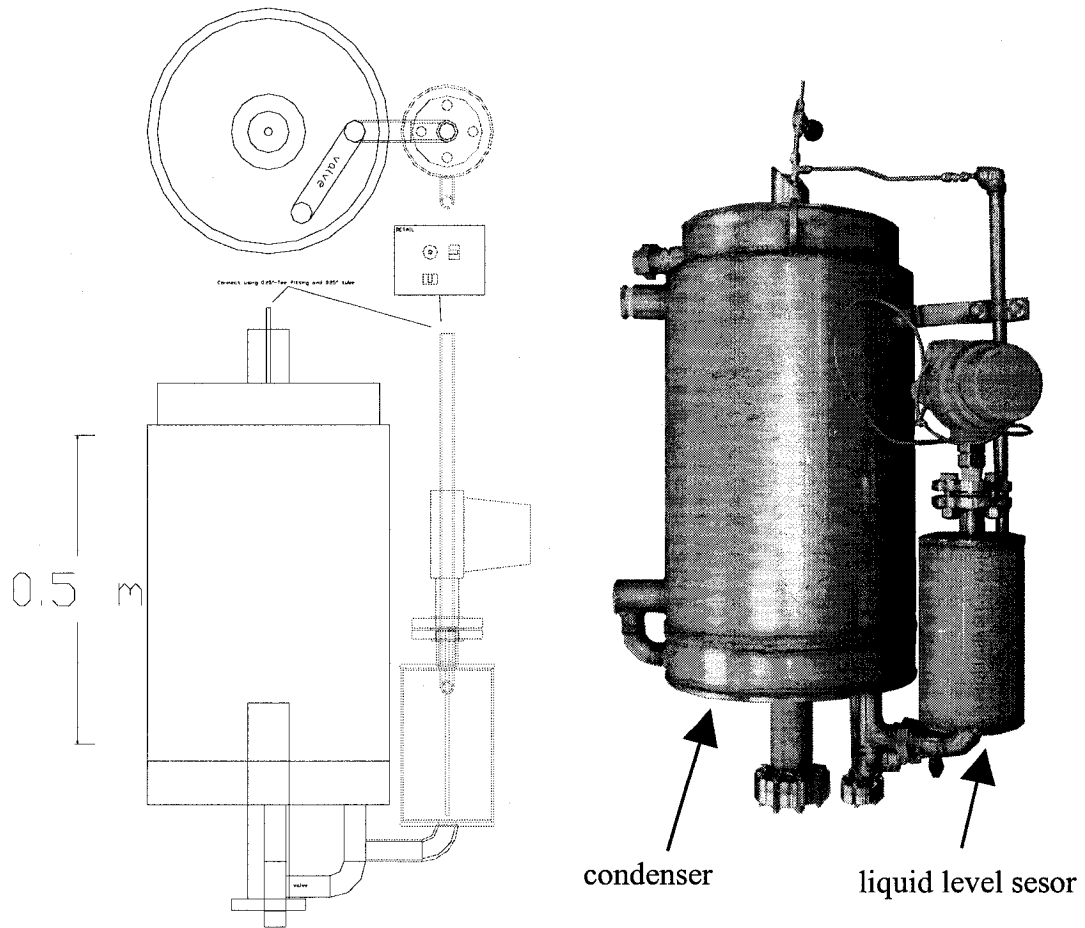


Figure 4.23 Liquid level monitor retrofitted onto the condenser (capacitance-based level transmitter, model 9080, Arjay Engineering, Ontario Canada)

4.4.3 Analysis of Design

As previously mentioned, the two operating limitations associated with the novel water-based heat pipes used in the design are the film boiling and dry-out limitations.

4.4.3.1 Film Boiling Limitation

The peak heat flux predicted for the HSF=3cm simulation was calculated as 660 kW/m². Previous experiments with water based heat pipes have shown that this heat flux can be attained without experiencing the film boiling limitation. Notably, modeling of the tapblock tests described in Chapter 3 indicated that a maximum heat flux of 2.4 MW/m² was attained using a water-based heat pipe system. Therefore, film boiling was not anticipated to occur under the heat loads predicted from the model (maximum 660 kW/m²).

4.4.3.2 Dry-out Limitation

As previously explained in Chapter 3 (section 3.3.4.3), the possibility of encountering dry-out in a given heat pipe design can be judged using an expression for \bar{v}_{\min} , and comparing these values to previous experiments. Refer to equation (3-10).

The evaporator configuration has a return line outer radius (r_1) of 8.6 mm and an evaporator inner radius (r_2) of 17.5 mm. As the working fluid is water, $H_{fg} = 2260$ J/g. The density of the vapour, ρ_v , is a function of the saturation pressure at the heat pipe operating temperature.

Laboratory experiments with heat pipes comparable in size to the ones incorporated into the slag launder design typically experience dry-out at vapour velocities approaching 500 km/hr [59]. However, larger systems experience dry-out at lower vapour velocities due to the increased pressure drops associated with scale-up. For example, dry-out was achieved in the tapblock cooling system with vapour velocities approaching 170 km/hr [81].

Table 4.9 summarizes the values of \bar{v}_{\min} for the slag launder system under the heat loads predicted in the model. The leading evaporator will produce the largest velocity (and pressure gradient) because it is exposed to the greatest heat load.

Table 4.9 Predicted values of \bar{v}_{\min} for the HSF=3cm simulation configuration

		Evaporator		
		Leading	Middle	Trailing
Operating temperature	90°C	70 km/hr	46 km/hr	38 km/hr
	100°C	50 km/hr	33 km/hr	27 km/hr
	110°C	36 km/hr	24 km/hr	20 km/hr

These values indicated that the vapour velocities in the proposed slag launder system would be relatively low, particularly given the fact that the system would most likely operate between 100-110°C. Therefore the pressure drop across the evaporators would also be low.

A condenser height of 1.5m (Δh) was considered adequate to ensure the abundant refluxing of the evaporators. However, there would be a greater excess fed to the middle and trailing evaporators compared with the leading evaporator, which would have the largest pressure gradient.

4.4.4 Experimental Setup

The slag launder and heat pipe cooling system was assembled and tested at Umicore Research's pilot facility in Olen Belgium between August 14th and September 11th, 2005.

The external cooling circuit was coupled to the condenser from Umicore's tower water (open circuit), which was capable of supplying an adequate flow rate for these experiments (200-300 ml/s).

Figure 4.24 illustrates the experimental setup employed for the pilot tests before the refractory had been installed. The burner is shown applying a heat load to the slag launder in Figure 4.25. This heat load was used to simulate industrial heat loading conditions that were predicted by the model presented in section 4.3.

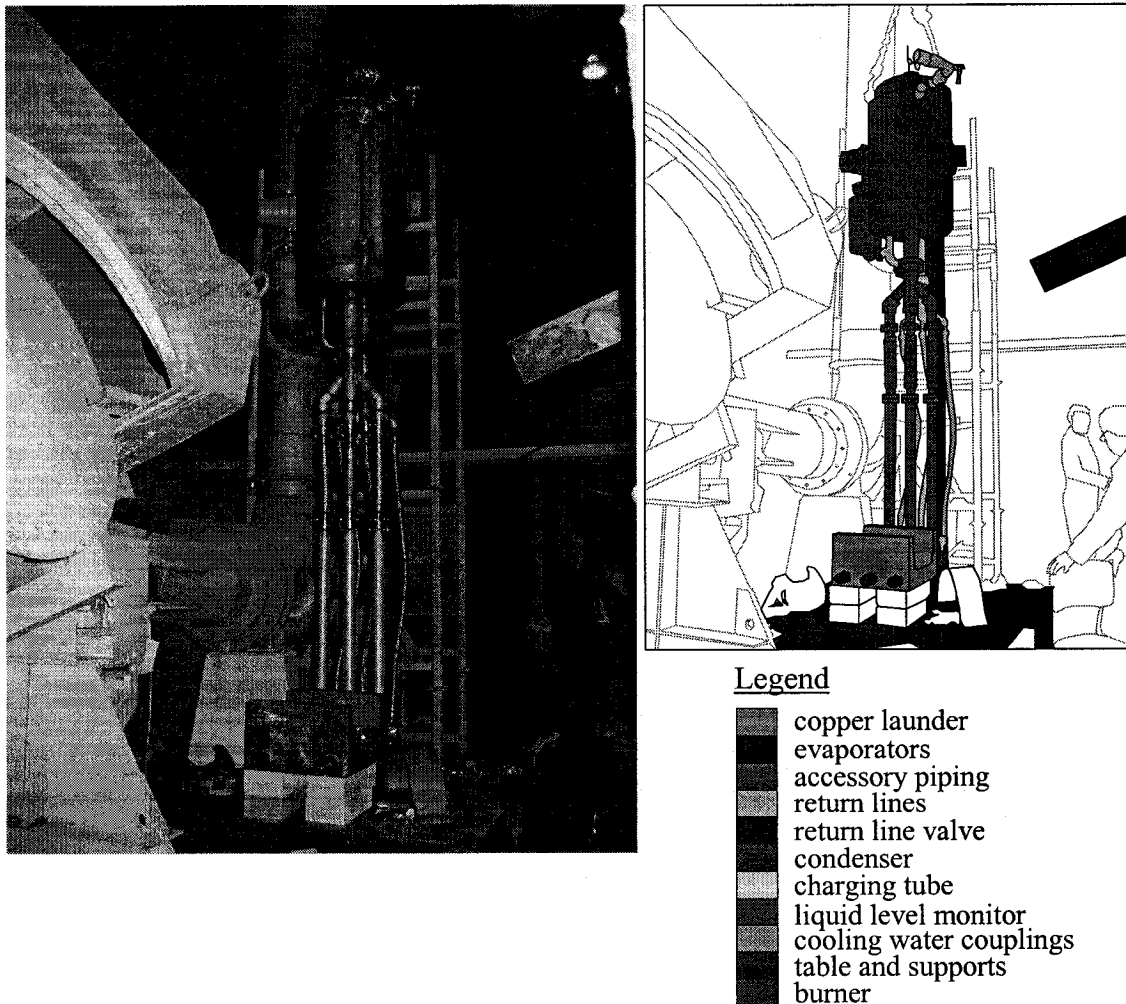


Figure 4.24 Experimental setup

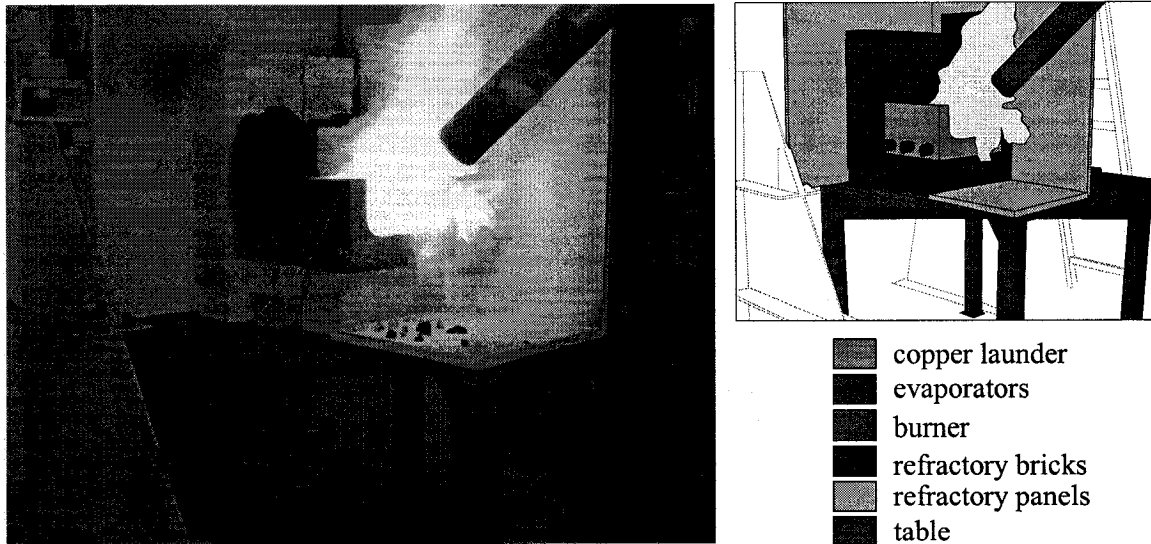


Figure 4.25 Applying a heat load using the burner

4.4.4.1 Sensors

A total of four 2mm-diameter wells were drilled into the copper launder so that thermocouples could be cemented into them to monitor the launder temperature. Two of the wells were drilled between the evaporators, 10 cm deep from the surface (designated *copper 1* and *copper 2*). The other two thermocouples were drilled into the top corners of the launder walls, 2.5 cm from the surface, diagonally opposite from one another (designated *copper 3* and *copper 4*).

Two additional thermocouples were inserted into a thermocouple well located at the top of the condenser. The thermocouples were placed at different heights to register the temperatures at the top and bottom of the condenser.

The input and output temperatures of the cooling water were also measured along with the cooling water flowrate. These values allowed for the calculation of the heat extraction rate of the cooling system, using equation (3-1).

Figure 4.26 illustrates the location of the various sensors used in the experiment.

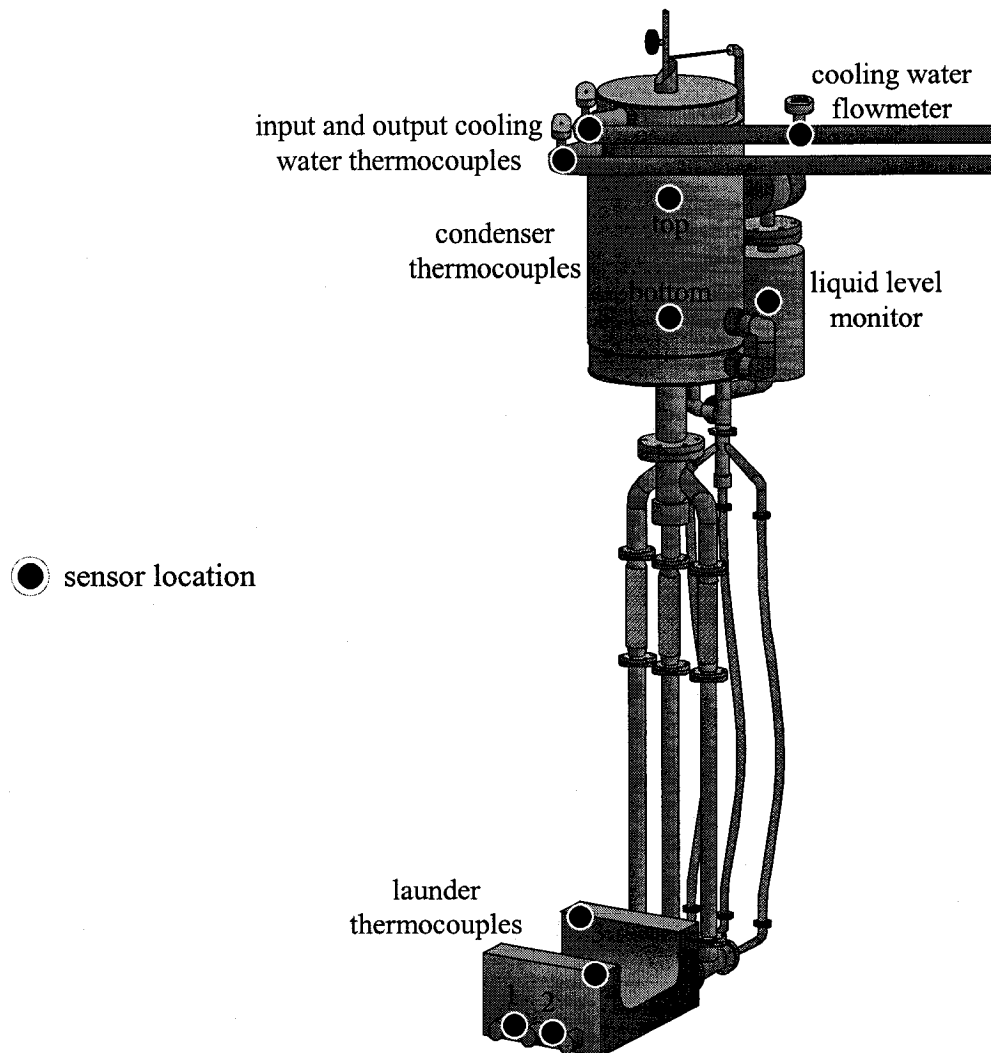


Figure 4.26 Diagram of the sensor positioning

4.5 Results and Discussion

There were two types of tests that were performed to evaluate the operation of the slag launder system: steady-state tests described in section 4.5.1 and transient “impact” tests described in section 4.5.2.

4.5.1 Steady-State Testing

For the steady-state tests, the burner was used to supply several heat loads, each of which was kept constant for a period of time. Smaller heat loads were first used, and were incrementally increased to larger heat loads. The transient periods of time between each steady-state heat load were kept to a minimum. Figure 4.27 presents the results from one such test, which are explained in the following sections.

4.5.1.1 Overview of Test

The burner was initially turned on at an applied heat load of 37kW. It required approximately 15 minutes to reach steady-state conditions, which were maintained for an additional 15 minutes. The burner power was then increased to a heat load of 42 kW, although it was temporarily set at a value much higher than this, evident from the peaks observed at a test time of 0:45 (h:mm). Steady-state conditions were again maintained until a test time of 1:20. The burner was then increased to a value of 54 kW and then finally to 65 kW at 2:00. The latter value was maintained for over 4 hours. The heat pipe cooling system was capable of dissipating the required heat loads throughout the test with no signs of instability.

4.5.1.2 Copper Temperatures

Firstly, the results from this test are reasonable. For example, as the burner setting is increased, a larger heat load is applied to the launder which causes larger thermal gradients to develop in the copper. These larger thermal gradients correspond to larger temperatures in the copper as the heat sink (heat pipe evaporators) is maintained at a relatively constant temperature throughout the test.

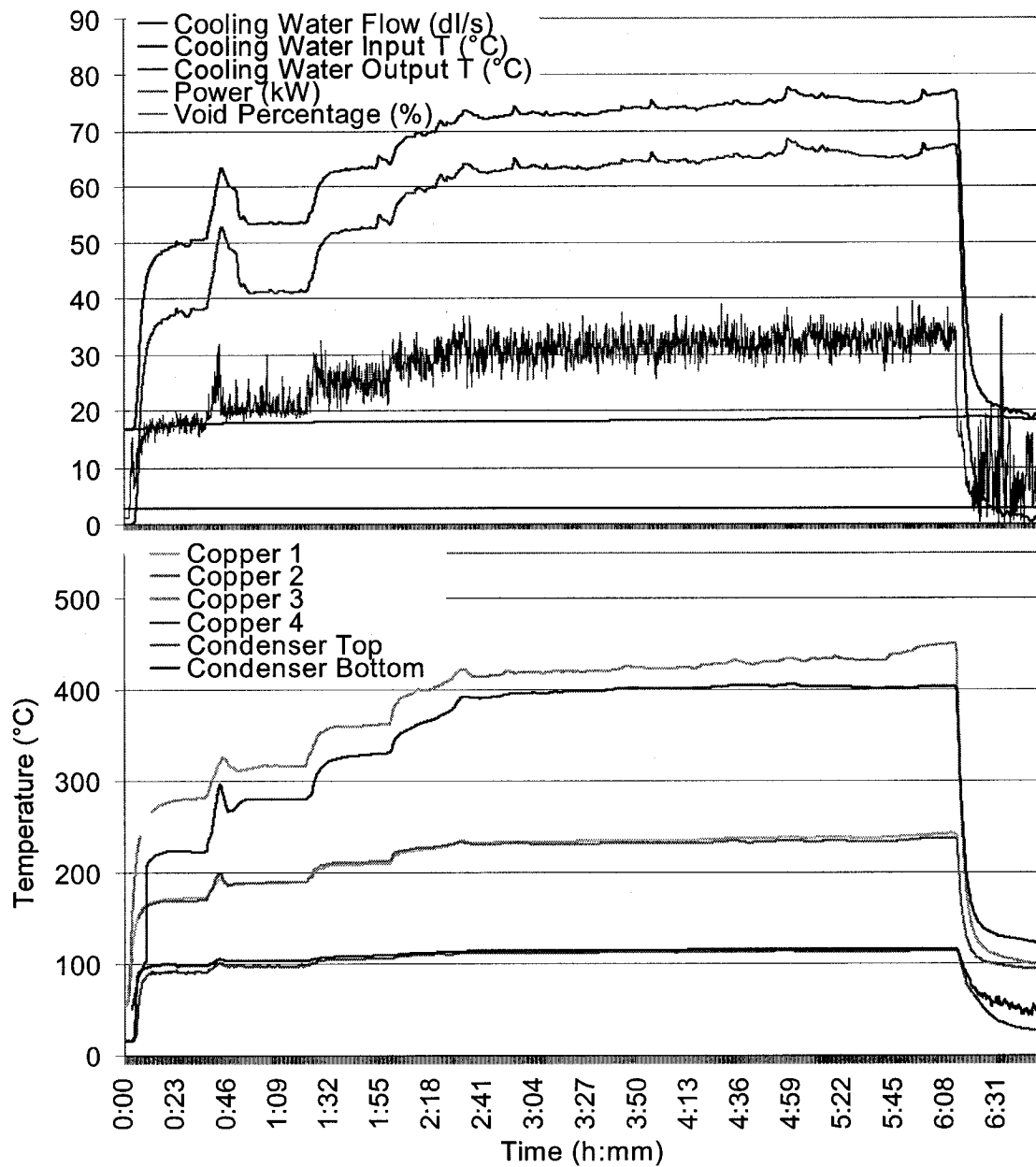


Figure 4.27 Steady-state test results

The heat pipe system responded well to the increased heat loads, dampening the corresponding increase in the copper temperatures. At the end of the test (6:12), the burner was shut off and the copper cooled down very rapidly (1.2°C/s), clearly demonstrating the cooling capacity of the heat pipe system.

At 65 kW, the largest temperatures in the copper approached 450°C , which would typically be unacceptable for any copper furnace equipment. There are several factors which contributed to this. Firstly, these temperatures were reached at a heat load 2-3 times greater than what would be expected in an industrial environment according to the modeling in section 4.3. Secondly, the heat load in this test was applied to the entire slag channel, whereas slag would mostly apply heat to the bottom of the channel in industry, close to the evaporators. Therefore, the top of the slag channel walls which are furthest from the evaporators would be exposed to less heat in industry and therefore operate colder than what was observed in the pilot test. Finally, the use of cast-in monel pipes also contributed significantly to the elevated copper temperatures as will be further discussed in section 4.5.3.2.

4.5.1.3 Heat Pipe Operating Temperature

Because the cooling water flow rate was not changed throughout the test (maintained at 0.31 l/s, confirmed by several manual measurements), the larger heat loads also tended to increase the heat pipe operating temperature.

Operating temperatures of between 90°C and 120°C were attained from heat loads of between 37 kW to 65 kW, respectively.

4.5.1.4 Evaporator Void Fraction

Using the methodology described in section 4.4.2, results from the liquid level monitor were correlated to the average void fraction within the evaporator/piping, seen in Figure 4.27.

It is interesting to note that these readings increased as the heat load increased, as is expected. Larger heat loads corresponded to larger vapour generation rates, and consequently larger void fractions. Although there were some sources of error in the

calculation of the void fraction, the values observed were quite low (17-35%), indicating that the evaporators were amply refluxed and that dry-out was not a problem.

Increased scatter in the void fraction data was observed at the end of the test as the heat extraction rate decreased. This intermittent behaviour is typical for a heat pipe system functioning at a heat load significantly lower than the designed heat load. The void fraction readings confirm the theory that this cyclic mode of operation consists of sudden and violent boiling which expulses the working fluid from the evaporator. This is followed by the refluxing of under-cooled working fluid from the condenser reservoir which must then be reheated to the saturation temperature before again suddenly boiling and so on.

4.5.2 Impact Testing

For the transient tests, the return line valve was closed while the burner was applied to the launder. Once the evaporators had dried out, as they were no longer refluxed via the return line, the launder temperature increased to a desired temperature (typically 500°C). The burner was then turned off and the return line valve was opened, instantly refluxing the evaporators with working fluid and initiating heat transfer.

4.5.2.1 Attaining Dry-out

Results from the first impact test are shown in Figure 4.28. At the start of the test, the return line valve had already been turned off and the evaporators had completely dried out. This is indicated by the liquid level monitor which registered the reservoir as almost full, corresponding to a void fraction of unity in the evaporators and accessory piping.

Therefore, the heat extraction rate decreased to zero. It should be noted that a heat load was initially still recorded (20 kW at the start of the test) as the thermal mass of the condenser was being cooled off by the cooling water. The condenser began the test at a temperature approaching 100°C, but cooled to between 40-70°C after dry-out was achieved.

As the burner was still applied to the copper while no heat was being extracted, the copper temperatures increased. At values of approximately 500°C, the burner was shut off and the return line valve was rapidly opened. This occurred at a test time of approximately 0:14.

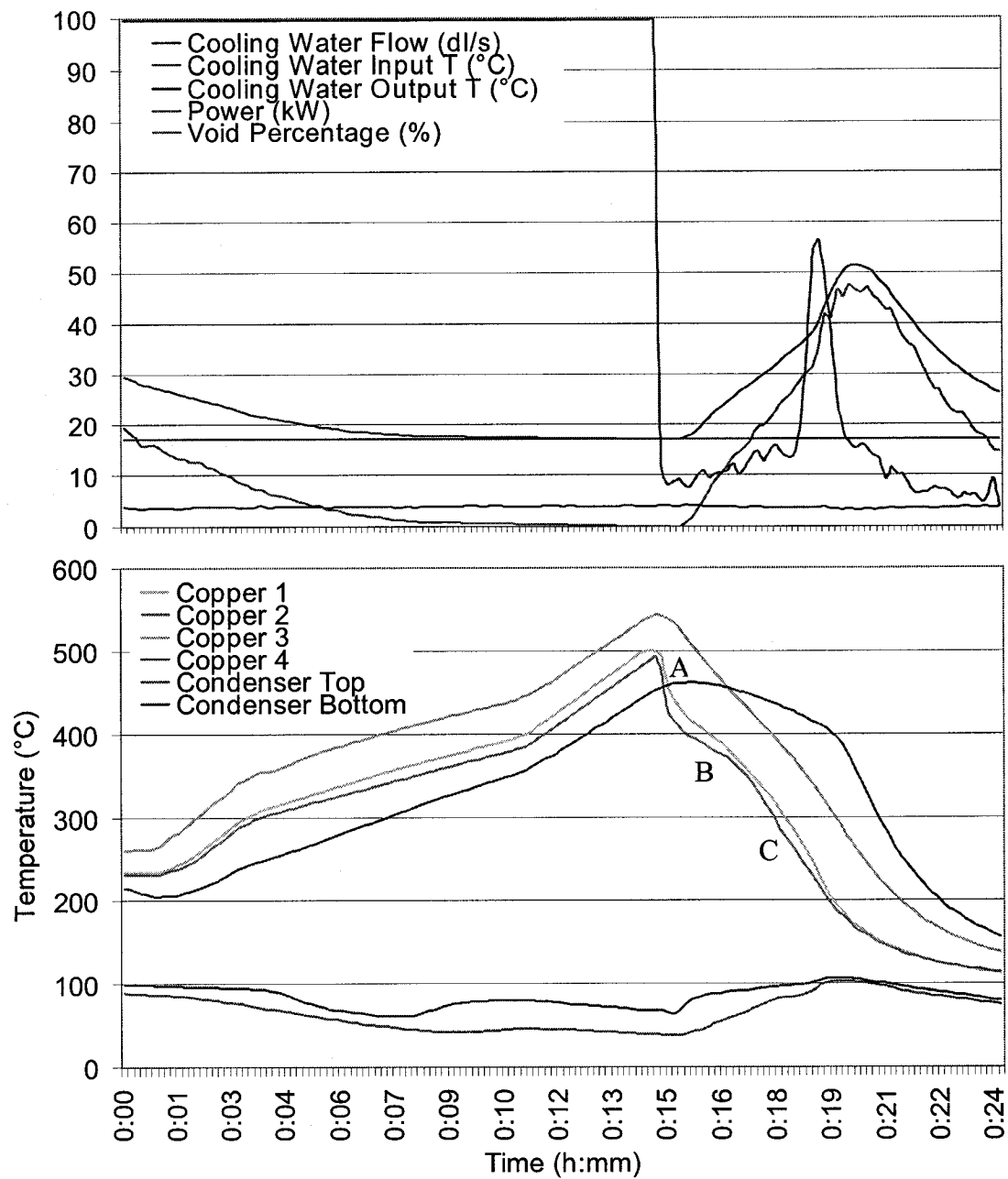


Figure 4.28 Impact test results

4.5.2.2 Heating the Copper

In order to understand the temperature curves while the copper was being heated (test time 0:00 to 0:14), it must first be known that the slag launder channel was completely enclosed in refractory except for the front, where the burner was applied. This being said, the back of the slag launder channel was subjected to more radiation than the front, which was able to radiate out to the environment more easily (because of the larger view factor).

Therefore while heating up the copper with the evaporators completely dry, the slag launder temperature closest to the back was the fastest to heat up. This trend generally held as the *copper 3* thermocouple was positioned closest to the back, and registered the highest temperatures. The *copper 4* thermocouple was positioned closest to the front, and thus was slowest to increase in temperature during the heat-up process. The *copper 1* and *copper 2* thermocouples were toward the center, and registered temperatures in between the *copper 3* and *copper 4* thermocouples.

4.5.2.3 Refluxing the Evaporators

Immediately after the return line was opened, the reservoir almost completely emptied itself, which was recorded by the liquid level monitor. Thus the void fraction of the evaporators decreased dramatically from 100% to less than 10%, as indicated in Figure 4.28.

Heat transfer began instantaneously, causing the copper temperatures to decrease. Furthermore, the vapour produced resulted in a rise in the condenser temperature (from 40-70°C to 105-110°C) and cooling water output temperature (from 17°C to 52°C). It should be noted that the values for power are under-represented during this transient period as the portion of the heat being used to warm the condenser is not included in the calculation of the heat load using equation (3-1).

4.5.2.4 Partial Film Boiling

It is interesting to consider the *copper 1* and *copper 2* thermocouples, which record the temperatures directly between the evaporators. The associated temperature curves seem to be segmented into 3 regions indicated by letters A, B and C on Figure 4.28: a large negative slope (A), then a lesser negative slope (B), followed by a large negative slope (C). These results can be explained as follows:

In segment A, the initial drainage of liquid to the evaporators caused considerable turbulence and excellent heat transfer, manifesting itself as the initial rapid decrease in temperature (2.7°C/s). In segment B, the system was at the onset of film boiling, discussed in more detail in Chapter 5 (section 5.3). Film boiling caused a deceleration in the cooling of the copper (0.5°C/s).

Segment C of the *copper 1* and *copper 2* temperature curves has a large negative slope. At this point of the test, the copper temperatures had decreased sufficiently (400°C) such that film boiling no longer occurred. Once this was the case, large quantities of vapour began to form, causing swirling and turbulence which further suppressed film boiling, etc. Large quantities of liquid working fluid were expelled from the evaporator with the vapour, indicated by the sudden increase in the void fraction, which reached 55%.

At this point, the heat pipe system began to function normally, confirmed by the sudden increase in power (45 kW) and by the acceleration in the cooling of the copper launder (1.1°C/s).

4.5.3 Analysis of Results

4.5.3.1 Refinement of the Model - Monel/Copper Interface Contact Resistance

It was possible to use the heat loads measured experimentally together with the copper launder temperatures to analyze the heat transfer in the pilot tests using the model described in section 4.2. With some basic assumptions of how the heat load was applied to the copper launder, the temperatures measured experimentally could be compared with the model temperatures at identical locations using various monel/copper contact resistances. Using a guess and test methodology, several simulations were run and the actual contact resistance could then be extrapolated from the results.

The following outlines the final assumptions used for this analysis. The assumptions were refined several times with each simulation to match the steady-state experimental conditions shown on Figure 4.27 at a time of 4:15 (65 kW heat load). Therefore, an additional benefit of the present modeling is the analysis of the most intense steady-state conditions attained during the slag launder experiments.

Final Assumptions:

- The heat pipe operating temperature was 117°C (from experimental results).
- The heat was applied only to the slag channel with all other launder faces assumed as adiabatic (from visual observations of the experimental setup and testing).
- The most intense heat fluxes were applied to the bottom surface of the launder, as this is where the burner flame was aimed at (from visual observations). In addition, the bottom surface was facing a large refractory brick placed on top of the launder. The refractory brick radiated downwards towards the bottom of the launder. It can be supposed that the bottom wall of the launder had a larger view factor of the refractory compared with the corner and side walls for example, and thus was exposed to a larger heat flux.
- Radiation was more intense towards the back of the channel because there were refractory bricks placed at the back of the launder channel in addition to a larger brick placed on top of it. Therefore the front end of the slag channel had a larger view factor of the surroundings which were at room temperature. The back of the channel

had a smaller view factor of the surroundings while having a larger view factor of the refractory bricks which were a significant source of radiation. Therefore it was assumed that the applied heat flux along the launder channel increased linearly from front to back (along the z-axis). The total heat load was set at 65 kW with the breakdown described below (refer to Figure 4.29):

- 43% applied to the bottom of the launder channel (area = 444 cm²) at an average of 632kW/m², from 566kW/m² (front) to 698 kW/m² (back), varied linearly.
- 31% applied to the corners of the launder channel (area = 377 cm²) at an average of 542kW/m², from 485kW/m² (front) to 599 kW/m² (back), varied linearly.
- 26% applied to the sidewalls of the launder channel (area = 480 cm²) at an average of 344kW/m², from 292kW/m² (front) to 396 kW/m² (back), varied linearly.

It was found that a contact resistance at the monel/copper interface taken as $3.8 \cdot 10^{-5}$ m²·°C/W gave results which matched the experimental results very closely, as shown in Table 4.10.

Table 4.10 Comparison between the experimental and simulation results

	Experimental	Model
Copper 1 temperature	235.4°C	236.0°C
Copper 2 temperature	231.6°C	231.6°C
Copper 3 temperature	425.4°C	425.4°C
Copper 4 temperature	402.0°C	402.0°C

The contact resistance determined by the model is equivalent to a 1.0µm air gap between the monel evaporators and the copper launder (properties of air taken at 127°C). To put these values into perspective, a comparison can be made to the monel evaporator pipes, which had a thermal resistance 4.8 times greater than the thermal resistance of the contact between the monel evaporators and the copper launder.

It can therefore be concluded that the quality of the copper launder casting was good. The contact resistance at the copper/monel interface comprised a relatively small fraction of the overall thermal resistance (the copper launder and monel pipes themselves being the major components of the total thermal resistance).

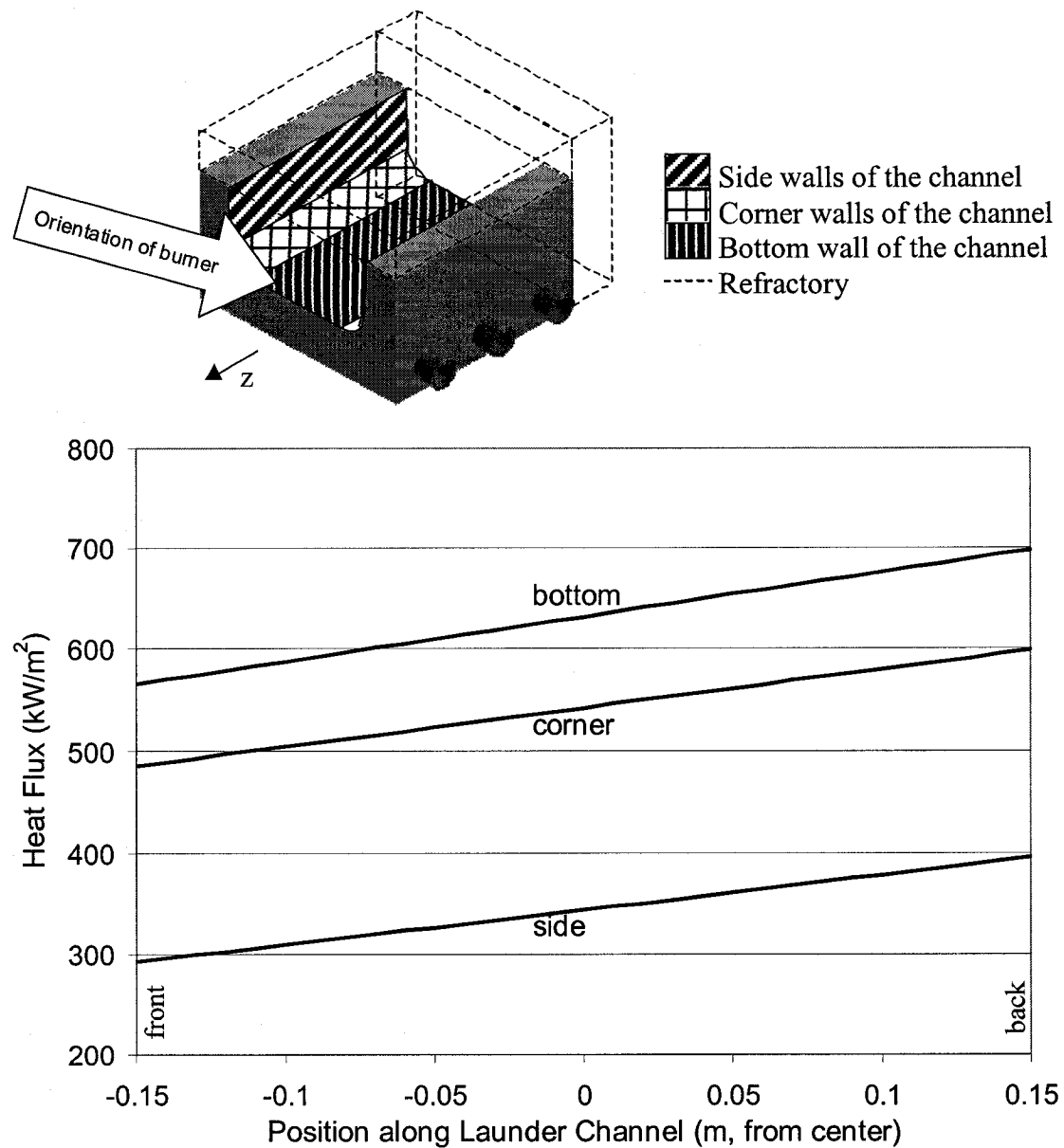


Figure 4.29 Breakdown of the assumed heat flux distribution

Therefore the zero-contact resistance assumption used in the model outlined in section 4.2 was not unreasonably far from the actual value. The actual contact resistance determined via this analysis was then used to refine the model. The only remaining unverified assumption from the model was the zero-contact resistance between the slag and launder channel.

4.5.3.2 Copper Temperatures

The assumptions used to determine the contact resistance yielded results that matched the experimental temperatures very closely. The refined model was therefore used to approximate the steady-state test conditions shown on Figure 4.27 at a time of 4:15, which were the most intense conditions achieved at steady-state (65kW). The temperature contours of the model are shown in Figure 4.30.

It should be noted that the copper temperatures observed during the experiments were above what is normally acceptable for cooled copper equipment (maximum 300°C). The elevated temperatures can be attributed to the following:

- higher-than normal heat loads being applied
- the relatively large thermal resistance of the monel evaporators ($k = 21.7 \text{ W/m}\cdot^\circ\text{C}$)
- the contact resistance at the monel/copper interface ($3.8\cdot 10^{-5} \text{ m}^2\cdot^\circ\text{C/W}$)
- the relatively high operating temperature of heat pipes (80-120°C) compared with water-cooled channels (25-45°C)
- a significant portion of the burner heat load was applied to the channel sidewalls (furthest from the cooling elements), which would not normally occur during an industrial test (slag would flow along the bottom of the channel)

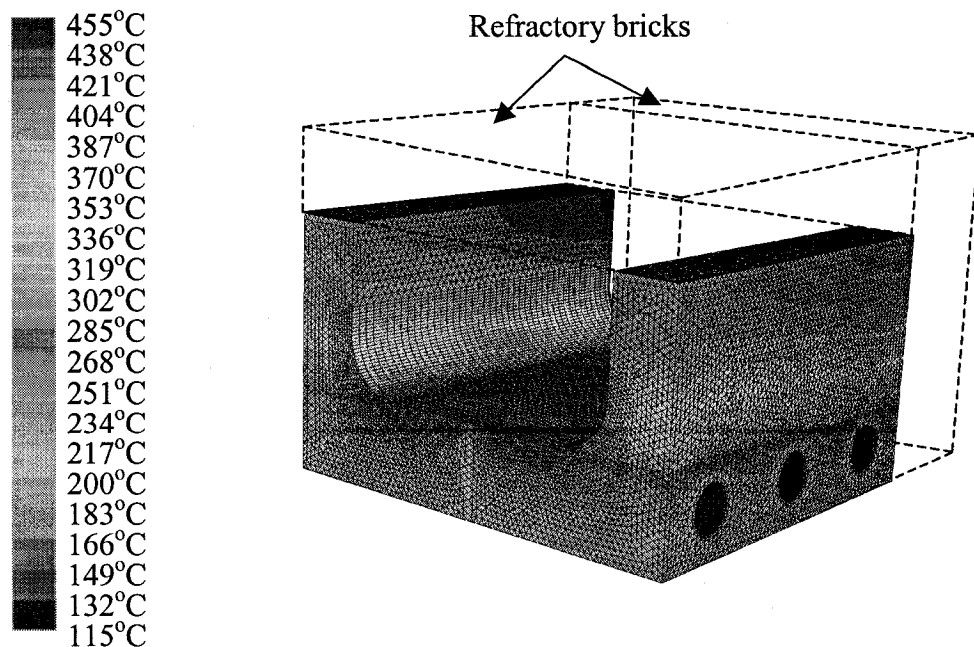


Figure 4.30 Temperature contours of the modeled 65 kW test

4.5.3.3 Heat Flux

The heat flux contours applied to the evaporators were determined using the refined model (65 kW test), shown in Figure 4.31. According to the model, a maximum heat flux of 880 kW/m^2 was transferred across the evaporator and into the working fluid. Although this heat flux is significantly inferior to the 2.4 MW/m^2 observed in the tapblock experiments (see Chapter 3), 880 kW/m^2 represents the largest heat flux successfully dissipated into horizontal water-based McGill heat pipes in a full-scale test.

Heat loads of 20.8kW, 21.8kW and 22.7kW were applied to the front, middle, and back evaporators, respectively.

An important assumption used to calculate the evaporator heat fluxes is that the entire evaporator surface is wetted. However, no dry-out or film boiling was detected during the steady-state test, and so the wetted evaporator assumption may be considered valid.

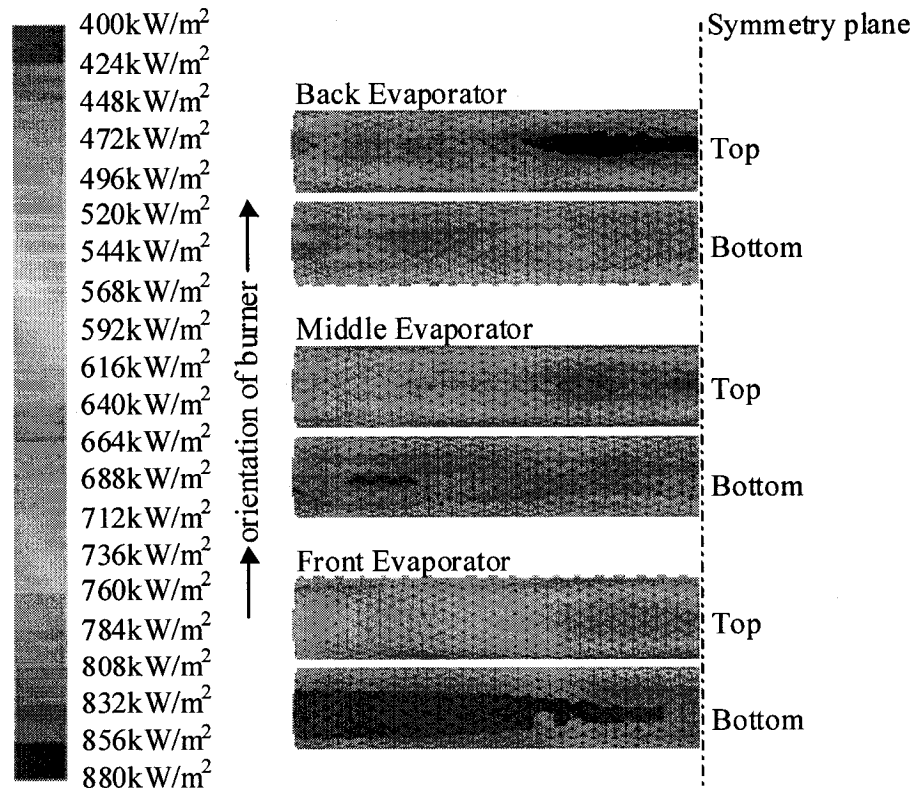


Figure 4.31 Evaporator heat flux contours during the 65 kW steady-state test

4.5.3.4 Comparative Evaluation of Heat Pipe Cooling

The testing discussed in this chapter has shown with a high degree of confidence that the heat pipe technology is capable of dissipating heat loads which would be encountered as part of a blast furnace. In this section, the refined model is used to predict and compare the performance of the following cooling systems under industrial conditions (i.e. slag flowing across the slag channel):

- cast-in monel heat pipes (present design)
- heat pipes drilled directly into the copper casting (alternate design)
- cast-in monel water cooling channels (conventional cooling)

With the exception of the cooling elements, all parameters were identical to those described in section 4.2 (i.e. slag flowing over the launder channel with a height of 3cm). Figure 4.32 compares the launder temperatures of all three scenarios at steady-state.

The applied heat loads were predicted to be almost identical for all three scenarios. The results show that a slag launder with evaporators drilled directly into the copper would operate significantly cooler (100-175°C) than the slag launder tested at Umicore (100-232°C). Such a launder would have a maximum operating temperature slightly warmer than an identical launder cooled with cast-in monel water cooling channels (maximum launder temperature: 160°C, with the cooling water temperature set to: 35°C).

It can be concluded from these results that it may be desirable to fabricate any future slag launders out of copper only. However, the cooling systems of copper-only launders are more susceptible to impacting heat loads, as there are less thermal resistances (monel and interfacial contact) which tend to spread the effects of varying heat loads over time.

Figure 4.33 illustrates this concept. The transient results presented in this figure correspond to a heat pipe-cooled copper launder with the evaporators drilled directly into the copper (no monel pipes). Conditions identical to those described in section 4.2 (transient) were used. In contrast to the results illustrated in Figure 4.15 of section 4.3.2, note the large initial heat load applied to the evaporators (time 0 to 50 seconds) as molten slag flows over the copper launder which has not yet formed a fully developed skull.

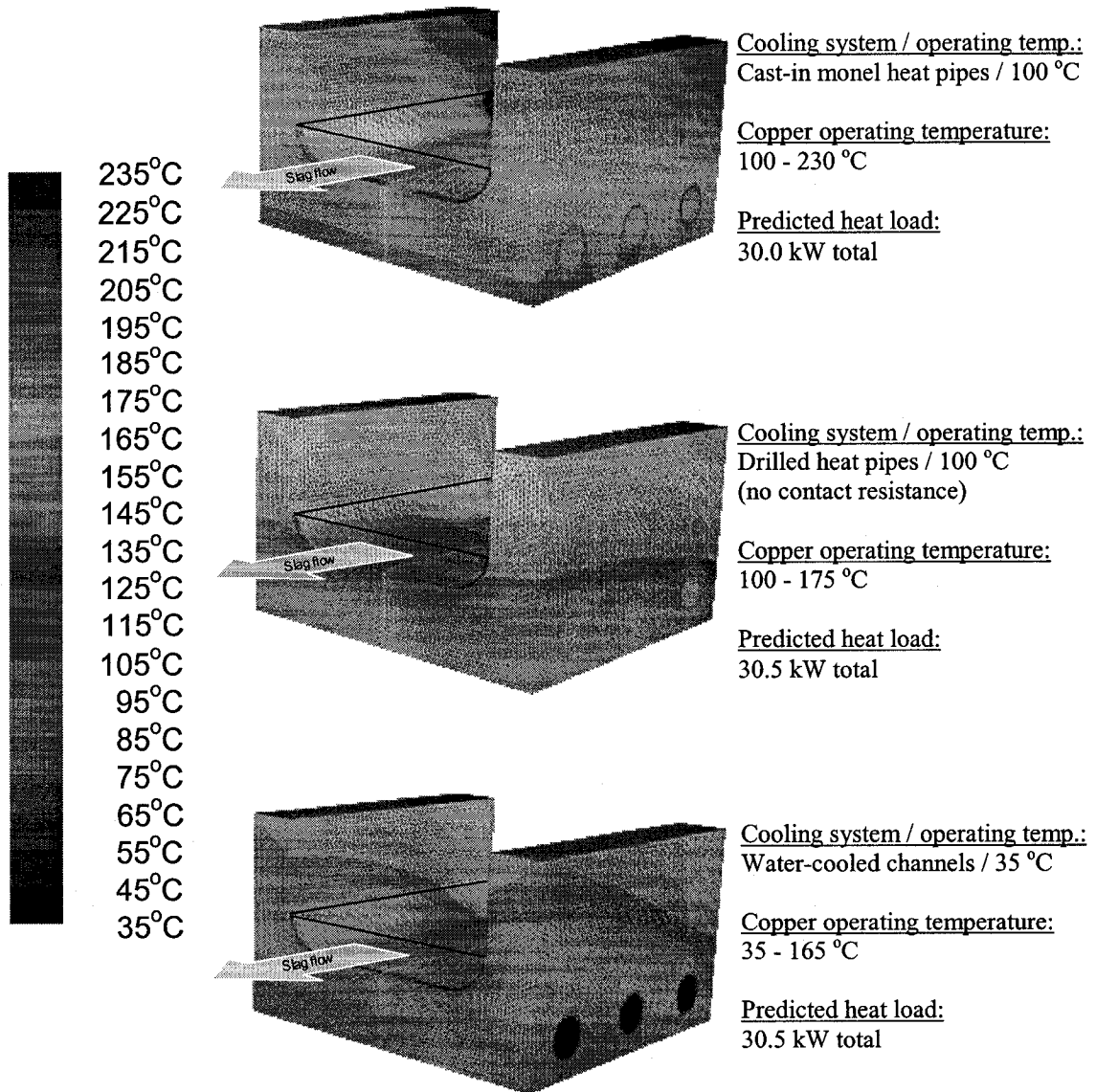
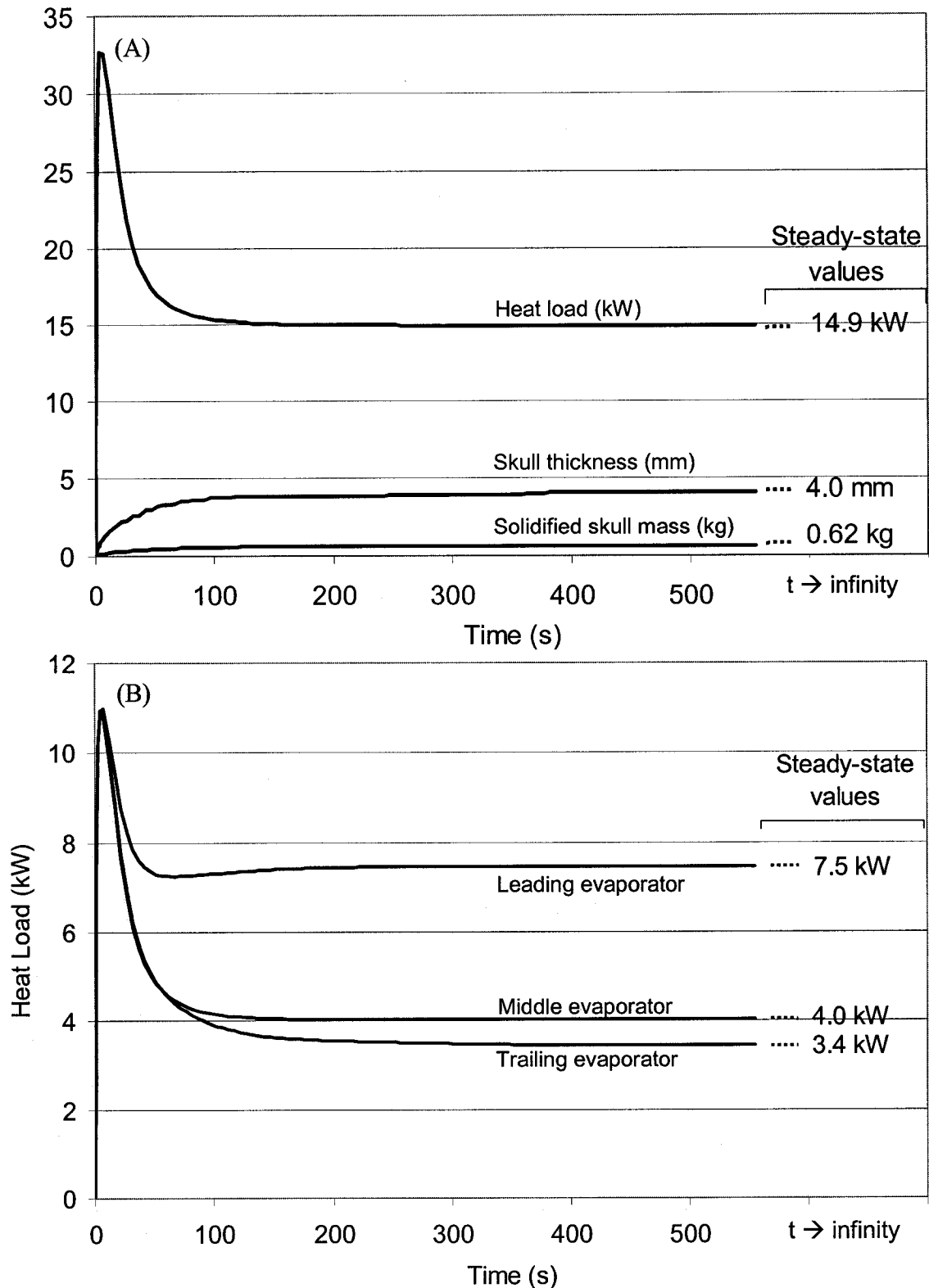


Figure 4.32 Comparison of copper launder temperature contours

Figure 4.33 Transient results for a copper-only launder, $HSF=3\text{cm}^*$

(A) Summary of total heat load and skull solidification

(B) Breakdown of evaporator heat load

* Recall that the heat loads and slag skull mass presented here corresponds to one half of the actual launder.

4.5.3.5 Cooling Water

The cooling water flowrate was maintained at 0.31 l/s for the present slag launder test. Water entered the condenser at 17°C, exiting the system at temperatures of between 50°C and 75°C for heat loads of 37 kW to 65 kW, respectively. Using the Dittus-Boelter equation and the same methodology described in section 3.5.4.1, it was possible to compare the cooling water requirements of the heat pipe system to an equivalent water cooling system. The calculations are shown in Table 4.11.

The results indicate that a flow rate of between 1.9 l/s and 3.0 l/s would be required to cool the slag launder safely under the same test conditions (510% - 900% more) using a forced convection water cooling system.

Table 4.11 Equivalent cooling water requirement calculation summary

	Average heat flux	Maximum heat flux
Applied heat flux, q''	600 kW/m ²	880 kW/m ²
Pipe interface temperature, $T_{surface}$	117°C	117°C
Cooling water bulk temperature, T_{bulk}	35°C	35°C
Average heat transfer coefficient, \bar{h}	7,300 W/m ² ·°C	10,700 W/m ² ·°C
Nu_D	410	600
Re_D	93,500	152,000
Required cooling water velocity, v	1.9 m/s	3.1 m/s
Required cooling water flowrate (conventional)	1.9 l/s	3.0 l/s
Cooling water flowrate (heat pipe experiments)	0.31 L/s	
Increase in cooling water requirement for conventional cooling	510 %	900 %

4.5.3.6 Liquid Level Monitor Results

Throughout the testing of the slag launder, steady-state conditions were reached several times. The evaporator void fraction measurements and heat loads during these conditions are plotted against one another in Figure 4.34 below.

A linear trendline was fit to the data points with excellent correlation over the given range. The trend is as one would expect, i.e. larger heat loads cause larger vapour velocities within the evaporator. The larger velocities generate a larger pressure buildup at the bottom of the evaporator which tends to reduce the flow of liquid down the return line, according to the Bernoulli equation [73]. Therefore at larger heat loads, the vapour:liquid ratio in the evaporator tends to increase.

The linearity of the trendline indicates the proper functioning of the liquid level monitor as a sensor useful in measuring the evaporator void fraction.

Figure 4.34 also indicates that evaporator void fractions measured throughout the experiments were generally low (7-33%). This indicates a large excess of working fluid being discharged to the evaporators.

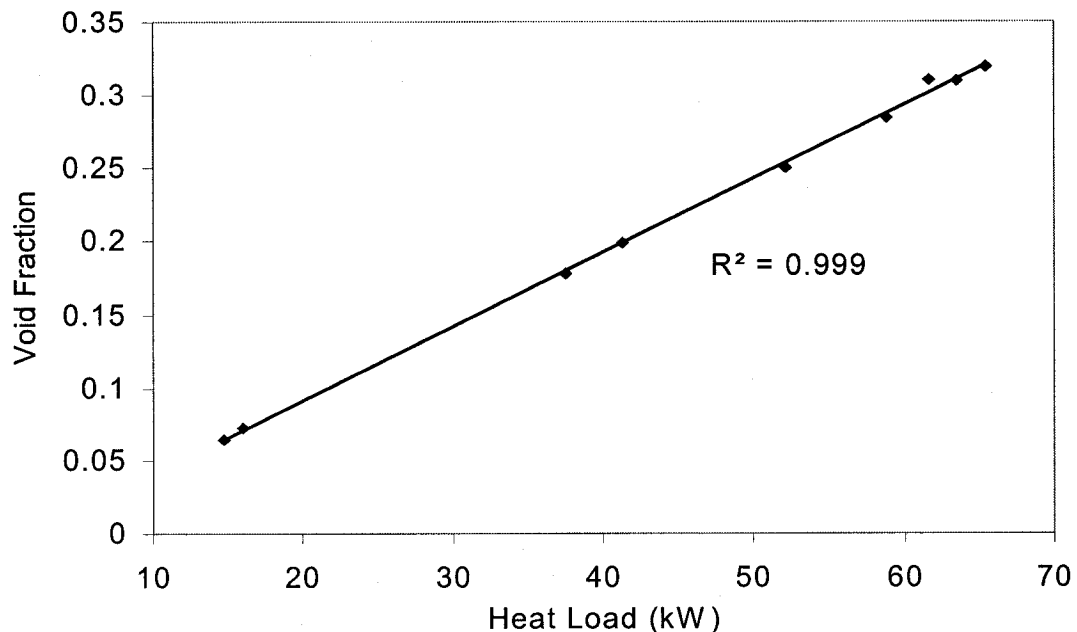


Figure 4.34 Average evaporator void fraction vs. heat load (steady-state)

Chapter 5 Heat Pipe Limitations

5.1 Introduction

The main focus of this thesis is the scale-up of McGill heat pipe technology for use in pyrometallurgical applications. An integral part of this work is to investigate the limitations of the technology in full-scale applications. An effort was made during testing to push the technology beyond its capacity in order to determine and study the factors that contribute to the proper functioning of the device. It is hoped that through understanding the limitations, knowledge of the principles behind the technology is gained and further improvements to McGill heat pipe technology can be made.

The two main limitations encountered with industrial-scale heat pipe systems were:

- the dry-out limitation
- the film boiling limitation

Dry-out was encountered in some of the initial tapblock experiments, and is described in section 5.2. Once the importance of dry-out in full-scale McGill heat pipes was realized, the slag launder was designed to avoid dry-out. However, film boiling was achieved during the most intense slag launder test conditions. These results are described in section 5.3.

5.2 Dry-out Limitation

Recall that the tapblock cooling system was composed of two heat pipes drilled vertically on either side of the taphole (refer to Chapter 3). The purpose of the test discussed in this section was to determine the maximum heat extraction capability of the heat pipe system. Under the operating parameters used for the test, dry-out was achieved and it proved to be the limiting factor when operating this particular heat pipe system.

5.2.1 Test Results

In order to maximize the heat load into a single heat pipe, the burner was positioned over the left heat pipe, centered vertically. For simplicity, only measurements from the left side of the tapblock are discussed in this section. The right heat pipe extracted a relatively small quantity of heat during this test and operated in a stable manner, described in Table 5.1. Refer to section 3.3 (Chapter 3) for a description of the experimental setup and sensors.

Table 5.1 Operating parameters of the right side of the tapblock

Parameter	Value
Heat load	35 kW
Tapblock temperature (right side)	100 - 130°C
Cooling water flow rate	1.8 l/s
Operating temperature	80°C
Vapour density	293 g/m ³
\bar{v}_{min}	112 km/hr

After the burner was ignited, the gas flow rate was set to 40Nm³/hr, but was gradually brought to 57.5Nm³/hr. Figure 5.1 presents results from this point. Quasi-steady-state conditions were reached, with the left heat pipe extracting 75kW of heat (from a time of 13:40 to 14:00).

Peculiar observations were made at about 14:00 regarding the left tapblock temperatures: these temperatures (particularly the top one) seemed to be continuing to rise whereas the other temperatures of the system remained at steady-state.

The burner was decreased a few minutes later (14:04) in order to determine if the left tapblock temperatures would react to the decreased heat load being applied. However,

the temperature of the top of the tapblock continued to rise at an accelerated rate. This trend began to cause alarm as the heat pipes appeared to be functioning, and the burner setting had been decreased. Therefore, there was no apparent reason explaining why the top temperature of the tapblock should have been increasing so rapidly.

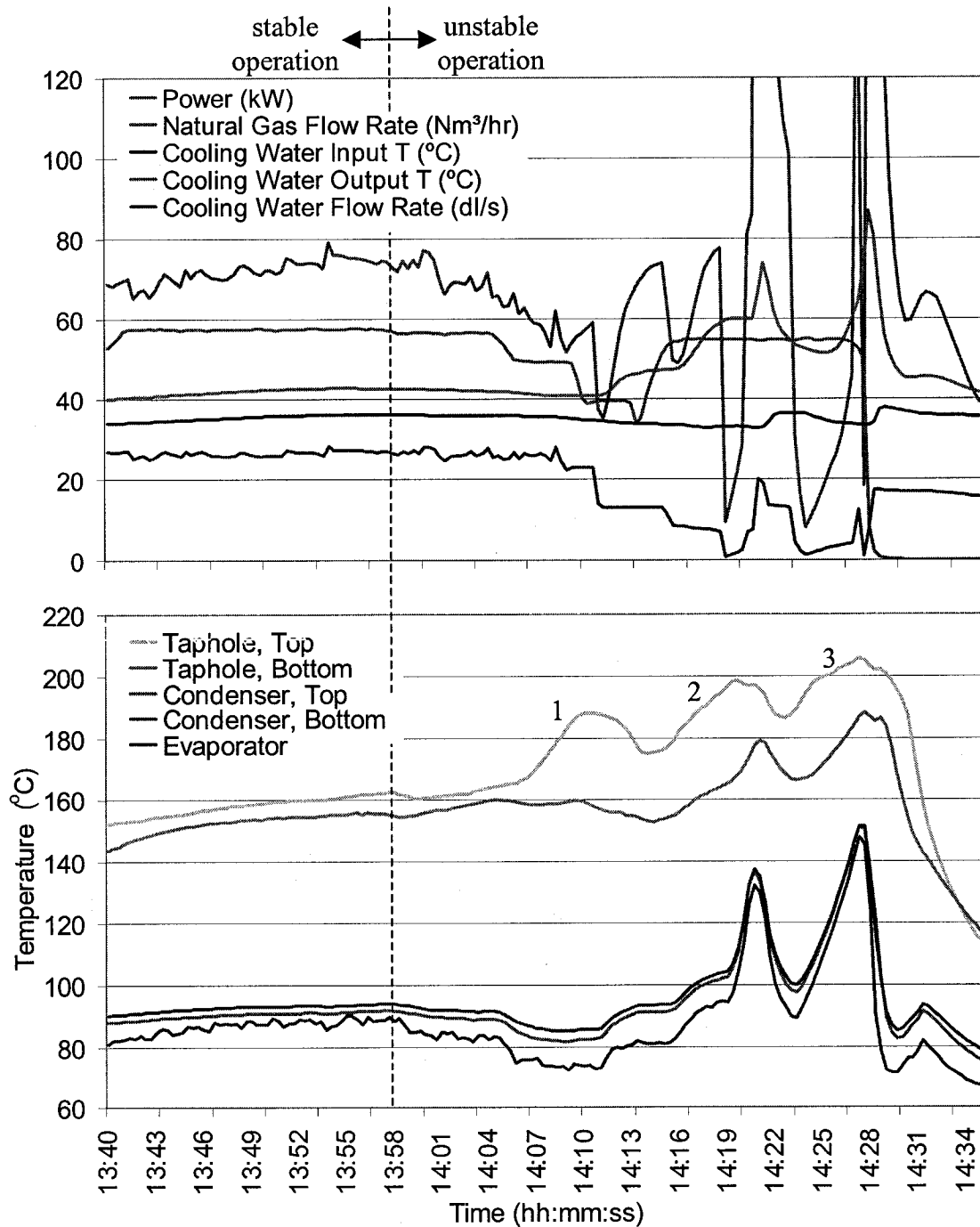


Figure 5.1 Dry-out test results (left side of the copper tapblock)

In fact, there was an explanation that was realized at this point during the test, which stems from experience gained from previous tests with laboratory-scaled heat pipes. The observed experimental circumstances indicated on all accounts that the dry-out limitation of the left heat pipe had been inadvertently reached, and the heat pipe was beginning to operate in an unstable manner.

5.2.2 Operational Solution to Dry-out

The external cooling water flow rate of the left condenser was decreased several times from 2.3 l/s, beginning at a time of 14:09. This was done in order to increase the left heat pipe operating temperature. From previous experience, it was known that doing so would help eliminate dry-out and bring the left heat pipe back to stable operation.

Indeed, the decreased cooling water flow rate did temporarily increase the left heat pipe heat extraction rate. Unfortunately, these measures were taken too late. Once the dry-out limitation is reached, it can become difficult to bring the system back to stable operation. Because the cooling water flow rate was manually controlled during testing, reacting appropriately to the observed trends was difficult. This led to the three cycles seen in the data between 14:06 and 14:30. During each of these cycles, the dry-out limitation was reached, and then overcompensated for, producing three “humps” labeled 1, 2 and 3 in the left top taphole temperature curve of Figure 5.1.

As the operating temperatures of the system were increasing, it was therefore decided to end the test before damaging any of the equipment. It should be noted that the heat loads presented in Figure 5.1 after unstable operation (from 14:10 onwards) are not reliable. This is because the cooling water flowrate was changed several times and the cooling water output temperature was being measured far from the outlet on the condenser. Therefore when changing the cooling water flowrate, it took some time before corresponding changes in the cooling water temperature were measured, temporarily skewing the heat load calculated using equation (3-1).

5.2.3 Explanation of Dry-out

Because it is very difficult to make visual observations or precise measurements within a heat pipe, concepts such as dry-out are still not completely understood, although much progress has been made in recent years. Yuan first observed dry-out in a laboratory test, reported in 2002 [59]. Although largely academic in nature, this work helped formulate the present explanation of dry-out phenomena in a heat pipe, explained in the next section. The results from the tapblock tests showed that dry-out is a major limitation in full-scale heat pipe systems operating at their capacity. Following the tapblock tests, Zhao did additional experimental work in 2003 using an air-water heat pipe model which simulated a heat pipe [89]. The visual observations and measurements also support the present theory about dry-out.

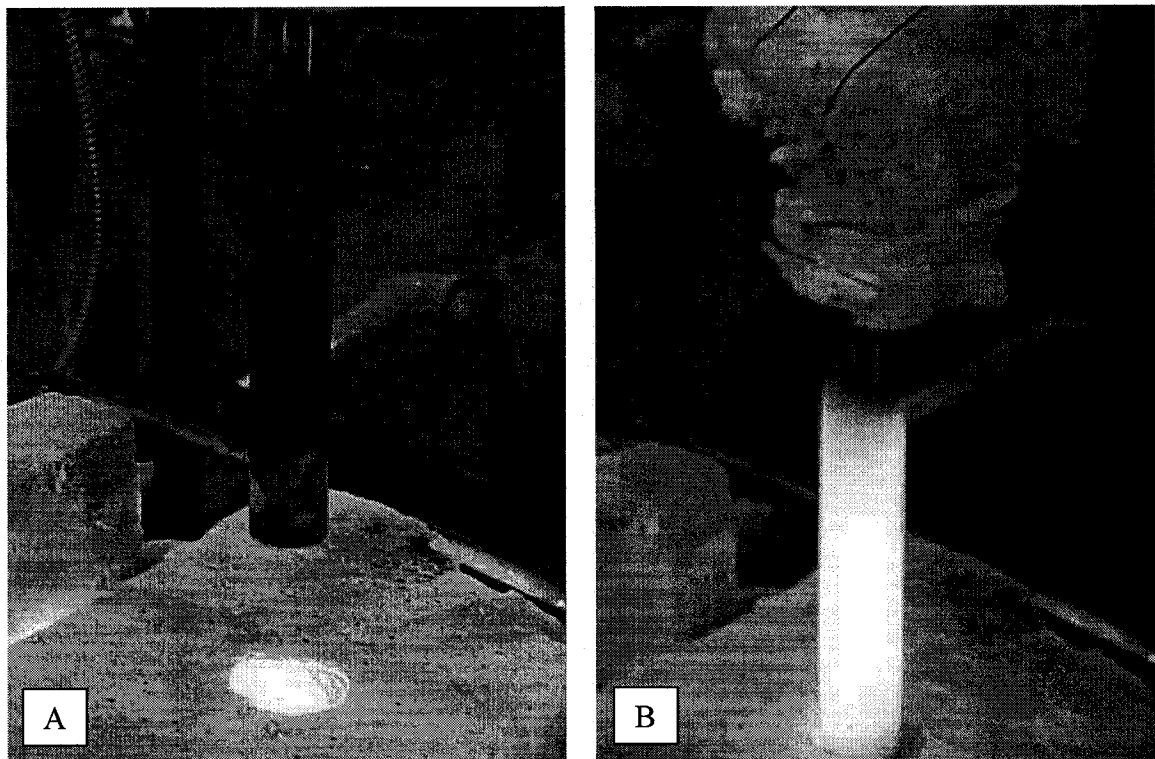


Figure 5.2 Dry-out limitation in McGill heat pipes [57]

- A. McGill heat pipe after 2 hour test, stable operation.
- B. McGill heat pipe after 1 minute test, conditions for dry-out limitation.

It is generally accepted that the zone of the heat pipe that operates at the lowest pressure is the condenser, as this section of the device is cooled and vapour condenses there. Similarly, the zone of the heat pipe operating at the highest pressure is the evaporator, as this is the heat source of the device and vapour is formed there. Therefore, in a correctly operating heat pipe, there exists a pressure difference between the evaporator (high) and the condenser (low).

Flow of liquid through the return line is primarily due to the head of liquid working fluid filling the return line, from the point of discharge in the bottom of the evaporator to the reservoir in the condenser. In the case of the present experimental setup, the head of liquid was 1.9m. This driving force must overcome the pressure difference between the evaporator and the condenser such that sufficient condensed working fluid flows down the return line and is discharged into the evaporator, cooling it by vaporizing.

Under relatively high heat loads and low operating temperatures (causing low vapour densities), the vapour velocities within a heat pipe are rather large. For example, at the point identified as the onset of dry-out in this test, \bar{v}_{\min} in the left heat pipe was calculated to be approximately 48.3m/s, or 178 km/hour, using equation (3-10). With large velocities, it is thought that the flow resistance of vapour as it rises to the condenser can be quite high, as flow resistance is generally found to be proportional to the fluid velocity squared. The high flow resistance causes a large pressure gradient in the evaporator, resulting in a relatively high pressure at the bottom of the evaporator.

Therefore, at the onset of dry-out, the large flow resistance caused by the high vapour velocities accounts for too large a portion of the head of liquid working fluid in the return line, the remainder of which drives condensed working fluid downwards. This slows the flow of liquid down the return line such that an insufficient flow rate of liquid working fluid is discharged into the evaporator. Refer to Figure 5.3.

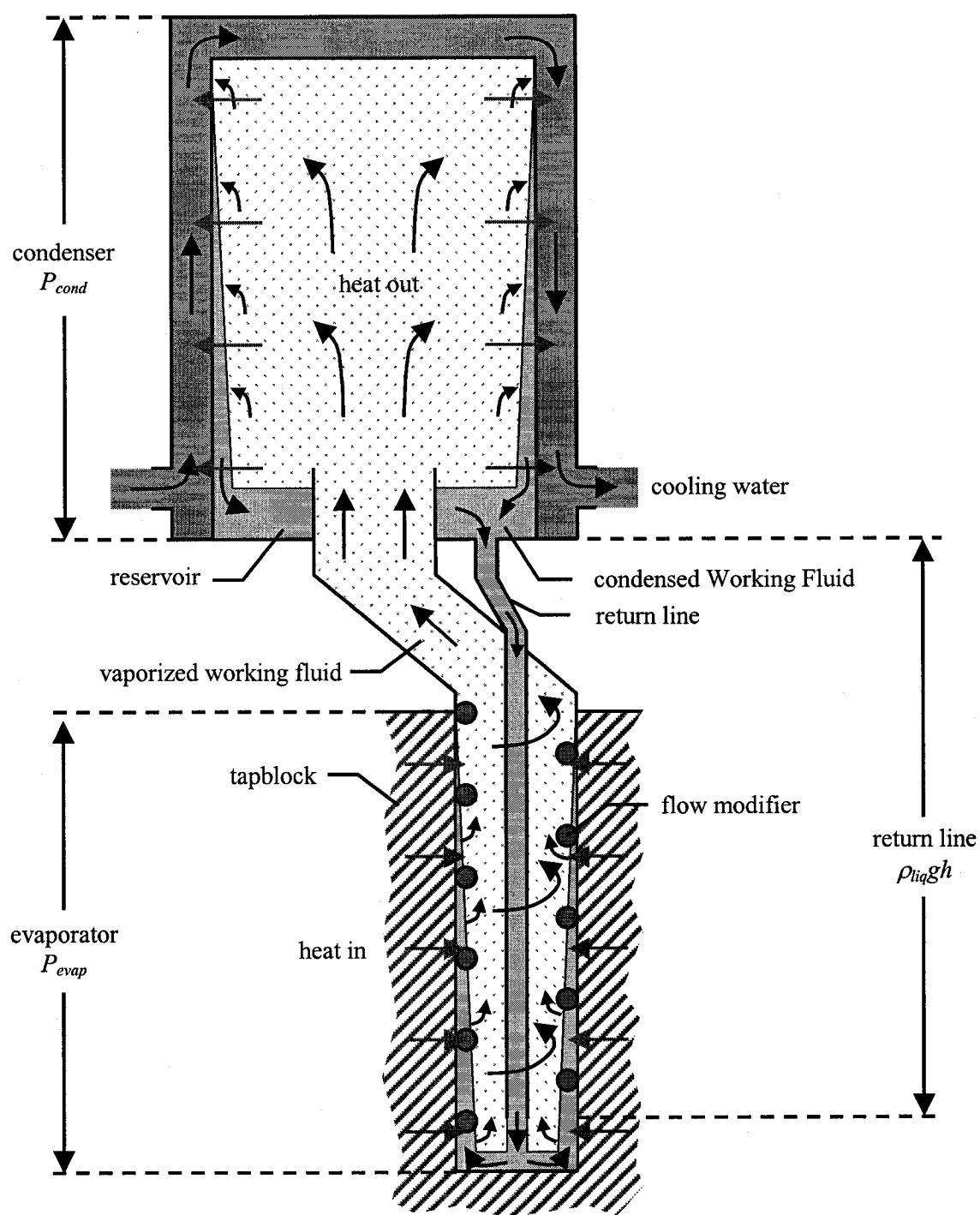


Figure 5.3 Conceptual diagram of the tapblock heat pipe cooling system

When the flow of liquid working fluid travelling through the return line is insufficient, a large fraction of the liquid working fluid being discharged in the evaporator (and entrained with the rising vapour produced) is transformed into vapour prior to traveling to the upper region of the evaporator. The remaining liquid exists as a mist, and is dominated by drag forces. Therefore the body forces propelling the liquid towards the wall become insignificant, and proper wetting of the upper evaporator inner wall becomes impossible.

When this is the case, the top region of the evaporator, which is still subjected to a heat load, is no longer able to dissipate the heat into the working fluid as the latent heat of vaporization. The result is an accumulation of heat manifesting itself as a temperature increase to the surrounding copper. Dry-out also results in a reduction of the heat exchange area within the evaporator, causing both an overall decrease in the heat extraction rate from the copper into the heat pipe, and a decrease in the heat pipe operating temperature. All of these indications were observed between 14:06 and 14:11.

During this time, the top tapblock temperature was increasing, the heat extraction rate of the left heat pipe was decreasing, and the left heat pipe operating temperature was decreasing, all indicating dry-out.

5.2.4 Elimination of Dry-out

The heat pipe operating temperature can be controlled by adjusting the external cooling water flow rate. Decreasing the flow of the external cooling fluid reduces the heat transfer coefficient between the stainless steel tubes in the condenser and the cooling water. This increases the thermal resistance across this interface, causing the heat pipe to operate at a higher temperature in order to overcome the increased thermal resistance and maintain the same heat flux (as the system re-establishes steady-state). Therefore, increasing the cooling water flowrate decreases the heat pipe operating temperature. Conversely, decreasing the flowrate increases the operating temperature.

In general, an increased operating temperature helps ensure stable operation, but care must be taken not to decrease the flowrate such that boiling occurs in the external cooling circuit. It is recommended that the output water temperature be kept below 85°C.

As a heat pipe is a closed system with only water inside of it (working fluid), the system operates at the saturation pressure which is a function of temperature. An increased operating temperature causes an increased operating pressure which increases the density of vapour within the heat pipe.

As the major mode of heat transfer within a heat pipe is via storing the heat as the latent heat of vaporization of the working fluid vapour, which is constant per unit of mass, then the mass rate of vapor production is constant with a constant heat load. Therefore, increasing the density of the vapour has the effect of decreasing the vapour velocities within the heat pipe, as indicated by equation (3-10). This in turn decreases the flow resistance of the evaporator, resulting in an increased flow of liquid working fluid to the bottom of the evaporator, alleviating dry-out.

Following the test results discussed in this section, plans were made to operate the heat pipe at a higher temperature for the next test, which resulted in the successful test described in Chapter 3. Table 5.2 compares the operating parameters of the present test and the test described in Chapter 3.

Table 5.2 Comparison of the tapblock test operating parameters and results

Test	Max. heat load	Cooling water flow	Operating temperature	Vapour density	\bar{v}_{max}
Unstable operation (dry-out)	75 kW	1 – 2.5 L/s	93.5 °C	480 g/m ³	170 km/hr
Stable operation (see Chapter 3)	135 kW	0.1 – 0.8 L/s	120 °C	1120 g/m ³	73 km/hr

Therefore the experimental results from the tapblock tests help confirm the present theory which explains dry-out in McGill heat pipes.

5.3 Film Boiling Limitation

Recall that the slag launder was composed of three evaporators positioned horizontally across the copper launder, connected to a single condenser. The purpose of the test described in this section was to study the ability of the heat pipe system to operate in a stable manner under the most difficult operating conditions, and is very similar to the successful impact test described in Chapter 4 (section 4.5.2). Recall that this test consisted of drying out the evaporator and causing the copper launder to increase in temperature to approximately 500°C. However, unlike the test described in section 4.5.2, the burner was kept on in the present test even after the return line valve was opened. This resulted in an even more intense heat flux to the evaporators.

In actuality, the present test simulates the most extreme situations encountered industrially, for example matte accidentally being tapped from the slag taphole. Even the most sophisticated conventional water cooling system would have difficulty to start cooling copper that had already reached 500°C.

5.3.1 Test Results

5.3.1.1 Attaining Dry-out

The return line valve was closed at the beginning of the test (0:00). Dry-out occurred immediately, as the void fraction reading increased to 100% almost instantly. It should be noted that this indicated excellent working fluid circulation during normal operation. Refer to Figure 5.4.

From a test time of 0:00 to 0:13, the copper temperatures gradually increased to approximately 500°C. The results indicate fluctuations in the heat extraction rate (power) and the output cooling water temperature during this period. These results should be ignored as they simply reflect changes made in the cooling water flowrate, also shown on the graph. The dashed lines on the graph are an estimate of what the correct readings were during this period. As in section 4.5.2, the values for power correspond to the heat extracted from the condenser, essentially an 85 kg mass of stainless steel.

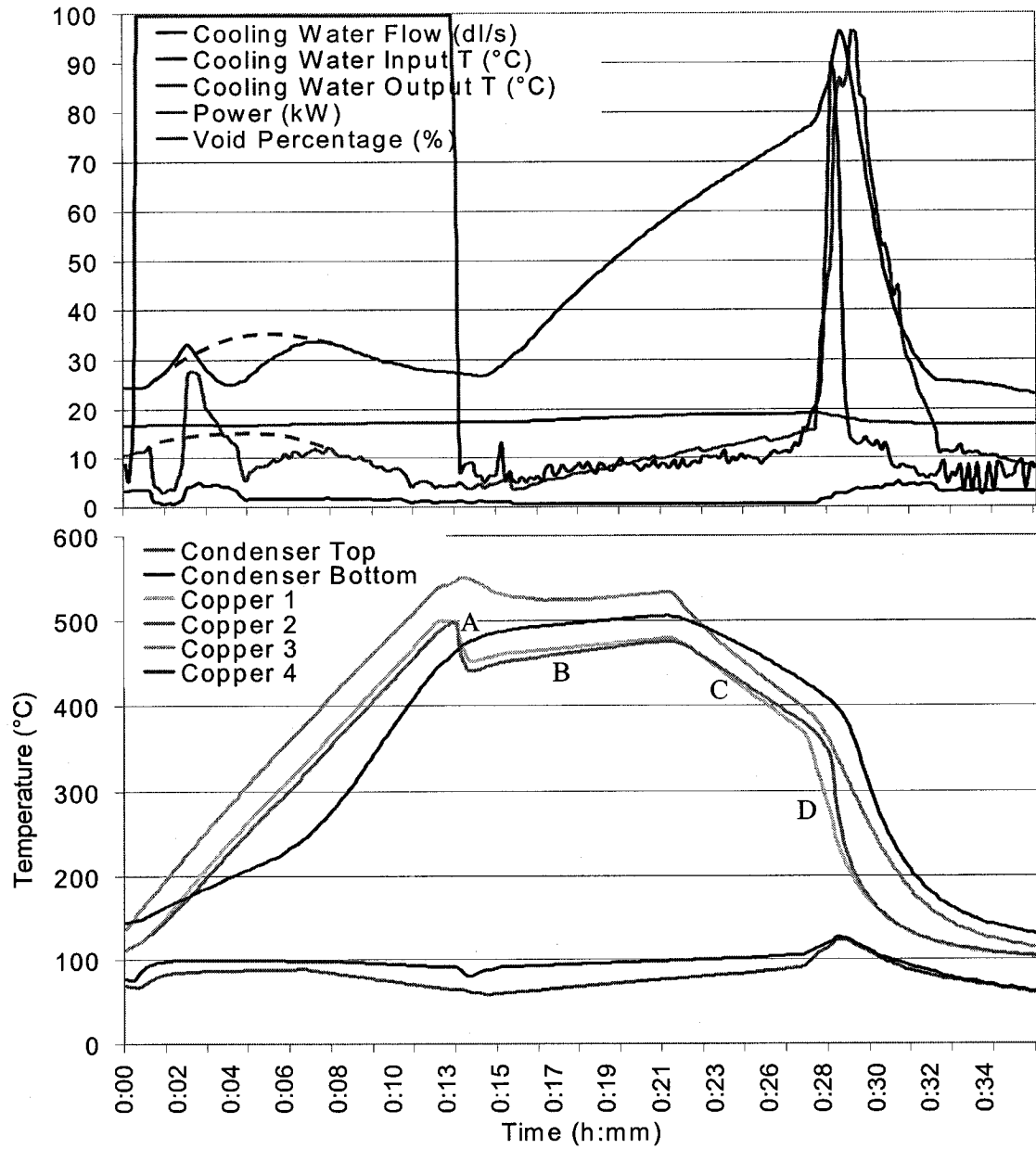


Figure 5.4 Film boiling test results (copper launder)*

*Refer back to Figure 4.26 for thermocouple positioning

5.3.1.2 Heating of the Copper and Evaporator Refluxing

The copper temperatures recorded during the heating up of the copper launder were similar to those observed in the test described in section 4.5.2. Recall that the configuration of the refractory brick and burner caused more radiation to strike the slag launder further back (away from the burner). This caused a more rapid increase in the temperatures read by thermocouple *copper 3*, whereas thermocouple *copper 4* was positioned closer to the front of the slag launder, and was the slowest to measure increases in temperature. At 0:13, the return line valve was completely opened, indicated by the rapid decrease in the void fraction (from 100% to 7%) as liquid working fluid rushed to the evaporators.

5.3.1.3 Attaining Film Boiling

Very little heat transfer was observed after opening the valve, as the power and output cooling water temperature readings failed to increase, remaining at approximately 5kW and 27°C, respectively. As well, the void fraction seemed to stall at 7-10%. The only indication that any heat transfer took place is the *copper 1* and *copper 2* temperatures which decreased momentarily (1.5°C/s), corresponding to the initial rush of working fluid to the evaporators. This is shown as segment A on Figure 5.4.

Film boiling was experienced under these conditions. This is indicated by the temperature of the copper launder that increased steadily even after the return line valve was opened (0.1°C/s), indicated by segment B on Figure 5.4. This situation simulated the worst type of scenario encountered in the cooling of furnace equipment. As the temperature of the copper increased, film boiling became more and more pronounced, further decreasing heat transfer, which can eventually lead to failure.

5.3.2 Explanation of Film Boiling

Film boiling was achieved in the slag launder tests because of three reasons:

- Firstly, the temperature gradient between the launder and the working fluid was considerable in this test, contributing to film boiling conditions ($\sim 400^{\circ}\text{C}$).
- Secondly, as the evaporators were flooded, any vapour that was produced had difficulty escaping. It is believed that the flow resistance imposed on the vapour by the flow modifier is what causes the swirling motion in the evaporator, which normally suppresses film boiling. With little vapour flow and thus little swirling, wetting of the evaporator walls was difficult.
- Thirdly, with the burner still applying a heat load to the slag launder, the heat flux which was expected to be dissipated across the evaporator interface was even higher than in the impact test described in Chapter 4 (section 4.5.2). This heat flux was ultimately greater than the CHF of the heat pipe system under startup conditions.

Therefore the film boiling regime was attained because the evaporators were completely flooded during startup of the impact test as a result of the return lines being opened in a rapid fashion. Any vapour which formed encountered a large flow resistance when travelling to the condenser as the evaporators were almost completely full of liquid. Therefore, the two-phase flow regime most likely resembled bubbly or slug flow. The vapour traveled slowly, did not generate adequate turbulence/swirl, and thus a stable vapour film was formed at the evaporator/working fluid interface.

This is similar to Yuan's film boiling experiment conducted in 2002 (Figure 5.5), where the lack of swirl also contributed to the formation of a stable vapour film. However the lack of swirl in Yuan's experiment was due to the removal of the flow modifier normally present within the evaporator.

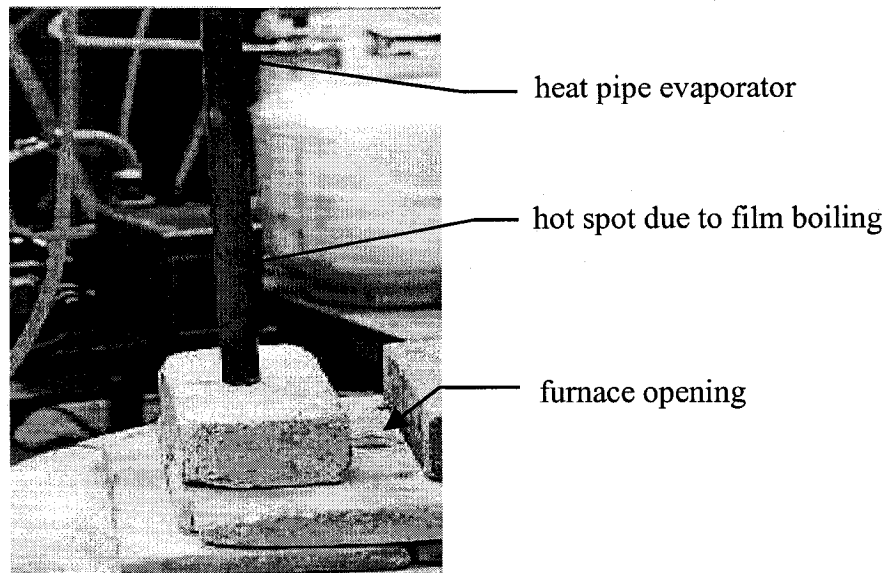


Figure 5.5 Hot spot in a lab-scale heat pipe after removing the flow modifier [5-1]

5.3.3 Elimination of Film Boiling

Generally speaking, there is very little alternative to eliminate film boiling other than to shut off the heat source to the cooling system. This can be problematic industrially when the heat source is the molten product of a furnace, which cannot simply be made to disappear.

The change in the slope of the temperature curves at a time of 0:21 (start of segment C of Figure 5.4) corresponds to the shutting off of the burner, which was done because the copper temperatures continued increasing to well over 500°C. Like segment B, segment C also corresponds to the film boiling regime of the heat pipe system. However with the burner off, it was now possible to see that the system was indeed extracting some heat as the copper temperatures began to decrease, although not very rapidly (0.35°C/s).

Film boiling was eliminated at a test time of 0:28. This occurred at a threshold copper temperature of 375-400°C, similar to the threshold observed in the impact test described in section 4.5.2. At this point, the temperature gradient between the copper and the working fluid was low enough such that boiling heat transfer efficiency began to increase. This initiated a vicious cycle of increased vapour production and increased

turbulence/swirl until stable operation quickly established itself. This was observed in the results (segment D of Figure 5.4) as the copper temperatures began to decrease rapidly (1.5°C/s), while sudden increases were recorded in the power, condenser temperature (from 95°C to 125°C) and void fraction (from 12% to 90%). Note that the power readings calculated using equation (3-1) at this time were temporarily exaggerated as the cooling water flow rate was increased at this point to keep cooling water temperatures below 100°C .

5.3.4 Copper Temperature Curves

In order to understand the individual temperature curves while cooling the copper (test time 0:13 to end of the test), it is sufficient to consider the position of the thermocouples from the bottom of the evaporators (recalling that the evaporators are horizontal). During operation, the bottom of the evaporators had the smallest velocities as only the vapour generated at the bottom end must travel across the heat pipe cross-section. At the top end of the evaporator, the vapour generated along the entire length must travel across the cross-section. As the evaporator cross-section is a constant, the velocities are larger at the top of the evaporator compared to the bottom.

Therefore larger vapour velocities exist at the top of the evaporators and the swirling flow is more developed there, suppressing film boiling. Therefore it can be assumed that at the onset of film boiling, the top of the evaporator can dissipate heat at larger heat fluxes compared to the bottom. This is observed in the results, as the *copper 3* thermocouple (closest to the top) decreased in the most stable manner. The *copper 4* temperature (closest to the bottom) initially decreased at the slowest rate, indicating the most severe film boiling conditions at the bottom.

5.3.5 Improved Startup Methodology

Musmar has done work with heat pipe technology applied to thermal analysis [67]. An integral part of this work involves the startup of water-based heat pipes in thermally extreme situations.

Briefly stated, the heat pipe-cooled thermal analysis equipment must be continuously immersed into a bath of super-heated aluminum metal. The cooling system must be turned on and off at intervals of approximately 5 minutes. During the “off” cycle, the evaporator is dry and the equipment heats up to the bath temperature of between 700°C and 900°C. The system must then start up from this condition during the “on” cycle and freeze a layer of aluminum onto a probe for analysis. This is done by refluxing the evaporator with working fluid.

The operation of this technology is of great relevance to the film boiling test discussed here. Based on the work of Musmar, it should be possible to circumvent the film boiling encountered by careful control of the evaporator refluxing procedure [68].

By simply opening the return line valve gradually during startup and limiting the flow of liquid working fluid to the evaporator via the return line, the evaporator is not initially flooded. The liquid entering the evaporator eventually evaporates and can therefore travel easily to the condenser as the evaporator is mostly empty (i.e. has very little liquid within it). Therefore larger vapour velocities are generated and a more developed swirl is produced. As more and more liquid working fluid is allowed to reflux the evaporator, the swirling flow pattern is already initialized. The centrifugal forces suppress film boiling, bringing the system back toward stable operation. The startup procedure takes approximately 15 seconds.

Future test work should be done to confirm that the “hot startup” procedure described above can indeed lead to stable heat pipe cooling despite thermally extreme conditions.

5.3.6 Improved Heat Pipe Design

Following the tapblock tests, where dry-out proved to be the main concern, the slag launder cooling system was designed to try to prevent dry-out. Therefore the height of the condenser was chosen as 1.5 m. This value is similar to the 1.9 m height of the condenser for the tapblock cooling system, despite being designed for a heat load (50 kW) which is 66% less than the design heat load of the tapblock test (150 kW).

The slag launder design worked as expected, perhaps too well. The evaporator void fractions measured during testing were generally very low (between 7 and 30% depending on the heat load, see Figure 4.34), indicating a large excess of working fluid being discharged to the three evaporators. An excess of liquid working fluid is normally positive as it prevents the dry-out of the upper portions of the evaporators. However, the film boiling experiment shows that under certain conditions, too large an excess can be detrimental to heat pipe operation.

In order to reduce the flow of liquid working fluid to the evaporator in future designs: (1) the condenser height (h) can be reduced and/or (2) the velocities/pressure gradients in the evaporators can be increased by reducing the evaporator cross-section.

5.4 Maximizing the Heat Extraction Capacity

As mentioned in Chapter 2, one of the main limitations of classical heat pipe technology was the film boiling limitation. The realization that the replacement of the capillary wick with a helical flow modifier can largely suppress film boiling led to the invention of the McGill heat pipe.

Although beneficial from a film boiling perspective, the presence of the flow modifier also has a “price” from a fluid mechanics perspective, in the form of an increased resistance to the flow of vapour and liquid traveling to the condenser. This increased resistance causes a buildup of pressure at the bottom of the evaporator, which hinders the return of liquid through the return line to this region. Therefore, the dilemma is that in general, an “aggressive” flow modifier generates more centrifugal force and suppresses

the film boiling limitation, but causes a pressure buildup and promotes evaporator dry-out. Similarly, a more “passive” flow modifier may alleviate dry-out, but is limited in suppressing film boiling. Refer to Table 5.3 and Figure 5.6.

Table 5.3 Explanation and comparison of aggressive and passive flow modifiers

	Flow modifier	
	“Aggressive”	“Passive”
Pitch	smaller	larger
Diameter	larger	smaller
Film boiling	increased swirl, reduced chance of film boiling	reduced swirl, increased chance of film boiling
Dry-out	increased evaporator pressure drop, increased chance of dry-out	reduced evaporator pressure drop, reduced chance of dry-out

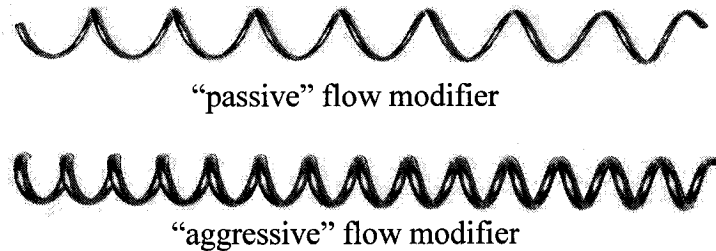


Figure 5.6 Comparison of different flow modifiers

Therefore, for a well-defined system where the following factors are known:

- expected heat load
- geometric constraints (heat pipe dimensions)
- operating parameters (ideal operating temperature)

an optimum flow modifier that balances these two opposing limitations to achieve maximum heat extraction capability must exist. At this point, a well-developed method to determine the configuration of such a flow modifier is lacking.

Chapter 6 Evaporator Modeling Methodology

6.1 Modeling of the Heat Pipe

In order to optimize the design of a heat pipe, a mathematical model is necessary in order to quantify how the design parameters affect the operation. A summary of the theory which describes the various sections of the heat pipe is given below.

- Condenser

Shell-and-tube condenser theory is well developed and can be examined in several heat transfer textbooks [44, 90, 91]. In application, the condenser of a heat pipe has very few design constraints because it can be located away from the heat source.

- Return Line

Theory on how to predict the flow of liquid working fluid from the reservoir down the return line and into the evaporator is given by the Bernoulli equation and is available in any standard fluid flow text book [38].

- Evaporator

The fact that the film boiling and dry-out limitations of McGill heat pipes are centered around the evaporator suggests that modeling of this section is the next logical step in understanding the overall functioning of the device.

Because of the geometric complexity of the evaporator, very few generalized film boiling theories can be applied. In 2003, Zhao developed an analytical model to predict the critical heat flux in McGill heat pipes [92], but this model still needs to be validated with experimental data.

Very little is known about the flow field within a heat pipe evaporator. Therefore modeling the pressure drop across the evaporator to understand dry-out is also very difficult. Zhao's air-water experiment gives some insight but the applicability of this work to an industrial heat pipe is questionable [89].

Given the limited success of investigating the heat pipe evaporator from an analytical and experimental perspective, a different approach was considered. The wide accessibility of powerful computers and the recent development of robust numerical techniques capable of solving complex multiphase systems enables the development of numerical models for systems such as the heat pipe evaporator.

6.2 Objective

The objective of the work presented in this chapter was to develop a methodology for the numerical modeling of a heat pipe evaporator.

Future work can focus on validating the model against experimental data. Refinements can then be made and semi-empirical relationships can be formulated. For example, the linear pressure drop of the evaporator can be related to the evaporator geometric configuration as well as to the operating parameters of the heat pipe.

Engineering guidelines can then be developed to optimize heat pipe design to the thermal and spatial requirements of a given application.

6.3 Evaporator Model

Similar to the technique used for the slag launder model discussed in Chapter 4, parameterization of the evaporator geometry, meshing, and boundary conditions was done. A software program was written which interfaces with the geometry building program (GAMBIT 2.1.6) and CFD solver (FLUENT 6.2.16). The capability of the software is described in the following sections:

6.3.1 Geometry

The evaporator geometry was broken down into eight fundamental parameters, summarized in Table 6.1 and Figure 6.1. The user simply changes these parameters to model a given heat pipe, and the software automatically builds the evaporator geometry. Figure 6.2 demonstrates some of the different heat pipes which can be modeled.

Table 6.1 Evaporator geometric parameters

Label	Description
EL	Total length of the evaporator
EID	Inner diameter of the evaporator
MPL	Length of pipe between the evaporator and the condenser
RLDD	Distance between return line discharge and evaporator bottom
RLID	Inner diameter of the return line
RLOD	Outer diameter of the return line
SD	Flow modifier diameter
SP	Flow modifier pitch

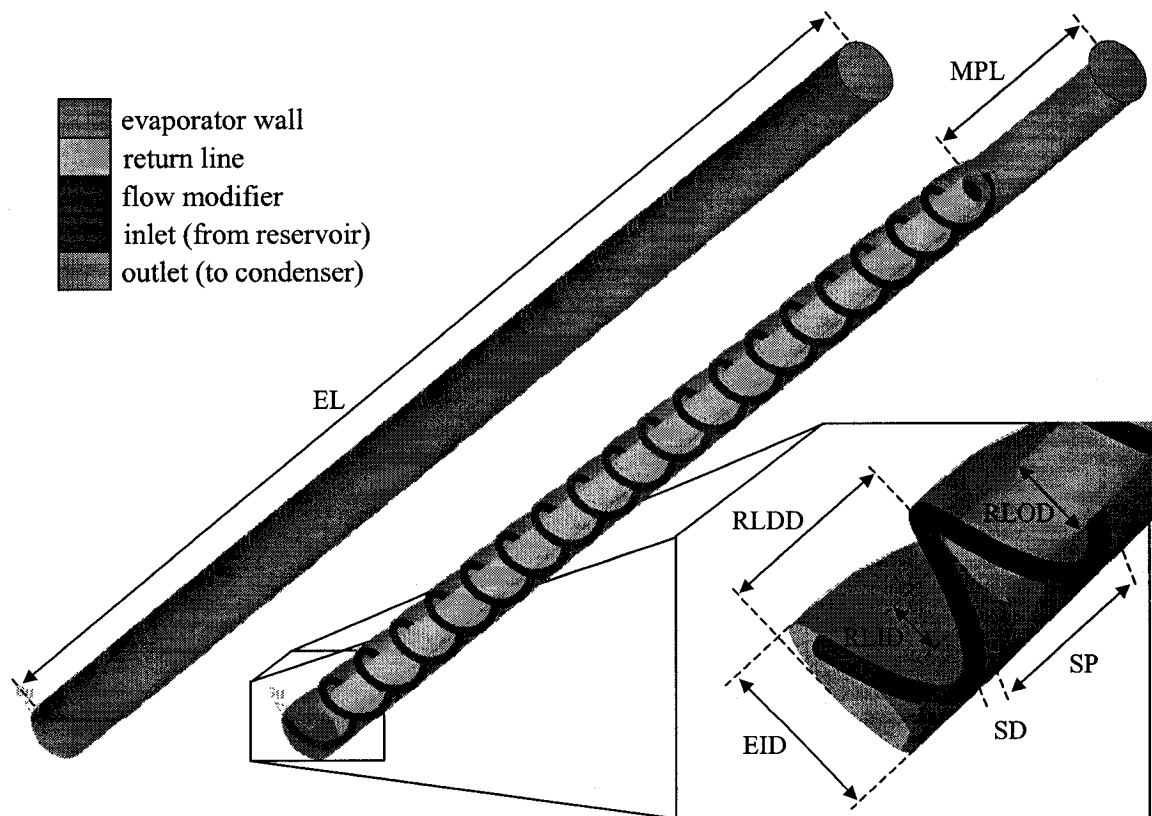


Figure 6.1 Geometric parameters of the evaporator

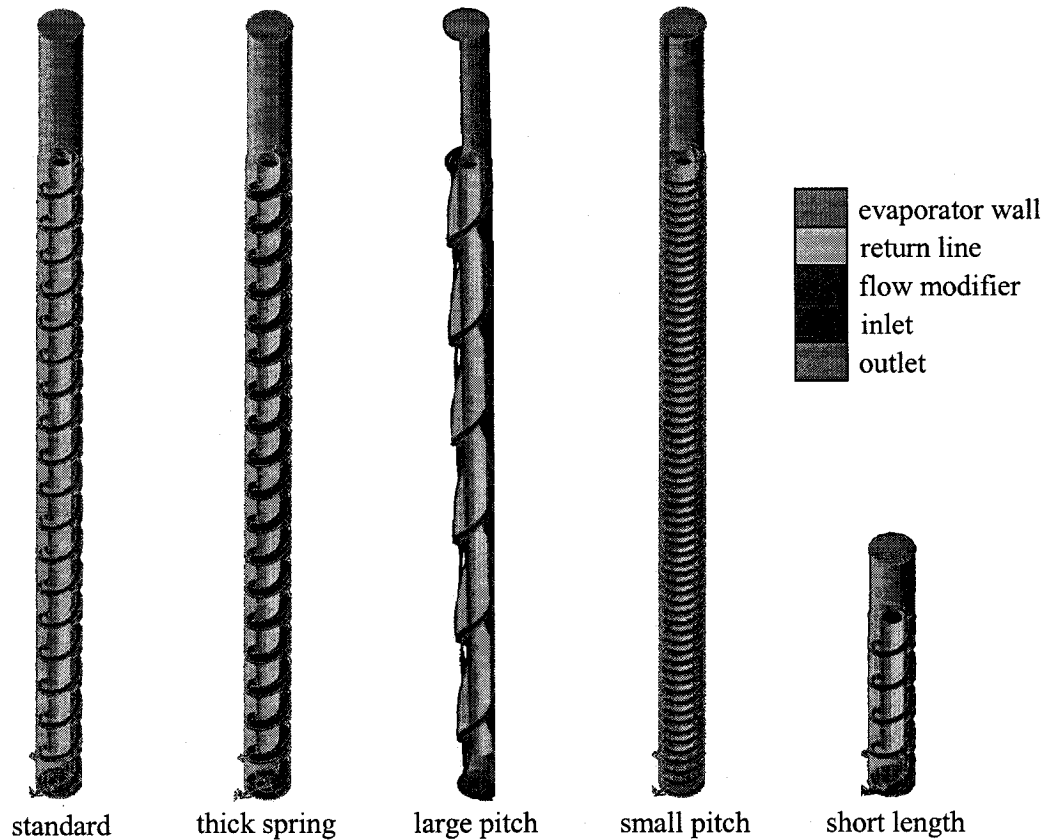


Figure 6.2 Examples of evaporator geometries

6.3.1.1 Limitations of the Evaporator Geometry Building Software

Heat pipes which have been fabricated thus far have particular geometric properties. For example, the evaporator and return line are cylinders, while the flow modifier is typically helical. These properties were used to simplify the geometry building software. However, doing so meant that the software has several limitations, which are described below:

- The evaporator and return line are cylindrical and co-axial

The evaporator and return line are most often made from pipe, and therefore this limitation should not normally be a problem. However, designs with unconventional geometries cannot be modeled using the software.

- The flow modifier must be a spring with a constant pitch and diameter

It is likely that future flow modifiers will be optimized to the flow field within the evaporator, which is not constant. Therefore, the flow modifiers will most likely not be strictly helical. Again, this is beyond the capability of the software.

- The return line inlet begins abruptly in the center of the evaporator

Perhaps the most significant simplification is that the return line inlet begins abruptly in the center of the evaporator. Normally, either the return line or the evaporator has an elbow-type joint which allows the separation of these two pipes. However, encoding this into the geometry building software would have greatly increased its complexity.

6.3.2 Meshing

The evaporator geometry building software also includes a comprehensive meshing subroutine. The importance of proper meshing becomes particularly important when modeling complex systems such as the heat pipe evaporator. The errors caused by approximating the governing equations as systems of linear equations are enhanced by non-ideal discretization, which can cause divergence.

6.3.2.1 Cell Types and Equiangle Skew

The most favourable type of cell is a cubic hexahedron. Of course, complex geometries cannot be filled with perfect cubes. Therefore, the hexahedrons must be skewed to accommodate curves, etc. The greater the skew of the cell, the more likely it is that larger errors are being generated during the solution procedure.

In areas of the domain where angles are acute, wedge-shaped cells can be placed to minimize the skew and join with adjacent hexahedral cells.

Excessively complex regions of the domain cannot be meshed using hexahedrons, and so tetrahedrons are used. Again, the greater the skew of the tetrahedron from a perfect pyramidal shape, the larger the error.

Equiangle skew is a value between 0 and 1 which gauges the skew (or deviation from ideality) of a cell. A value of 0 indicates an ideal cell. Equation (6-1) defines equiangle skew for hexahedral and tetrahedral cells:

$$\text{Equiangle skew} = \max \left[\frac{\theta_{\max} - \theta_e}{180 - \theta_e}, \frac{\theta_e - \theta_{\min}}{\theta_e} \right] \quad (6-1)$$

where θ_{\max} and θ_{\min} are the maximum and minimum angles of all the faces of the cell (°)

θ_e is 90° for a hexahedron and 60° for a tetrahedron

6.3.2.2 Evaporator Meshing

The meshing subroutine adapts itself to the helical structure of the evaporator, filling it with hexahedral cells that are close to ideal. Small regions around the flow modifier are meshed with wedge-shaped cells.

The return line and pipe joining the evaporator to the condenser are cylinders. Therefore the meshing subroutine meshes these regions with hexahedrons aligned with the evaporator axis. However, because the cells of the return line are misaligned with the cells from the evaporator, which are aligned with the helical flow modifier, tetrahedral cells are used to interface these two regions.

When considering the complexity of the evaporator domain, the meshing subroutine generates meshes of excellent quality. Figures 6.3 and 6.4 demonstrate the equiangle skew of a typical evaporator domain composed of 570,185 cells.

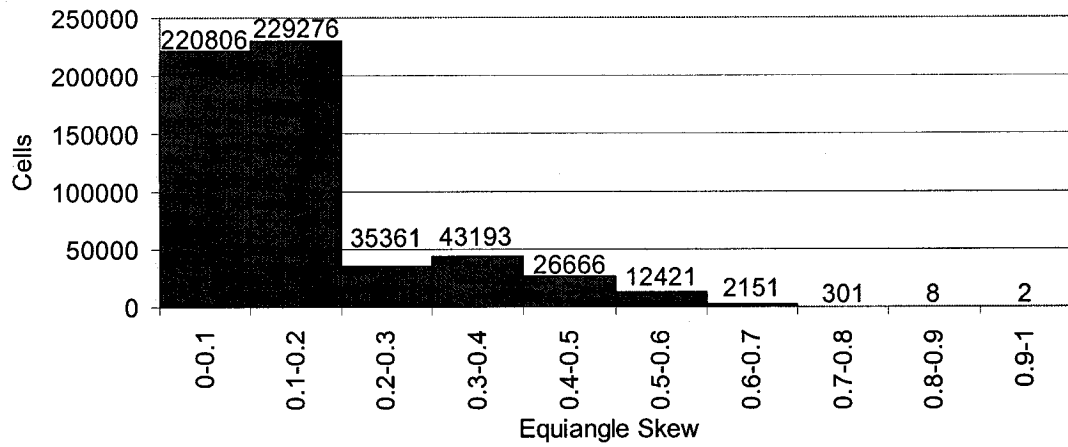


Figure 6.3 Typical equiangle skew distribution of the evaporator

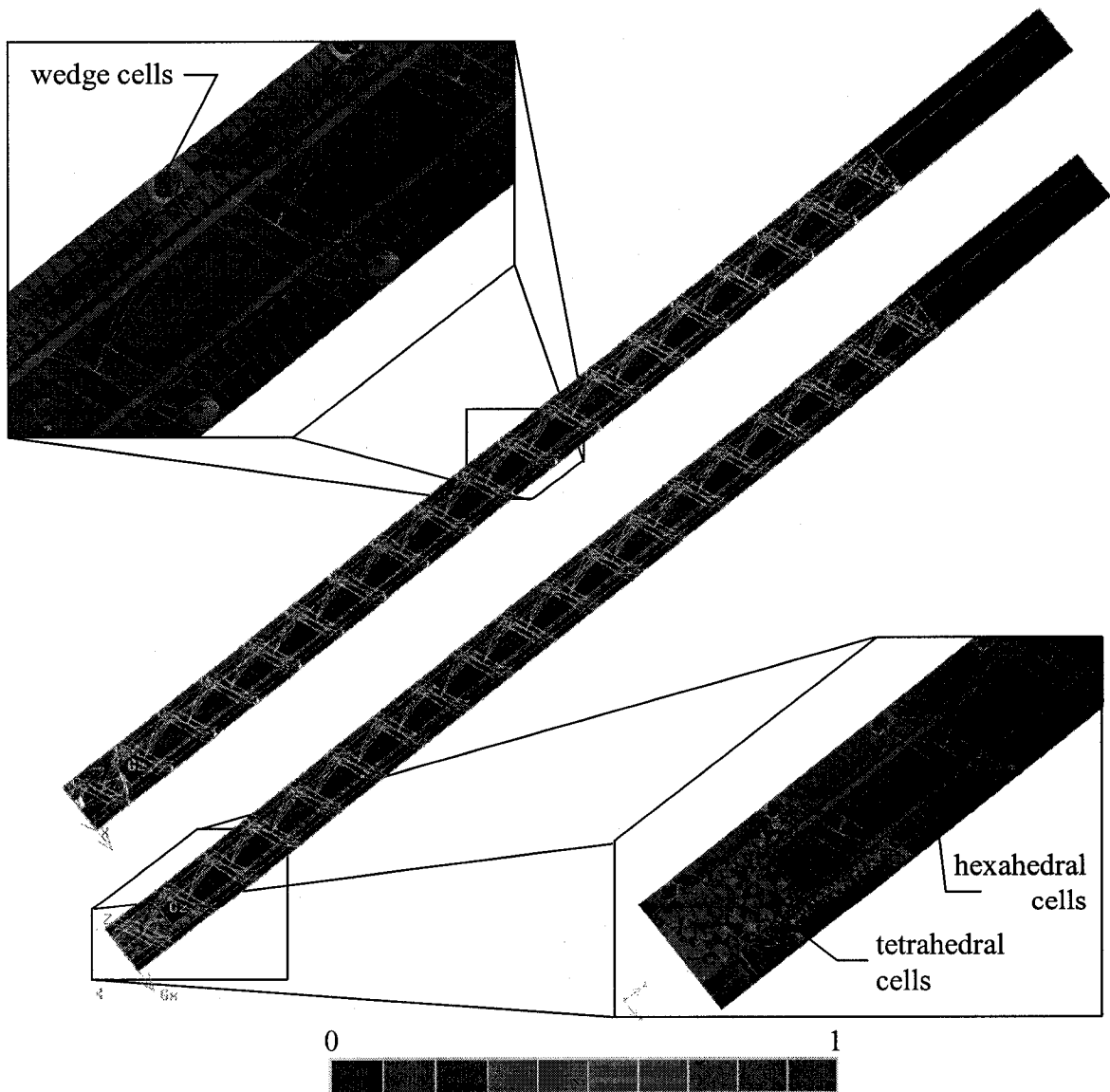


Figure 6.4 Equiangle skew of a typical evaporator mesh

6.3.3 Boundary Conditions

There are three types of boundary conditions used to simulate operating conditions in the evaporator: a pressure inlet condition, a pressure outlet condition, and several wall conditions. Refer back to Figures 6.1 and 6.2 for the locations of the inlet and outlet.

The pressure applied to the outlet approximates the pressure within the condenser. Therefore, this pressure can be assumed as the heat pipe operating pressure, which is a function of the saturation pressure of the working fluid. For example, a water-based heat pipe operating at 100°C will be operating at a pressure of one atmosphere. Therefore the outlet can be set at a pressure of 101.3 kPa. The temperature of the liquid should also be set to the operating temperature (or slightly less to simulate the undercooling in the reservoir).

The pressure inlet condition is applied to the top-most point of the return line in the domain. It is assumed that the return line is completely filled with liquid working fluid. Therefore the inlet pressure, P_{inlet} , can be approximated as the following equation:

$$P_{inlet} = P_{outlet} + \rho_{liquid} g \Delta h \quad (6-2)$$

where P_{outlet} is the pressure applied at the outlet boundary (Pa)

ρ_{liquid} is the density of the liquid working fluid (kg/m^3)

$\bar{\rho}_{evaporator}$ is the average density of the fluid within the evaporator (kg/m^3)

g is gravitational acceleration (9.8 m/s^2)

Δh is the vertical height between the return line inlet and reservoir (m)

The density of the liquid and vapour are a function of the heat pipe operating temperature, which can be assumed as a constant. Equation (6-2) assumes the evaporator is vertical, with gravity acting along the axis of the return line.

The return line, the flow modifier, and the inner evaporator wall surfaces are set to wall boundary conditions, which signifies that mass cannot be transported across them.

A heat flux distribution can be imposed on the evaporator wall to simulate an applied heat load. Some of the heat flux distributions determined from the applications in previous chapters can be used, for example Figure 4.9 of Chapter 4.

6.3.4 Material Properties

The material properties of the liquid and vapour (density, viscosity and thermal conductivity) are functions of the operating temperature of the heat pipe. To simplify the problem, they can be assumed as constant, as the temperature inside the heat pipe varies very little.

6.3.5 Governing Equations

The mass, momentum, and energy transport equations are used for this simulation. Because the velocities within the evaporator are relatively large, turbulent modeling is necessary.

Turbulence is a fundamentally transient phenomenon, and can be described as random variations in the viscosity of a fluid. The causes of turbulence are still not completely understood. However, several models are available which can accurately simulate turbulence at steady-state, depending on the application. Two-equation models have become the standard for engineering, the most common of which is the k - ε model, where k is the turbulent kinetic energy (m^2/s^2) and ε is the turbulent dissipation rate (m^2/s^3). Because of their simplicity and years of validation, k - ε models are recommended for the evaporator model.

Literature indicates that the “realizable” k - ε model performs well for applications with swirling flows and significant body forces (cyclones). Therefore this particular turbulence model should be used [93].

The computational limitation of machines available to most engineers necessitates that the mesh resolution be too coarse to resolve individual droplets of liquid or vapour. Therefore, mass transfer to simulate boiling must be modeled “macroscopically” in a manner similar to turbulence.

Boiling is presently a field of active research. Therefore there are only a handful of numerical models that simulate nucleate boiling and its effects on flow variables. One such model is the RPI model developed in 1967 for cooling systems in the nuclear power industry [94, 95]. However, these models are typically developed for a particular application, and are not computationally robust (i.e. easily lead to divergence). In addition, the vapor/liquid droplet diameter is unknown and must be calibrated to a particular application by experimentation.

6.3.6 Multiphase Models

There are two multiphase models which can be used to simulate the two-phase flow within the evaporator: the mixture model and the Eulerian model.

The mixture model considers the two fluids as a single phase with the physical properties averaged according to the respective volume fractions. Differences in the velocities of the two phases are accommodated for using a concept referred to as “slip velocity”.

The Eulerian model treats the two phases separately. Therefore two sets of mass, momentum and energy transport equations must be solved, which increases the complexity of the simulation.

The mixture model is simple, and is therefore more stable and is more rapid to converge. However, the Eulerian model is more accurate, but can be difficult to converge, and is computationally much more expensive. Further details about multiphase modeling are available in the literature [91].

6.3.7 Solution Procedure

The model described in this section is extremely complex from a CFD perspective. Therefore the solution must be attained in several steps in order to avoid divergence. The following solution procedure is recommended:

- Single-phase flow field
- Two-phase flow field
- Turbulence model activated
- Energy equation and boiling model activated

However, even with the above procedure, the under relaxation factors (i.e. step sizes) need to be very small to avoid divergence. This leads to extremely long solution procedures, which become prohibitively long for most personal computers.

6.3.8 Convergence

Convergence of the model can be checked through the use of several monitors:

- The net mass flow rate across the inlet and outlet boundaries should be zero
- The mass flow rate of vapour, liquid, and the mixture across the outlet boundary should converge
- The mass flow rate of liquid across the inlet boundary should converge

6.4 Results

The solution time required to fully solve a heat pipe evaporator model made it impossible to obtain results in a reasonable time frame. However, results for simplified systems were obtained in order to demonstrate the operability of the model.

6.4.1 Single Phase Flow

A typical evaporator geometry was modeled using single-phase flow. A fluid with a density of 500 kg/m^3 and a viscosity averaged between that of water and water vapour at 100°C was used ($147\mu\text{Pa}$). A pressure differential of $150,000 \text{ Pa}$ was imposed on the inlet and outlet boundaries.

Figure 6.5 presents the pressure, turbulence and velocity contours of the simulation. The velocities inside the return line are the greatest, reflecting the relative cross-sectional area. The velocities within the evaporator itself are of the order of 140 km/hr .

Under these conditions, the most turbulent region is at the return line discharge. In a heat pipe evaporator, this may not be the case, as a relatively small volumetric flow rate of liquid is discharged in this region. The greatest velocities would be attained at the top of the evaporator.

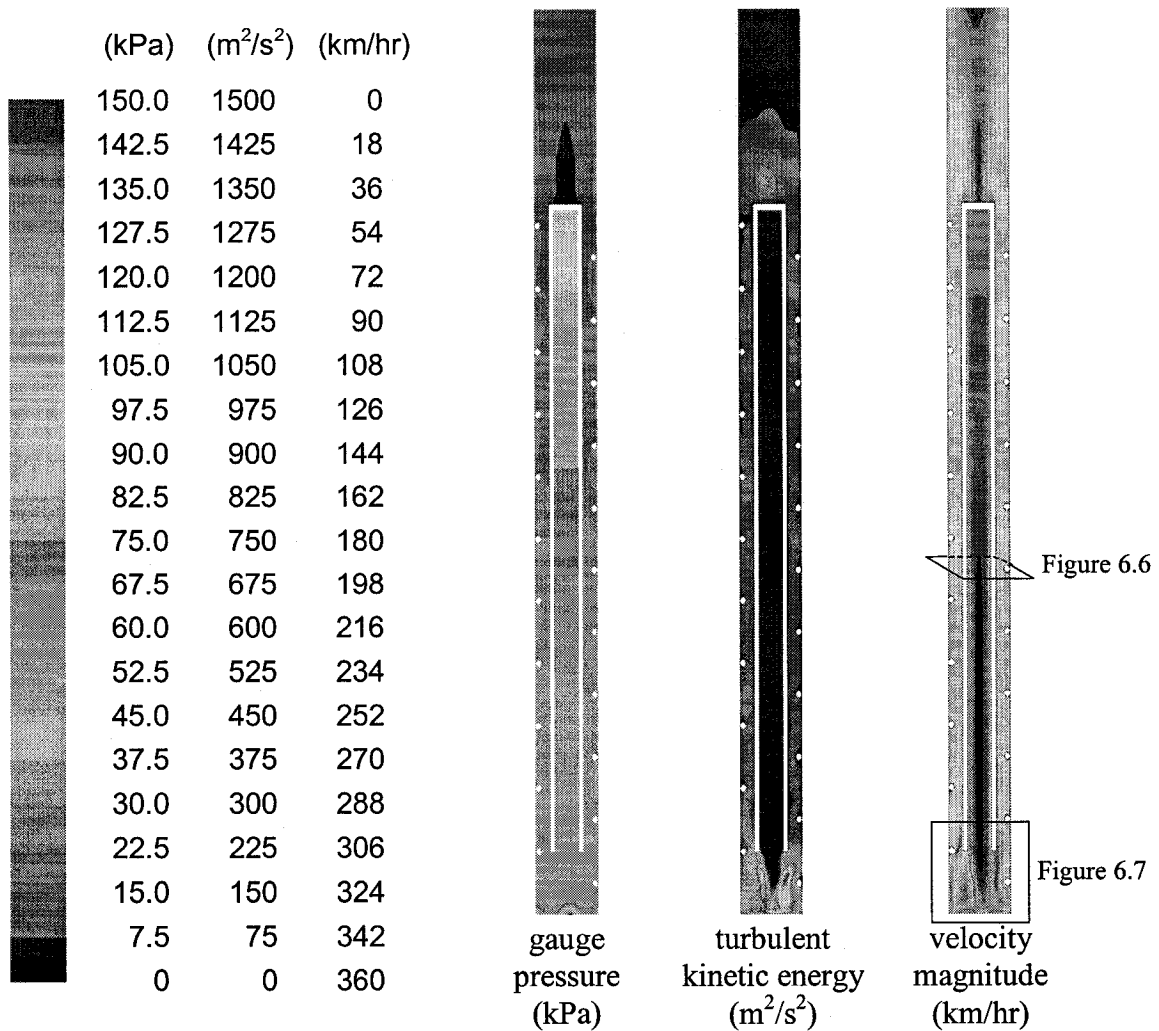


Figure 6.5 Gauge pressure, turbulent kinetic energy, and velocity magnitude contours of the evaporator (single phase flow)

Some turbulence is also present above the return line, as a result of the abrupt change in geometry. Very little turbulence is observed in the evaporator in the region of the flow modifier. This is partially due to the structured flow which develops as a result of the flow modifier.

Figure 6.6 presents the velocity field across a transverse cross-section of the evaporator, and clearly indicates the rotational component of the flow. The largest velocity occurs near the flow modifier, where the area through which fluid can flow is constricted.

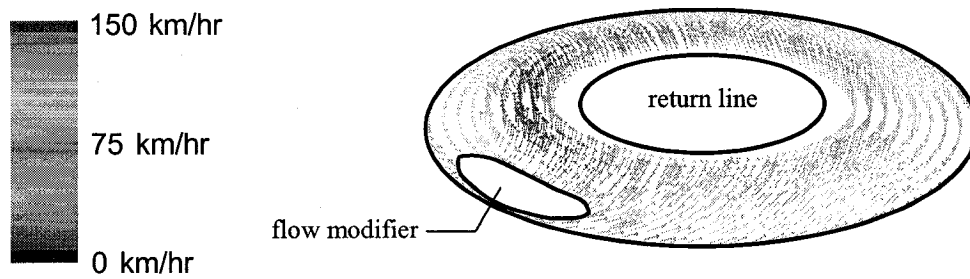


Figure 6.6 Cross-sectional slice of the evaporator velocity field

The rotational component of the flow is more pronounced near the outer edge, whereas the greatest velocities are observed towards the inner part of the annulus. Therefore the modeling supports the theory that the flow resistance due to the flow modifier causes a helically-structured velocity field to develop in a heat pipe evaporator.

By comparison, Figure 6.7 presents the velocity field near the return line discharge. The flow is unstructured, and the presence of several eddies is observed.

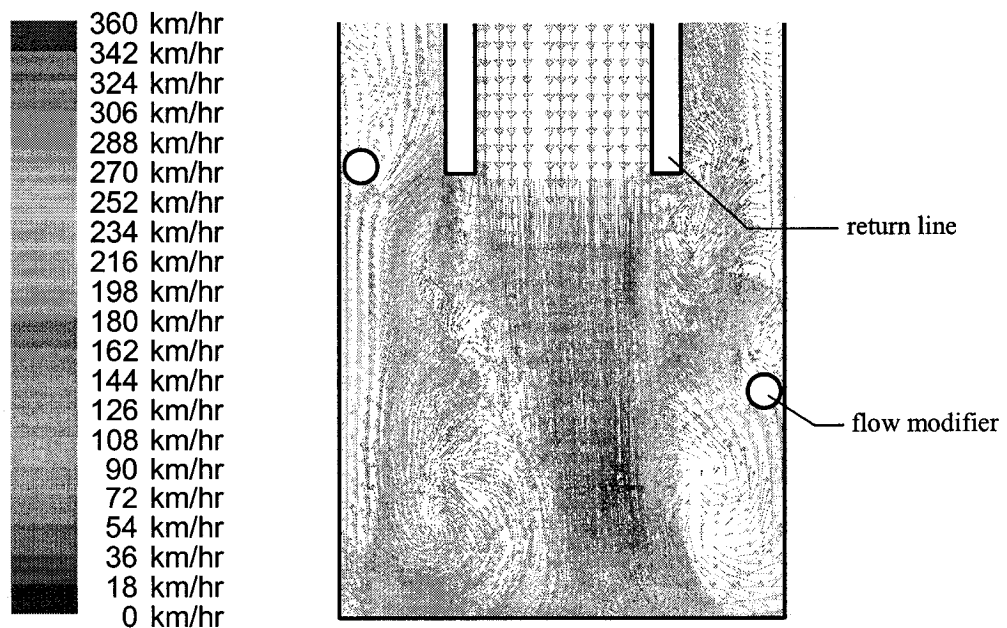


Figure 6.7 Axial slice of the return line discharge velocity field

6.4.2 Two-phase flow

The mixture model was used to simulate two-phase flow within the evaporator. A mixture of water (70%) and steam (30%) are injected from the return line inlet. The pressure difference between the inlet and outlet boundaries was set at 140 kPa, generating velocities in the evaporator of approximately 140km/hr. In order to increase the stability and speed of convergence, a shorter evaporator geometry was used, and turbulence was not considered. Figure 6.8 indicates the phase distributions contours within the evaporator for assumed bubble diameters of 0.1 mm and 0.4 mm.

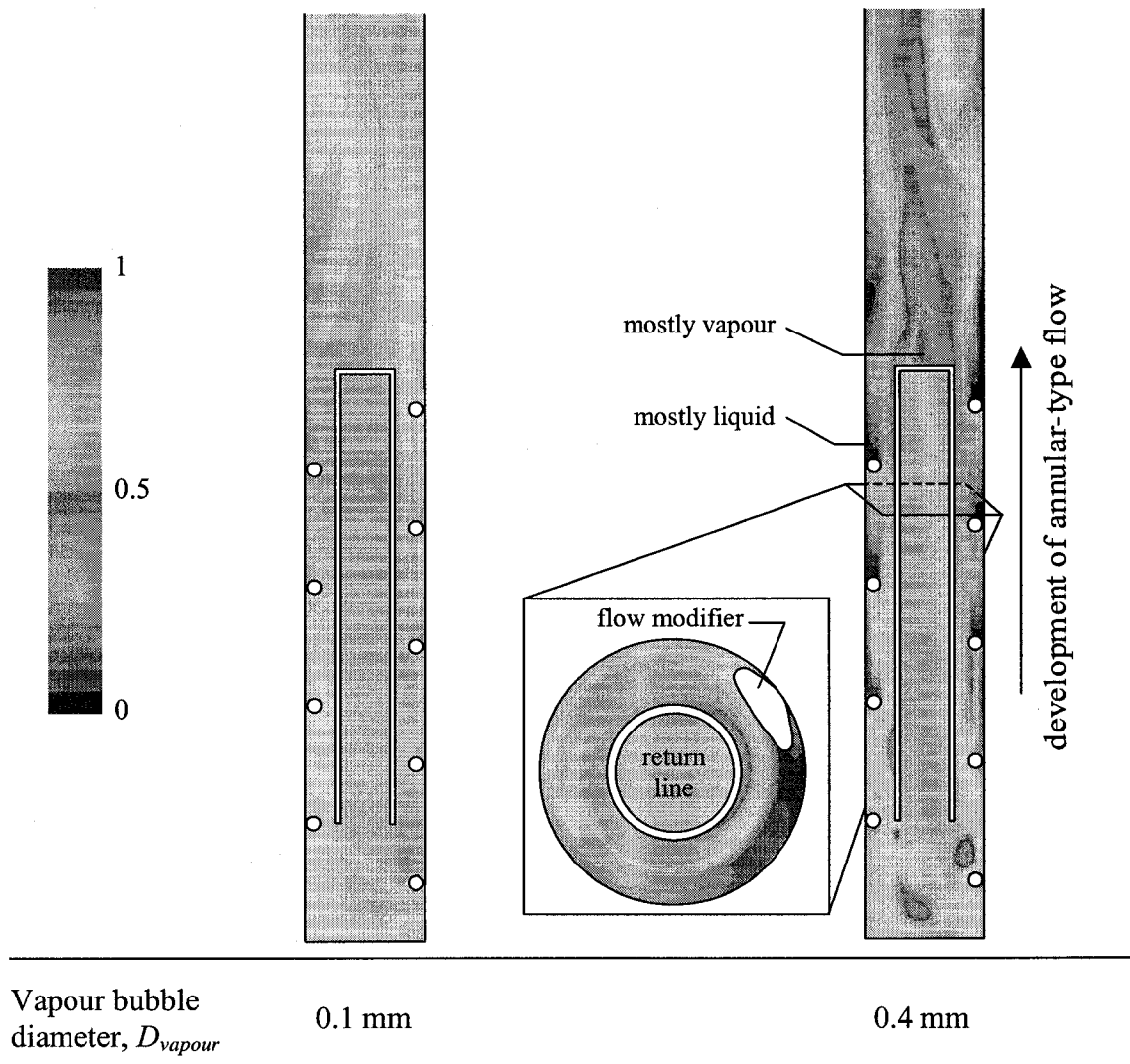


Figure 6.8 Contours of liquid volume fraction in the evaporator

The centrifugal forces generated by the swirling flow separate the liquid and vapour. Note that a smaller vapour bubble diameter signifies that the ratio of drag forces to body forces is larger. Therefore the centrifugal forces are more prevalent in the simulation with a larger vapour bubble diameter. This can be seen as more phase separation occurs for this simulation, stabilizing annular-type flow in the upper region of the evaporator. The lower regions have less separation as the structured helical flow has not fully developed there. The transverse section of the $D_{vapour} = 0.4$ mm simulation indicates that there is a wide difference in the phase distribution along the outer circumference. This suggests that the flow modifier configuration does not provide uniform wetting of the evaporator surface. The axial cross-section suggests that decreasing the pitch of the helix may provide better wetting of the evaporator inner wall, particularly directly below the flow modifier, where less liquid is present.

In summary, these results support the theory that the centrifugal forces generated by the flow modifier propel liquid against the inner evaporator wall, helping establish an annular flow pattern which raises the critical heat flux.

These results also suggest that future flow modifiers should be more aggressive in the lower regions of the evaporator where the helical flow is more difficult to form. The upper region of the evaporator does not need a flow modifier which is as aggressive, as the flow pattern is already well developed.

Distributing the flow modifier properties in this manner will maximize the wetting of the evaporator to avoid film boiling, while minimizing the flow resistance along the evaporator to avoid dry-out.

Chapter 7 Conclusions

The conclusions from the experimental and modeling results presented in this thesis are summarized as follows.

1. Heat Pipe Cooling of a Copper Tapblock

- A single heat pipe was able to provide 135 kW of cooling under steady-state conditions, and 142 kW under transient conditions.
- The overall maximum cooling attained under steady-state conditions (both heat pipes) was 200 kW. It was not possible to test the system at greater heat loads due to the limited heating efficiency of the burner.
- Modeling of the experimental conditions indicates that the maximum heat flux applied to the evaporator was in the order of approximately 2.4 MW/m^2 .
- CFD modeling of upset conditions at a blast furnace indicate that the current system would perform effectively if installed, as the heat fluxes were less than those successfully tested.
- The cooling water flow rates required to cool the condenser were a fraction (between 4% to 12%) of the cooling water flow rates which would be required using conventional cooling technology.
- The effluent cooling water from the condensers was generated at temperatures of up to 85°C . These temperatures are large enough to allow the effluent to be used as hot water in a metallurgical plant.

2. Heat Pipe Cooling of a Slag Launder

- Modeling of the operating conditions at the Hoboken blast furnace indicated an operating heat load of 22-30 kW would be applied to a copper launder. Testing showed that the heat pipe cooling system performed beyond these requirements, being able to dissipate over 65 kW of heat at steady-state. This indicated that the cooling system design was adequate for the application.
- The modeling done to analyze the experiments indicated that a maximum heat flux of 880 kW/m^2 was applied to the evaporators with no indication of film boiling.
- Transient jumps as high as 40 kW in the applied heat load were imposed without encountering operational difficulties.
- Cast-in monel evaporators were used for the launder. However, modeling of the experimental conditions indicates that copper-only equipment should be considered in the future. Doing so will significantly reduce the slag launder operating temperature under industrial operating conditions (from 100-220°C to 100-174°C).

3. Heat Pipe Limitations

- The results from having achieved dry-out (tapblock tests) suggest that the flow resistance within the evaporator is the main cause. It was demonstrated that reducing the vapour velocities within the heat pipe can increase the circulation of liquid working fluid and alleviate dry-out. This can be accomplished by increasing the operating temperature, which increases the vapour density within the heat pipe.
- Although the latest heat pipe designs have shown that the critical heat flux has been greatly raised over classical heat pipes, film boiling can still be encountered under extreme conditions. This was shown in the slag launder impact tests, where film boiling was achieved when the copper launder was preheated to over 500°C.

4. Evaporator Modeling Methodology

- Based on the results, the evaporator geometry and meshing software have been successfully developed. However, more simulations are needed which include Eulerian multiphase models together with boiling and turbulence. As more powerful computers are made available, the solution time considerations, which limited the present work, will be within reach.
- Future work should focus on systematically simulating dozens of evaporator geometries over a range of operating conditions, and establish relationships between the applied heat load, operating conditions, and functionality of the heat pipe. Doing so will lead to improvements in heat pipe technology.
- Modeling of the heat pipe evaporator has shown the impact the flow modifier has on the flow pattern, causing a structured helical motion and stabilizing the annular flow regime.
- Boiling models are required that have been validated for a wider range of applications. The CFD iterative solution procedures should be improved to increase the stability of simulations that incorporate boiling. As well, models to predict the droplet/bubble size of the working fluid phases are needed, as this is important in calculating the drag forces acting within the system.

Statement of Originality

At the start of the research presented in this thesis, McGill heat pipe technology was in its early stages of development, but showed great potential as a thermal management solution. The original contributions from this work can be separated into two categories.

Firstly, through the application of heat pipes to full-scale equipment used in pyrometallurgical furnaces, such as the tapblock and launder, a distinct cooling technology has been developed and demonstrated as a viable alternative for the demanding cooling needs of the metals industry.

Secondly, a greater understanding of the capabilities and limitations of heat pipe technology has been gained. In addition, a methodology for modeling the heat pipe itself has been developed, which gives some direction as to where future research should be concentrated.

These contributions are summarized as follows:

1. A novel cooling system for copper tapblocks and launders

The tapblock and slag launder pilot tests are the first successful full-scale tests of water-based McGill heat pipe technology.

The heat load attained in the tapblock test is an order of magnitude greater than previous heat loads extracted into a single water-based McGill heat pipe (142 kW compared to 15 kW). Modeling of the experimental conditions revealed a maximum heat flux of 2.4MW/m^2 , which is the greatest to date with a water-based McGill heat pipe. Previous tests on lab-scale systems were able to generate maximum heat fluxes of approximately 1.5MW/m^2 .

The cooling systems that were designed and built are the first viable water-based systems based on boiling which can be applied to thermally-intense metallurgical applications. The tests demonstrated exceptional responsiveness to changing heat loads, in addition to

an elevated heat flux capability which is comparable to forced convection water cooling systems.

The slag launder cooling system is the first full-scale heat pipe system which successfully incorporated horizontal heat pipes. In addition, this system was the first to include multiple evaporators feeding a single condenser. The validation of this configuration leads to the possibility of constructing much larger heat pipe cooling systems in the future.

The first liquid level monitor was developed for the launder cooling system. The monitor is necessary in monitoring the evaporator void fraction and is useful in gauging the circulation of working fluid within the heat pipe.

Both the tapblock and launder cooling systems are the first water-efficient cooling systems available for high-intensity furnace applications.

2. Development of McGill heat pipe theory

The experimental results together with the numerical modeling have contributed to the validation and further development of McGill heat pipe theory, which explains the exceptional heat extraction capabilities of the device, as well as its limitations.

The complexity of the heat pipe signifies that analytical models are very difficult to derive. Therefore, a methodology based on numerical modeling was developed to investigate the relationship between a heat pipe's configuration and its operation. This methodology includes a comprehensive geometry and mesh creation program which can be used in conjunction with commercial CFD software.

The modeling results confirmed the rotational component of the flow due to the presence of the flow modifier. The ensuing centrifugal forces propel liquid towards the evaporator wall, and induce an annular-like flow pattern which is believed to raise the CHF.

The importance of operating at the proper void fraction to obtain a favourable flow pattern was shown during the launder impact tests. The experimental data indicated that excessively refluxing the evaporator with liquid working fluid can lead to the flooding of

the evaporator. When the void fraction is too low, the flow resistance is large, and obtaining a helical flow pattern is difficult and can lead to film boiling.

Dry-out was phenomenon of mostly academic interest in water-based laboratory-scaled heat pipes. However, the tapblock tests showed that this limitation is a major concern in full-scale designs. The experimental data supports the theory that the flow resistance across the evaporator can be considerable at large vapour velocities. The resulting pressure buildup at the bottom of the evaporator can oppose the return line pressure head sufficiently to cause evaporator dry-out.

References

1. C. Zhang, F. Mucciardi, and J.E. Gruzleski, "Heat Pipe Cooling of Permanent Mold Castings of Aluminum Alloys", AFS Transactions, May 2002, Vol. 110, pp. 435-448.
2. C. Zhang, F. Mucciardi and J.E. Gruzleski, "Controlled Cooling of Permanent Molds in the Casting of Aluminum", Light Metals Sym. of MetSoc, CIM, Aug. 2001, pp. 431-441.
3. Wise, D.A., et al., "Blast Furnace Taphole Repair at AK Steel Middletown Works", Steel Technology, AISE, February 2000, pp. 47-53.
4. Veenstra, R, Voermann, N., Wasmund, B., "Prototype Metal Tap Block Design", Pyrometallurgical Operations, Environment, and Vessel Integrity Symposium in Non-Ferrous Smelting Proceedings, Vol. 3, CIM, 1997, pp. 595-607.
5. Joubert, H., Leong, B., and Tomlinson, R., "Innovative Taphole and Launder Design Using Computer Assisted Engineering Tools", (Paper presented at the Extractive Metallurgical Processing Symposium on Advances in Furnace Integrity, TMS Annual Meeting, 2006).
6. Van Laar, K., "The Taphole: The Heart of the Blast Furnace", The Taphole – The Blast Furnace Lifeline: Design/Maintenance/Operating Practices Symposium Proceedings, Department of Materials Science and Engineering, McMaster University, 2001, pp. 1-21.
7. Walsh, E., et al., "Amanda Taphole Repair", Iron and Steel Engineer, AISE, September 1999, Vol. 76, No.9, pp. 31-35.
8. N. Voermann et al., "Furnace Cooling Design for Modern High-Intensity Pyrometallurgical Processes", 4th International Conference on Copper 99 - Cobre 99, Vol. V: Smelting Operations and Advances, 1999, pp. 573-582.

9. Guthrie, R., "A Thermal Analysis of Tuyere Performance in Iron Blast Furnaces", AIME Ironmaking Proce., Vol. 82, pp. 587-592.
10. Odekirk, R. "Furnace Fails at Kennecott", The Salt Lake Tribune, January 11th, 1999, pp. B2.
11. Edwards, B., Hutchinson, S., "Emergency Taphole Repair at No. 4 Blast Furnace at Stelco Hilton Works", The Taphole – The Blast Furnace Lifeline: Design/Maintenance/Operating Practices Symposium Proceedings, Department of Materials Science and Engineering, McMaster University, 2001, pp. 273-290.
12. Nightingale, R.J., Rooney, B.J., "Damage to Taphole and Sidewalls of Port Kembla No. 5 Blast Furnace – Causes and Remedies", The Taphole – The Blast Furnace Lifeline: Design/Maintenance/Operating Practices Symposium Proceedings, Department of Materials Science and Engineering, McMaster University, 2001, pp. 294-307.
13. DiCosimo, J.E., "Replacement of the South Iron Notch at Lake Erie Steel's Blast Furnace", The Taphole – The Blast Furnace Lifeline: Design/Maintenance/Operating Practices Symposium Proceedings, Department of Materials Science and Engineering, McMaster University, 2001, pp. 311-321.
14. J. Janz, et al., "Installation of Copper Staves in Blast Furnace Hearths and their Influence on Refractory Design", AISE Steel Technology, 2003, pp. 42-51.
15. Karjalahti, T., Swanljung, J., "Taphole Design and Casthouse Practice on the High Efficiency Blast Furnaces at Rautaruukki Steel, Raahel", The Taphole – The Blast Furnace Lifeline: Design/Maintenance/Operating Practices Symposium Proceedings, Department of Materials Science and Engineering, McMaster University, 2001, pp. 22-34.

16. A. Daenuwy et al., "Development of Electric Furnace Design and Operation and P.T. Inco (Indonesia)", (Paper presented at the International Symposium on Trace Metals and Furnace Practices in Non-Ferrous Pyrometallurgy, Met. Soc. of CIM, 1992, available at electronic address: <www.hatch.ca/technologies/Articles>, August 2006).
17. J. Sarvinis, et al., "Improvements to BHP Hartley Platinum Smelting Furnace", 4th International Conference on Copper 99 - Cobre 99, Vol. V: Smelting Operations and Advances, 1999, pp. 613-628.
18. Shinotake, A., "Liquid Flow Analysis in Blast Furnace Hearth Considering Taphole Location", The Taphole – The Blast Furnace Lifeline: Design/Maintenance/Operating Practices Symposium Proceedings, Department of Materials Science and Engineering, McMaster University, 2001, pp. 83-101.
19. Brunnbauer, G., et al., "Tapping Practice at Voest Alpine Stahl Linz", The Taphole – The Blast Furnace Lifeline: Design/Maintenance/Operating Practices Symposium Proceedings, Department of Materials Science and Engineering, McMaster University, 2001, pp. 178-186.
20. Estrabillo, L.S., "Taphole Management Practices at Lake Erie Steel", The Taphole – The Blast Furnace Lifeline: Design/Maintenance/Operating Practices Symposium Proceedings, Department of Materials Science and Engineering, McMaster University, 2001, pp. 233-242.
21. Niknejad, NICICO, electronic correspondences, July 2003.
22. Steigauf, C., Storm, L., "Optimization of Taphole Construction, Maintenance, and Casting Practice for High Productivity, High Reliability, and Long Campaign Life", The Taphole – The Blast Furnace Lifeline: Design/Maintenance/Operating Practices Symposium Proceedings, Department of Materials Science and Engineering, McMaster University, 2001, pp. 37-45.

23. De Pagter, J., Molenaar, R., "Taphole Experience at BF6 and BF7 of Corus Strip Products Ijmuiden", The Taphole – The Blast Furnace Lifeline: Design/Maintenance/Operating Practices Symposium Proceedings, Department of Materials Science and Engineering, McMaster University, 2001, pp. 107-125.
24. Pertruccelli, A., et al., "Taphole Design, Casting Equipment, and Operating Practices at Dofasco", The Taphole – The Blast Furnace Lifeline: Design/Maintenance/Operating Practices Symposium Proceedings, Department of Materials Science and Engineering, McMaster University, 2001, pp. 128-147.
25. J. Merry, J. Sarvinis, N. Voermann, "Designing Modern Furnace Cooling Systems", Journal of Metallurgists, February 2000, pp. 62-64.
26. M.L. Trapani, A.K. Kylo, N.B. Gray, "Improvements to Taphole Design", Sulfide Smelting Symposium, 2002 TMS Annual Meeting, 2002, pp. 339-348.
27. A.G. Matyas, et al., "Application of New Technology in the Design of High-Power Electric Smelting Furnaces", (Paper presented at the International Symposium on Non-Ferrous Pyrometallurgy, Trace Metals, Furnace Practices and Energy Efficiency, Met. Soc. Of CIM, 1992, available at electronic address: <www.hatch.ca/technologies/Articles>, August 2006)
28. K.M. Donaldson, et al., "Design of Refractories and Bindings for Modern High-Productivity Pyrometallurgical Furnaces", (Paper presented at the International Symposium on Trace Metals and Furnace Practices in Non-Ferrous Pyrometallurgy, Met. Soc. of CIM, 1992, available at electronic address: <www.hatch.ca/technologies/Articles>, August 2006).
29. S. de Vries et al., "Novel DC Furnace Design for Smelting Nickel and Cobalt Bearing Concentrate from Spent Alumina Catalyst", Recycling of Metals and Engineered Materials, TMS, 2000, pp. 773.

30. Ostlund, P., "Developments in Taphole Design, Tapping Methods and Refractory Repair over the Last Twenty Years at SSAB Oxelosund", The Taphole – The Blast Furnace Lifeline: Design/Maintenance/Operating Practices Symposium Proceedings, Department of Materials Science and Engineering, McMaster University, 2001, pp. 322-340.
31. M.L. Trapani, et al., "Instrumentation of a Production Taphole", EPD Congress, TMS Annual Meeting, 2003, pp. 1095-1104.
32. Black, B., Bobek, J., "Improvements in Taphole Life and Casting Performance at Ispat Inland's No. 7 BF", The Taphole – The Blast Furnace Lifeline: Design/Maintenance/Operating Practices Symposium Proceedings, Department of Materials Science and Engineering, McMaster University, 2001, pp. 156-177.
33. Tanzil, F.W.B.U., et al., "The Application of Novel Techniques and New Sensors to Taphole Management Practice at Port Kembla No. 6 Blast Furnace", The Taphole – The Blast Furnace Lifeline: Design/Maintenance/Operating Practices Symposium Proceedings, Department of Materials Science and Engineering, McMaster University, 2001, pp. 193-209.
34. Altland, R., Grabietz, G., Pethke, J., "Taphole Design and Experience", The Taphole – The Blast Furnace Lifeline: Design/Maintenance/Operating Practices Symposium Proceedings, Department of Materials Science and Engineering, McMaster University, 2001, pp. 211-230.
35. Entwistle, J.W., "The Taphole: a Unique System", The Taphole – The Blast Furnace Lifeline: Design/Maintenance/Operating Practices Symposium Proceedings, Department of Materials Science and Engineering, McMaster University, 2001, pp. 243-258.
36. Ballewski, T., et al., "New Improvements of the Taphole Area at Thyssenkrupp Stahl", The Taphole – The Blast Furnace Lifeline: Design/Maintenance/Operating Practices Symposium Proceedings, Department of Materials Science and Engineering, McMaster University, 2001, pp. 48-66.

37. Nukiyama, S., "The Maximum and Minimum Values of the Heat Q Transmitted from Metal to Boiling Water under Atmospheric Pressure," Journal of the Japanese Society of Mechanical Engineers, 37, pp. 367-374, 1934.
38. Incopera, F.P. and DeWitt, D.P., "Fundamentals of Heat and Mass Transfer", John Wiley and Sons, 2002.
39. Kutateladze, S.S., "On the Transition to Film Boiling Under Natural Convection," Kotloturbostroenie, No. 3, pp. 10-12, 1948.
40. Zuber, N., "On the Stability of Boiling Heat Transfer," Trans. ASME, Vol. 80, pp. 711-720, 1958.
41. Lienhard, J.H., Dhir, V.K., and Riherd, D.M., "Peak Pool Boiling Heat Flux Measurements on Finite Horizontal Flat Plates," Journal of Heat Transfer, 95, 477-482, 1973.
42. Van Stralen, S., and Cole, R., "Boiling Phenomena", McGraw-Hill/Hemisphere, New York, 1979.
43. Lienhard, J.H., and Eichhorn, R., "Peak Boiling Heat Flux on Cylinders in a Cross Flow," International Journal of Heat and Mass Transfer, 19, pp. 1135-1141, 1976.
44. Tong, L.S., "Boiling Heat Transfer and Two Phase Flow", Wiley, New York, 1965.
45. Gaugler, R.S., "Heat transfer device," US Patent No 2350348, June 6th 1944.
46. Grover, G.M., "Evaporation-condensation heat transfer device," US Patent 3229759, January 18th 1966.
47. Faghir, A., "Heat Pipe Science and Technology," Taylor & Francis, Washington, DC, USA, 1995.

48. _____, "Refrigerant History." Refrigeration Historical Information Page. Electronic address: <<http://www.trane.com/commercial/issues/environment/cfc6b.asp>> (June, 2003).
49. Koepfer, C., "Drilling Dry with a Heat Pipe", Modern Machine Shop, pp. 56-57, May, 2003.
50. Peterson, G.P., "An Introduction of Heat Pipes," John Wiley and Sons, Inc., New York, USA, 1994.
51. Dunn, P.D., Reay, D.A., "Heat Pipes," 4th Edition, Elsevier Science Ltd, Oxford, England, 1994.
52. Chi, S.W., "Heat Pipe Theory and Practice, A Sourcebook," Taylor & Francis, Washington DC, USA, 1976.
53. Silverstein, C.C., "Design and Technology of Heat Pipes for Cooling and Heat Exchange," Taylor & Francis, Washington DC, USA, 1992.
54. Mucciardi, and Jin, N., "Extending Lance Life in Top Blowing", Copper '99, TMS, Oct. 1999, pp. 207-222.
55. Mucciardi, F., "Improving Injection Lances with Heat Pipe Technology", The Brimacombe Memorial Sym. – Poster Proceedings, MetSoc-CIM, Oct. 2000, pp. 205-218.
56. Mucciardi, F., and Jin, N., "Mathematical Model of a Heat Pipe Lance", (Paper presented at the Computer Applications in Metallurgy and Materials Processing Sym., CIM, 1998, available at electronic address: <www.mmpc.mcgill.ca/~frank>, August 2006)
57. Mucciardi, F., and Yuan, Z., "Waterless Oxygen Lance for Steelmaking and Refining", Sym. on Innovative Technologies for Steel and Other Materials, MetSoc-CIM, 2001, pp. 159-170.

58. Mucciardi, F., et al., "Heat Pipe", U.S. Patent Application, Filed on Feb. 25, 2002 (34 claims).
59. Yuan, Z., and Mucciardi, F., "Heat Fluxes from Aluminum Melts to Isothermal Surfaces", MetSoc-CIM, 2002, pp. 335-349.
60. Yuan Z., and Mucciardi, F., "Waterless Non-Consumable Thermopump Lances," *International Symposium on Ecomaterials and Ecoprocesses*, 2003, pp. 229-242.
61. Zhang, C., Mucciardi F., and Gruzleski, J.E., "Heat Pipe Cooling of Permanent Mold Castings of Aluminum Alloys," AFS Transaction, Vol. 110, 2002, pp. 435-448.
62. Elalem, K., et al., "Development of Heat Pipe Technology for Permanent Mold Casting of Magnesium Alloys", MetSoc-CIM, Aug. 2002, pp. 399-413.
63. Elalem, K., Mucciardi, F., and Gruzleski, J.E., "Industrial Applications of Heat Pipe Technology to the Permanent Mold Casting of Magnesium Alloys," 42nd Conference of Metallurgists, Vancouver, British Columbia, COM 2003, Light Metals Proceedings, pp. 243-259.
64. Zhang, C., Mucciardi, F., and Gruzleski, J.E., "Effects of Heat Pipe Cooling on Permanent Mold Casting of Aluminum Alloys," *Light Metals*, 2002, pp. 321-334.
65. Y. Carbonneau, et al., "Permanent Mold Casting of Magnesium Alloys", Proc. Of 59th Annual Magnesium Conference, May 2002, pp. 33-43.
66. Mucciardi, F., Yuan, Z., and Zhang, C., "The Heat Pipe as a Sensor of Temperature, Level and Flow", Process Sensors Sym. of AISE, Feb. 2001, pp. 1-17.
67. Musmar, S., et al., "Investigation of Iron and Copper Intermetallics in 356 Aluminum Alloy and in Al-7%Si Binary Alloy by an in-Situ Thermal Analysis Probe", paper accepted for 110th Metalcasting Congress (AFS), Columbus, OH, USA, April 18-21 2006.

-
68. Musmar, S., "In-Situ Thermal Analysis Probe," Ph.D. Thesis, McGill University, Montreal, Canada, 2006.
69. Zhang, C., Mucciardi, F., Gruzleski, J.E., "Heat Pipe Cooling of Permanent Mold Castings of Aluminum Alloys", AFS Transactions, May 2002, Vol. 110, pp. 435-448.
70. Zhang, C., Mucciardi, F., and Gruzleski, J.E., "Application of Controllable Heat Pipe Cooling During the Low Pressure Die Casting of Aluminum Alloys," Transactions of American Foundry Society, 111, pp. 69-79.
71. Zhang, C., Mucciardi, F., and Gruzleski, J.E., "Controlled Cooling of Permanent Molds in the Casting of Aluminum", Light Metals Sym. of MetSoc, CIM, Aug. 2001, pp. 431-441.
72. Mucciardi, F., and Zheng, G., "Heat Transfer in the Boiling Regime", Fundamentals of Metallurgical Processing – J.M. Toguri Sym., MetSoc-CIM, Aug. 2000, pp. 335-350.
73. Batchelor, G.K., "An Introduction to Fluid Dynamics," Cambridge Univ. Press, Cambridge, England, 1967.
74. Patankar, S.V., "Numerical Heat Transfer and Fluid Flow," Hemisphere, Washington, D.C., 1980.
75. _____, "Fluent 6.2 User's Guide." CFD Modeling Software Online User Manual Page. Electronic address: <http://www.fluentusers.com/fluent/doc/doc_f.htm> (August, 2006).
76. Iserles, A., "A First Course in Numerical Analysis of Differential Equations," Cambridge University Press, Cambridge, UK, 2000.
77. Verguts, P., "A Two-Dimensional Steady-State Simulation Model of a Lead Blast Furnace for Secondary Raw Materials," Ph.D. Thesis, Katholieke Universiteit Leuven, Leuven, Belgium, 2005.

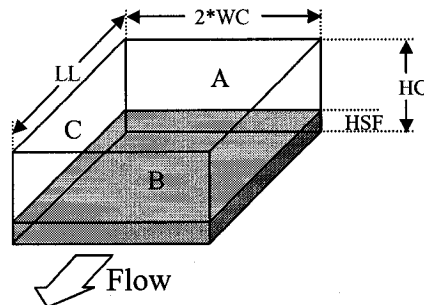
78. McCable L.W., Smith C.J., Harriott, P., "Unit Operations of Chemical Engineering", 6th edition, McGraw-Hill Inc., New York, USA, 2001.
79. Ruz, P., et al., "Numerical Modeling of Heat Transfer of a Smelter Ladle, With and Without a Refractory Lining", Copper-Cobre 99 – Smelting, Technology Development, Process Modeling and Fundamentals, 1999, pp. 433-445.
80. Anderson, W.G., et al., "Evaluation of Heat Pipe Working Fluids in the Temperature Range of 450 to 700K", Space Technology and Applications International Forum, 2004, pp. 20-27.
81. P. Navarra, et al., "Heat Pipe Cooling of a Slag Tapblock", Converter and Fire Refining Processes, EPD Congress (TMS), 2005, pp. 701-712.
82. P. Navarra, et al., "Mathematical Modeling and Design of Heat Pipe-Cooled Metallurgical Furnace Equipment", Materials Processing Fundamentals: Process Modeling, EPD Congress (TMS), 2006, pp. 679-688.
83. P. Navarra, "Heat Pipe Cooling of a Slag Launder – Project Update 2", internal report submitted to Umicore Research, December 2002.
84. _____, "Copper Development Association Inc." Copper Information Page. Electronic address: <http://www.copper.org/resources/properties/> (August 2006).
85. _____, "Goodfellow Cambridge Limited." Materials Supplier Information Page. Electronic address: <http://www.goodfellow.com> (August 2006).
86. Correspondences via email with Sybolt Brouwer, plant manager of Umicore Hoboken blast furnace, March 1st 2005.
87. J. Yen, et al., "Effect of FeO, MgO, and SiO₂ Additions on Viscosities of Lead Blast Furnace Slags", SME Annual Publication, 2005, pp. 1-7.

88. V.R. Voller and C.R. Swaminathan, "Generalized Source-Based Method for Solidification Phase Change", *Journal of Numerical. Heat Transfer*, 19(2), pp. 175-189, 1991.
89. Zhao, H., "Development of a Sulfur-Based McGill Heat Pipe," Ph.D. Thesis, McGill University, Montreal, Canada, 2006.
90. Carey V.P., "Liquid-Vapour Phase-Change Phenomena: An Introduction to the Thermophysics of Vaporization and Condensation Processes in Heat Transfer Equipment", Taylor and Francis, 1992.
91. Levy, S., "Two-Phase Flow in Complex Systems", Wiley-Interscience, 1999.
92. Navarra, P., Zhao, H. and Mucciardi, F., *Improvement of Flow Modifiers used in McGill Heat Pipes*, Paper presented at the Multiphase Phenomena in Materials Processing Symposium (TMS Annual Meeting), 2004.
93. _____, "Advanced Turbulence Modeling," Fluent Inc, Lebanon, NH, USA, 2005.
94. Bartolomei, G.G., Chanturiya, V.M., "Vapor Content of Boiling Coolant in Tube and Rod Assemblies," *Teploenergetika*, 14 (2), pp. 123-128, 1967.
95. Kurul, N., Podowski, M.Z., "Multidimensional Effects in Forced Convection Subcooled Boiling," 9th International Heat Transfer Conference, Jerusalem, pp.. 21-26, 1990.

Appendix A

Slag Launder Radiation Analysis

The slag channel geometry can be roughly represented as a box with the following dimensions:



In the present model:

WC = 11.5 cm

HC = 12 cm

LL = 30 cm

HSF = 3 or 6 cm

Where:

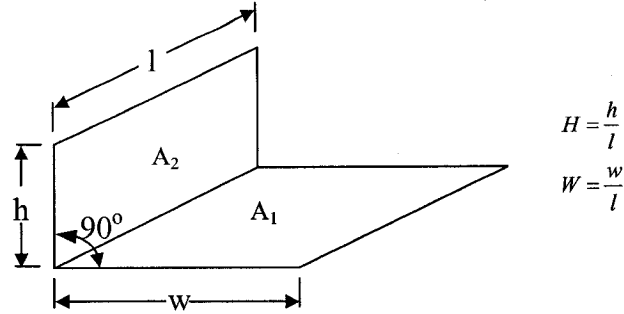
A – entrance to the decantation vessel

B – slag surface

C – launder sidewall

The following assumptions were used:

- All surfaces are diffuse and have uniform radiosity.
- The decantation vessel is very large, and its radiative heat flux can be approximated by the radiative heat flux from an imaginary surface A at a temperature of 1493 K (1220°C).
- The slag surface (B) is at a uniform temperature of 1493 K (1220°C).
- All emissivities are equal to unity.
- Only surfaces A and B emit significant radiation in the above enclosure.



$$F_{1-2} = \frac{1}{\pi W} \left(W \tan^{-1} \frac{1}{W} + H \tan^{-1} \frac{1}{H} - \sqrt{H^2 + W^2} \tan^{-1} \frac{1}{\sqrt{H^2 + W^2}} + \frac{1}{4} \ln \left[\frac{(1+W^2)(1+H^2)}{(1+W^2+H^2)} \right] \left[\frac{W^2(1+W^2+H^2)}{(1+W^2)(W^2+H^2)} \right]^{W^2} \left[\frac{H^2(1+H^2+W^2)}{(1+H^2)(H^2+W^2)} \right]^{H^2} \right)$$

From this relationship, we find that the view factors are as follows:

	HSF = 3 cm	HSF = 6 cm
F_{A-C}	0.138	0.108
F_{B-C}	0.132	0.099

Using the relationship:

$$G_{1-2} = F_{1-2} \epsilon_1 \alpha_2 \sigma T_1^4$$

where

G_{1-2} is the net radiation absorbed by surface 2 from radiation emitted by surface 1

F_{1-2} is the view factor between surfaces 1 and 2

ϵ_1 is the emissivity of surface 1

α_2 is the absorptivity of surface 2 (is equal to ϵ_2 for a diffuse black body)

σ is the Stephan-Boltzmann constant ($5.67 \times 10^{-8} \text{ W/m}^2 \cdot \text{K}^4$)

The following radiative heat fluxes applied to surface C (launder inner wall) were calculated:

	HSF = 3 cm	HSF = 6 cm
Flux from surface A	38.8 kW/m ²	30.5 kW/m ²
Flux from surface B	37.2 kW/m ²	27.7 kW/m ²
Total Heat Flux onto C	76.0 kW/m ²	58.2 kW/m ²
Surface Area of Surface C	0.027 m ²	0.018 m ²
Radiative Heat Load to C	2.5 kW	1.4 kW